8-29-2018

Applications of mineral chemistry to petrogenesis and exploration in conduit-type Cu-PGE deposits

Matthew Jacek Brzozowski
University of Windsor

Applications of mineral chemistry to petrogenesis and exploration in conduit-type Cu- PGE deposits

By

Matthew Brzozowski

A Dissertation
Submitted to the Faculty of Graduate Studies
through the Department of Earth and Environmental Sciences
in Partial Fulfillment of the Requirements for
the Degree of Doctor of Philosophy at the
University of Windsor

Windsor, Ontario, Canada

2018

Applications of mineral chemistry to petrogenesis and exploration in conduit-type Cu-PGE deposits

by

Matthew Brzozowski

APPROVED BY:

_____
P. Hollings, External Examiner
Lakehead University

_____
D. Good
Western University

_____
R. Linnen
Western University

_____
S. Loeb
Department of Chemistry and Biochemistry

_____
J. Gagnon
Department of Earth and Environmental Sciences

_____
A. Polat
Department of Earth and Environmental Sciences

_____
I. Samson, Advisor
Department of Earth and Environmental Sciences

August 9, 2018

Author's Declaration of Co-Authorship/Previous Publication

I. Co-Authorship

I hereby declare that this thesis incorporates material that is result of joint research, as follows:

Chapter 1 of the thesis was co-authored with Dr. Joel Gagnon, Dr. Robert Linnen, Dr. David Good, Dr. Doreen Ames, and Dr. Roberta Flemming under the supervision of Dr. Iain Samson. Chapters 2 through 4 of the thesis were co-authored with Dr. Joel Gagnon, Dr. Robert Linnen, Dr. David Good under the supervision of Dr. Iain Samson. In all cases, the key ideas, primary contributions, experimental designs, data analysis, interpretation, and writing were performed by the author. The contribution of co-authors was primarily through the refinement of ideas and models, and editing of the manuscripts. In addition, for Chapter 2 of this thesis, Dr. Doreen Ames also analyzed several samples using the electron microprobe.

I am aware of the University of Windsor Senate Policy on Authorship and I certify that I have properly acknowledged the contribution of other researchers to my thesis, and have obtained written permission from each of the co-author(s) to include the above material(s) in my thesis.

I certify that, with the above qualification, this thesis, and the research to which it refers, is the product of my own work.

II. Previous Publication

This thesis includes 1 original paper that has been previously published/submitted for publication in peer reviewed journals, as follows:

Thesis Chapter	Publication title/full citation	Publication status*
Chapter 2	Controls on the chemistry of minerals in late-stage veins and implications for exploration vectoring tools for mineral deposits: an example from the Marathon Cu-Pd deposit, Ontario, Canada	Published in the Journal of Geochemical Exploration

I certify that I have obtained a written permission from the copyright owner(s) to include the above published material(s) in my thesis. I certify that the above material describes work completed during my registration as a graduate student at the University of Windsor.

III. General

I declare that, to the best of my knowledge, my thesis does not infringe upon anyone's copyright nor violate any proprietary rights and that any ideas, techniques, quotations, or any other material from the work of other people included in my thesis, published or otherwise, are fully acknowledged in accordance with the standard referencing practices. Furthermore, to the extent that I have included copyrighted material that surpasses the bounds of fair dealing within the meaning of the Canada Copyright Act, I certify that I have obtained a written permission from the copyright owner(s) to include such material(s) in my thesis.

I declare that this is a true copy of my thesis, including any final revisions, as approved by my thesis committee and the Graduate Studies office, and that this thesis has not been submitted for a higher degree to any other University or Institution.

Abstract

The mineralogy and mineral chemistry of Fe-Ti oxides, sulfides, and vein-hosted silicates has been used to characterize the petrogenesis of the Eastern Gabbro of the Coldwell Complex, Ontario, to better characterize the processes that generated and modified copper and platinum-group element (PGE) mineralization that it contains, and to develop and test exploration tools in this system. Understanding these processes is critical to an understanding of conduit-type Cu-PGE systems and their exploration potential.

Fe-Ti oxides in the Eastern Gabbro exhibit a continuum of mineralogically distinct exsolution textures. Trellis-type intergrowths, which have systematically higher Fe^{3+} : Fe^{2+} and multivalent-element concentrations than cloth-type intergrowths, formed through subsolidus oxidation of the latter by a CO_2-rich fluid. Variable distribution of cloth- and trellis-type intergrowths in different rock types and mineralized occurrences in the Eastern Gabbro indicate that they experienced different degrees of fluid-induced oxidation. The elements that are typically used for petrogenesis were not affected by subsolidus oxidation as this process only affected the concentration of a few multivalent elements. Accordingly, oxide chemistry indicates that the metabasalt and Layered Series of the Eastern Gabbro crystallized from magmas that experienced little to no magma mixing, with the latter having crystallized from a more evolved magma than the former. The later, mineralized Marathon Series crystallized from mixtures of several physically and compositionally distinct magmas. These features are consistent with formation of the mineralization in the Marathon Series in a magma conduit. The data from the Eastern Gabbro indicate that the chemistry of oxides is not a robust indicator of mineralization because oxide chemistry is

the same in mineralized and barren rock, and because mineralization could not be accurately identified using previously-developed petrogenetic tools that use oxide chemistry.

An understanding of the processes that generate and modify mineralization can help identify exploration targets in variably mineralized plutons. The compositional similarity between magmatic and hydrothermal chalcopyrite, which occur throughout the Eastern Gabbro, indicate that the latter formed through the local dissolution and re-precipitation of the former. Variations in whole-rock Cu/Pd and sulfide S/Se demonstrates that two dominant processes generated the variable Cu/Pd mineralization in the Eastern Gabbro. First, mineralized zones in different parts of the system were variably contaminated by rocks with low and high S/Se. Second, sulfides in different zones experienced different R factors, which resulted in mineralization with variable PGE grades.

The trace-element chemistry of vein minerals in late-stage hydrothermal veins is largely independent of local controls (e.g., host rock, host mineral). Although their chemistry appears to vary with proximity to mineralization, this interpretation is misleading as the same variability is observed with proximity to the footwall contact. Their chemistry is, therefore, not a robust vector for mineralization. Variations in vein density, however, may provide a valuable tool for locating zones of mineralization. This demonstrates the need to assess the sources of metals in vein-hosted minerals prior to the application of their chemistry to mineral exploration.

This dissertation is dedicated to my parents, my sister, and my girlfriend who provided the love, support, and encouragement throughout my educational career. I could not have done this without you.

Acknowledgments

I would like to express my sincere gratitude to Dr. Iain Samson, my advisor, for his continued scientific and financial support, and his encouragement to always strive to do great research. His dedication to science has truly shaped the way that I view scientific research and has motivated me to continue expanding our knowledge with impactful research. Without his inspiration and guidance throughout my graduate work, this dissertation would not be possible. I would also like to thank Dr. Joel Gagnon for his scientific advice, as well as the motivation that he instilled through his uplifting spirit. This research was funded by an NSERC research grant to Dr. Iain Samson and Dr. Joel Gagnon.

I would like to graciously thank Dr. David Good from Western University who provided me the opportunity to work for Stillwater Canada Inc. during my undergraduate and graduate careers. The time spent in the field and looking at drill core were invaluable to my research. I would also like to thank him for his financial support that he provided through Stillwater Canada Inc., his insights into the geology of the study area, as well as his motivating attitude. I would like to thank Dr. Robert Linnen from Western University for his contributions and helpful suggestions, which not only strengthaned this dissertation, but also inspired me to continue to do great scientific research. I am thankful to Dr. Doreen Ames for her financial support through TGI4, as well as her suggestions.

The entire staff at Stillwater Canada Inc., including Rachel Epstein, Katrina McLean, Ryan Ruthart, and John McBride are thanked for their support during field work and sampling, and for providing their knowledge of the study area. I would graciously like to thank Melissa Price from the University of Windsor for her support during analytical work, as well as her encouragement. Sharon Lackie and J.C. Barrette from the Great Lakes Institute of Environmental Research are thanked for their support during SEM and LA-ICP-MS analyses. I would like to express my thanks to all of the faculty, staff, former and current graduate students in the Department of Earth and Environmental Sciences for their support. I would like to give a special thanks to Maryam Shahabi Far for her help with this study and her constant encouragement.

I would lastly like to extend my sincerest gratitude to my parents, my sister, and my girlfriend. Without their love and support I would not be where I am today.

Table of Contents

List of Tables

List of Figures

List of Electronic Appendices

List of Abbreviations

4D	Four Dams mineralization
A41	Area 41 mineralization
Ap	Apatite
Bdy	Baddeleyite
BIF	Banded iron formation
Bn	Bornite
BSE	Backscatter electron
Ccp	Chalcopyrite
C_o	Concentration of an element in the original liquid
Cpx	Clinopyroxene
C_{sul}	Concentration of an element in the sulfide liquid
Cub	Cubanite
$D^{MSS/ISS}$	Monosulfide solid solution-intermediate solid solution partition coefficient
$D^{MSS/sul}$	Monosulfide solid solution-sulfide liquid partition coefficient
$D^{sul/sil}$	Sulfide liquid-silicate melt partition coefficiention
EDS	Energy-dispersive spectrometry
EELS	Electron energy loss spectroscopy
EPMA	Electron probe microanalysis
FMQ	Fayalite-magnetite-quartz buffer
fO_2	Oxygen fugacity
FZ	Footwall zone
HFSE	High-field strength element (Zr, Hf, Nb, Ta)
HW	Hanging Wall
Ilm	Ilmenite
IOCG	Iron oxide copper gold deposit
ISS	Intermediate solid solution
LA-ICP-MS	Laser ablation inductively-coupled plasma mass spectrometry
LS	Layered Series mineralization
LV	Liquid-vapor
MAC	Magnetite-apatite-clinopyroxene cumulate
MSS	Monosulfide solid solution
Mt	Magnetite
MZ	Main Zone
Ol	Olivine
PGE	Platinum-group element
PGM	Platinum-group mineral
Pl	Plagioclase

Pn	Pentlandite
Po	Pyrrhotite
Px	Pyroxene
R	Sulfide-silicate mass ratio
RS	Redstone mineralization
RSD	Relative standard deviation
S.E.	Standard error
SEDEX	Sedimentary exhalative deposit
SEM	Scanning electron microscope
Sil	Silicate
Sp	Spinel
Sph	Sphalerite
Sul	Sulfide
TDLG	Two Duck Lake gabbro
USGS	United States Geological Survey
Usp	Ulvöspinel
V	Vapor
VMS	Volcanogenic massive sulfide deposit
WDS	Wavelength-dispersive spectrometry
WH	W Horizon
XANES	X-ray absorption near edge structure
XRD	X-ray diffraction

Chapter 1

Introduction

1.1 Introduction

The platinum-group elements (PGE) consist of six elements (Pt, Pd, Ir, Os, Rh, and Ru) that share similar chemical properties, but have diverse physical properties (Gunn and Benham 2009). All of the PGE are depleted in the Earth's crust, with average crustal abundances of 1-5 parts per billions (ppb) (Gunn and Benham, 2009). Given their importance in a number of industries and processes, including computer electronics, biomedical equipment, as catalysts in industrial processes, and in the refinement of petroleum (Gunn and Benham, 2009), finding economic concentrations of the PGE is important. This, in turn, requires a comprehensive understanding of the natural processes that concentrate the PGE, as well as the processes that can modify their concentration in rocks.

Economic concentrations of PGE principally occur in magmatic Ni-Cu-PGE sulfide deposits, the largest of which are hosted by mafic to ultramafic rocks (Holwell and McDonald, 2010). The Coldwell Complex in northwestern Ontario contains several Cu-Pd sulfide deposits that are hosted in a series of mafic to ultramafic rocks, and include the Marathon, Four Dams, Area 41, and Redstone Cu-Pd deposits (Fig. 1.1). Although research in the past several years has greatly enhanced our understanding of these deposits and their host rocks, there are still unanswered questions regarding the processes that generated and modified the mineralization, the petrogenetic relationship between barren and mineralized rock, and whether any mineralogical-geochemical signatures exist that can aid in the exploration for additional Cu-Pd mineralization.

1.2 Magmatic Ni-Cu-PGE sulfide deposits

Although economically-viable PGE concentrations can occur in sulfide deposits associated with chromitites in ophiolites and as placer deposits associated with Ural-Alaskan-type

ultramafic plutons, the most important sources of PGE occur in base-metal sulfide deposits hosted by mafic to ultramafic igneous plutons (i.e., magmatic Ni-Cu-PGE sulfide deposits) (Holwell and McDonald, 2010). Key processes in the formation of magmatic Ni-Cu-PGE deposits include i) saturation of the host magma with respect to sulfur and segregation of an immiscible sulfide liquid, ii) equilibration of the sulfide liquid with large volumes of silicate melt to allow the effective scavenging of metals that favour the sulfide phase, and iii) concentration of the metal-enriched sulfide liquid into a small volume of rock (Naldrett, 1999; Robb, 2004).

Several processes can contribute to a silicate melt becoming sulfur saturated. Although sulfide saturation can be achieved by fractional crystallization of the silicate melt, this requires extensive fractionation and is unfavorable for the formation of economically-viable mineral deposits because metals (e.g., Ni) would have been removed from the melt by the crystallization and fractionation of silicates and oxides (Robb, 2004). The most obvious way to achieve sulfide saturation relatively early in the evolution of a silicate melt is by the direct addition of external S as a result of, for example, assimilation of S-bearing rocks (Robb, 2004). Because sulfide solubility is inversely related to the SiO_2 content of the silicate melt, saturation can also be achieved by addition of SiO_2 as a result of, for example, assimilation of siliceous rocks (Robb, 2004). Injection of new magma can also promote sulfide saturation through the mixing of variably-evolved melts with more primitive melt (Robb, 2004).

In order for a sulfide deposit to form, not only does sulfide liquid need to segregate, but it also has to be enriched in metals. The enrichment of a sulfide liquid in metals is dependent on two parameters: i) the sulfide liquid/silicate melt partition coefficient ($D^{SL/SM}$) and ii) the R factor. The $D^{SL/SM}$ values for chalcophile elements are very high, ranging from ~ 275 for Ni up to 10^6 for the PGE (Barnes and Ripley, 2016). The R factor is the silicate melt to sulfide liquid mass ratio and is a measure of the extent to which the sulfide liquid interacts with the silicate melt from which it segregated (Campbell and Naldrett, 1979; Robb, 2004). Because of the high $D^{SL/SM}$ of chalcophile elements, high R factors through, for example, mixing of multiple batches of magma, are required for metals to become

highly concentrated in the sulfide liquid. High R factors, however, are difficult to attain given the tendency for two liquids with different densities to separate (Kerr and Leitch, 2005). Multistage dissolution upgrading (Kerr and Leitch, 2005) is a potential mechanism which permits sulfides to attain high R factors by fluxing batches of magma through a magma conduit, which dissolves some proportion of previously-exsolved sulfide liquid. This dissolution releases the PGE in the sulfide liquid to the surrounding silicate melt, allowing the remaining sulfide liquid to scavenge them. Multistage dissolution upgrading has important implications for the formation of economically-viable PGE deposits. i) It permits the generation of PGE deposits using less silicate melt than is required in a closed-system model. ii) It results in higher PGE/base metal ratios in the sulfide liquid than would be possible in closed systems because elements with high $D^{SL/SM}$ (i.e., PGE) can increase without limit, whereas elements with moderate $D^{SL/SM}$ (i.e., base metals) cannot.

As the sulfide liquid cools, it fractionates into monosulfide solid solution (MSS; an Fe-Ni-rich phase) and intermediate solid solution (ISS; a Cu-rich phase), which recrystallize to pyrrhotite + pentlandite, and to chalcopyrite, respectively. In S-rich, main-group-element-poor systems, the iridium-group PGE (IPGE; Ir, Ru, Os) partition into MSS and are concentrated in pyrrhotite and pentlandite, whereas the platinum-group PGE (PPGE; Pt, Pd, Rh) partition into ISS and are concentrated in chalcopyrite. If the sulfide liquid contains high concentrations of main-group elemnets (e.g., As, Sb, Te), however, a late-stage immiscible melt rich in main-group elements can form and concentrate the PPGE and eventually crystallize to discrete platinum-group minerals (PGM) (Cabri and Laflamme, 1976; Helmy et al., 2007) or the PGM can crystallize directly from the sulfide melt.

1.3 Hydrothermal mobility of PGE

The spatial association of high salinity fluid inclusions, Cl-rich hydroxy-silicates, and PGE halide minerals (Pd-Bi-Cl) with sulfide-bearing PGE mineralization in Ni-Cu-PGE deposits has commonly been cited as evidence for the remobilization of PGE by low-temperature (< 500 ºC) hydrothermal fluids (Hanley, 2005). Under highly oxidizing (log fO_2 > -25 atm) and/or highly acidic (pH < 2) conditions, Pd and Pt have been

experimentally-demonstrated to be mobile as chloride complexes (Gammons, 1996, 1995). Because these conditions are not typical of magmatic Ni-Cu-PGE environments, however, it is unlikely that the PGE were transported as chloride complexes, which is consistent with the lack of alteration mineral assemblages in these systems (e.g., muscovite) that are indicative of low pH, high fO_2 conditions (Hanley, 2005). Rather, Ni-Cu-PGE deposits typically contain chlorite-actinolite-epidote-calcite alteration assemblages, indicative of near-neutral pH fluids (Hanley, 2005). Under these conditions, the solubility of PGE has been demonstrated to be many orders of magnitude greater as bisulfide complexes than as chloride complexes (Hanley, 2005). Although potentially unimportant for the mobilization of PGE in Ni-Cu-PGE deposits, chlorine-rich fluids have been demonstrated to mobilize base metals (e.g., Cu, Fe, Zn) from sulfides, which can modify the original metal tenor (e.g., Cu/Pd) of the deposit (Hemley et al., 1992).

Several lines of evidence have also been noted for the mobility of PGE, predominantly Pd and Pt, in high-temperature (800 to 900 ºC) hydrothermal fluids (Hanley, 2005 and references therein). At these temperatures, chloride was experimentally-demonstrated to be the dominant ligand (Wood et al., 1992). Consequently, although concentration of PGE by sulfide melts is the most accepted model for formation of PGE deposits, models that involve mobilization of PGE by high-temperature (e.g., deuteric) fluids have been proposed (e.g., chromatographic separation, Boudreau and McCallum, 1992; Boudreau and Meurer, 1999).

Given the variable mobility of base metals and PGE in hydrothermal fluids, the composition of sulfides that precipitate from fluids should be different than those that crystallize from sulfide liquids. This characteristic is critical in assessing the origin of sulfides and understanding the processes that generated and modified mineralization in magmatic Ni-Cu-PGE deposits. Chapter 5 of this dissertation integrates textural variations in sulfides throughout the various mineralized zones in the Eastern Gabbro with variations in their trace-element chemistry in an effort to understand the magmatic and postmagmatic processes that generated and modified the mineralization.

1.4 Application of mineral chemistry to mineral deposit exploration and petrogenesis

1.4.1 Mineral deposit exploration

Although the use of indicator minerals for mineral deposit exploration is not a new concept, the use of mineral chemistry has been described less often, particularly with respect to their use as vectoring tools in magmatic Ni-Cu-PGE deposits. The minerals used for exploration can be subdivided into those that formed after mineralization (i.e., vein minerals) and those that formed during the crystallization of the rocks (i.e., the rock-forming minerals).

Few studies have characterized the composition of vein-hosted minerals with proximity to mineralization, particularly in systems that experienced low fluid:rock ratios. Hanley and Bray (2009) and Wilkinson et al. (2015) demonstrated that some metals can be used as vectors in Ni-Cu-PGE and porphyry Cu-Au systems, respectively. Hanley and Bray (2009) noted that the concentration of Ni varied systematically with distance to mineralization in the footwall deposit of the Sudbury Igneous Complex, whereas Wilkinson et al. (2015) noted that Zn, Mn, Co, and Ni varied systematically with proximity to porphyry centres. Neither of these studies, however, characterized how the chemistry of vein minerals varied in response to other factors, such as host rock and host mineral. This is critical because, to be a successful exploration tool, any dispersion haloes recorded by the vein minerals must be independent of any local effects (e.g., host rock and mineral chemistry). Rather, the chemistry of the fluid from which the minerals precipitated needs to be the dominant control. Chapter 2 of this dissertation integrates detailed mineralogical and textural characterization of vein-hosted minerals with variations in their trace-element chemistry as a function of numerous parameters (e.g., host rock, host mineral), including proximity to mineralization, to assess the applicability of vein mineral chemistry to exploration in systems with low fluid:rock ratios.

In the past decade, there has been an increase in the characterization of Fe-Ti oxide chemistry for potential use in exploration (Boutroy et al., 2014; Dare et al., 2014a; Dupuis

and Beaudoin, 2011; Rusk et al., 2009; Ward et al., 2018). Many studies have noted that oxides hosted in different styles of mineralization (e.g., iron-oxide-copper-gold (IOCG), volcanogenic massive sulfide (VMS), skarn) were compositionally distinct (e.g., Carew et al., 2006; Kamvong et al., 2007; Rusk et al., 2009; Singoyi et al., 2006). In a recent comprehensive study, Dupuis and Beaudoin (2011) created several discrimination diagrams to distinguish low-Ti magnetite from a variety of magmatic and hydrothermal mineral deposits, including Ni-Cu, VMS, and IOCG. Dare et al. (2014a) and Ward et al. (2018) noted that the Ni content of magnetite varies between those hosted in barren and mineralized rock, with the former noting that magnetite hosted in mineralized rock is depleted in Ni, and the latter noting that it is enriched. Despite this recent work, few studies (e.g., Ward et al., 2018) have characterized in detail how the composition of Fe-Ti oxides vary between barren and mineralized rock in magmatic Ni-Cu-PGE deposits that are hosted in the same igneous pluton or which are genetically related.

1.4.2 Mineral deposit petrogenesis

The past decade has seen a growing interest in the use of magnetite and ilmenite chemistry for petrogenesis in magmatic(-hydrothermal) sulfide deposits. Most of the work that has been done pertaining to the petrogenesis of such deposits has focused on characterizing variations in the most compatible elements into magnetite (i.e., V, Cr) in an effort to identify primitive magma injection events, magma mixing, and contamination (e.g., McCarthy et al., 1985; McCarthy and Cawthorn, 1983; Namur et al., 2010; Tegner et al., 2006). These can be identified by deviations away from the variations expected in these elements due to fractional crystallization. Very few studies have incorporated multiple compatible and incompatible elements in their interpretations (e.g., Dare et al., 2014b). The use of both compatible and incompatible elements, however, is critical for characterizing magmatic processes as they should behave coherently during, for example, fractional crystallization. Dare et al. (2014b) summarized the variations expected in the composition of magnetite as a function of melt fractionation, noting that magnetite that crystallized from a primitive melt will be enriched in magnetite-compatible elements (e.g., Cr, Ni, V, Co, Mg) and depleted in magnetite-incompatible elements (e.g., Zn, Ga, HFSE, Sn).

Conversely, magnetite that crystallized from an evolved melt will be depleted in compatible elements and enriched in incompatible elements.

Many of the studies discussed above regarding mineral deposit petrogenesis and exploration focused on end-members with respect to magma evolution (e.g., primitive vs. evolved melts) and style of mineralization (e.g., magmatic vs. hydrothermal). Although studies such as these are required in order to understand how mineral chemistry varies as a result of different magmatic and post-magmatic processes, the results of these studies have not been extensively applied to complex Ni-depleted igneous suites that formed through the emplacement of multiple batches of magma, are variably mineralized, and which experienced low fluid:rock ratios during subsequent hydrothermal activity.

Chapter 3 of this dissertation integrates the textural variations in Fe-Ti oxide intergrowths throughout the Eastern Gabbro with variations in their trace-element chemistry to assess the role of fluids in their generation and how this fluid interaction affected their chemistry. This is of particular importance to Chapter 4, which characterizes the variation in trace-element chemistry of Fe-Ti oxide intergrowths hosted in the different rock series, rock types, and zones of mineralization in the Eastern Gabbro with the goal of understanding their petrogenetic relationships. In addition, Chapter 4 also examines the applicability of previously-developed discrimination diagrams and exploration criteria that employ magnetite chemistry to Ni-depleted systems.

1.5 Geological setting

1.5.1 Coldwell Complex

The Midcontinent Rift-related Coldwell Complex, located on the northeast shore of Lake Superior, is a composite pluton that intruded into Archean rocks of the Schreiber-White River greenstone belt at circa 1.1 Ga. The Coldwell Complex is composed of three intrusive centres, which, in order intrusion are Centre I, Centre III, and Centre II (Currie, 1980; Kulakov et al., 2014; Mitchell and Platt, 1982; Walker et al., 1993). Centre I is silica-

saturated and consists of syenite, the Geordie Lake Gabbro, the Western Gabbro, and the Eastern Gabbro, the latter of which is host to the Marathon, Four dams, Area 41, and Redstone Cu-Pd deposits (Walker et al., 1993). Centre III is silicate-oversaturated and is composed of syenite and granite (Mitchell and Platt, 1982; Mitchell et al., 1991). Centre II is silica-undersaturated and composed of nepheline syenite and alkaline gabbro (Walker et al., 1993).

1.5.2 Eastern Gabbro

The Eastern Gabbro occurs around the eastern margins of the Coldwell Complex (Good et al., 2015; Good and Crocket, 1994). It was subdivided by Good et al. (2015) into three genetically-distinct rock series termed metabasalt, Layered Series, and Marathon Series. The metabasalt, which makes up 20 to 30% of the Eastern Gabbro, is the earliest of the intrusive series and comprises homogenous and equigranular basalt that has been metamorphosed to hornfels grade (Good et al., 2015). Unlike the other two rock series, however, it lacks any form of mineralization (Good et al., 2015). The Layered Series makes up the majority of the Eastern Gabbro and occurs above the metabasalt at the Marathon Cu-PGE deposit (Good et al., 2015). Although it is texturally homogenous throughout the Eastern Gabbro, it is compositionally variable (Cao, 2017; Shaw, 1997). It has an average composition of olivine gabbro, which grades into oxide augite melatroctolite, and displays modal layering characterized by variations in the proportions of plagioclase and pyroxene (Good et al., 2015). The Layered Series is devoid of PGE mineralization, but secondary chalcopyrite and pyrrhotite occur locally in association with actinolite and albite alteration (Good et al., 2015). The Marathon Series is the youngest of the intrusive series and hosts significant Cu and PGE mineralization, including the Marathon, Four Dams, Area 41, and Redstone deposits (Good et al., 2015). At the Marathon deposit, the Marathon Series is dominated by the Two Duck Lake gabbro, a coarse to pegmatitic gabbro that displays ophitic to subophitic texture (Good et al., 2015). This intrusive series also contains several sill- to pod-like bodies of oxide melatroctolite and apatitic olivine clinopyroxenite (Good et al., 2015).

1.5.3 Mineralization in the Eastern Gabbro

Mineralization at the Marathon deposit occurs in three lenses that are texturally, mineralogically, and geochemically distinct. In order of increasing distance from the footwall contact, these include the Footwall Zone, Main Zone, Hanging Wall Zone, and W Horizon (Good et al., 2015). The Footwall Zone occurs at the base of the Two Duck Lake gabbro at the contact with the Archean footwall rocks. The Main Zone is the thickest and most continuous zone of mineralization and occurs stratigraphically above the Footwall Zone. The W Horizon occurs above the Main Zone in the southern portion of the Marathon deposit, but is absent in the northern portion.

Sulfides in the Footwall Zone comprise semi-massive to net-textured pyrrhotite with lesser chalcopyrite (Good et al., 2015; Samson et al., 2008). Sulfides in the Main Zone are disseminated and occur interstitial to silicates, oxides, and apatite. In the Main Zone, sulfides are dominated by chalcopyrite and pyrrhotite, with lesser cubanite and bornite (Good et al., 2015; Samson et al., 2008). Although sulfides in the W Horizon are also disseminated and interstitial to primary minerals, the W Horizon is distinguished from the Main Zone by a lower modal abundance of sulfides and hydrous silicates, a distinct suite of platinum-group minerals (PGM), a notably higher proportion of bornite and lower proportion of pyrrhotite, lower S concentrations, and lower Cu/Pd values (Ames et al., 2017, 2016; Good, 2010; Good et al., 2017; Ruthart, 2013). According to McBride (2015), sulfides at Four Dams, Area 41, and Redstone, are dominated by chalcopyrite with lesser pyrrhotite, and minor bornite.

1.6 Research objectives

The objectives of this study fall into two broad groups that encompass i) the development of exploration tools that can be used to identify buried mineralization and ii) the development of genetic models for the formation of mineralization in the Eastern Gabbro. The *exploration* aspect focuses on i) characterizing the chemistry of post-mineralization products (i.e., veins) and how it varies with proximity to mineralization, ii) characterizing

the geochemical signatures of mineralized versus barren gabbros (i.e., characteristics affected by the mineralizing processes), and iii) assessing the applicability of current exploration tools (e.g., petrogenetic discrimination diagrams) to low-Ni, Cu-PGE systems (i.e., the Eastern Gabbro). The *genetic* aspects focus on iv) characterizing the petrogenetic relationship between the various rock series of the Eastern Gabbro (i.e., metabasalt, Layered Series, Marathon Series), and v) developing well-constrained models for the processes that caused base metal and PGE enrichment (cf. *Section 1.2*). To address these topics, the following questions are explored:

- Can the chemistry of vein-hosted minerals and Fe-Ti oxides be used to identify and vector towards Cu-PGE mineralization?
- What factors need to be considered when using vein-hosted mineral and Fe-Ti oxide chemistry for mineral exploration (i.e., what factors affect the chemistry of these minerals and how?)
- Are the previously-developed exploration tools that involve the chemistry of late-stage minerals and Fe-Ti oxides applicable to Ni-depleted Cu-PGE systems that experienced low fluid to rock ratios?
- What is the petrogenetic relationship between the metabasalt, Layered Series, and Marathon Series?
- What processes (e.g., exsolution of PGM, contamination, R factor, sulfide dissolution) generated or modified the mineralization in the various mineralized zones in the Eastern Gabbro?
- What role did hydrothermal fluids play in generating the Cu-PGE mineralization? Were base metals and PGE added to different mineralized zones or remobilized within a given zone?

This dissertation consists of six chapters. Chapters 1 and 6 are the Introduction and Conclusion, respectively, and Chapters 2 through 5 are manuscripts. Chapter 2 has now been published in the Journal of Geochemical Exploration. Chapters 3, 4, and 5 are in preparation for publication.

The studies rely heavily on a combination of detailed mineralogy and mineral-textural characterization using petrography, energy- and wavelength-dispersive spectroscopy (EDS, WDS), Raman spectroscopy, and micro X-ray diffraction (μXRD), with high-resolution trace-element characterization of minerals using laser ablation inductively-coupled plasma mass spectrometry (LA-ICP-MS). In *Chapter 2*, the mineralogy of veins and patchy alteration within and around the Marathon Cu-PGE deposit is characterized, along with their relationship to silicates, oxides, and sulfides. This is combined with detailed characterization of their trace-element chemistry to identify the factors that control the chemistry of vein-hosted minerals (e.g., host rock, host mineral), characterize the variation in the chemistry of vein-hosted minerals as a function of proximity to mineralization, and describe the evolution of the hydrothermal system in and around the Marathon Cu-PGE deposit. In *Chapter 3*, the mineralogy of texturally-diverse Fe-Ti oxide intergrowths is characterized, along with variations in their bulk chemistry to determine the mechanism of formation of magnetite-ulvöspinel-ilmenite intergrowths (e.g., subsolidus oxidation, direct exsolution), characterize the affects that this had on the bulk chemistry of Fe-Ti oxide intergrowths, and determine if these effects hinder the applicability of Fe-Ti oxide chemistry to petrogenesis and mineral exploration. In *Chapter 4*, the bulk chemistry of Fe-Ti oxide intergrowths hosted in metabasalt, Layered Series, and barren and mineralized Marathon Series is characterized in order to understand the petrogenetic relationship between these rock series and identify geochemical signatures that can distinguish between barren and mineralized rock. The bulk chemistry of Fe-Ti oxide intergrowths is also used to determine if previously-developed mineral exploration tools that employ Fe-Ti oxide chemistry are applicable to Ni-poor Cu-PGE systems, such as the Eastern Gabbro. In *Chapter 5*, the mineralogical, textural, and chemical variations of sulfides hosted in the various mineralized zones throughout the Eastern Gabbro are characterized in order to determine the processes that generated the diverse Cu/Pd ratios in each of the zones (e.g., S contamination, R factor variations, sulfide dissolution) and characterize the role that hydrothermal fluids played, if any, in generating or modifying the metal budget of each of the zones.

1.7 References

Ames, D.E., Kjarsgaard, I.M., Good, D.J., McDonald, A.M., 2016. Ore mineralogy of Cu-PGE mineralized gabbros, Coldwell Alkaline Complex, Midcontinent rift: supporting databases, scanning electron microscope, and mineral chemistry. Geological Survey of Canada Open File No. 8006.

Ames, D.E., Kjarsgaard, I.M., McDonald, A.M., Good, D.J., 2017. Insights into the extreme PGE enrichment of the W Horizon, Marathon Cu-Pd deposit, Coldwell Alkaline Complex, Canada: Platinum-group mineralogy, compositions and genetic implications. Ore Geol. Rev. 90, 723–747.

Barnes, S.-J., Ripley, E.M., 2016. Highly Siderophile and Strongly Chalcophile Elements in Magmatic Ore Deposits. Rev. Mineral. Geochem. 81, 725–774.

Boudreau, A.E., McCallum, I.S., 1992. Concentration of platinum-group elements by magmatic fluids in layered intrusions. Econ. Geol. 87, 1830–1848.

Boudreau, A.E., Meurer, W.P., 1999. Chromatographic separation of the platinum-group elements, gold, base metals and sulfur during degassing of a compacting and solidifying igneous crystal pile. Contrib. Mineral. Petrol. 134, 174–185.

Boutroy, E., Dare, S.A.S., Beaudoin, G., Barnes, S.-J., Lightfoot, P.C., 2014. Magnetite composition in Ni-Cu-PGE deposits worldwide: application to mineral exploration. J. Geochem. Explor. 145, 64–81.

Cabri, L.J., Laflamme, J.H.G., 1976. The mineralogy of the platinum-group elements from some copper-nickel deposits of the Sudbury area, Ontario. Econ. Geol. 71, 1159–1195.

Campbell, I.H., Naldrett, A.J., 1979. The influence of silicate: sulfide ratios on the geochemistry of magnetic sulfides. Econ. Geol. 74, 1503–1506.

Cao, Y., 2017. Cu-Pd mineralization and exploration geochemistry of the Eastern Gabbro, Coldwell Alkaline Complex, ON, Canada (PhD Dissertation). Western University, London, Ontario.

Carew, M.J., Mark, G., Oliver, N.H.S., Pearson, N., 2006. Trace element geochemistry of magnetite and pyrite in Fe oxide (±Cu-Au) mineralised systems: Insights into the geochemistry of ore-forming fluids, in: Goldschmidt. p. A83.

Currie, K.L., 1980. A conrtibution to the petrology of the Coldwell alkaline complex, northern Ontario. Geol. Surv. Can. Bull. 287.

Dare, S.A.S., Ames, D.E., Lightfoot, P.C., Barnes, S.-J., Beaudoin, G., 2014a. Mineral chemistry and supporting databases for TGI4 project on "Trace elements in Fe-oxides from fertile and barren igneous complexes: Investigating their use as a vectoring tool in the intrusions that host Ni-Cu-PGE deposits". Geological Survey of Canada Open File No. 7538.

Dare, S.A.S., Barnes, S.-J., Beaudoin, G., Méric, J., Boutroy, E., Potvin-Doucet, C., 2014b. Trace elements in magnetite as petrogenetic indicators. Miner. Deposita 49, 785–796.

Dupuis, C., Beaudoin, G., 2011. Discriminant diagrams for iron oxide trace element fingerprinting of mineral deposit types. Miner. Deposita 46, 319–335.

Gammons, C.H., 1996. Experimental investigations of the hydrothermal geochemistry of platinum and palladium: V. Equilibria between platinum metal, Pt (II), and Pt (IV) chloride complexes at 25 to 300 C. Geochim. Cosmochim. Acta 60, 1683–1694.

Gammons, C.H., 1995. Experimental investigations of the hydrothermal geochemistry of platinum and palladium: IV. The stoichiometry of Pt (IV) and Pd (II) chloride complexes at 100-300°C. Geochem. Cosmochem. Acta 59, 1655–1667.

Good, D.J., 2010. Applying multistage dissolution upgrading and 3D-GIS to exploration at the Marathon Cu-PGE deposit, Canada, in: 11th International Platinum Symposium, Sudbury, Ontario, Canada.

Good, D.J., Cabri, L.J., Ames, D.E., 2017. PGM Facies variations for Cu-PGE deposits in the Coldwell Alkaline Complex, Ontario, Canada. Ore Geol. Rev. 90, 748-771.

Good, D.J., Crocket, J.H., 1994. Genesis of the Marathon Cu-Platinum-Group Element Deposit, Port Coldwell Alkalic Complex, Ontario: A Midcontinent Rift-Related Magmatic Sulfide Deposit. Econ. Geol. 89, 131–149.

Good, D.J., Epstein, R., McLean, K., Linnen, R., Samson, I., 2015. Evolution of the Main Zone at the Marathon Cu-PGE Sulfide Deposit, Midcontinent Rift, Canada: Spatial Relationships in a Magma Conduit Setting. Econ. Geol. 110, 983–1008.

Gunn, A.G., Benham, A.J., 2009. Platinum, Commodity Profiles. British Geological Survey.

Hanley, J.J., 2005. The Aqueous Geochemistry of the Platinum Group Elements (PGE) in Surficial, Low-T Hydrothermal and High-T Magmatic-Hydrothermal Environments, in: Mungall, J.E. (Ed.), Exploration for Platinum-Group Element Deposits. Mineralogical Association of Canada, Oulu, Finland, pp. 35–56.

Hanley, J.J., Bray, C.J., 2009. The trace metal content of amphibole as a proximity indicator for Cu-Ni-PGE mineralization in the footwall of the Sudbury Igneous Complex, Ontario, Canada. Econ. Geol. 104, 113–125.

Helmy, H.M., Ballhaus, C., Berndt, J., Bockrath, C., Wohlgemuth-Ueberwasser, C., 2007. Formation of Pt, Pd and Ni tellurides: experiments in sulfide–telluride systems. Contrib. Mineral. Petrol. 153, 577–591.

Hemley, J.J., Cygan, G.L., Fein, J.B., Robinson, G.R., d'Angelo, W.M., 1992. Hydrothermal ore-forming processes in the light of studies in rock-buffered systems; I, Iron-copper-zinc-lead sulfide solubility relations. Econ. Geol. 87, 1–22.

Holwell, D.A., McDonald, I., 2010. A Review of the Behaviour of Platinum Group Elements within Natural Magmatic Sulfide Ore Systems. Platin. Met. Rev. 54, 26–36.

Kamvong, T., Zaw, K., Siegele, R., 2007. PIXE/PIGE microanalysis of trace elements in hydrothermal magnetite and exploration significant: a pilot study, in: 15th Australian Conference on Nuclear and Complementary Techniques of Analysis and 9th Vacuum Society of Australia Congress. University of Melbourne, Melbourne, Australia.

Kerr, A., Leitch, A.M., 2005. Self-Destructive Sulfide Segregation Systems and the Formation of High-Grade Magmatic Ore Deposits. Econ. Geol. 100, 311–332.

Kulakov, E.V., Smirnov, A.V., Diehl, J.F., 2014. Paleomagnetism of the ~1.1 Ga Coldwell Complex (Ontario, Canada): Implications for Proterozoic geomagnetic field morphology and plate velocities. J. Geophys. Res. Solid Earth 119, 8633–8654.

McBride, J., 2015. Assessment Report for Diamond Drilling on the Stillwater Canada Inc. Bermuda Property (Assessment Report No. NTS 42D/16), Assessment Report.

McCarthy, T.S., Cawthorn, R., 1983. The Geochemistry of Vanadiferous Magnetite in the Bushveld Complex: Implications for Crystallization Mechanisms in Layered Complexes. Miner. Deposita 18, 505–518.

McCarthy, T.S., Cawthorn, R.G., Wright, C.J., McIver, J.R., 1985. Mineral layering in the Bushveld Complex; implications of Cr abundances in magnetite from closely spaced magnetitite and intervening silicate-rich layers. Econ. Geol. 80, 1062–1074.

Mitchell, R., Platt, G., 1982. Mineralogy and petrology of nepheline syenites from the Coldwell alkaline complex, Ontario, Canada. J. Petrol. 23, 186–214.

Mitchell, R.H., Platt, R.G., Downey, M., Laderoute, D.G., 1991. Petrology of alkaline lamprophyres from the Coldwell alkaline complex, northwestern Ontario. Can. J. Earth Sci. 28, 1653–1663.

Naldrett, A.J., 1999. World-class Ni-Cu-PGE deposits: key factors in their genesis. Miner. Deposita 34, 227–240.

Namur, O., Charlier, B., Toplis, M.J., Higgins, M.D., Liegeois, J.P., Vander Auwera, J., 2010. Crystallization Sequence and Magma Chamber Processes in the Ferrobasaltic Sept Iles Layered Intrusion, Canada. J. Petrol. 51, 1203–1236.

Robb, L., 2004. Introduction to Ore-Forming Processes, 1st ed. Wiley-Blackwell.

Rusk, B.G., Oliver, N.H.S., Zhang, D., Brown, A., Lilly, R., Jungmann, D., 2009. Compositions of Magnetite and Sulfide from Barren and Mineralized IOCG Deposits in the Eastern Succession of the Mt Isa Inlier, Australia, in: 2009 Portland GSA Annual Meeting.

Ruthart, R., 2013. Characterization of High-PGE Low-Sulphur Mineralization at the Marathon PGE-Cu Deposit, Ontario (MSc). University of Waterloo.

Samson, I.M., Fryer, B.J., Gagnon, J.E., 2008. The Marathon Cu-PGE deposit, Ontario: Insights from sulphide chemistry and textures. Presented at the Goldschmidt, p. A820.

Shaw, C.S.J., 1997. The petrology of the layered gabbro intrusion, eastern gabbro, Coldwell alkaline complex, Northwestern Ontario, Canada: evidence for multiple phases of intrusion in a ring dyke. Lithos 40, 243–259.

Singoyi, B., Danyushevsky, L., Davidson, G.J., Large, R., Zaw, K., 2006. Determination of trace elements in magnetites from hydrothermal deposits using the LA ICP-MS technique, in: SEG Keystone Conference. Denver, USA.

Tegner, C., Cawthorn, R.G., Kruger, F.J., 2006. Cyclicity in the Main and Upper Zones of the Bushveld Complex, South Africa: Crystallization from a Zoned Magma Sheet. J. Petrol. 47, 2257–2279.

Walker, E.C., Sutcliff, R.H., Shaw, C.S.J., Shore, G.T., Penczak, R.S., 1993. Precambrian Geology of the Coldwell Alkalic Complex. Ontario Geological Survey Open File No. 5868.

Ward, L.A., Holwell, D.A., Barry, T.L., Blanks, D.E., Graham, S.D., 2018. The use of magnetite as a geochemical indicator in the exploration for magmatic Ni-Cu-PGE sulfide deposits: A case study from Munali, Zambia. J. Geochem. Explor. 188, 172–184.

Wilkinson, J.J., Chang, Z., Cooke, D.R., Baker, M.J., Wilkinson, C.C., Inglis, S., Chen, H., Bruce Gemmell, J., 2015. The chlorite proximitor: A new tool for detecting porphyry ore deposits. J. Geochem. Explor. 152, 10–26.

Wood, S.A., Mountain, B.W., Pan, P., 1992. The aqueous geochemistry of platinum, palladium and gold: Recent experimental constraints and a re-evaluation of theoretical predictions. Can. Mineral. 30, 955–982.

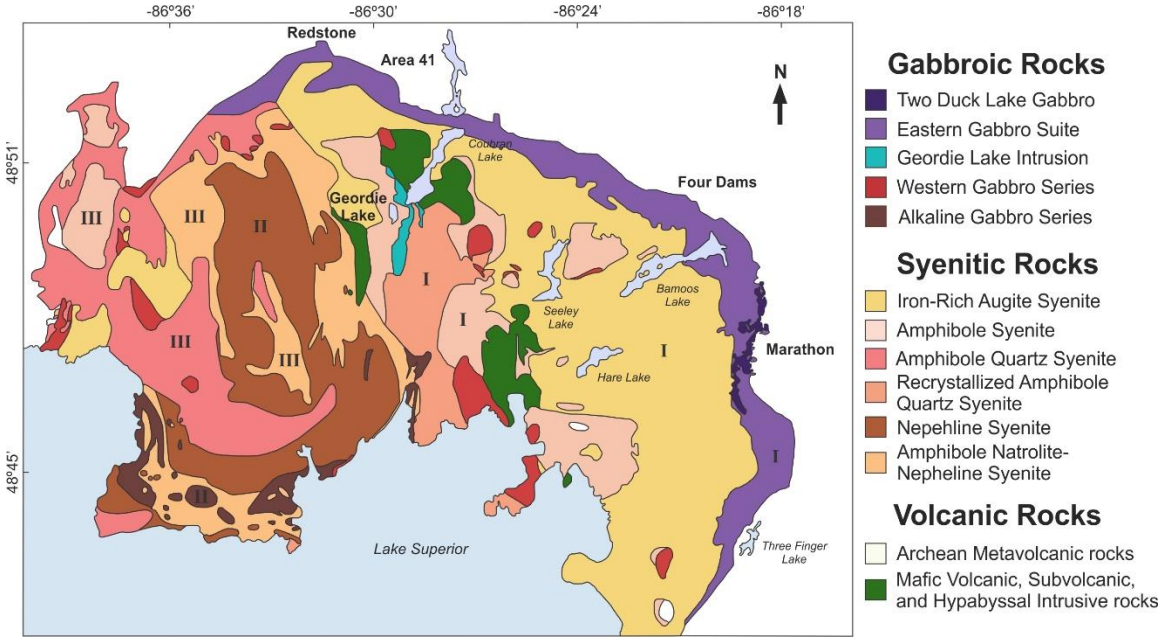

Figure 1.1 Geological map of the Coldwell Complex showing the location of the Eastern Gabbro and the various mineralized occurrences that it hosts. The numbers represent the three intrusive centers from Mulja and Mitchell (1991). Modified from Good et al. (2015).

Chapter 2

Controls on the chemistry of minerals in late-stage veins and implications for exploration vectoring tools for mineral deposits: an example from the Marathon Cu-Pd deposit, Ontario, Canada

2.1 Introduction

Geochemical vectors, including mineral and rock chemistry, thermal anomalies, and fluid pathways, have been used in exploration for iron oxide copper gold (IOCG), porphyry deposits, volcanogenic massive sulfide (VMS), orogenic gold, and SEDEX deposits (Kelley et al., 2006 and references therein). Much of the literature related to geochemical vectoring describes the use of surficial criteria (e.g., soil gas, groundwater, and heavy mineral chemistry), whereas the use of mineralogical (mineral chemical) halos has been described less often, particularly with respect to their use as vectoring tools in magmatic Ni-Cu-PGE deposits. One of the few studies that focused on the use of geochemical haloes in a magmatic deposit was by Hanley and Bray (2009) in the magmatic Ni-Cu-PGE footwall deposit in the Sudbury Igneous Complex. These authors demonstrated that the concentration of Ni in vein-hosted amphibole increased in a predictable manner with increasing proximity to mineralization. Nickel content in amphibole poikiloblasts in the gneissic wallrock, however, contained only background Ni values. Other metals (Cu, Sn, Pb, Co, Zn) did not show as distinct a relationship between concentration and proximity to mineralization. A significant amount of work has recently demonstrated the effectiveness of chlorite chemistry as an exploration tool for porphyry Cu-Au systems (i.e., magmatic-hydrothermal) (Wilkinson et al., 2015). In this study, a number of metals (e.g., Zn, Mn, Co, Ni) exhibited anomalous concentrations up to 4.5 km from, and varied systematically with proximity to, the porphyry center. This variability was not as obvious in the whole-rock metal contents and illustrates the strength of mineral chemistry as an exploration tool.

This study focuses on the characterization of vein-hosted mineral chemistry in the vicinity of the low-sulfide, conduit-related, Marathon Cu-Pd deposit, a 97.4 metric ton sulfide deposit with 0.27 % Cu, 0.75 ppm Pd, 0.23 ppm Pt, and 0.09 ppm Au (Puritch et al., 2009).

The Marathon deposit is hosted by the Marathon Series of the Eastern Gabbro, a composite pluton emplaced along the eastern and northern margins of the 1.1 Ga North American rift-related Coldwell Alkaline Complex (Good et al., 2015). Mineralization occurs in three texturally, mineralogically, and geochemically distinct zones, described by increasing distance from the footwall contact as the Footwall Zone, Main Zone, and W Horizon. Of these zones, the Main Zone and W Horizon are of greatest economic interest as they host significant Cu and PGE mineralization.

This contribution assesses the controls on vein-hosted mineral chemistry and whether vein-hosted mineral chemistry can be used as a vector for Cu-PGE mineralization in low sulfide Cu-PGE deposits. To be useful as an exploration tool, the fluid chemistry must be the dominant control and the affect, whatever it may be, should vary systematically with distance from mineralization. In this respect, we assess the scale at which vein-hosted mineral chemistry is controlled by fluid chemistry as compared to host rock and associated mineral chemistry.

2.2 Geological setting

2.2.1 Regional and local geology

The Coldwell Alkaline Complex is a composite alkaline pluton emplaced into Archean rocks of the Schreiber-White River greenstone belt at 1.1 Ga (Dahl et al., 2001; Good et al., 2015; Good and Crocket, 1994; Watkinson and Ohnenstetter, 1992). The Eastern Gabbro is an arcuate-shaped series of mafic to ultramafic rocks that wraps around the eastern and northern margins of the complex and is the oldest intrusive phase within the complex (Good et al., 2015; Shaw, 1997) (Fig. 2.1). Work by Good et al. (2015) has led to a new subdivision of the Eastern Gabbro into three Magmatic series encompassing an early metabasalt, the Layered Series, and the Marathon Series. The Marathon Series is defined as comprising all the mafic and ultramafic rocks that host Cu-PGE mineralization. The Layered Series also hosts Cu mineralization, which is associated with albite and actinolite alteration, but lacks PGE.

The metabasalt occurs along the base of the Eastern Gabbro and comprises basalt to picritic basalt that have been metamorphosed to hornfels grade by injection of large volumes of Layered and Marathon series magmas (Fig. 2.2) (Good et al., 2015). The Layered Series occurs above the metabasalt and makes up the majority of the Eastern Gabbro (Fig. 2.2). It is texturally homogenous throughout the entire Eastern Gabbro and, up until the recent investigation by Cao et al. (2016), who identified normal and reverse trends in whole-rock and mineral chemistry, was also thought to be compositionally homogenous. The Layered Series is dominated by olivine gabbro, with modal layering that ranges in composition from olivine melagabbro to olivine gabbroic anorthosite. The Marathon Series, host to the Cu and PGE mineralization in the deposit, mostly comprises the Two Duck Lake gabbro, along with a layered troctolite sill, and sill- to pod-like bodies of oxide melatroctolite and apatitic olivine clinopyroxenite (Good et al., 2015). This series represents the youngest intrusive event in the Eastern Gabbro. The Two Duck Lake gabbro is a 250 m-thick body that intruded the metabasalts near their contact with the Archean metavolcanics (Fig. 2.2). It is typically coarse-grained to pegmatitic, with an ophitic to subophitic texture. The oxide- and apatite-rich rocks, which can host significant concentrations of PGE, occur as sill- to pod-like bodies that intruded the metabasalts.

2.2.2 Mineralization

Mineralization at Marathon occurs in three zones that are texturally, mineralogically, and geochemically distinct. With increasing distance from the footwall contact, these zones are termed Footwall Zone, Main Zone, and W Horizon (Fig. 2.3) (Good et al., 2015). The Footwall Zone occurs at the base of the Two Duck Lake gabbro at the contact with the Archean country rocks. Sulfides in the Footwall Zone are dominated by semi-massive to net-textured pyrrhotite with lesser chalcopyrite (Samson et al., 2008; Watkinson and Ohnenstetter, 1992). The Main Zone is the thickest and most continuous zone of mineralization. Sulfides in the Main Zone are dominated by disseminated chalcopyrite and pyrrhotite, with minor pentlandite and cubanite, and rare bornite. The W Horizon only occurs in the southern portion of the deposit and typically occurs a few meters to tens of

meters above Main Zone mineralization. Sulfides in the W Horizon are also disseminated, but this zone differs from the Footwall Zone and Main Zone in having a lower abundance of hydrous silicates, a distinct suite of PGM, a lower proportion of pyrrhotite, a greater proportion of bornite, lower S contents, and noticeably lower Cu/Pd ratios (Good, 2010; Ruthart, 2013). Mineralization also occurs in irregular sill- to pod-like bodies of oxide-apatite-rich rocks, termed magnetite-apatite-clinopyroxene cumulate.

2.3 Analytical techniques

Diamond drill core samples were collected from eight drill holes located along the length of the Eastern Gabbro (Fig. 2.2). All of the drill holes intersect mineralized intervals apart from drill hole M-11-513, which is located to the west of mineralization and is not underlain by mineralization. The mineralized holes intersected the Footwall Zone, Main Zone, and W Horizon, as well as unmineralized rock. Chlorite ± carbonate veins and patchy alteration were sampled systematically down each hole at intervals of 10-20 meters, and thin and thick polished sections were prepared for a subset of these samples. Vein density was measured by counting the number of veins present in 3-meter intervals for the entire length of each drill core.

Raman spectra of vein-hosted minerals were obtained at the University of Windsor using a Renishaw inVia Raman spectrometer in conjunction with a Spectra-Physics 163A 514.5 nm air-cooled argon-ion laser operated at a laser power of 20 mW. Raman spectra of patchy alteration were collected using a WiTec Confocal Raman Spectrometer fitted with a 532 nm laser at the Advanced Microscopy and Materials Characterization Facility at the University of Windsor. Most spectra were collected between 100 and 1500 cm-1. Spectra were background-corrected using the Crystal Sleuth software (Laetsch and Downs, 2006). X-ray diffraction (XRD) patterns were collected using Co Kα radiation (λ = 1.7889 Å) on a Bruker D8 Discover micro XRD at the Department of Earth Sciences at Western University. This instrument was equipped with a 60 mm Co gobel mirror and a 100 μm snout, producing a resolution of 50 μm. For more information about this technique see

(Flemming, 2007). Micro-XRD patterns were analyzed using Match© developed by Crystal Impact.

The major-element chemistry of minerals was determined using both energy- and wavelength-dispersive spectrometry (EDS and WDS) using a scanning electron microscope (SEM) at the Advanced Microscopy and Materials Characterization Facility at the University of Windsor and an electron microprobe (EPMA) at the Department of Earth Sciences, Carleton University, Ottawa, respectively. The EDS analyses were carried out using an FEI Quanta 200 FEG SEM fitted with an EDAX EDS. Analyses were acquired under high vacuum at an accelerating voltage between 15 and 20 kV. Well-characterized plagioclase from the Marathon Cu-Pd deposit, quartz from the Thor Lake rare earth element deposit, and olivine from Micro-Analysis Consultant Ltd. were analyzed during each experiment to ensure the precision and accuracy of the EDS. The standard deviation of replicate analyses (n = 5 to 24) of these minerals yielded standard deviations that are all less than 1 wt. % for all major elements, apart from Si in quartz, which has a standard deviation in the range of 1.4 wt. %. The major-element concentrations of these minerals acquired by EDS are systematically overestimated as they plot below the 1:1 line on Figure 2.4a. The systematic nature of the overestimation allows a correction factor to be applied to the major-element concentrations of chlorite obtained by EDS. A subset of samples analyzed by EDS were analyzed using EPMA to determine the accuracy of the corrected EDS analyses. The WDS analyses were obtained using a Cameca Camebax MBX electron microprobe operated at an accelerating voltage of 20 kV, beam current of 20 nA, beam diameter of 2 μm, and counting times of 20 seconds or 40,000 counts. Raw data were converted to element weight percent using the Cameca PAP matrix correction program. Figure 2.4b illustrates the accuracy of the corrected EDS results, which lie very close to the 1:1 line, with $r^2 = 0.96$. Given the good accuracy and precision of the EDS, it is the primary means by which the major-element chemistry of chlorite was characterized.

Trace-element concentrations of minerals were obtained using laser ablation inductively-coupled plasma mass spectrometry (LA-ICP-MS) at the Element and Heavy Isotope Analytical Laboratories at the University of Windsor using a Thermo X Series II ICP-MS

equipped with a femtosecond laser ablation system operated at a laser energy of 26.7 μJ, repetition rate of 100 Hz, pinhole size of 2.5, and 10x objective lens. Minerals were analyzed for a variety of transition (^{47}Ti, ^{48}Ti, ^{50}Ti, ^{51}V, ^{52}Cr, ^{53}Cr, ^{54}Fe, ^{55}Mn, ^{57}Fe, ^{59}Co, ^{60}Ni, ^{63}Cu, ^{66}Zn, ^{70}Zn) and main-group elements (^{24}Mg, ^{27}Al, ^{29}Si, ^{35}Cl, ^{44}Ca, ^{75}As, ^{114}Cd, ^{118}Sn, ^{121}Sb, ^{208}Pb, and ^{209}Bi). Multiple isotopes of Ti, Cr, and Zn were measured to assess isobaric interferences from ^{48}Ca, ^{50}V, and ^{50}Cr on ^{48}Ti and ^{50}Ti, and from ^{26}Mg^{40}Ar and ^{30}Si^{40}Ar on ^{66}Zn and ^{70}Zn, respectively. Calibration was achieved using the NIST 610 synthetic glass standard. Typical analyses included 60 seconds of gas background followed by up to 120 seconds of ablation and signal collection. Aluminum was used as the internal standard for analyses that consisted primarily of chlorite, whereas Si was used as the internal standard for analyses that comprised predominantly amphibole and serpentine. Internal standards consisted of corrected EDS analyses from each sample that were further adjusted to account for the presence of water in the structure of these minerals.

2.4 Characteristics and mineralogy of veins and patchy alteration

2.4.1 Vein distribution

Thin veins that range in thickness from 20 μm to 3 mm (with most between 20-400 μm) are ubiquitous in the Eastern Gabbro. Vein density varies considerably in and around the deposit and shows no correlation with rock type (Fig. 2.5). A correlation does, however, exist between vein density and mineralization, in which rocks with high Cu and Pd (roughly 10 times background Cu and Pd) have distinctly lower vein densities; this relationship is observed in all the drill holes examined, but is particularly evident in drill hole M-06-221 (Fig. 2.5).

2.4.2 Vein mineralogy

Minerals in the veins are fine grained and their optical properties are, in general, consistent with chlorite. In thin section, vein-hosted minerals occur as fine-grained (< 5 μm), randomly-oriented, radiating, or aligned aggregates of acicular crystals. They are weakly

pleochroic and most commonly are light to dark brown, but can also be colorless, light to dark green, yellow, and orange. They display first-order interference colors. In some veins, the optical properties change along the vein as the vein crosscuts different minerals (Fig. 2.6a). Calcite is present in most veins, but is significantly less abundant than the other vein minerals. It occurs as fine-grained anhedral crystals in aggregates that typically occupy the center of veins, or as fine-grained disseminated crystals intermixed with chlorite. In segments of some veins, calcite is the dominant mineral (Fig. 2.6b). In rare cases, calcite is the only mineral present in a vein. In rare instances, veins can be comprised predominantly of euhedral actinolite, quartz, or homogeneous magnetite. Sulfides and platinum-group minerals (PGM) have not been observed in the veins.

Veins are classified by mineralogic or textural relationships into four types. Type 1 veins are homogenous with no zonation (Fig. 2.7). Type 2 veins consist of a central zone surrounded symmetrically by multiple zones of different mineralogy (Fig. 2.7). Type 3 veins consist of later, mineralogically-distinct "veinlets" that weave throughout the vein and can crosscut earlier vein stages (Fig. 2.7). Type 4 veins consist of a repeating series of texturally, optically, and mineralogically distinct zones (Fig. 2.7). Veins that exhibit these various types of zonation can occur in all rock types throughout the Eastern Gabbro. Type 2 zonation is controlled by the mineral that the vein crosscuts; this is largely represented by the abrupt disappearance of its outermost zone (Fig. 2.6c).

A large population of optically-diverse vein minerals were analyzed by Raman spectroscopy, and a subset by micro XRD. Analyses indicate that the veins contain mixtures of chlorite, serpentine, saponite, and amphibole (Figs. 2.8, 2.9). Measured Raman spectra were compared to reference spectra of chamosite, clinochlore, chrysotile, antigorite, tremolite and actinolite from the RRUFF database (Downs, 2006), as well as saponite from Kloprogge and Frost (2000). Similarity in the Raman peak positions amongst the various species of chlorite (chamosite, clinochlore), serpentine (antigorite, chrysotile), and saponite (Fig. 2.8), along with the fine-grained nature of the aggregates in the veins, makes characterization of the vein mineralogy difficult. Nevertheless, the Raman spectra can be classified into distinct groups based on their spectral characteristics. Group 1 spectra

represent predominantly serpentine-group minerals with lesser chlorite- and amphibole-group minerals (Fig. 2.8). They display strong peaks at ~ 128, 212, 368, 430, 617 (or at 627 as a shoulder on the 688 peak), and 688 cm^{-1}, which are consistent with serpentine-group minerals (Fig. 2.8). The wide peak at 520-550 cm^{-1} likely consists of 2 peaks, one of which can be assigned to the serpentine-group minerals, and the other to the chlorite-group minerals (Fig. 2.8). The low-intensity, broad peak between ~ 750-770 cm^{-1} can be assigned to the amphibole-group minerals (Fig. 2.8). Spectra in groups 2-4 represent mixtures of predominantly chlorite-group minerals with lesser saponite, serpentine-, and amphibole-group minerals (Fig. 2.8). The most intense peak occurs at ~ 675 cm^{-1} and is unique to the chlorite-group minerals (Fig. 2.8). The peaks at ~ 190 and 740 cm^{-1} (group 4) are unique to the amphibole-group minerals (Fig. 2.8). Peaks at ~ 275 and 360 cm^{-1} could be assigned to chlorite-group minerals and/or saponite and/or amphibole-group minerals, but the absence of peaks at ~ 432, 464, and between 494-550 cm^{-1}, which are characteristic of saponite, suggests that the peaks at 275 and 360 cm^{-1} represent a mixture of chlorite- and amphibole-group minerals (Fig. 2.8). The wide peaks between 400-475 cm^{-1} and 500-550 cm^{-1} can be assigned to a mixture of chlorite- and serpentine-group minerals (Fig. 2.8). The peak at ~ 621 cm^{-1} occurs as a shoulder on the 675 cm^{-1} peak and is unique to serpentine (Fig. 2.8). Micro-XRD analyses indicate the same mineralogy as determined from Raman spectroscopy, in which the peaks can be assigned to chlorite ± serpentine ± saponite ± amphibole (Fig. 2.9).

Vein-hosted minerals from 61 veins were analyzed using EDS, and a subset by EPMA. Analyses of single crystals proved difficult given the extremely fine-grained nature of the vein-hosted minerals (μm-scale) and, as a result, the major-element chemistry represents analyses of small aggregates. Vein-hosted minerals are compositionally diverse and exhibit a large variability in Fe/Mg (Mg# 0.03-0.82), Si (8.7-26 at. %), and Al (0-7 at. %). On a molar Al-Fe-Mg ternary diagram, the major-element chemistry of vein-hosted minerals trend from ideal chlorite compositions towards compositions representing saponite, serpentine, and amphibole (Fig. 2.10). On a molar (Fe+Mg)-Si-Al ternary diagram, vein-hosted minerals have higher and more variable Si contents than end-member chlorite (Fig. 2.10). Three compositional trends in the major-element chemistry are observed on Figure

2.10: i) compositions that lie between chlorite and saponite, ii) those that lie between chlorite-saponite and serpentine, and iii) those that lie between serpentine and actinolite. The chlorite-saponite trend, however, extends past the compositional field of saponite. There is a significant amount of Ca (up to 3 wt. %) in some analyses. Those analyses that do not contain Ca plot closer to the chlorite field on the (Fe+Mg)-Si-Al ternary diagram than those that do contain Ca. On a molar (Fe+Mg)-Al-Ca ternary diagram, a large proportion of vein mineral compositions trend from chlorite towards saponite and actinolite, whereas only a subset trend towards or plot as pure serpentine (Fig. 2.10). The results obtained by EPMA (open crosses) mimic those obtained by EDS (Fig. 2.10).

2.4.3 Patchy alteration mineralogy

Patchy alteration is common throughout the deposit and in the surrounding rocks. The minerals in this type of alteration are coarser than vein-hosted minerals, and so they are easier to characterize optically. Patchy alteration consists predominantly of amphibole, with lesser chlorite and serpentine, and rare muscovite, epidote and carbonate. These minerals occur as aggregates that have partially to completely replaced silicates, principally pyroxene, but also olivine and, to a lesser extent, plagioclase. In many cases the replacement minerals, mainly amphibole, are intergrown with sulfide minerals. Patchy alteration can be categorized as being isolated from sulfides or associated with sulfides. Patchy alteration can be crosscut by veins.

The only mineral that is abundant in both types of alteration is chlorite. Chlorite in patchy alteration occurs as randomly-oriented, aligned, or radiating acicular crystals. They exhibit less color diversity than vein-hosted minerals, and are typically only green, yellow, and brown, and are more distinctly pleochroic than vein-hosted minerals.

The most intense peaks in Raman spectra of chlorite from patchy alteration occur at ~ 548 and 675 cm^{-1}, as well as at ~ 365 cm^{-1}, and are assigned to the chlorite-group minerals (Fig. 2.8). The lower intensity peaks at ~ 200 and between 760-820 cm^{-1} are also unique to the chlorite-group minerals (Fig. 2.8). The broad peak between 260-315 cm^{-1} can be assigned

to the chlorite-group minerals and/or saponite and/or amphibole-group minerals (Fig. 2.8). The absence of the three peaks at ~ 432, 464, and between 494-550 cm^{-1}, however, suggests that saponite is likely not present (Fig. 2.8). The peak at ~ 120 cm^{-1} is assigned to the amphibole-group minerals (Fig. 2.8). Large crystals of patchy tremolite-actinolite were analyzed for comparison with the spectra from vein assemblages. Raman spectra of these crystals exhibit an intense peak at ~ 670 cm^{-1}, a series of lower-intensity peaks at ~ 120, 155, 180, and 222 cm^{-1}, ~ 294 cm^{-1}, and broad peaks between 340-415 and 500-580 cm^{-1}, all of which are consistent with the reference spectra for tremolite-actinolite (Fig. 2.8).

The major-element chemistry of chlorite in the patchy alteration is significantly different from that of vein-hosted minerals in that they have notably higher Al contents (6-13 at. %), lower Si (10-12.5 at. %), a smaller range in Mg# (0.18-0.64), and generally contain no Ca (Fig. 2.10). The composition of this chlorite consistently lies within the chlorite field on an Al-Fe-Mg ternary diagram and ranges from clinochlore to chamosite (Fig. 2.10). On an (Fe+Mg)-Si-Al ternary diagram, the composition of chlorite in patchy alteration lies closer to the chlorite field than vein-hosted minerals (Fig. 2.10).

2.5 Trace-element chemistry

2.5.1 Vein-hosted minerals

Vein-hosted minerals from 51 thick sections, which represent various depths in the 8 drill holes and span the entire Marathon deposit, were analyzed by LA-ICP-MS for a variety of major and trace elements. Laser traverses were always run perpendicular to a vein, starting in a host mineral of the gabbro, and if the vein was thin enough, ending in a host mineral on the other side of the vein.

2.5.1.1 Variations in trace-element chemistry

Repeat analyses of minerals in a single vein hosted by a single grain of pyroxene and by a single grain of plagioclase in the same sample were carried out to assess the variability of

trace metals in vein minerals on the scale of hundreds of microns. The relative standard deviation (RSD) for all transition metals in these repeat analyses, excluding Ti in the portion of the vein hosted by plagioclase, is less than 30% and most are less than or equal to 10% (Cr, Mn, Co, Ni, Zn). The RSD of Ti from the portion of the vein hosted by plagioclase is 36%.

To assess the controls on vein-hosted mineral chemistry at different scales, the trace-element composition was characterized for vein minerals that occur within different host minerals and that are hosted by different rock types. For the more abundant metals, there are consistent differences in the concentrations of Ti, V, and Cr between minerals in veins hosted by Fe-Ti oxides, pyroxene, and plagioclase. The concentration of Ti, V and Cr in minerals in veins that are hosted by Fe-Ti oxides are consistently higher than in those veins hosted by plagioclase and pyroxene (Fig. 2.11). The concentrations of these elements at the 10^{th}, 25^{th}, 50^{th}, 75^{th}, and 90^{th} percentile are always higher than the corresponding concentrations in veins hosted by plagioclase and pyroxene (Fig. 2.11). Minerals in veins hosted by pyroxene also have higher Ti, V, and Cr concentrations compared to those hosted by plagioclase, but the difference is not as significant as observed in Fe-Ti oxides (Fig. 2.11). Again, the concentrations at the various data percentiles are always higher than the corresponding concentrations in veins hosted by plagioclase, but there is significant overlap in the range of concentrations (Fig. 2.11).

The difference in metal concentration between veins that are hosted by pyroxene and Fe-Ti oxides and those that are hosted by plagioclase within a single sample was calculated to determine if the relationships described above are true for individual samples. Differences in vein mineral compositions are referenced to those veins that are hosted by plagioclase because the elements of interest in vein minerals (e.g., Ti, V, Ni, Cr, Co) typically do not occur in any great concentration in plagioclase. For most elements, minerals in veins that are hosted by pyroxene show essentially no difference in chemistry from those that are hosted by plagioclase (Fig. 2.12). The exceptions are Ti, V, and Cr, for which 75% of the analyses show enrichments relative to plagioclase of up to 500 ppm, but with a large proportion that are less than 100 ppm (Fig. 2.12). Minerals in veins that are hosted by Fe-

Ti oxides, however, show large differences in concentration for many of the metals analyzed (Fig. 2.12). Titanium, V, and Cr show the largest and most consistent differences in concentration compared to veins that are hosted by plagioclase. Unlike veins that are hosted by pyroxene, 100% of analyses of minerals in veins hosted by Fe-Ti oxides are enriched in Ti, V, and Cr relative to those hosted by plagioclase by up to 400 ppm, 500 ppm (75% of values are < 200 ppm), and 30 ppm, respectively (Fig. 2.12). Seventy-five percent of analyses of minerals in veins hosted by Fe-Ti oxides are depleted and enriched by less than 20 ppm in Cu and Zn, respectively, relative to those hosted by plagioclase (Fig. 2.12). These differences exhibit no correlation with the rock type that hosts the vein.

Because the composition of minerals in veins hosted by pyroxene and Fe-Ti oxides are affected by the composition of their host mineral, as will be discussed below, only those veins that are hosted by plagioclase are used to assess the effects of host rock. Vein-hosted minerals in metabasalt have largely similar trace-element concentrations to those hosted by Marathon Series, with the exception of Co, Ni, and Zn. The concentrations of these elements at the 10^{th}, 25^{th}, 50^{th}, 75^{th}, and 90^{th} percentile are always higher in veins hosted by metabasalt compared to the corresponding concentrations in veins hosted by Marathon Series (Fig. 2.13a).

To assess potential host-rock controls on vein mineral chemistry, the whole-rock composition of metabasalt and Two Duck Lake gabbro, the most abundant rock in the Marathon Series, are compared to the composition of vein minerals on Figure 2.13. The whole-rock composition of the metabasalt and Two Duck Lake gabbro are very similar (Fig. 2.13b). Those elements that exhibit variations in concentration in veins hosted by metabasalt and Marathon Series (i.e., Co, Ni, Zn ± Mn) show no difference in their whole-rock concentrations in the two rock types (Fig. 2.13b). In fact, for most of the elements of interest, the ranges of concentrations, based on standard deviation at 1σ, overlap (Fig. 2.13b). Copper is the exception in that its whole-rock concentration is distinctly higher in the Two Duck Lake gabbro (Fig. 2.13b).

2.5.1.2 Relationship between trace-element chemistry and mineralization

The concentration of some metals (Ti, V, Cr ± Zn, Cu) appears to have been affected by the composition of Fe-Ti oxides and pyroxene, and so to circumvent the host-mineral effects on the composition of vein minerals, the comparisons that are presented below only include veins that are hosted by plagioclase. The population statistics for Co, Ni, and Zn are distinctly different in veins hosted above and within mineralization; the same is true of V and Cr, albeit to a lesser degree. The 10^{th}, 25^{th}, 50^{th}, 75^{th}, and 90^{th} percentiles for Co, Ni, and Zn concentrations are always higher in veins hosted by rocks above mineralization compared to the corresponding percentiles in veins hosted by rocks within mineralization (Fig. 2.14). Vanadium and Cr concentrations are lower and higher, respectively, in veins located above mineralization than their corresponding percentile ranges in veins located within mineralization, although there is significant overlap (Fig. 2.14). These same trends are observed in vein minerals hosted throughout individual drill holes.

Drill hole M-07-391 is located proximal to the main feeder channel for the deposit (Good et al., 2015). In those veins hosted above mineralization and that are hosted by plagioclase, Co and As show distinct and consistent differences in concentration from drill holes located at varying distances from M-07-391 (Fig. 2.15). The concentration of Co in veins in M-07-366, M-07-391, and M-08-424 is consistently greater than Co concentrations in veins in M-05-99 and M-06-221, which occur further from the feeder channel (Fig. 2.15). Likewise, As concentrations in veins in M-07-391 are consistently greater than the As concentrations in those veins in the other drill holes (Fig. 2.15). Veins hosted in drill hole M-11-513, which is located west of mineralization (Fig. 2.2), also follows this trend and are depleted in Co relative to those veins hosted in M-07-366, M-07-391, and M-08-424. The other elements of interest, including Cu (Fig. 2.15), show no variation as a function of distance from the main feeder channel.

The concentrations of Mn, Co, Ni, and Zn in vein minerals that are hosted by plagioclase and that are located both above and within mineralization correlate with whole-rock Cu/Pd ratios. The concentration of Mn in vein-hosted minerals exhibit a weak systematic increase

as whole-rock Cu/Pd increases (not shown), whereas the concentrations of Co, Ni, and Zn decrease as whole-rock Cu/Pd increases (Fig. 2.16). Of these metals, Ni exhibits the best correlation and the largest difference in concentration between high- and low-Cu/Pd rocks. Cobalt, Ni, and Zn show similar trends relative to whole-rock Cu, but no correlation with whole-rock Ni or Pd (Fig. 2.17). The Ni and Cu content of vein minerals also do not exhibit any correlation with their respective whole-rock concentration (Fig. 2.17).

Figure 2.18 plots the composition of vein minerals hosted by plagioclase as a function of depth from the top of the mineralized interval. The top of mineralization is defined as the depth in a given drill hole at which point the whole-rock Cu and Pd initially show an increase in concentration that is roughly 10 times the background concentration. These are aggregate plots in that data from all drill holes are plotted for a given element on each binary diagram. The concentrations of Co, Ni, and Zn vary systematically with distance from mineralization. With increasing distance from mineralization, the concentrations of Co, Ni, and Zn increase by roughly an order of magnitude relative to the most proximal sample (Fig. 2.18). Within mineralization, the concentration of these elements in the veins shows no correlation with distance from the top of mineralization. Using only those vein minerals that are located above mineralization (n = 34), the trends exhibited by Co, Ni, and Zn can be described by the power equations shown on Figure 2.18. Vein minerals in drill hole M-11-513, which is situated to the west of mineralization (Fig. 2.2) and is not underlain by mineralization, exhibit Co, Ni, and Zn concentrations that range over an order of magnitude (Fig. 2.18). Vein minerals from this drill hole have concentrations of Co, Ni, and Zn that straddle the median concentrations of these metals in veins located within mineralization and are consistently lower than in veins hosted above mineralization (Fig. 2.18). Vein-hosted minerals within individual drill holes do not show the same trend with distance from mineralization as in the aggregate plots. The concentrations of Co, Ni, Zn, and other metals exhibit no systematic change with distance from mineralization (Fig. 2.19). The concentration of Co, Ni, and Zn are, however, consistently greater in veins hosted above mineralization than within mineralization (Fig. 2.19).

The composition of vein minerals hosted by plagioclase varies systematically as a function of distance from the footwall contact. The concentration of Co, Ni, and Zn in vein-hosted minerals systematically increases with increasing distance from the footwall contact (Fig. 2.20) and mirrors the trend exhibited by vein minerals hosted above mineralization in Figure 2.18. Using vein-hosted minerals located within and above mineralization, the trends exhibited by Co, Ni, and Zn can be described by the power equations shown on Figure 2.20. These trends are also evident in individual drill holes (Fig. 2.21).

2.5.2 Chlorite from patchy alteration

The trace-element chemistry of chlorite from patchy alteration is significantly different from that of vein-hosted minerals. More than 75% of analyses of vein-hosted minerals have higher Cr, As, Sn, and Sb compared to their concentration in chlorite from patchy alteration, whereas more than 75% of analyses of chlorite from patchy alteration have higher Mn, Co, Ni, and Zn compared to their concentration in vein-hosted minerals (Fig. 2.22).

Chlorite hosted in patchy alteration that is isolated from sulfides is compositionally similar to chlorite hosted in patchy alteration that surrounds sulfides (Fig. 2.23). Chromium, Cu, Cd, Sn, and Bi are the exception. Chromium and Bi are present in chlorite from patchy alteration isolated from sulfides, but are below detection in those chlorite crystals in patchy alteration that surrounds sulfides (Fig. 2.23). The concentration of Cd is always enriched in chlorite from patchy alteration that surrounds sulfides, whereas Sn and, to an extent, Cu extend to higher concentrations in these chlorite assemblages (Fig. 2.23).

2.6 Discussion

2.6.1 Fluid-related processes inferred from mineralogy

The minerals hosted in veins and patchy alteration had to have resulted from fluid infiltration because they are principally low-temperature hydrous minerals that occur in

veins and as the replacement of pyroxene and olivine. The majority of vein-hosted minerals do not have major-element compositions consistent with end-member chlorite, serpentine, amphibole, or saponite (Fig. 2.10). Rather, the veins represent mixtures of variable proportions of the various minerals. This has been confirmed by Raman spectroscopy (Fig. 2.8) and micro XRD (Fig. 2.9). The presence of saponite in these mixtures is difficult to assess because the major-element chemistry of vein-hosted minerals plot along a trend that can intersect either saponite or amphibole-group minerals (Fig. 2.10) and because no Raman peaks can be uniquely assigned to saponite (Fig. 2.8). Only micro XRD patterns show a few peaks that can be uniquely assigned to saponite, but they are of low intensity (Fig. 2.9). Therefore, the mineralogy of late-stage veins is represented by mixtures of Fe-Mg chlorite, serpentine, and Fe-Mg-Ca amphibole, ± saponite.

Chlorite from patchy alteration is compositionally closer to ideal end-member Fe-Mg chlorite than are the vein-hosted minerals, but are also characterized by higher Si contents than ideal chlorite (Fig. 2.10). Their Raman spectra predominantly contain peaks that can be uniquely assigned to the chlorite-group minerals, but a few low-intensity peaks can be assigned to amphibole-group minerals (Fig. 2.8). The latter can explain the higher Si contents relative to end-member chlorite. These observations have important implications for the applicability of mineral geothermometers, such as the chlorite geothermometer by Cathelineau (1988), if the wrong assumptions are made about the mineralogy of veins and patchy alteration. Applying single-mineral geothermometers to mixtures such as these would yield incorrect temperatures of formation given the variability in composition of mixed minerals and the different controls on composition for each of these minerals (e.g., ^{IV}Al is positively correlated with temperature in chlorite, but not necessarily other sheet silicates; Cathelineau, 1988). It emphasizes the need for detailed mineral characterization prior to any interpretations of major- to trace-element chemistry.

Veins that exhibit types 1, 3, and 4 zonation (Fig. 2.7) are represented by mixtures of Fe-Mg chlorite, serpentine, Fe-Mg-Ca amphibole, ± saponite (Fig. 2.10). Their mineralogy does not correlate with either the mineral or the rock type the vein is hosted by, suggesting that their chemistry was principally controlled by the fluid and high fluid-rock ratios. Along

with the textural characteristics of the fine-grained, acicular crystals, this is consistent with their formation as a result of open-space precipitation from a fluid. The occurrence of multiple optically-, texturally-, and mineralogically-distinct veinlets that can crosscut each other in veins that exhibit types 3 and 4 zonation (Fig. 2.7) indicates precipitation from fluids with varying compositions during multiple events of fluid migration.

The outer zone of type 2 veins consists principally of Fe-Mg chlorite ± saponite. Chemically, this outer zone differs from the inner zone in type 2 veins in that all of the minerals contain Al, whereas the inner zone also contains minerals that are Al-free (i.e., serpentine, actinolite) (Fig. 2.11). Because the outer zone is only present when the vein is hosted by plagioclase, and disappears abruptly when the vein crosscuts Al-poor pyroxene (Shahabi Far, 2016) and olivine (Fig. 2.6c), this zone represents a local effect where Al ± Ca was supplied by reaction with plagioclase to precipitate chlorite and saponite.

2.6.2 Controls on vein-hosted mineral trace-element chemistry

If the trace-element chemistry of vein-hosted minerals is to be used as an exploration tool, any dispersion haloes recorded by the minerals must be independent of any local effects. That is, the chemistry of vein-hosted minerals cannot be principally controlled by the chemistry of the rock in which the vein is hosted, or, on a smaller scale, by the chemistry of the mineral adjacent to the vein being analyzed. Rather, the chemistry of the fluid from which the minerals precipitated needs to be the dominant control. To assess such effects, vein minerals hosted by metabasalt and Marathon Series and that are hosted by plagioclase, pyroxene, and Fe-Ti oxides were analyzed.

2.6.2.1 Host mineral

Relative to those veins that are hosted by plagioclase, those that are hosted by Fe-Ti oxides are significantly and consistently enriched in Ti, V, and Cr, whereas Zn and Cu exhibit minor enrichments and depletions, respectively (Figs. 2.11, 2.12). Veins hosted by pyroxene show only minor enrichments in Ti, V, and Cr compared to those hosted by

plagioclase (Figs. 2.11, 2.12). Fe-Ti oxides at Marathon is Ti-rich (up to 14 wt. %, Brzozowski et al., 2017a) and contains lamellae of ulvöspinel and/or ilmenite (Brzozowski et al., 2017a). It exhibits a large range in Cr, V, Zn, and Cu contents from single-digit ppm to wt. % levels (Brzozowski et al., 2017a). Pyroxene at Marathon shows a large range of Ti, V, and Cr that varies from sub-ppm to thousands of ppm (Shahabi Far, 2016). These concentrations are orders of magnitude lower than those in Fe-Ti oxides. It is therefore expected that any control on the Ti, V, and Cr content of vein-hosted minerals by pyroxene would not be as pronounced as that exerted by Fe-Ti oxides. This is what is observed, with the enrichments in Ti, V, and Cr in veins hosted by pyroxene generally being a quarter of the magnitude of those hosted by Fe-Ti oxides (Fig. 2.12). These enrichments are statistically significant as they are much greater than the RSD for most transition metals (< 30%). Such effects may, however, be less important in systems, such as porphyry deposits, in which alteration developed at higher fluid-rock ratios than observed at Marathon and in which minerals, such as magnetite, have low concentrations of Ti, V, and Cr (cf. Wilkinson et al., 2015).

2.6.2.2 Host rock

If the composition of vein-hosted minerals is controlled by the composition of the host rock, than the composition of vein-hosted minerals should mimic the composition of the rock in which they are hosted. The metabasalt and Two Duck Lake gabbro are mineralogically (plagioclase, pyroxene, olivine, Fe-Ti oxides) and chemically similar, with the exception of whole-rock Cu, which occurs in elevated concentrations in the Two Duck Lake gabbro (Fig. 2.13). The transition metal content of vein minerals hosted by plagioclase in metabasalt and Marathon Series exhibit similar distributions, except for Co, Ni, and Zn, which occur in higher concentrations in vein minerals hosted by metabasalt compared to those hosted by Two Duck Lake gabbro (Fig. 2.13). The concentrations of Co, Ni, and Zn in vein minerals clearly does not mimic their concentrations in the rocks in which they are hosted (Fig. 2.13). Additionally, the concentration of Ni in vein minerals does not correlate with the whole-rock Ni concentration (Fig. 2.17). This indicates that the concentration of Co, Ni, and Zn in vein minerals was not controlled by the composition of

rocks that host the vein. Copper is the only metal that shows a distinct difference in concentration between the metabasalts and Two Duck Lake gabbro, and occurs in distinctly higher concentrations in Two Duck Lake gabbro (Fig. 2.13). But the concentration of Cu in vein minerals does not vary with rock type (Fig. 2.13) and exhibits no correlation with whole-rock Cu (Fig. 2.17). This indicates that the concentration of Cu in vein minerals was likewise not controlled by the composition of the rock that hosts the vein. Therefore, the composition of the host rock did not play a significant role in modifying the composition of the vein minerals.

The fact that the composition of vein minerals is unaffected on a large scale by the composition of the rock it is hosted by, but is affected on a small scale by the composition of the mineral it is hosted by has two important implications for the application of vein-mineral chemistry for exploration at Marathon. The first is that the composition of vein minerals hosted in any rock can be used to vector towards mineralization. The second is that only the chemistry of those minerals hosted in veins that crosscut plagioclase can be used to vector towards mineralization.

2.6.3 Sources of Co, Ni, and Zn in vein minerals

The Co, Ni, and Zn in vein minerals, and hence the fluid, could not principally have originated locally from either the rock or mineral that hosts the vein for a number of reasons. Firstly, the veins largely represent open-space precipitation, in which the fluids did not significantly interact with surrounding minerals (vein types 1, 3, and 4; Fig. 2.7). Only in the case of type 2 veins did the fluid interact with the neighbouring mineral to precipitate an outer zone dominated by chlorite (vein type 3; Fig. 2.7), with the inner zone representing lower fluid-rock ratios. Secondly, the composition of the vein minerals is not correlated with or controlled by the composition of the host rock (cf. section 2.5.2.2; Fig. 2.13). Lastly, vein mineral chemistry is only affected when Fe-Ti oxides and pyroxene are the host minerals to the vein, in which case the Ti, V, and Cr contents of the vein minerals are enriched compared to veins hosted by plagioclase (Figs. 2.11, 2.12). The Co, Ni, and

Zn contents, however, are unaffected and do not correlate with any of the host rocks or minerals (Figs. 2.11, 2.12).

Sulfide minerals are significant hosts of Co, Ni, and Zn in the Eastern Gabbro, with chalcopyrite being the principal host of Zn and pentlandite, and to a lesser extent pyrrhotite, being the principal hosts of Co and Ni (Brzozowski et al., 2017b). Therefore, if the fluids derived their metals from sulfide minerals, it would be expected that the Co, Ni, and Zn content of vein minerals would correlate positively with sulfide content. Whole-rock Cu and Ni content can be used as a proxy for sulfide mineralization because the majority of Cu is held in chalcopyrite and, although olivine represents a significant host of Ni, a large proportion is also held in pentlandite and pyrrhotite. Conversely, because the platinum-group elements (PGE) largely occur as platinum-group minerals (PGM) rather than in solid solution in sulfides (Ames et al., 2016, 2017; Brzozowski et al., 2017b; Good et al., 2017), the Co, Ni, and Zn content of vein minerals should not exhibit any correlation with Pd, the most abundant PGE in the Eastern Gabbro. Although the Co, Ni, and Zn content of vein minerals do not exhibit any correlations with whole-rock Pd or Ni, they do correlate with whole-rock Cu (Fig. 2.17), but the correlation is negative rather than positive as would be expected if the fluids derived their metal content from sulfides. This indicates that mineralization was not the source of the Co, Ni, and Zn in the fluid and is likely the reason why there is no correlation between vein-hosted mineral chemistry and distance from mineralization within individual drill holes (Fig. 2.19).

Because olivine, pyroxene, and Fe-Ti oxides are significant hosts of Co, Ni, and Zn (Ruthart, 2013; Shahabi Far, 2016; Brzozowski et al., 2017a), the alternative is that the fluids derived these metals by progressive interaction with these minerals as the fluids migrated upwards through the pluton (i.e., increasing cumulative fluid-rock interaction with increasing height in the pluton). If this hypothesis is correct, than the concentration of Co, Ni, and Zn in vein-hosted minerals should increase systematically with increasing distance from the footwall contact (i.e., height in the pluton). This is what is observed in the aggregate downhole plots (Fig. 2.20) and in the downhole plots of individual drill holes (Fig. 2.21). An explanation for the lack of systematic variation in Cu (not shown) with

distance from the footwall contact is that most of the Cu was added to the fluids in the lower parts of the system, where there are abundant Cu-sulfides, and insignificant Cu was added to the fluid as it migrated through the overlying gabbro because the silicates and oxides contain negligible amounts of Cu compared to, for example, chalcopyrite. In addition, no Cu was removed from the fluid by precipitation of a Cu-rich phase.

2.6.4 Evolution of the hydrothermal system

The mineralogy and trace-element chemistry of minerals hosted in veins and in alteration patches are different. Vein-hosted minerals consist predominantly of chlorite with lesser actinolite, serpentine, and saponite. Minerals hosted in patchy alteration consist predominantly of actinolite with lesser chlorite and epidote. Based on the Fe-Mg content of actinolite and on the pressure of crystallization, the lowest temperature at which it can crystallize ranges from approximately 375 ^{o}C (Fe-rich) to 500 ^{o}C (Mg-rich), with maximum temperatures above 600 ^{o} C (Ernst, 1968; Hellner and Schürmann, 1966). The predominance of coarse actinolite in patchy alteration compared to the minor abundance of fine-grained actinolite in veins suggests that the patchy alteration likely formed at higher temperatures than the veins. Unfortunately, mineral geothermometers cannot be used on the Marathon veins to estimate the temperature of precipitation because they represent mineral aggregates and are too fine grained to obtain single-crystal analyses. Veins have also been observed to crosscut patchy alteration, requiring that the veins formed after the patchy alteration. Vein-hosted minerals are enriched in Cr, As, Sn, and Sb compared to chlorite in patchy alteration, whereas the latter are enriched in Mn, Co, Ni, and Zn (Fig. 2.22). Because the composition of chlorite in patchy alteration that is isolated from sulfides is similar to those which are associated with sulfides (Fig. 2.23), this chlorite could not have obtained these elements through direct replacement of the sulfides. This suggests that the concentration of these elements in chlorite from patchy alteration was not influenced by local reaction with the host rocks and minerals. Accordingly, the composition of the fluid from which the vein-hosted minerals and chlorite in patchy alteration precipitated must have been different. The sources of these compositionally-distinct fluids, however, is unknown, and was not a focus of this study. All of these textural, mineralogical, and

compositional characteristics indicate that the veins and patchy alteration formed from different fluids during temporally different events. The veins must have formed during a later, lower-temperature hydrothermal event than the patchy alteration. This is also consistent with the lower temperature required for brittle deformation and fracturing.

Previous work by Watkinson and Ohnenstetter (1992) and Ames et al. (2017) characterized the coincidence of abundant PGM with patchy hydrous alteration. Many of these PGM were intergrown with hydrous silicates and were identified as low-temperature phases in the system Pd-Ag-Te (Ames et al., 2017). Accordingly, these PGM were interpreted to result from redistribution of Pd by late-stage magmatic-hydrothermal fluids (Ames et al., 2017; Vymazalová et al., 2017). It is important to note that no PGM were observed in the late-stage veins that crosscut the rocks in the Eastern Gabbro. This indicates that any redistribution of PGE must have occurred during the earlier, higher-temperature hydrothermal event that formed the patchy alteration.

2.6.5 Vein characteristics as a tool for Cu-PGE exploration

An important objective of this study was to test whether the distribution and composition of vein-hosted minerals can be used during exploration as vectors towards potential Cu-Pd mineralization. The characteristics tested include: (1) vein density as an indicator of low-sulfide mineralization, and (2) vein mineral chemistry as an indicator of a) location relative to mineralization (i.e., above or within mineralization), b) distance from thick zones of sulfide, and c) distance from high-grade mineralization.

2.6.5.1 Vein density

The density of veins, measured as the number of veins per 3-meter interval of drill core, is lower in areas where mineralization is present (Fig. 2.5). The relationship between vein density and mineralization can therefore be used to predict if a drill hole hosts mineralization, and roughly where that mineralization is located. The presence of sulfides is an obvious indication of mineralization, however, in mineralized zones such as the W

Horizon, where PGE grades are high and sulfide content is very low, mineralization can only be identified from whole-rock assays, which are not available during core logging. Vein density, which is routinely measured during core logging, may be used as a preliminary indication of mineralization, providing a basis for targeted assaying.

2.6.5.2 Vein-hosted mineral chemistry

As Co, Ni, and Zn in the fluids that precipitated the vein-hosted minerals was not obtained from mineralization, but rather from the major rock-forming minerals (olivine, pyroxene, and Fe-Ti oxides), none of the relationships between vein-hosted mineral chemistry and mineralization (Figs. 2.14-2.18) can be used as exploration vectoring tools. Because the Co, Ni, and Zn content of vein-hosted minerals increases systematically with height in the pluton (Figs. 2.20, 2.21) and the mineralized zones (Footwall Zone, Main Zone, W Horizon) occur at different heights in the pluton (Fig. 2.3), the correlation between vein-hosted mineral chemistry and mineralization is a coincidence and does not relate to the Co, Ni, and Zn content of mineralization, but rather to the height in the pluton at which the vein minerals precipitated. This is corroborated by the similarity in compositional variation of vein-hosted minerals as a function of distance from mineralization (Fig. 2.18) and distance from the footwall contact (Fig. 2.20).

2.7 Conclusions

The application of geochemical vectors to mineral exploration is becoming more common as novel techniques become a necessity to find deeply-buried mineral deposits. Yet, very few studies have characterized the large- and local-scale controls that affect the variations exhibited by the geochemical vector. Similarly, the application of mineral geothermometers without rigorous characterization of mineralogy is detrimental, particularly when the geothermometer uses complex minerals, such as phyllosilicates, which can occur as fine-grained mixtures. Detailed petrographic and mineral chemical characterization of vein-hosted minerals and minerals in patchy alteration indicate that:

i. Vein-hosted minerals (Fe-Mg chlorite, serpentine, saponite, Ca-bearing amphibole) and minerals in patchy alteration (Ca-rich amphibole and Fe-Mg chlorite) crystallized from different fluids during temporally-different events, with the vein minerals forming later and from multiple pulses of lower-temperature fluids.

ii. The trace-element chemistry of vein-hosted minerals (Ti, V, Cr) is controlled on a local scale by the mineral that the vein is hosted by, namely Fe-Ti oxides and pyroxene. The host rock, however, does not exert a strong control on the trace-element chemistry of vein-hosted minerals.

iii. Variations in vein density may provide a valuable tool for locating zones of low-sulfide mineralization. Because the source of most of the Co, Ni, and Zn in the fluid that precipitated the vein minerals was pyroxene, olivine, and Fe-Ti oxides, rather than sulfide mineralization, none of the apparent relationships between the concentration of these elements and mineralization can be utilized as an exploration vectoring tool. These results act as an example of how mischaracterization of the small- and large-scale controls on mineral chemistry can lead to erroneous interpretations and should be viewed as a cautionary example for the application of the chemistry of such minerals as exploration tools in other systems.

2.8 References

Ames, D.E., Kjarsgaard, I.M., Good, D.J., McDonald, A.M., 2016. Ore mineralogy of Cu-PGE mineralized gabbros, Coldwell Alkaline Complex, Midcontinent rift: supporting databases, scanning electron microscope, and mineral chemistry. Geological Survey of Canada Open File No. 8006.

Ames, D.E., Kjarsgaard, I.M., McDonald, A.M., Good, D.J., 2017. Insights into the extreme PGE enrichment of the W Horizon, Marathon Cu-Pd deposit, Coldwell Alkaline Complex, Canada: Platinum-group mineralogy, compositions and genetic implications. Ore Geol. Rev. 90, 723-747.

Brzozowski, M.J., Samson, I.M., Gagnon, J.E., Good, D.J., Linnen, R.L., 2017a. Textural and chemical characteristics of oxide minerals as a record of postmagmatic processes

in the Eastern Gabbro, Coldwell Complex, NW Ontario. Presented at GAC-MAC, Kingston.

Brzozowski, M., Samson, I., Gagnon, J., Good, D., Linnen, R., 2017b. On the controls of low- and high-Cu/Pd mineralization in the Eastern Gabbro, Canada: evidence from sulfide textures, S/Se ratios, and PGE contents. Presented at the SGA 14th Biennial Meeting, Quebec City.

Cao, Y.H., Linnen, R.L., Good, D.J., Samson, I.M., Epstein, R., 2016. The application of portable XRF and benchtop SEM-EDS to Cu-Pd exploration in the Coldwell Alkaline Complex, Ontario, Canada. Geochem. Explor. Environ. Anal. 16, 193–212.

Cathelineau, M., 1988. Cation site occupancy in chlorites and illites as function of temperature. Clay Miner. 23, 471–85.

Dahl, R., Watkinson, D.H., Taylor, R.P., 2001. Geology of the Two Duck Lake Intrusion and the Marathon Cu-PGE Deposit, Coldwell Complex, Northern Ontario. Explor. Min. Geol. 10, 51–65.

Deer, W.A., Howie, R.A., Zussman, J., 1992. An introduction to the rock-forming minerals. Wiley, New York, N. Y.

Downs, R.T., 2006. The RRUFF project : an integrated study of the chemistry, crystallography, Raman and infrared spectroscopy of minerals. Program and Abstracts of the 19th General Meeting of the International Mineralogical Association in Kobe, Japan, 2006.

Ernst, W.G., 1968. Amphiboles. Springer-Verlag, New York, N.Y.

Flemming, R.L., 2007. Micro X-ray diffraction (μXRD): a versatile technique for characterization of Earth and planetary materials. Can. J. Earth Sci. 44, 1333–1346.

Good, D.J., 2010. Applying multistage dissolution upgrading and 3D-GIS to exploration at the Marathon Cu-PGE deposit, Canada, in: 11th International Platinum Symposium, Sudbury, Ontario, Canada.

Good, D.J., Cabri, L.J., Ames, D.E., 2017. PGM Facies variations for Cu-PGE deposits in the Coldwell Alkaline Complex, Ontario, Canada. Ore Geol. Rev. 90, 748-771.

Good, D.J., Crocket, J.H., 1994. Genesis of the Marathon Cu-Platinum-Group Element Deposit, Port Coldwell Alkalic Complex, Ontario: A Midcontinent Rift-Related Magmatic Sulfide Deposit. Econ. Geol. 89, 131–149.

Good, D.J., Epstein, R., McLean, K., Linnen, R., Samson, I., 2015. Evolution of the Main Zone at the Marathon Cu-PGE Sulfide Deposit, Midcontinent Rift, Canada: Spatial Relationships in a Magma Conduit Setting. Econ. Geol. 110, 983–1008.

Gruner, J.W., 1936. The structure and chemical composition of greenalite. Am. Mineral. 21, 449-455.

Hanley, J.J., Bray, C.J., 2009. The trace metal content of amphibole as a proximity indicator for Cu-Ni-PGE mineralization in the footwall of the Sudbury Igneous Complex, Ontario, Canada. Econ. Geol. 104, 113–125.

Hellner, E., Schürmann, K., 1966. Stability of metamorphic amphiboles: the tremolite-ferroactinolite series. J. Geol. 74, 322–331.

Kelley, D.L., Kelley, K.D., Coker, W.B., Caughlin, B., Doherty, M.E., 2006. Beyond the obvious limits of ore deposits: The use of mineralogical, geochemical, and biological features for the remote detection of mineralization. Econ. Geol. 101, 729–752.

Kloprogge, J.T., Frost, R.L., 2000. The effect of synthesis temperature on the FT-Raman and FT-IR spectra of saponites. Vib. Spectrosc. 23, 119–127.

Laetsch, T., Downs, R., 2006. Software For Identification and Refinement of Cell Paramters From Powder Diffraction Data of Minerals Using the RRUFF Project and American Mineralogist Crystal Structure Databases. Presented at the 19th General Meeting of the International Mineralogical Association, Kobe, Japan.

Mulja, T., Mitchell, R.H., 1991. The Geordie Lake Intrusion, Coldwell Complex, Ontario; a palladium- and tellurium-rich disseminated sulfide occurrence derived from an evolved tholeiitic magma. Econ. Geol. 86, 1050–1069.

Puritch, E.P., Orava, D., Armstrong, T., Yassa, A., Gowans, R., Wislesky, I., Jacobs, C., 2009. Technical report on the updated mineral resource estimate and feasibility study for the Marathon PGM-Cu project, Marathon, Ontario, Canada. P&E Mining Consultants Inc., Technical Report, NI 43-101.

Ruthart, R., 2013. Characterization of High-PGE Low-Sulphur Mineralization at the Marathon PGE-Cu Deposit, Ontario (MSc). University of Waterloo.

Samson, I.M., Fryer, B.J., Gagnon, J.E., 2008. The Marathon Cu-PGE deposit, Ontario: Insights from sulphide chemistry and textures. Presented at the Goldschmidt, p. A820.

Shahabi Far, M., 2016. The magmatic and volatile evolution of gabbros hosting the Marathon PGE-Cu deposit: evolution of a conduit system (PhD Dissertation). University of Windsor, Windsor.

Shaw, C.S.J., 1997. The petrology of the layered gabbro intrusion, eastern gabbro, Coldwell alkaline complex, Northwestern Ontario, Canada: evidence for multiple phases of intrusion in a ring dyke. Lithos 40, 243–259.

Vymazalová, A., Laufek, F., Kristavchuk, A.V., Chareev, D.A., Drábek, M., 2017. The system Ag–Pd–Te: phase relations and mineral assemblages. Mineral. Mag. 79, 1813–1832.

Watkinson, D.H., Ohnenstetter, D., 1992. Hydrothermal Origin of Platinum-Group Mineralization in the Two Duck Lake Intrusion, Coldwell Complex, Northwestern Ontario. Can. Mineral. 30, 121–136.

Wilkinson, J.J., Chang, Z., Cooke, D.R., Baker, M.J., Wilkinson, C.C., Inglis, S., Chen, H., Bruce Gemmell, J., 2015. The chlorite proximitor: A new tool for detecting porphyry ore deposits. J. Geochem. Explor. 152, 10–26.

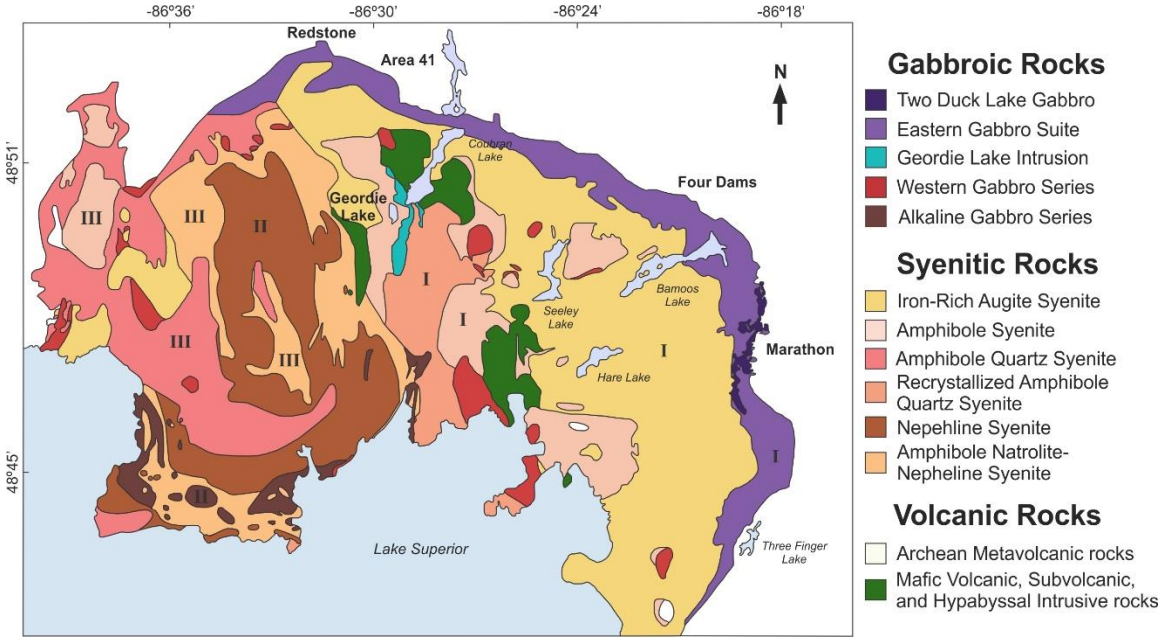

Figure 2.1 Geological map of the Coldwell Complex showing the location of the Eastern Gabbro (light purple) and the Two Duck Lake gabbro (dark purple), the host of the Marathon Cu-Pd deposit. The numbers represent the three intrusive centers from Mulja and Mitchell (1991). Modified from Good et al. (2015).

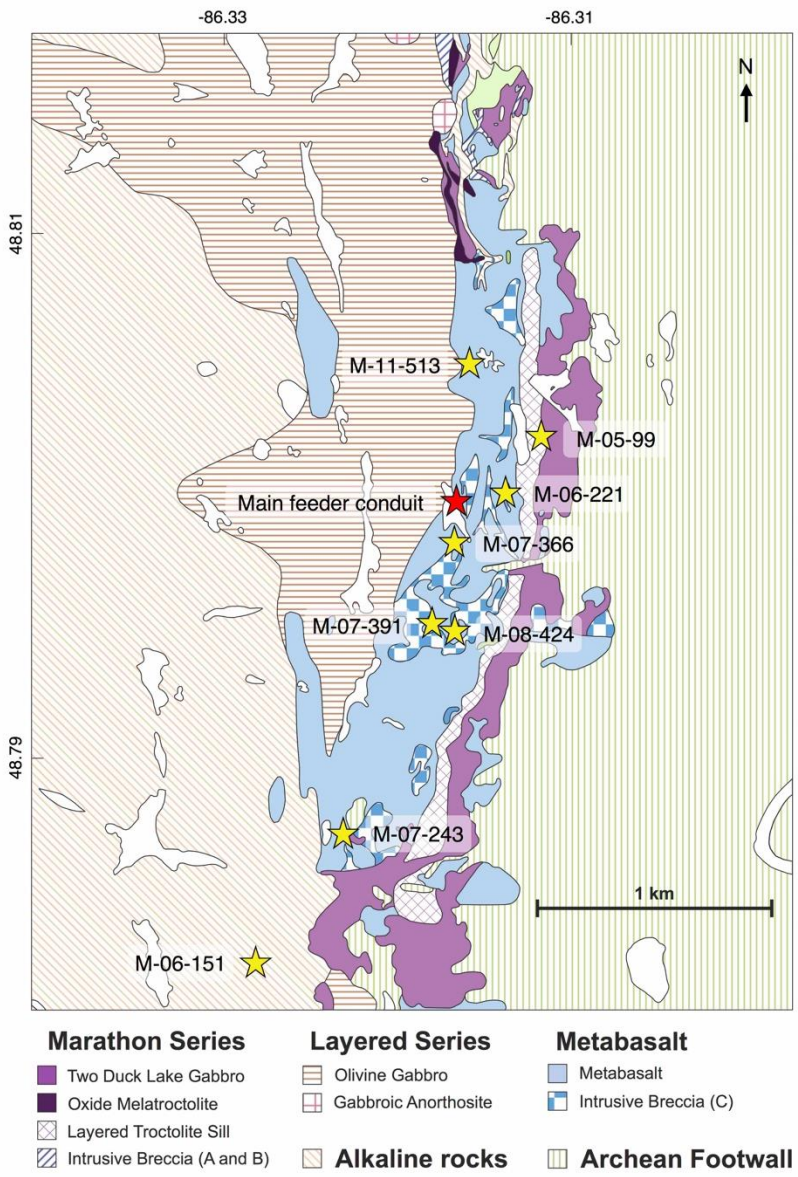

Figure 2.2 Geological map of the Marathon Cu-Pd deposit showing the locations of and relationships between the three gabbroic series: metabasalt, Layered Series, Marathon Series. The locations of the sampled drill holes, as well as the main feeder conduit, are illustrated. Modified from Good et al. (2015).

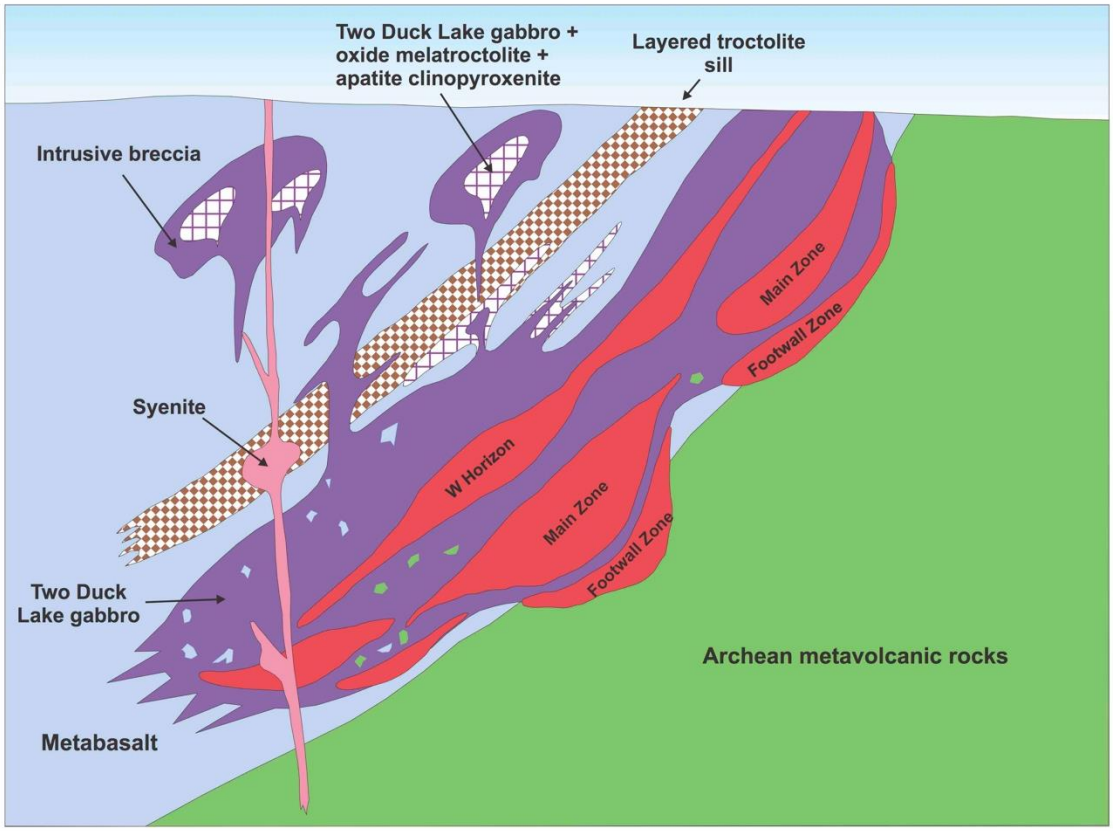

Figure 2.3 A cross-section of the Marathon deposit showing the hypothetical model whereby migrating fluids transport metals from the underlying mineralized Two Duck Lake gabbro upwards into the overlying unmineralized metabasalt and Two Duck Lake gabbro. The transport of metals in such fluids may be recorded in the trace-element chemistry of the vein-hosted minerals. Cross-section modified from Shahabi Far et al. (2016).

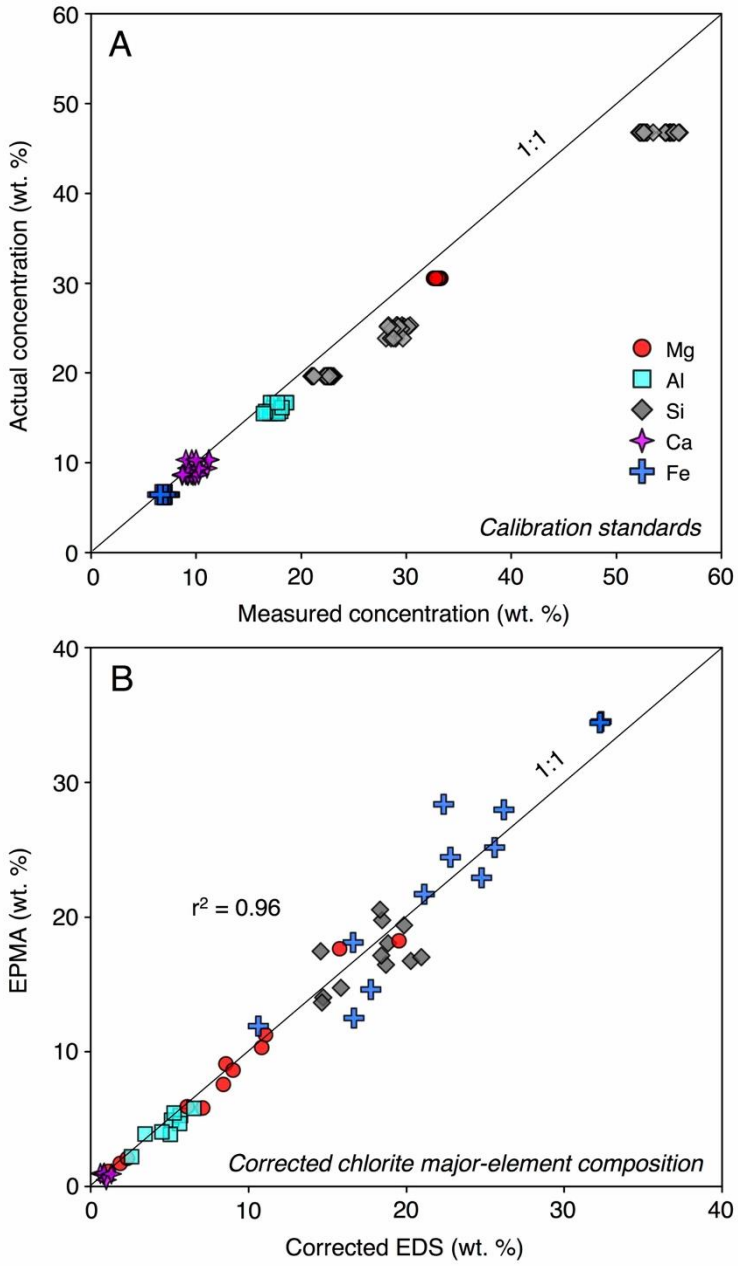

Figure 2.4 Binary diagrams showing a) the correlation between the composition of an olivine standard (characterized by EPMA), a plagioclase crystal from Marathon (characterized by EPMA), and a quartz crystal (stoichiometry) compared to that obtained by EDS and b) the correlation between the composition of vein-hosted minerals obtained by EDS (and corrected using a correction factor obtained from the calibration standards) and EPMA. Note the 1:1 relationship between major-element chemistry of vein-hosted minerals obtained by EDS (corrected) and EPMA and the good correlation ($r^2 = 0.96$).

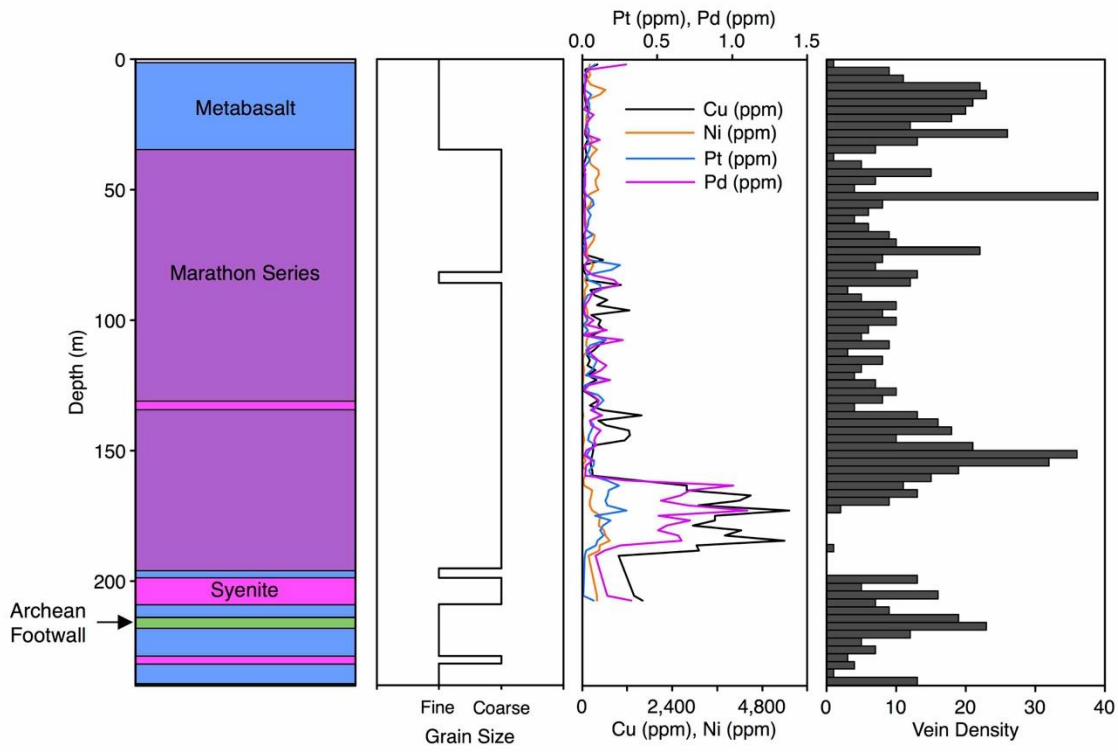

Figure 2.5 Down hole plot of drill hole M-06-221 illustrating the lithology, grain size, Cu, Ni, Pt, and Pd concentration (in ppm) from 2-m assay intervals, and vein density as counted per 3-m interval of drill core. Note the relationship between vein density and mineralization between depths 150-200 m.

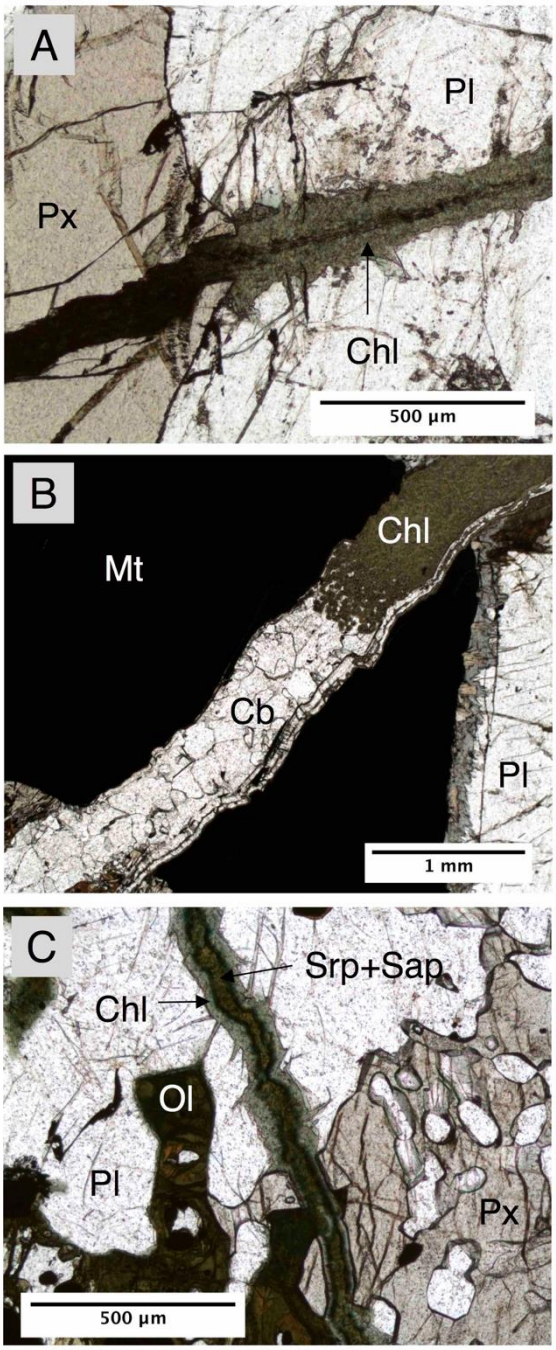

Figure 2.6 Transmitted light photomicrographs of a) vein-hosted minerals whose optical properties are controlled by the mineral the vein is hosted by (plagioclase, pyroxene), b) an Fe-Ti oxide-hosted vein that contains abundant carbonate, c) a zoned vein that contains an outer zone comprised predominantly of chlorite and an inner zone comprised of a mixture of chlorite, serpentine, and spaonite, and d) a symmetrically-zoned vein whose outer zone is controlled by the mineral that the vein crosscuts. Chl = chlorite, sap = saponite, srp = serpentine, pl = plagioclase, px = pyroxene, ol = olivine.

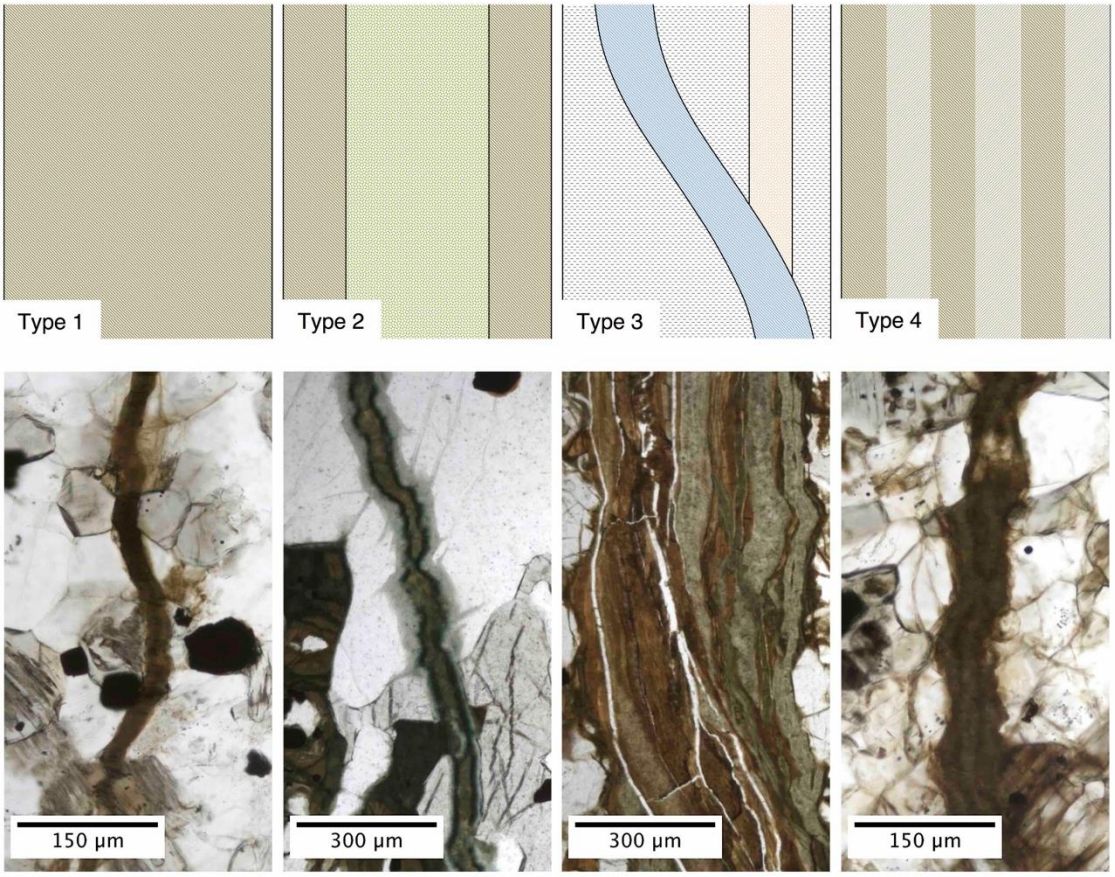

Figure 2.7 Cartoon representations of the four types of veins with example transmitted light photomicrographs.

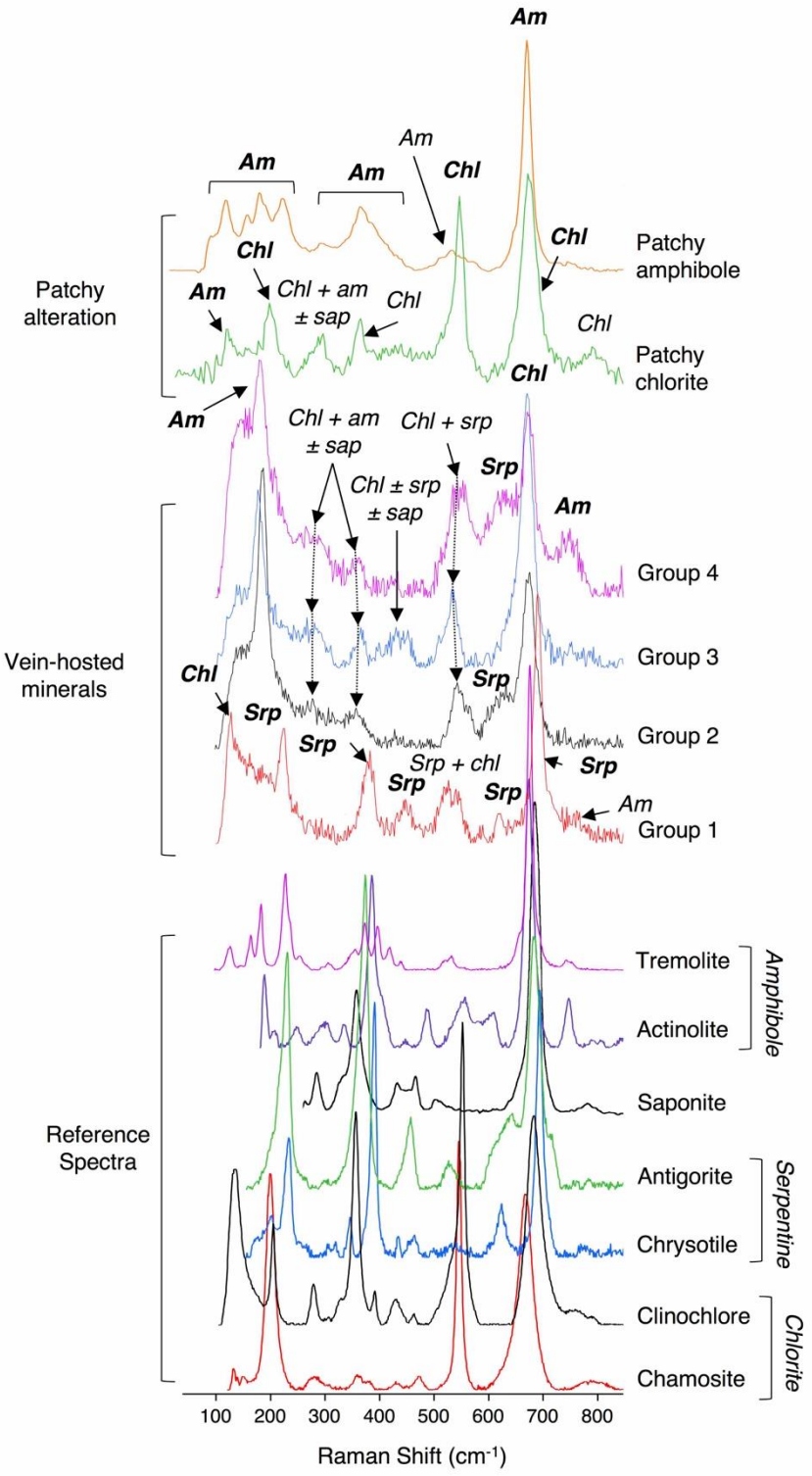

Figure 2.8 Measured Raman spectra of vein-hosted minerals and minerals in patchy alteration compared to Raman reference spectra for chlorite-, serpentine-, and amphibole-group minerals from Laetsch and Downs (2006) and saponite from Kloprogge and Frost (2000).

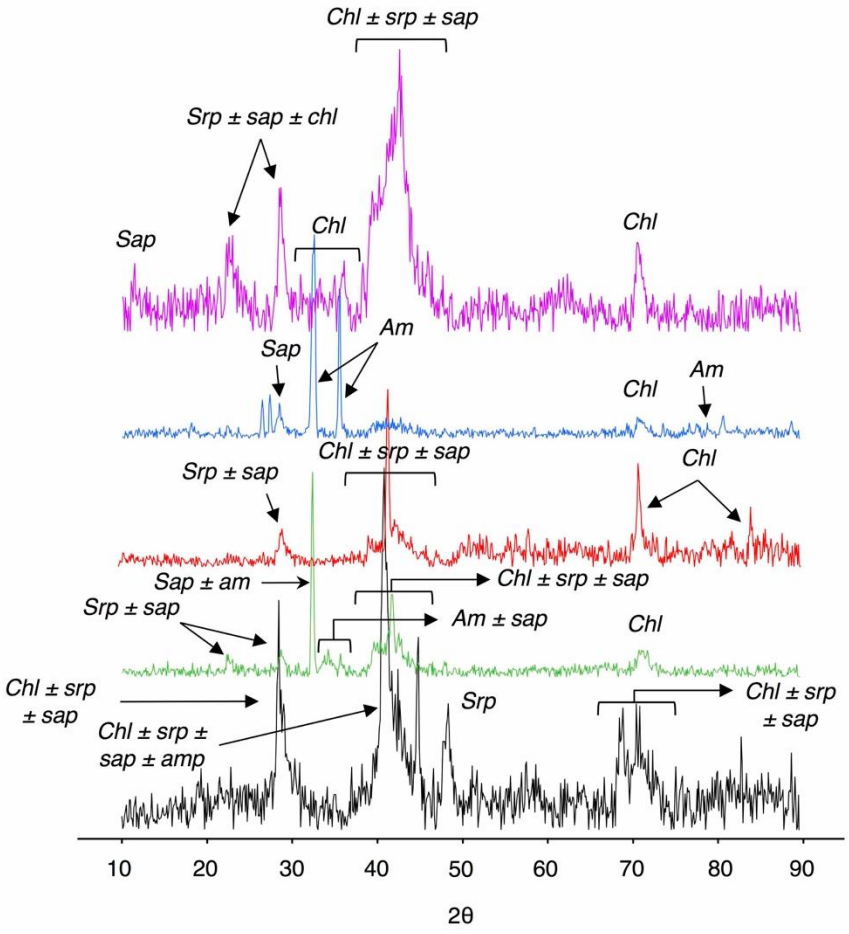

Figure 2.9 Micro-XRD spectra of a subset of vein-hosted minerals. Am = amphibole, chl = chlorite, sap = saponite, and srp = serpentine. Note that poorly-crystallized saponite and serpentine produce broad peaks, whereas well-crystallized amphibole produces narrow peaks. Chlorite appears to show a range of crystallinity (broad to narrow peaks).

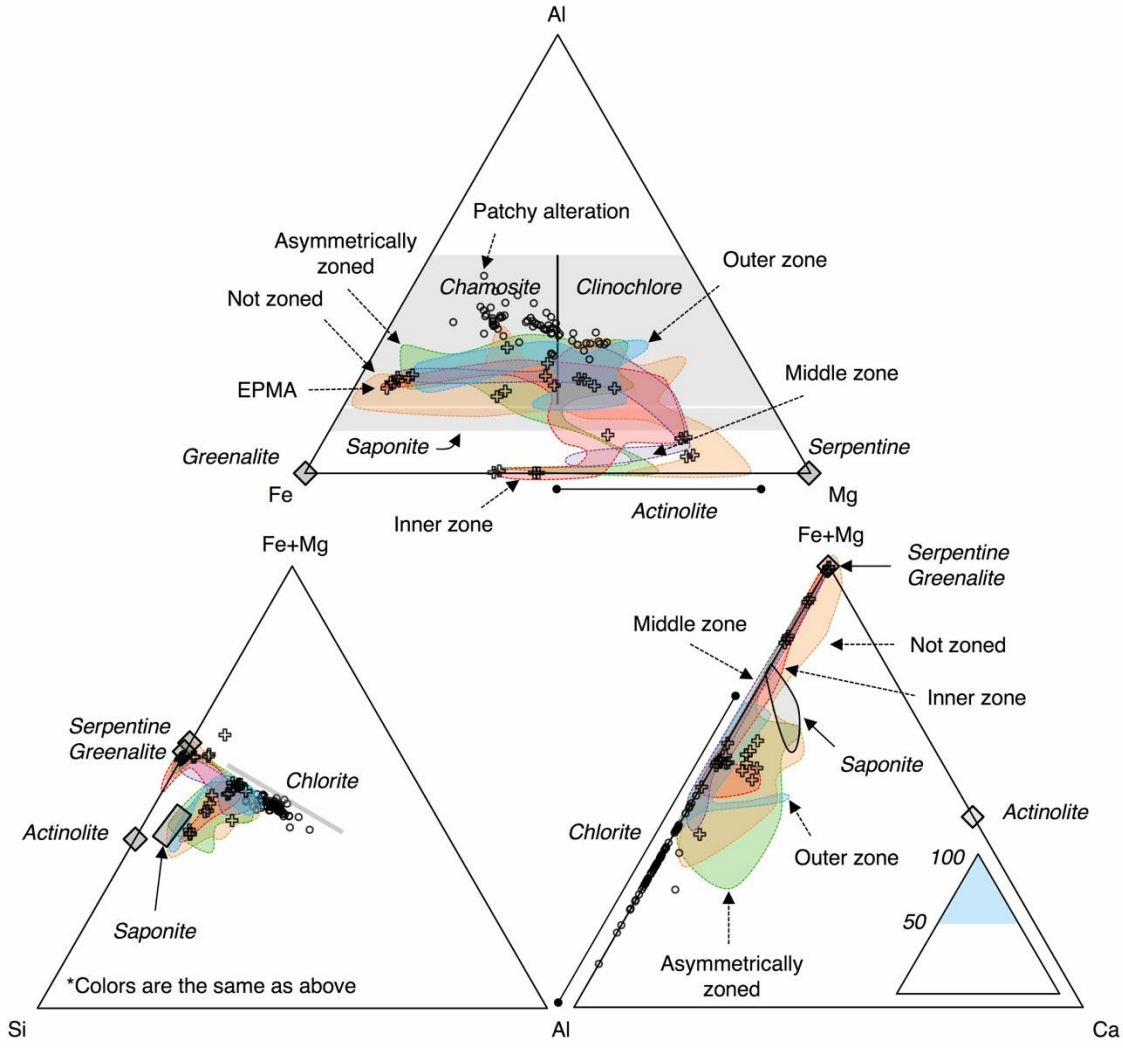

Figure 2.10 Major element ternary diagrams illustrating the molar proportions of Al-Fe-Mg, (Fe+Mg)-Si-Al, and (Fe+Mg)-Al-Ca for vein-hosted minerals and chlorite-group minerals in patchy alteration (open circles) obtained by EDS. A subset of replicate analyses obtained by EPMA are illustrated by the open crosses. Compositional limits for chlorite, saponite, actinolite, hornblende, and serpentine are from Deer et al. (1992) and greenalite from Gruner (1936).

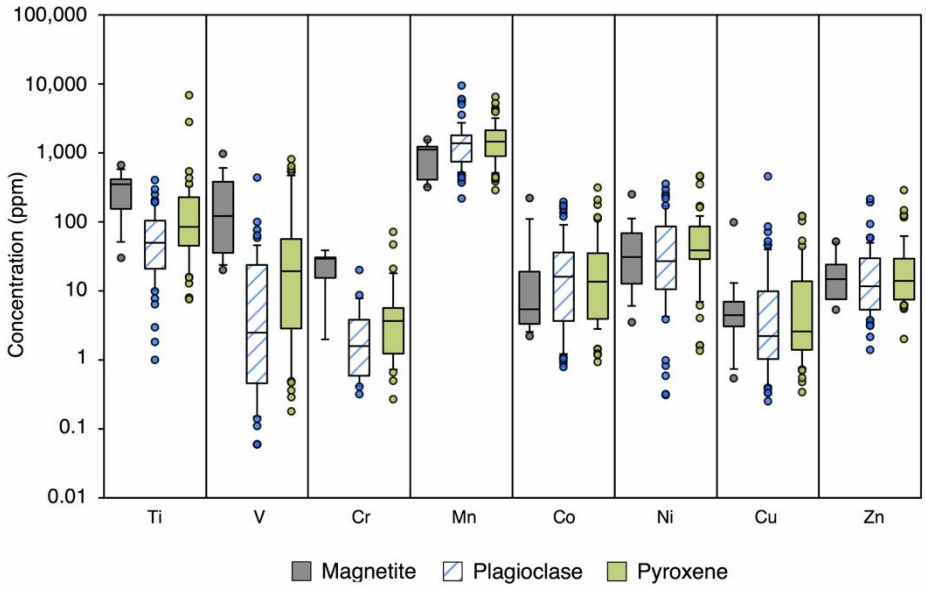

Figure 2.11 Box-whisker diagram illustrating the variation in transition metal content of vein minerals hosted by Fe-Ti oxides, plagioclase, and pyroxene in all rock series.

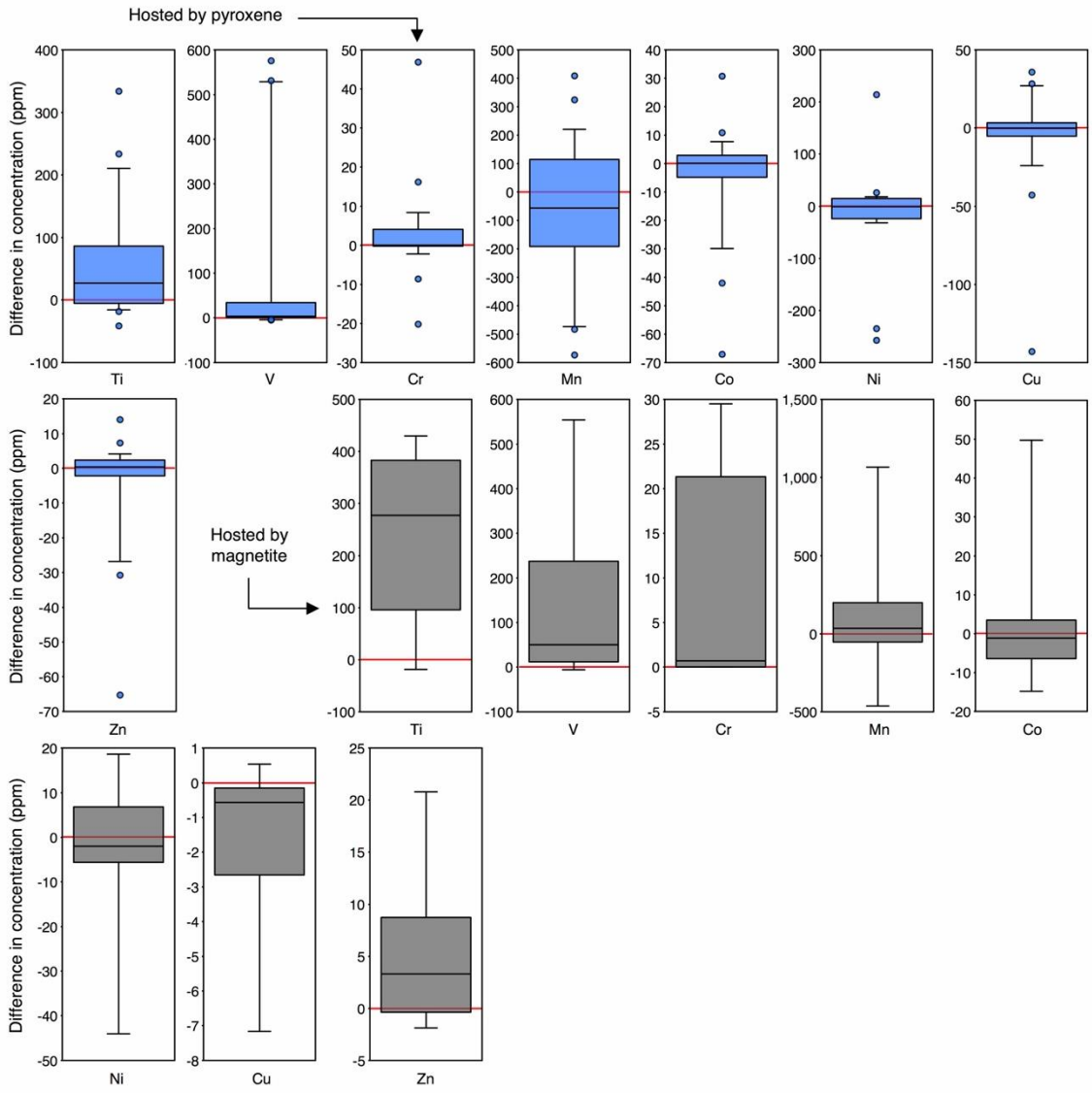

Figure 2.12 Box-plot diagram illustrating the difference in concentration, on a sample-by-sample basis, of vein minerals hosted in pyroxene and Fe-Ti oxides relative to plagioclase in all rock series.

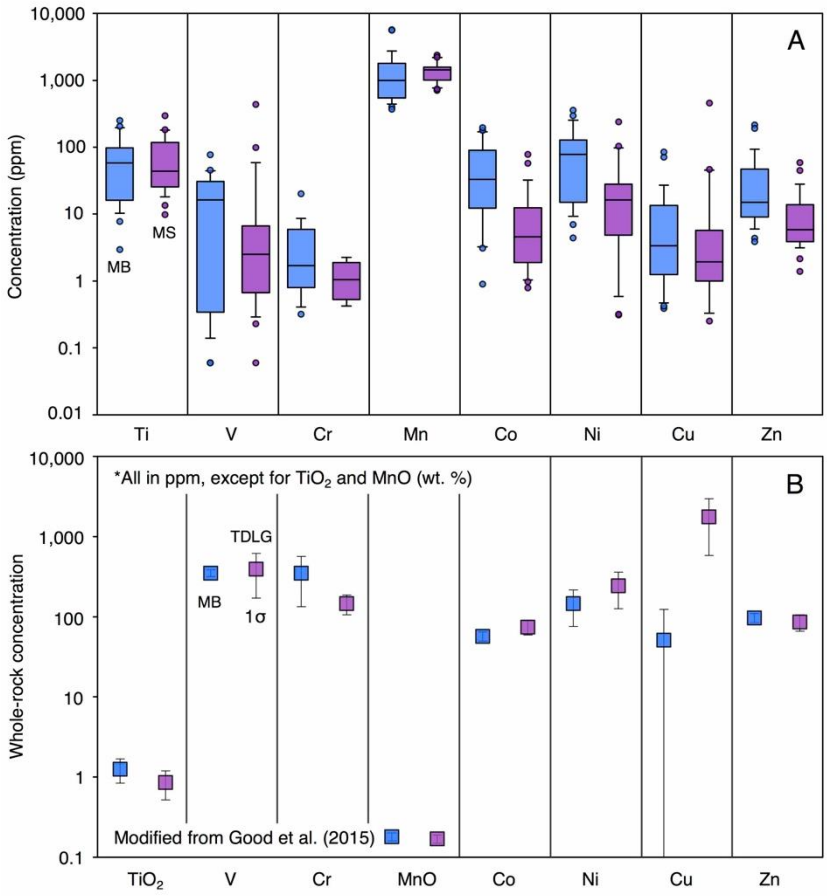

Figure 2.13 Box-whisker diagrams illustrating a) the variation in concentration of vein minerals hosted by metabasalt (MB) and Marathon Series (MS) and b) the average whole-rock composition of metabasalt and the Two Duck Lake gabbro (TDLG), the predominant rock type in the Marathon Series (from Good et al., 2015). Note that the only predominant difference between the two rock types is the concentration of Cu.

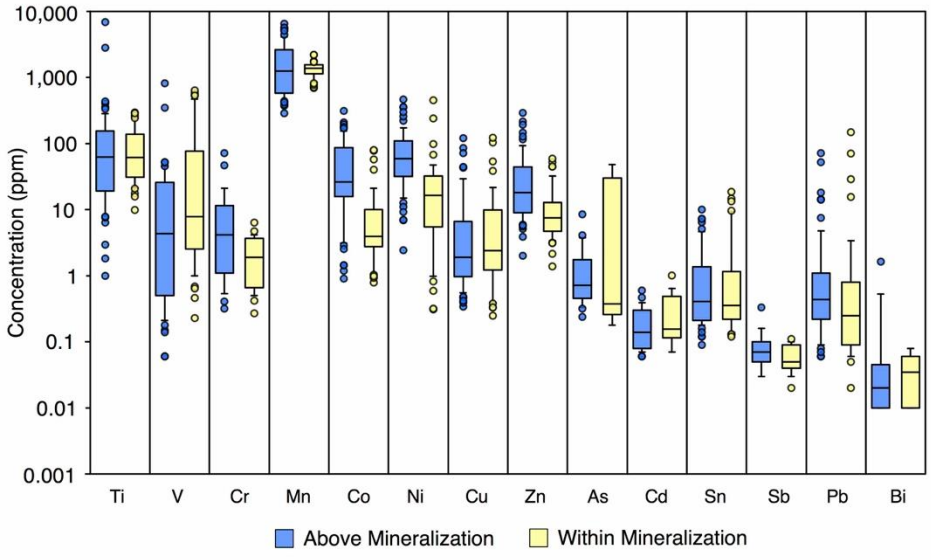

Figure 2.14 Box-whisker diagram illustrating the variation in composition of vein minerals hosted by rocks above mineralization and within mineralization.

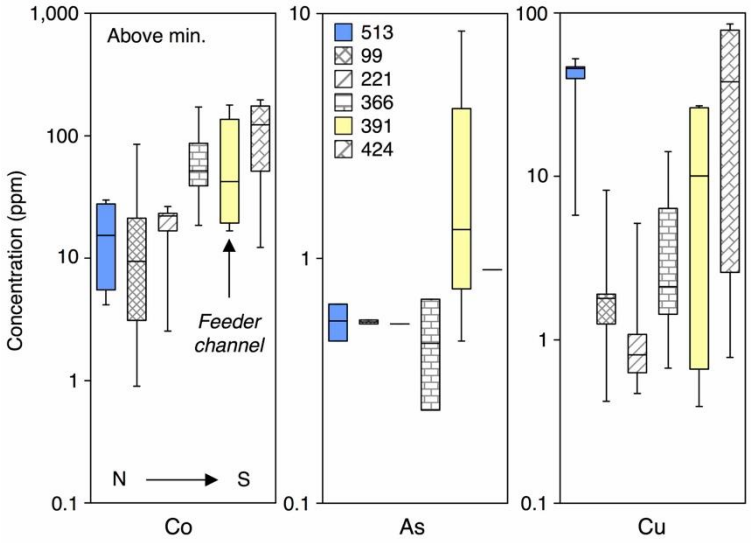

Figure 2.15 Box-whisker diagram illustrating the variation in composition of vein minerals hosted by rocks located above mineralization and that crosscut plagioclase relative to the main feeder channel of the Marathon Cu-Pd deposit. Drill hole M-11-513 is located west of mineralization and is not underlain by mineralization.

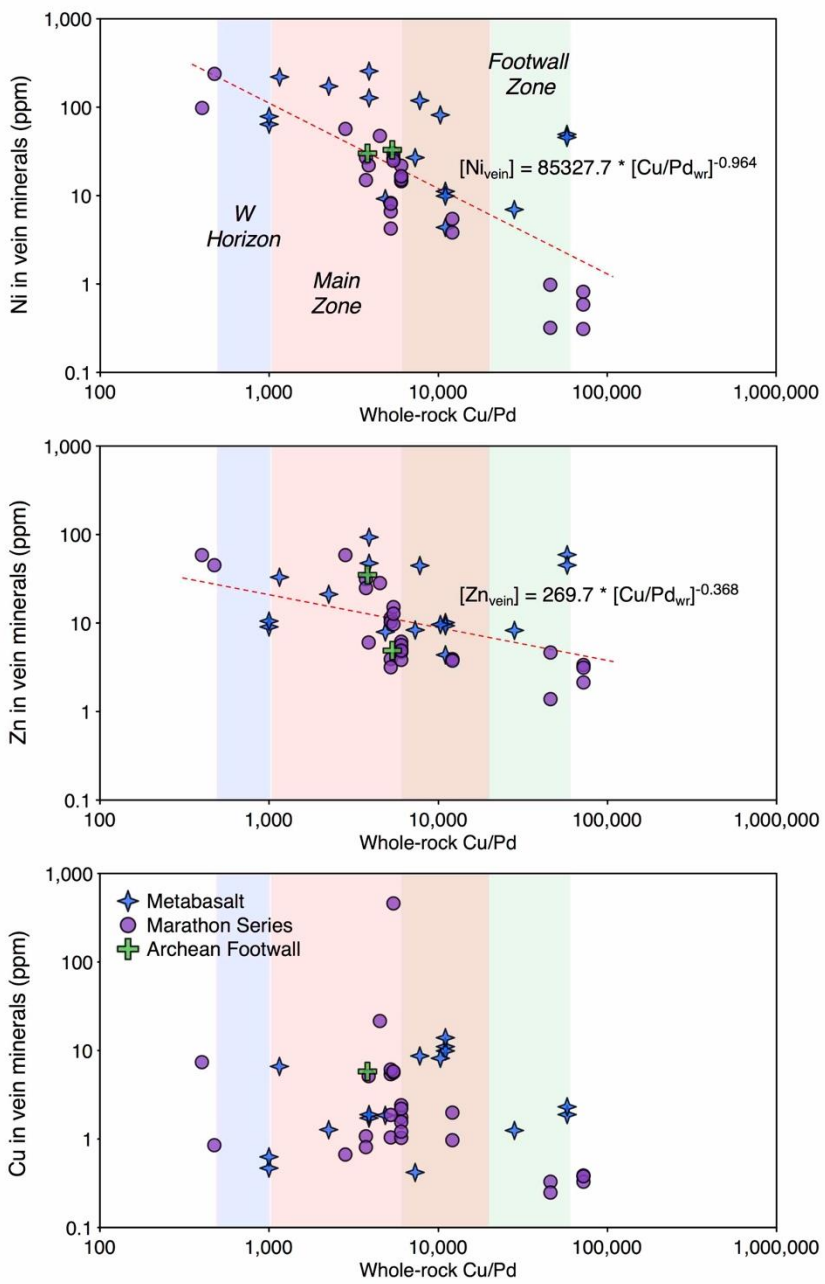

Figure 2.16 Binary diagrams illustrating the correlation between whole-rock Cu/Pd and Ni, Zn, and Cu (ppm) in vein-hosted minerals hosted above and within mineralization and that crosscut plagioclase. The colors represent the range of Cu/Pd for the various mineralized zones at Marathon. *Green* is the range of Cu/Pd for the Footwall Zone, *red* for the Main Zone, and *blue* for the W Horizon. The range of Cu/Pd for each of the zones is from Shahabi Far (2016).

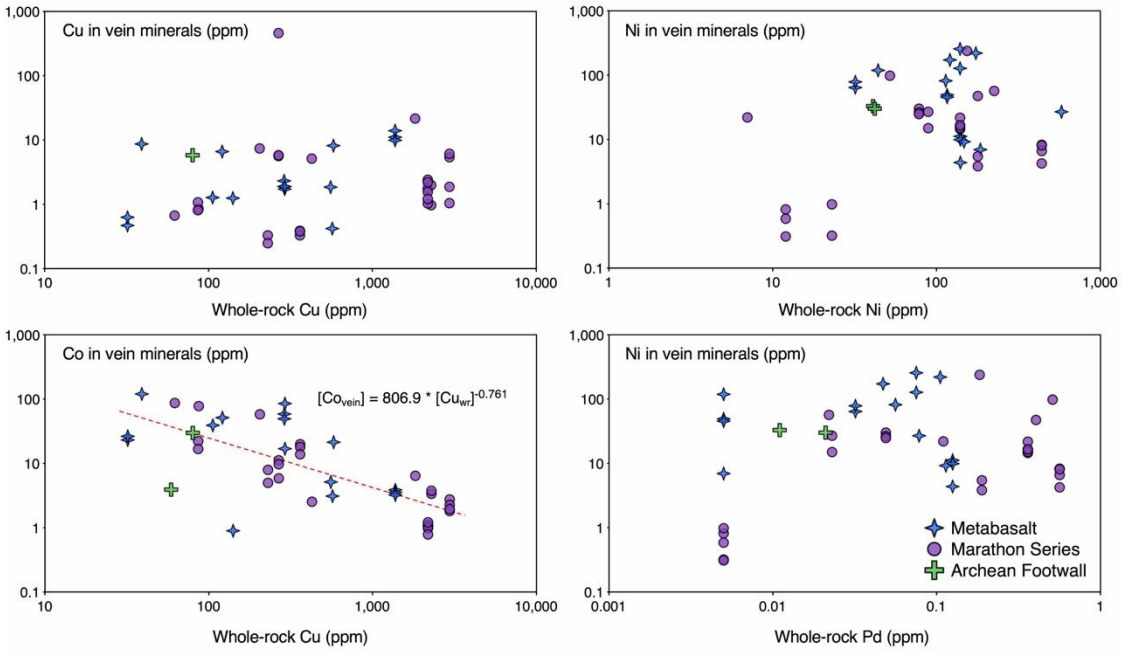

Figure 2.17 Binary diagrams illustrating the lack of correlation between whole-rock Cu and vein mineral Cu, whole-rock Ni and vein mineral Ni, and whole-rock Pd and vein mineral Ni. Veins hosted within and above mineralization and that crosscut plagioclase were used. Note the negative correlation between Co (and Ni and Zn) content in vein minerals and whole-rock Cu. [Co_{vein}] = concentration of Co in vein-hosted minerals, [Cu_{wr}] = whole-rock Cu concentration.

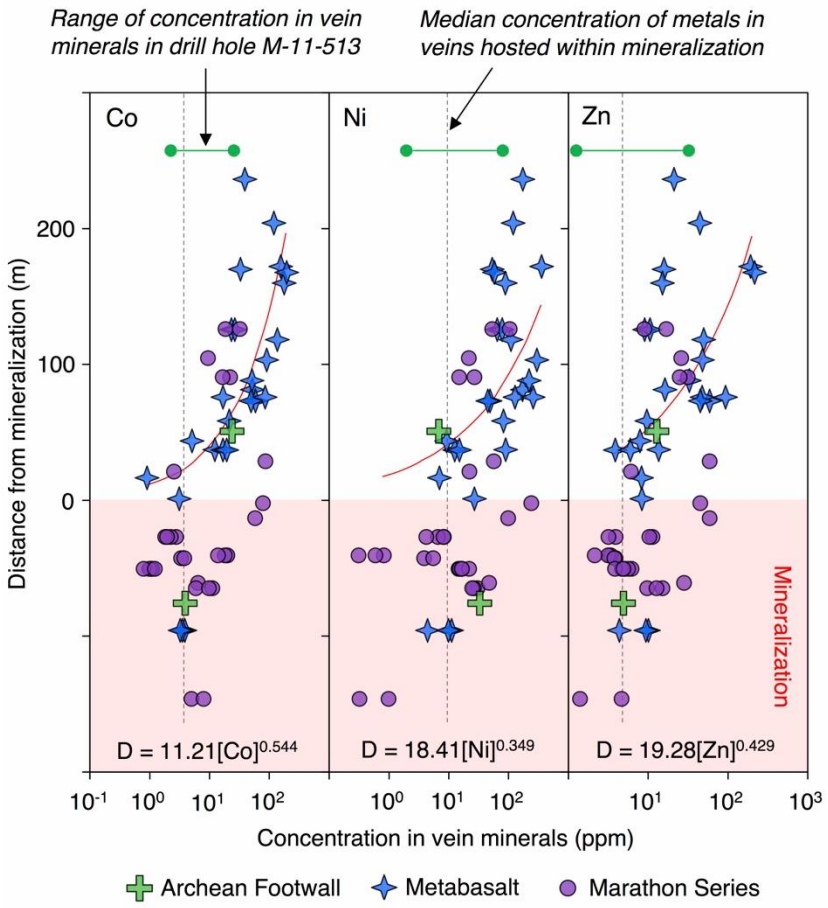

Figure 2.18 Aggregate downhole variation diagrams illustrating the concentration of Co, Ni, and Zn in vein minerals hosted by plagioclase relative to the top of mineralization. Veins from all of the drill holes sampled are incorporated into a single downhole diagram by normalizing their depths to the top of mineralization in their respective drill hole. The top of mineralization is defined as the depth in a given drill hole at which point the whole-rock Cu and Pd initially show an increase in whole-rock concentration that is roughly 10 times the background concentration. The green line represents the range of Co, Ni, and Zn concentration in vein-hosted minerals in drill hole M-11-513, which is located west of mineralization and is not underlain by mineralization. D is the distance to top of mineralization and [Co, Ni, Zn] are the concentrations of the metals in vein-hosted minerals.

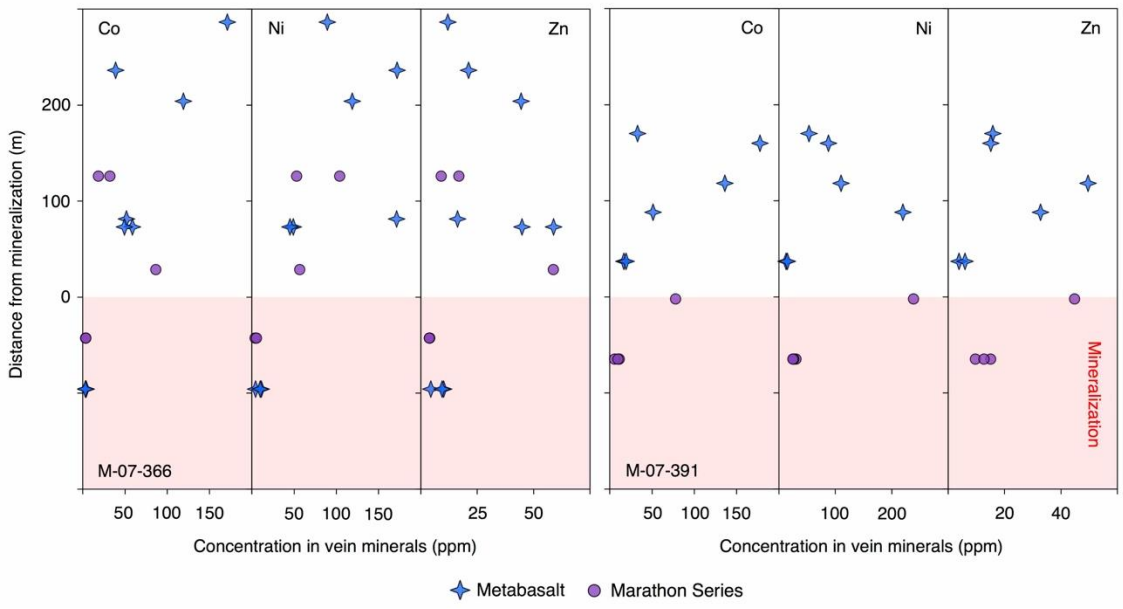

Figure 2.19 Downhole variation diagrams illustrating the concentration of Co, Ni, and Zn in vein-hosted minerals down individual drill holes relative to the top of mineralization. The top of mineralization is defined as above.

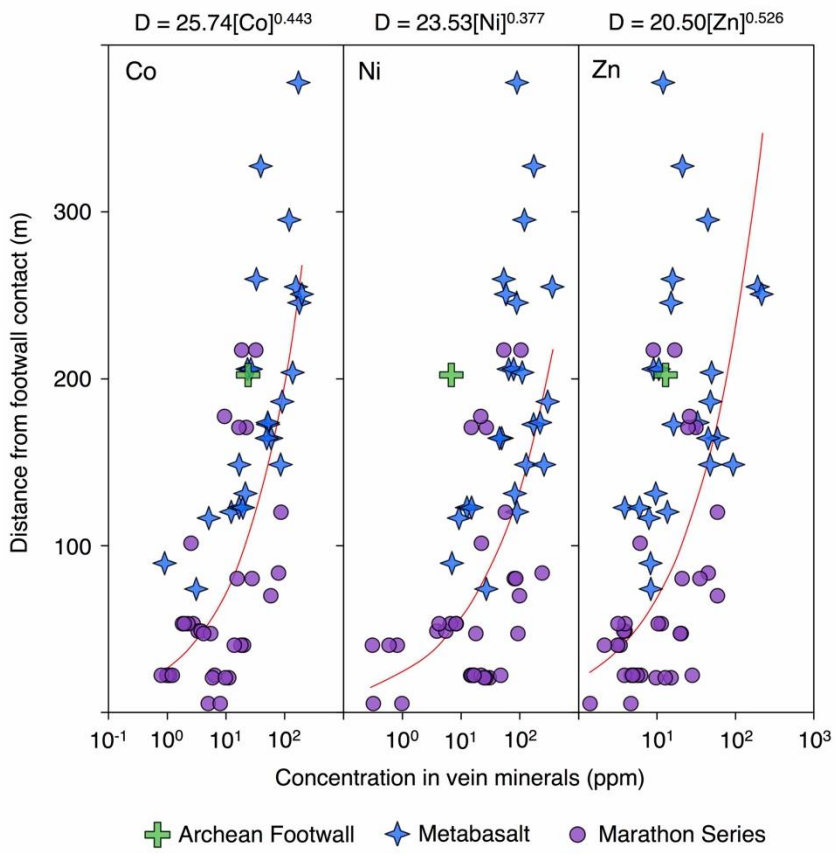

Figure 2.20 Aggregate downhole variation diagrams illustrating the concentration of Co, Ni, and Zn in vein minerals hosted by plagioclase relative to the footwall contact. Veins from all of the drill holes sampled are incorporated into a single downhole diagram by normalizing their depths to the footwall contact in their respective drill hole. In one instance where the drill hole did not intersect the footwall contact (M-06-151), the depth of the bottom of the drill hole was used.

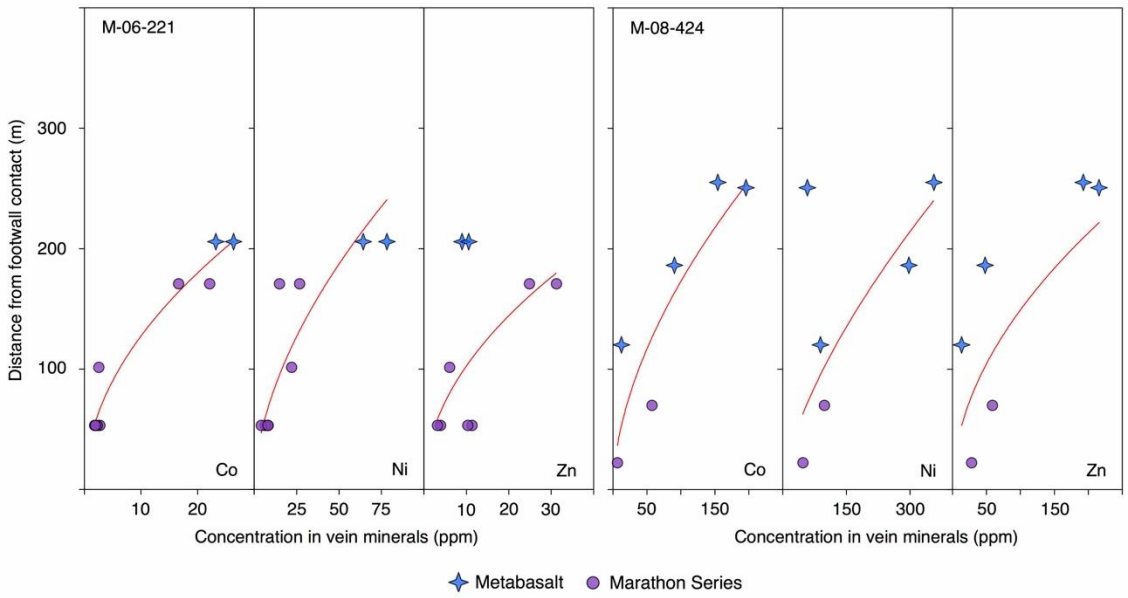

Figure 2.21 Downhole variation diagrams illustrating the concentration of Co, Ni, and Zn in vein-hosted minerals down individual drill holes relative to the footwall contact.

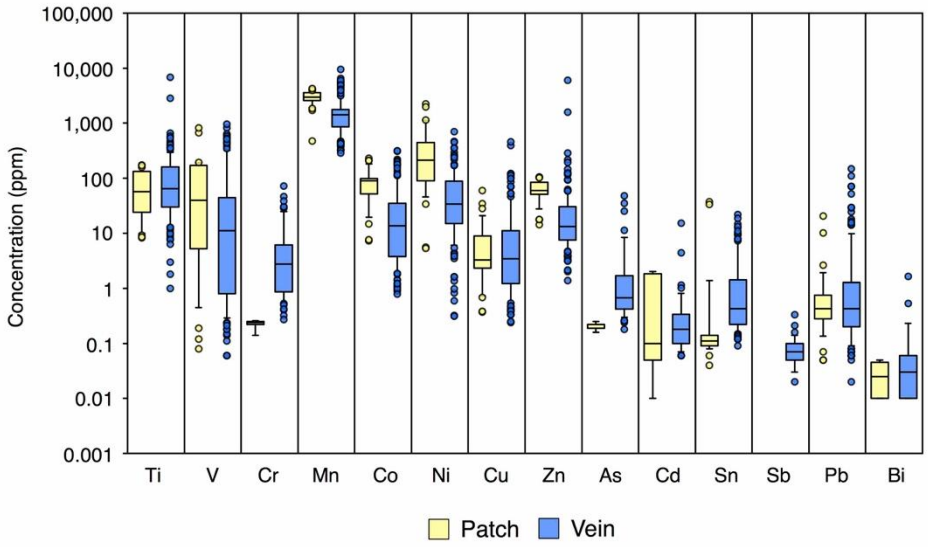

Figure 2.22 Box-whisker diagram comparing the composition of vein-hosted minerals and chlorite from patchy alteration.

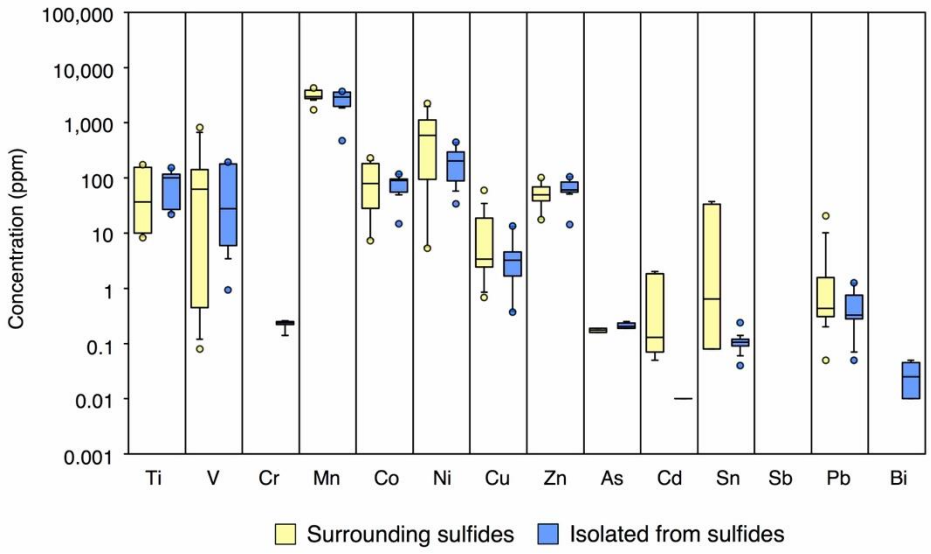

Figure 2.23 Box-whisker diagram comparing the composition of chlorite from patchy alteration that are associated with sulfides to those which are isolated from sulfides.

Chapter 3

C-mediated oxidation of Fe-Ti oxide intergrowths: Evidence from oxide textures and trace-element chemistry and implications for the postmagmatic evolution of the Eastern Gabbro, Coldwell Complex

3.1 Introduction

Magnetite (Fe_3O_4) is ubiquitous in a variety of magmatic and hydrothermal mineral deposit types (e.g., Ni-Cu-PGE, IOCG, skarn). Along with this ubiquity, its wide compositional variability that relates to its environment of formation has made magnetite a widely used pathfinder for mineral deposits and as a petrogenetic indicator (e.g., Boutroy et al., 2014; Dare et al., 2014a, 2014b, 2013, 2012; Dupuis and Beaudoin, 2011). Using laser ablation ICP-MS, Dare et al. (2011, 2014b, 2013, 2012) characterized the variation in bulk trace-element composition of Fe-Ti oxide intergrowths as a function of sulfide liquid and silicate melt evolution. Dare et al. (2014a) characterized differences in trace-element composition of Fe-Ti oxide intergrowths hosted in barren and fertile igneous complexes. Using the minor-element composition of low-Ti magnetite (< 2 wt. % Ti) obtained using electron microprobe, Dupuis and Beaudoin (2011) developed a series of binary discriminant diagrams to distinguish magnetite from different mineral deposit types (e.g., iron oxide copper gold, banded iron formations, Ni-Cu-PGE). Using laser ablation ICP-MS, Boutroy et al. (2014) characterized the differences in bulk trace-element composition of Fe-Ti oxide intergrowths that crystallized from sulfide a liquid from a number of Ni-Cu-PGE deposits hosted in different geologic environments (e.g., komatiite, flood basalt, impact-related). Magnetite typically contains a variety of exsolution features, most commonly ilmenite, but also spinel and ulvöspinel (Buddington and Lindsley, 1964). Detailed characterization of the type of exsolution and the grain-scale distribution of these exsolution features is critical prior to any geochemical analyses because they will redistribute elements that were once present in a homogenous magnetite-ulvöspinel solid solution at high temperature (e.g., Hu et al., 2015). Development of methods to integrate the composition of the lamellae with the matrices thus becomes paramount to obtaining accurate compositions of the original high temperature Fe-Ti oxide solid solution.

Ilmenite lamellae that occur in the {111} plane (Fig. 3.1) are very common in magmatic magnetite, but are less common in hydrothermal magnetite as a result of the lower Ti content in and lower temperature of hydrothermal fluids compared to silicate melts (Nadoll et al., 2014). Lamellae of ulvöspinel, which occur in the {100} plane of magnetite (Fig. 3.1), are less common (Buddington and Lindsley, 1964). A complete solid solution has been experimentally-demonstrated between magnetite and ulvöspinel (Buddington and Lindsley, 1964 and references therein; Lilova et al., 2012). Conversely, experimental evidence suggests that magnetite and ilmenite do not exhibit a complete solid solution given that experimental re-homogenization of magnetite-ilmenite intergrowths could not be achieved while maintaining bulk composition (i.e., ilmenite gains Fe_2O_3 and magnetite gains Fe_2TiO_4; ilmenite converts to hematite and eventually pseudobrookite) (Buddington and Lindsley, 1964; Lindsley, 1963; Verhoogen, 1962; Vincent et al., 1957; Wright, 1959). Vincent et al. (1957) suggested that ilmenite may be dimorphous with a cubic high temperature structure (γ-$FeTiO_3$), such that it could form a solid solution with magnetite at high temperatures. In this model, upon cooling below the solvus, γ-$FeTiO_3$ would exsolve and invert to a rhombohedral structure (Vincent et al., 1957). Accordingly, models have been proposed to explain the presence of ilmenite lamellae in magnetite through direct ilmenite exsolution, such as vacancy relaxation of a cation-deficient titanomagnetite (Haggerty, 1977; Haselton and Nash, 1975; Ramdohr, 1955). These latter processes, however, typically require very reducing conditions such as those of the moon, rather than terrestrial environments (Lattard, 1995).

The most widely accepted model for the presence of ilmenite lamellae is the oxy-exsolution model of Buddington and Lindsley (1964). According to this model, ilmenite lamellae do not exsolve from the magnetite itself, but rather form by oxidation of ulvöspinel (Fe_2TiO_4) (i.e., oxidation-exsolution) through interaction with a fluid (Buddington and Lindsley, 1964; Haggerty, 1976; Ramdohr, 1953; Verhoogen, 1962).

Experimental evidence suggests that ilmenite can be formed by oxidation of ulvöspinel given that i) magnetite-ilmenite intergrowths have been created by controlled oxidation of

ulvöspinel (Buddington and Lindsley, 1964; Verhoogen, 1962), ii) ilmenite and hematite can be formed during annealing of ulvöspinel in air at 700 to 1000°C (Groschner et al., 2013), and iii) magnetite-ilmenite intergrowths have been homogenized under reducing conditions (Wright, 1959). Although less common, ulvöspinel lamellae in magnetite have been documented from a variety of igneous rocks, including those that host Ni-Cu-PGE deposits (von Gruenewaldt et al., 1985), Fe-Ti-V deposits (Charlier et al., 2015; Duchesne, 1972, 1970; McEnroe et al., 2000; Speczik et al., 1988), and Kiruna-type deposits (Mücke, 2003). Accordingly, if the oxy-exsolution model is correct, this suggests that most igneous rocks underwent postmagmatic oxidation.

All of the aforementioned lines of evidence for the mechanism of ilmenite formation are based principally on mineral textures and no comparison is made between the trace-element composition of Fe-Ti oxide intergrowths that exhibit these textures. This, in part, is due to analytical limitations during the times the studies were undertaken. From one of the original studies that detailed the occurrence of magnetite-ulvöspinel intergrowths (Ramdohr, 1953) to one of the most recent studies that discuss the mechanisms of formation of various magnetite intergrowths (Tan et al., 2016), the most widely used forms of chemical analyses include x-ray fluorescence of Fe-Ti oxide grain separates and in situ electron microprobe analyses of Fe-Ti oxide intergrowths (bulk analyses and analyses of magnetite and exsolution products). Neither of these techniques, however, can analyze metals at detection limits lower than a few hundreds of parts per million (ppm). Current analytical instrumentation (e.g., laser ablation ICP-MS) provides avenues for the accurate and precise determination of trace elements in Fe-Ti oxide intergrowths in sub-ppm concentrations and on a scale of 10s of micrometers.

The presence of a variety of exsolution textures in magnetite from the Eastern Gabbro of the Coldwell Complex provides an opportunity to improve upon earlier studies through i) detailed mineralogical and textural characterization of Fe-Ti oxide intergrowths throughout a series of mafic-ultramafic rocks that are variably mineralized with Cu and PGE, ii) determination of the trace-element chemistry of these various intergrowths in an effort to understand their origin, and iii) development of methods for accurate and representative

determination of the trace-element composition of high temperature homogenous Fe-Ti oxide solid solution (i.e., magnetite + (oxy)-exsolution product), which could be used in future studies that focus on the characterization of oxide chemistry as a petrogenetic and exploration tool.

3.2 Geology of the Eastern Gabbro

The Eastern Gabbro occurs around the eastern and northern margins of the Midcontinent Rift-related Coldwell Complex, which was emplaced at 1.1 Ga (Fig. 3.2) (Good et al., 2015). Recent work by Good et al. (2015) subdivided the Eastern Gabbro into three genetically distinct rock series: metabasalt, Layered Series, and Marathon Series (Fig. 3.3). The metabasalt is the earliest, and is homogenous, equigranular, and metamorphosed to hornfels grade. It makes up 20 to 30% of the Eastern Gabbro package, but, unlike the other two rock series, lacks any form of mineralization. The Layered Series makes up the majority of the Eastern Gabbro and occurs above the metabasalt at the Marathon deposit. It is texturally homogenous throughout the Eastern Gabbro, but exhibits some compositional variations (Cao, 2017; Shaw, 1997). It has an average composition of olivine gabbro and displays modal layering that is characterized by variable amounts of plagioclase and pyroxene. The olivine gabbro grades into discontinuous lenses of layered oxide augite melatroctolite. Secondary chalcopyrite and pyrrhotite mineralization with negligible platinum-group elements (PGE) occurs locally in the Layered Series and is associated with actinolite and albite alteration. The Marathon Series is the youngest mafic intrusive series and is host to significant Cu and PGE mineralization, the most significant being the Marathon deposit. It is dominated by the Two Duck Lake gabbro (TDLG), a coarse to pegmatitic gabbro that displays ophitic to subophitic texture. The Marathon Series also contains multiple sill- to pod-like bodies of oxide melatroctolite and apatitic olivine clinopyroxenite. Other sulfide occurrences within the Eastern Gabbro are associated with smaller gabbroic to ultramafic intrusions of the Marathon Series. Mineralization located northwest of the Marathon deposit include Four Dams, Area 41, and the Redstone occurrences.

Sulfides at the Marathon deposit occur in three lenses. With increasing distance from the footwall contact, these are the Footwall Zone, Main Zone, Hanging Wall Zone, and W Horizon (Good et al., 2015). Sulfides consist predominantly of disseminated chalcopyrite and pyrrhotite with minor bornite, cubanite, pentlandite, cobaltite, and pyrite. In the Footwall Zone and Main Zone, sulfides are typically interstitial to silicates and oxides, but can occur in association with hydrous silicates, such as chlorite and amphibole. The distribution of high Cu and Pd contents mimic the shape of the footwall. The thickest zone of mineralization occurs in a keel-shaped trough in the Main Zone and is interpreted as the main feeder channel for the TDLG (Good et al., 2015). The W Horizon occurs at the south end of the Marathon deposit and is above, and partially overlaps, mineralization that resembles the Main Zone. It has a low sulfide abundance dominated by chalcopyrite and bornite and is distinguished from the other zones by its high PGE content and low Cu/Pd ratios (as low as 3). Sulfides at Four Dams, Area 41, and Redstone consists predominantly of chalcopyrite and pyrrhotite with trace bornite (McBride, 2015).

3.3 Samples and analytical methods

A suite of samples that are representative of the Eastern Gabbro assemblage and its various mineralized occurrences were collected from drill core at the Marathon deposit and the Four Dams, Area 41, and Redstone occurrences. Table 3.1 describes the number of thin sections used for petrography and chemical analyses from each of the mineralized occurrences and their rock types.

Reflected- and transmitted-light microscopy and scanning-electron microscopy (SEM) were used to characterize the various types of Fe-Ti oxide intergrowths, as well as their relationship to silicate and sulfide minerals. Raman spectra of magnetite and its intergrown phases were collected to characterize their mineralogy because the Fe-Ti oxides of interest have unique bands in Raman spectra that can be identified in mineral mixtures. Raman spectra of fluid inclusions in pyroxene were also collected to characterize their vapor phase. Spectra were collected using a WiTec confocal Raman spectrometer fitted with a 532 nm laser at the University of Windsor. For the Fe-Ti oxides, laser energy was kept low (~ 0.9

mW at the sample surface) to prevent heating and consequent oxidation of magnetite. Raman spectra represent an average of 10 to 20 spectra, each of which was acquired over a period of 10 to 100 seconds. For fluid inclusions, the laser was operated at an energy of 40 mW (at the sample surface). The Raman spectra represent an average of 20 spectra, each of which was acquired over of a period of 0.5 seconds. Mineral identification was achieved through comparison with reference spectra for magnetite, ilmenite (Downs, 2006), synthetic ulvöspinel (Wang et al., 2004), and titanomagnetite with different proportions of Fe and Ti as a means of comparing how band intensities vary as a function of Fe:Ti ratio (Zinin et al., 2011).

The proportions of magnetite and the various types of lamellae within Fe-Ti oxide intergrowths were estimated using image analysis on high-resolution backscatter electron images. The images were obtained using a JEOL JXA-8530F field-emission electron microprobe at the Earth and Planetary Materials Analysis Laboratory at Western University. Image analysis was based on the greyscale difference between magnetite, ulvöspinel, ilmenite, and spinel in backscatter electron images and was carried out using the Color Segmentation plugin for ImageJ (Sage and Unser, 2003). The proportion of Fe^{2+}, Fe^{3+}, and Ti in the Fe-Ti oxide intergrowths was calculated using the estimated mineral proportions, the density of each of the oxides, and treating each of the oxides as having ideal stoichiometric end-member compositions.

The major-element chemistry of Fe-Ti oxide intergrowths was principally obtained using an SEM-EDS. A subset of these Fe-Ti oxide intergrowths was also analyzed using an EPMA to determine the accuracy of the SEM-EDS analyses. An FEI Quanta 200 FEG SEM fitted with an EDAX x-ray detector was used at the Advanced Microscopy and Materials Characterization Facility at the University of Windsor to obtain semi-quantitative major-element chemistry of the various oxides and textures. Area analyses were conducted to obtain bulk major-element chemistry of magnetite and the intergrown phases that it hosts, which approaches the composition of the original Fe-Ti oxide solid solution at high temperature prior to exsolution and is similar to the volume of material sampled during laser ablation ICP-MS. These analyses were conducted under high vacuum at 20 kV.

Matrix corrections were achieved using the ZAF method. Point analyses were conducted on spinel using the same parameters. X-ray maps were made on the various types of Fe-Ti oxide intergrowths at high magnification to qualitatively characterize the distribution of major elements amongst magnetite and lamellae. Maps were obtained under high vacuum at 20 kV using dwell times of 200 μs. Major- and minor-element (Mg, Al, Si, P, Ca, Ti, V, Cr, Mn, Fe, Co, Ni, Zn, Zr) concentrations were obtained using a JEOL JXA-8530F field-emission electron microprobe at the Earth and Planetary Materials Analysis Laboratory at Western University. Analyses were conducted at 15 kV accelerating voltage, 50 nA current, and beam sizes of 300, 100, and 1 μm. A variety of Astimex and Smithsonian mineral and pure-element standards were used for calibration of the instrument. Corrections were applied to address overlaps of the Kβ peaks on the Kα peaks for V-Ti, Cr-V, Mn-Cr, and Fe-Co. Figure 3.4 compares the wt. % of Mg, Al, Ti, Cr, Fe, and Mn obtained by these two methods. When Fe is included in the regression, the fitted curve deviates from the 1:1 line with an equation of $0.912x$. When Fe is omitted from the regression, the fitted curve lies exceedingly close to the 1:1 line with an equation of $0.962x$. This suggests that the EDS accurately measures Mg, Al, Ti, Cr, Mn, and Si, but Fe is overestimated by ~ 6 wt. % on average. Given that EDS is much more readily available, time effective, and allows for raster analyses, it was used as the primary method for major element acquisition. This does, however, have implications for the internal standard chosen for laser ablation ICP-MS. Typically Fe is used as the internal standard for Fe-Ti oxides, but because the concentration of Ti obtained by EDS is more accurate than the concentration of Fe, and because the concentration of Ti in the Fe-Ti oxides in the Eastern Gabbro is high (wt. %), it is used as the internal standard for laser ablation ICP-MS.

Trace-element chemistry of oxides was obtained using an Agilent 7900 inductively coupled plasma mass spectrometer in the Element and Heavy Isotope Analytical Laboratories at the University of Windsor. The masses measured were ^{24}Mg, ^{27}Al, ^{29}Si, ^{31}P, ^{34}S, ^{44}Ca, ^{45}Sc, ^{47}Ti, ^{51}V, ^{52}Cr, ^{55}Mn, ^{57}Fe, ^{59}Co, ^{60}Ni, ^{63}Cu, ^{66}Zn, ^{71}Ga, ^{74}Ge, ^{89}Y, ^{91}Zr, ^{92}Zr, ^{93}Nb, ^{95}Mo, ^{101}Ru, ^{103}Rh, ^{105}Pd, ^{111}Cd, ^{120}Sn, ^{178}Hf, ^{181}Ta, ^{182}W, ^{189}Os, ^{193}Ir, ^{195}Pt, ^{197}Au, ^{208}Pb, and ^{209}Bi. A 193 nm excimer laser was used for in situ sampling at an output energy of 1.5 mJ, repetition rate of 20 Hz, and beam size of 50 μm. Analyses incorporated both magnetite

and all intergrown phases in order to obtain the original composition of the high-temperature Fe-Ti oxide solid solution. Two isotopes of Zr were analyzed to monitor for interferences of VAr on Zr^{91} and CrAr on Zr^{92}. The synthetic basalt standard GSE-1G was the external standard used to calculate sensitivity factors. Data reduction was carried out using the Iolite package (Paton et al., 2011).

3.4 Results

3.4.1 Oxide Minerals in the Eastern Gabbro

Iron-Ti oxides are ubiquitous in all of the gabbroic series of the Eastern Gabbro. They range in grain size from very fine-grained (< 100 μm) in the metabasalt to coarse-grained (> 1 mm) in the Layered and Marathon Series. They are typically disseminated, but can locally form semi-massive to massive pods in Cu-PGE-mineralized oxide- and apatite-rich cumulate rocks that i) intruded the metabasalt above the Two Duck Lake gabbro, ii) occur as thin lenses within the Two Duck Lake gabbro, and iii) cut across the footwall rocks (Good et al., 2015).

3.4.1.1 Textures of oxide minerals

Three principal textural types of Fe-Ti oxides have been identified: i) Fe-Ti oxide intergrowths that are generally interstitial to silicates, ii) replacement magnetite, and iii) myrmekitic Fe-Ti oxide intergrowths. Interstitial Fe-Ti oxide intergrowths are the most common (Fig. 3.5a,b). These intergrowths always host lamellae and typically have coarse-grained crystals of ilmenite associated with them (Fig. 3.5b). The lamellae are often too fine-grained to be visible under low-magnification reflected light (Fig. 3.5a) and can be easily missed. The ilmenite crystals can occur at the Fe-Ti oxide intergrowth grain boundaries, within Fe-Ti oxide intergrowth grains, or along fractures in Fe-Ti oxide intergrowths. In each case, the boundary between Fe-Ti oxide intergrowths and ilmenite is sharp. Ilmenite can occur isolated from Fe-Ti oxide intergrowths, but this is rare.

Replacement magnetite (Fig. 3.5c) is less common than Fe-Ti oxide intergrowths, but more common than myrmekitic Fe-Ti oxide intergrowths. It occurs as a replacement of sulfides along grain boundaries and cracks. It can also occur isolated from sulfides in intergrowths of hydrous silicates and within veinlets. Unlike Fe-Ti oxide intergrowths, replacement magnetite is devoid of exsolution lamellae and has no associated ilmenite. This is consistent with the nature of its Raman spectra that indicate it is end-member Fe_3O_4 (Fig. 3.6d).

Myrmekitic Fe-Ti oxide intergrowths (Fig. 3.5d) are the least common type of magnetite and occurs as fine-grained intergrowths in orthopyroxene rims on olivine and clinopyroxene. They host similar lamellar textures as interstitial Fe-Ti oxide intergrowths.

3.4.1.2 Exsolution textures in Fe-Ti oxide intergrowths

Two end-member types of exsolution lamellae are present, cloth lamellae and trellis lamellae. Cloth-textured Fe-Ti oxide intergrowths contain a network of extremely fine lamellae, whereas trellis-textured Fe-Ti oxide intergrowths contain isolated bladed to tabular lamellae that range in thickness from 1 to 20 μm. A spectrum of intermediate textures between these two end-members exist and these are termed intermediate-textured Fe-Ti oxide intergrowths. Because the orientation of the Fe-Ti oxide crystal will influence the exsolution features observed in reflected light, the characteristics of each of these textural types of intergrowths is based on description of Fe-Ti oxide intergrowths from 152 thin sections.

3.4.1.2.1 Cloth-textured Fe-Ti oxide intergrowths

Cloth-textured Fe-Ti oxide intergrowths consist of an interconnected network of extremely fine (< 1 μm wide) lamellae within magnetite (Fig. 3.7a,b). Given the fine-grained nature of these lamellae, Raman spectroscopy was used to aid in mineral identification. Raman spectroscopy is well-suited for the identification of oxide minerals because many oxides exhibit unique Raman spectra. Ilmenite exhibits very distinct bands in Raman spectra

compared to magnetite and ulvöspinel, with bands at 203 cm^{-1}, 230 cm^{-1}, 327 cm^{-1}, 366 cm^{-1}, 406 cm^{-1}, 445 cm^{-1}, 590 cm^{-1}, and 680 cm^{-1}. Magnetite exhibits bands in Raman spectra at 188 cm^{-1}, 308 cm^{-1}, 542 cm^{-1}, and 674 cm^{-1}. Ulvöspinel shares many of these bands, but also contains a strong band at 495 cm^{-1}. Accordingly, the lamellae have been identified as ulvöspinel using Raman spectroscopy (Fig. 3.6b). This observation is consistent with these lamellae containing a lower Ti/Fe ratio compared to ilmenite, shown semi-quantitatively as the difference in color intensity between Fe and Ti on Figure 3.8. These lamellae often form thick, linear, box-like patterns that occur in 3 orientations (Fig. 3.7a). Where ilmenite crystals occur in cloth-textured Fe-Ti oxide intergrowths, the lamellar network (cloth) remains continuous up to the boundary with the ilmenite crystal. Spinel lamellae are uncommon in cloth-textured Fe-Ti oxide intergrowths from most localities in the Eastern Gabbro, apart from Area 41 and Redstone (see below).

3.4.1.2.2 Trellis-textured Fe-Ti oxide intergrowths

Trellis-textured Fe-Ti oxide intergrowths consist of individual blades or tabular lamellae hosted by magnetite (Fig. 3.7c,d). These lamellae have been identified as ilmenite spectroscopically and chemically (Figs. 3.6c, 3.8). Trellis lamellae range in width from 1 to 20 μm. Two distinct size varieties of trellis lamellae commonly occur within a crystal of magnetite. Fine trellis lamellae range in width from 1 to 5 μm and have lengths that are typically less than 20 μm. Coarse trellis lamellae have widths in the range of 5 to 20 μm and lengths that can extend across the oxide grain or until they intersect another lamella, silicate inclusion, or ilmenite crystal. In some grains, however, only fine trellis lamellae are present. Thick trellis lamellae often taper and/or become discontinuous when they intersect another thick trellis lamella or when near the grain boundary of the host magnetite (Fig. 3.7c,d). Both fine and coarse trellis lamellae host anhedral spinel that is commonly more abundant along the edges of the lamellae (Fig. 3.7c,d). Spinel can also occur as blades (1 to 5 μm wide) in the magnetite in 2 or 3 orientations (Fig. 3.7c,d). Given their small size, accurate EDS and Raman analyses were difficult to obtain, but Figure 3.8 shows that these lamellae of spinel consist of Mg and Al and lack the other major elements, which is consistent with spinel.

In some magnetite grains that are dominated by cloth lamellae, thick trellis lamellae of ilmenite can also occur. In these examples, the thick trellis lamellae are more heterogeneously distributed throughout the Fe-Ti oxide intergrowth compared to their distribution in trellis-textured Fe-Ti oxide intergrowths and, in some cases, are concentrated along the edges of the Fe-Ti oxide intergrowth or around fractures that crosscut the intergrowth (Fig. 3.7e). Thick trellis lamellae in cloth-textured Fe-Ti oxide intergrowths are commonly surrounded by a light grey halo when viewed in reflected light (Fig. 3.7e), but there are instances where the cloth network extends up to the thick trellis lamellae. The halos can contain blebs or stringers of ilmenite that extend away from the lamellae (Fig. 3.7f). Spinel is locally concentrated at the boundary between the halo and the cloth-textured Fe-Ti oxide intergrowth (Fig. 3.7f). Spinel can also occur as bladed crystals within magnetite that contains predominantly cloth lamellae. These bladed spinel crystals are usually heterogeneously distributed with some areas of the cloth-textured Fe-Ti oxide intergrowth having a higher density of spinel than others. The magnetite directly adjacent to the bladed spinel is commonly free of cloth lamellae. Bordering this lamellae-free magnetite, the cloth lamellae are thicker in comparison to the cloth in spinel-free areas of the intergrowth (Fig. 3.9a). In some instances, cloth and trellis lamellae coexist where bladed spinel occurs in the Fe-Ti oxide intergrowth (Fig. 3.9a).

3.4.1.2.3 Intermediate-textured Fe-Ti oxide intergrowths

In high magnification BSE images, a continuum of lamellar textures is observed in Fe-Ti oxide intergrowths from “cloth-like” to “trellis-like”. In these examples, the Fe-Ti oxide intergrowth does not contain either cloth or fine trellis lamellae, but a mixture of the two. These textural varieties are termed intermediate-textured Fe-Ti oxide intergrowths. In low-magnification reflected light, some intermediate-textured Fe-Ti oxide intergrowths are patchy, with some areas of the grain exhibiting a cloth-texture hosted by magnetite and other areas lacking visible lamellae at this scale (Fig. 3.9b). Other intermediate-textured Fe-Ti oxide intergrowths contain thick trellis lamellae hosted by magnetite, but are homogenous with respect to fine lamellae in low-magnification reflected light (Fig. 3.9c).

Intermediate-textured Fe-Ti oxide intergrowths are broadly subdivided into two types according to their textural similarity to either cloth- or trellis-textured Fe-Ti oxide intergrowths. “Cloth-like” intermediate-textured Fe-Ti oxide intergrowths consist of magnetite and a cloth network (depicted by the blue lines in Fig. 3.9d) that is interrupted by linear features that cut obliquely across the network (depicted by the red lines in Fig. 3.9d). “Trellis-like” intermediate-textured Fe-Ti oxide intergrowths consists of magnetite and a mixture of cloth lamellae and fine trellis lamellae, with the cloth network (depicted by the blue lines in Fig. 3.9e) occurring in between the trellis lamellae, which are oriented oblique to the cloth network (depicted by the red lines in Fig. 3.9e). The different orientation of these lamellae types is consistent with the fact that ulvöspinel occurs in the {100} plane of magnetite, whereas ilmenite occurs in the {111} plane of magnetite (Ramdohr, 1953). A coarser variety of “trellis-like” intermediate-textured Fe-Ti oxide intergrowths also occurs in which the two sets of lamellae are readily visible under reflected light (Fig. 3.9f). Spinel lamellae are present in all of the intermediate-textured Fe-Ti oxide intergrowths, but are more abundant in the “trellis-like” varieties. Baddeleyite (ZrO_2) occurs within many thick trellis lamellae (Fig. 3.7f).

Fractures are common in Fe-Ti oxide intergrowths. Cloth-textured Fe-Ti oxide intergrowths can appear altered along these fractures, as well as grain boundaries and around thick trellis lamellae (Fig. 3.10a). In low-magnification reflected light, these altered areas appear brighter in reflected light compared to cloth-textured Fe-Ti oxide intergrowths. These altered areas contain abundant spinel, which are absent in the surrounding cloth lamellae. In high-magnification BSE images, these brighter, altered areas contain individual anhedral crystals of ilmenite (Fig. 3.10b), which were identified using Raman spectroscopy (Fig. 3.6c). These altered areas in cloth-textured Fe-Ti oxide intergrowths are termed recrystallized cloth-textured Fe-Ti oxide intergrowths. These fractures can also be surrounded by a halo that, in low-magnification reflected light, appears brighter compared to the cloth-textured Fe-Ti oxide intergrowths and seems to lack lamellae (Fig. 3.10c). In high-magnification BSE images, however, fine trellis-like lamellae are visible that radiate outward from the fracture in 2 to 3 orientations (depicted

by the red lines in Fig. 3.10d) that are oblique to the surrounding cloth network (depicted by the blue lines in Fig. 3.10d).

Typically, coarse ilmenite crystals associated with Fe-Ti oxide intergrowths do not contain any spinel. In some cases, however, spinel can occur concentrated along their boundary (Fig. 3.10e). Proximal to coarse ilmenite crystals, and coarse trellis lamellae, the density of fine trellis is lower and, in some cases, they are absent (Fig. 3.10e), such that point analyses in these areas approach end-member Fe_3O_4 (Fig. 3.6d). Some ilmenite can occur along fractures that crosscut Fe-Ti oxide intergrowths (Fig. 3.10e). They are typically associated with hydrous silicates and spinel.

3.4.1.3 Distribution of lamellae throughout the Eastern Gabbro

The distribution of the cloth- and trellis-textured Fe-Ti oxide intergrowths from each unit at each sample site in Eastern Gabbro (i.e., the Marathon deposit and Four Dams, Area 41, and Redstone occurrences; Fig. 3.2), rock series, rock types, and mineralized zones of the Eastern Gabbro was qualitatively estimated by measuring the proportion of samples that contain the various types of lamellae in a given population of samples defined by their location in the Eastern Gabbro and the respective host rock unit, rock type, and mineralized zone. Individual thin sections from each unit typically exhibit one textural type of Fe-Ti oxide intergrowth, but both textural types can also occur (Fig. 3.11).

Fe-Ti oxide intergrowths from the Four Dams and Redstone occurrences are predominantly of the cloth variety, whereas Marathon and Area 41 contain subequal proportions of cloth- and trellis-textured Fe-Ti oxide intergrowths (Fig. 3.11a). Fe-Ti oxide intergrowths from metabasalt are predominantly of the cloth variety, whereas the Layered Series only contains cloth-textured Fe-Ti oxide intergrowths (Fig. 3.11b). Marathon Series contains subequal proportions of cloth-and trellis-textured Fe-Ti oxide intergrowths.

In the mineralized zones at Marathon, Fe-Ti oxide intergrowths from the Footwall Zone are entirely of the trellis variety, whereas those from the Hanging Wall Zone are entirely

of the cloth variety (Fig. 3.11c). Although the Main Zone and W Horizon contain both textural varieties of Fe-Ti oxide intergrowths, the trellis variety is the most common (Fig. 3.11c).

For mineralized zones located northwest of the Marathon deposit, Fe-Ti oxide intergrowths at Area 41 are predominantly of the trellis variety, whereas those at the Four Dams and Redstone occurrences are predominantly of the cloth variety (Fig. 3.11c). The magnetite-apatite-clinopyroxene cumulate host subequal proportions of cloth- and trellis-textured Fe-Ti oxide intergrowths (Fig. 3.11c).

3.4.2 Fluid inclusions in pyroxene and apatite

Because one of the models for the formation of magnetite-ilmenite intergrowths proposes fluid-induced oxidation of ulvöspinel, the vapor phase in fluid inclusions was characterized using Raman spectroscopy. Pyroxene-hosted fluid inclusions in samples that only contain either cloth- or trellis-textured Fe-Ti oxide intergrowths were considered because they represent different degrees of fluid-induced oxidation (cf. Buddington and Lindsley, 1964; Verhoogen, 1962).

Throughout the Eastern Gabbro, fluid inclusions commonly occur in apatite and pyroxene. In the Marathon deposit, Smoke et al. (2013) noted that apatite predominantly contains vapor (*V*) and liquid-vapor (*LV*) inclusions. The *LV* inclusions are characterized by variable L/V ratios and they are commonly coeval with *V* inclusions, which were interpreted as always being secondary (Smoke et al., 2013). Although the vapor phase in apatite-hosted fluid inclusions could not be characterized using Raman spectroscopy due to strong fluorescence from the host, Smoke et al. (2013) used microthermometry to identify CO_2 as the main vapor phase in these inclusions.

Pyroxene-hosted fluid inclusions from Marathon and Four Dams are typically ≤ 10 μm and are predominantly *LV* inclusions, with the vapor phase being more dominant (Fig. 3.12). The fluid inclusions are secondary as they occur along two-dimensional

crystallographically-controlled planes. Raman spectra obtained from the vapor phase of fluid inclusions from samples that host cloth- and trellis-textured Fe-Ti oxide intergrowths contain CH_4 (peak at ~ 2919 cm^{-1}); CO_2 peaks (Burke, 2001 and references therein) were not observed in pyroxene-hosted fluid inclusions (Fig. 3.12).

3.4.3 Major-element chemistry of oxide minerals and associated textures

On an Fe-Ti-(Al+Mg) ternary diagram, ilmenite crystals have Fe:Ti ratios consistent with end-member $FeTiO_3$, but typically have higher Mg+Al contents, particularly when spinel crystals are incorporated into the bulk analyses (e.g., along the boundary of some ilmenite crystals) (Fig. 3.13a). The bulk compositions of cloth-, intermediate-, and trellis-textured Fe-Ti oxide intergrowths are indistinguishable (Table 3.2), with their Fe-Ti content intermediate to end-member magnetite and ulvöspinel or ilmenite (Fig. 3.13b). The recrystallized halos around fractures in cloth-textured Fe-Ti oxide intergrowths have the same major-element chemistry as the Fe-Ti oxide intergrowths (Fig. 3.13b). Myrmekitic Fe-Ti oxide intergrowths have similar major-element chemistry as the interstitial Fe-Ti oxide intergrowths, but some crystals lack Mg and Al (Fig. 3.13b). Magnetite proximal to ilmenite crystals and thick lamellae, which lack fine lamellae, have major-element compositions near end-member Fe_3O_4 (Fig. 3.13b). The major-element chemistry of replacement magnetite around the boundary of sulfides is consistent with end-member Fe_3O_4 (Fig. 3.13b).

Image analysis was used to estimate the proportions of magnetite and the ulvöspinel, ilmenite, and spinel lamellae in cloth-, intermediate-, and trellis-textured Fe-Ti oxide intergrowths. To assess the variability in the estimated mineral proportions, image analyses was conducted on three areas of two cloth-textured Fe-Ti oxide intergrowths within a single thin section. The variation in the estimated proportions of magnetite and ulvöspinel within a Fe-Ti oxide grain is less than 3%, with standard deviations being less than 1.6. Using the estimated mineral proportions, the density of each of the minerals, and treating each of the phases as having ideal stoichiometric end-member compositions, the proportion of Fe^{2+}, Fe^{3+}, and Ti in Fe-Ti oxide intergrowths was calculated. On an FeO-Fe_2O_3-TiO_2 ternary

diagram, the cloth-textured Fe-Ti oxide intergrowths that do not have thick trellis lamellae of ilmenite have compositions that lie along the titanomagnetite solid solution join between magnetite and ulvöspinel (Fig. 3.14). Trellis-textured Fe-Ti oxide intergrowths that lack thick trellis lamellae have consistently higher Fe^{3+}:Fe^{2+} ratios than cloth-textured Fe-Ti oxide intergrowths (Fig. 3.14). The compositions of these intergrowths lie on a tie line between end-member magnetite and ilmenite (inset diagram on Fig. 3.14). The Fe^{3+}:Fe^{2+} ratio of the intermediate-textured Fe-Ti oxide intergrowths lie in between the two solid solution joins (Fig. 3.14). The only example of a cloth-textured Fe-Ti oxide intergrowth that was imaged and that contains thick trellis lamellae has a higher Fe^{3+}:Fe^{2+} ratio than the cloth-textured Fe-Ti oxide intergrowths that do not have thick trellis lamellae (Fig. 3.14). Within individual samples (depicted by the arrows on Fig. 3.14), trellis-textured Fe-Ti oxide intergrowths have consistently higher Fe^{3+}:Fe^{2+} ratios compared to cloth varieties. For a given sample, the concentration of Ti is similar between cloth- and trellis-textured Fe-Ti oxide intergrowths (Fig. 3.14).

To assess the variability between the same textural type and between the different textural types of Fe-Ti oxide intergrowths within an individual thin section, multiple grains of each textural type of intergrowth were analyzed using EDS. On average, the standard deviations (2σ) for Mg, Al, and Ti are 0.1 wt. %, 0.2 wt. %, and 0.5 wt. %, respectively, for cloth-textured Fe-Ti oxide intergrowths in an individual sample ($n_{samples}$ = 32). For trellis varieties, the average standard deviations for these elements are 0.2 wt. %, 0.2 wt. %, and 0.5 wt. %, respectively ($n_{samples}$ = 20). In those thin sections that contain more than one textural type of Fe-Ti oxide intergrowth, the differences in Ti and Al content between them are typically less than 2 wt. % and 0.5 wt. %, respectively. This is illustrated in Figure 3.15, in which the individual vectors represent the difference in Ti and Al content between cloth- and either intermediate- or trellis-textured Fe-Ti oxide intergrowths hosted within a single thin section. These differences are similar to those observed amongst Fe-Ti oxide intergrowths that exhibit the same texture within a single thin section and are in the range of analytical precision.

To assess whether the location of analyses, and thus the number of lamellae that are incorporated in a given analysis, affects the measured bulk chemistry, EDS raster analyses were conducted in 3 to 5 areas within a single i) cloth-textured Fe-Ti oxide intergrowth without thick trellis, ii) cloth-textured Fe-Ti oxide intergrowth with thick trellis, and iii) trellis-textured Fe-Ti oxide intergrowth. For each variety of Fe-Ti oxide intergrowth, standard deviations (2σ) for Fe, Ti, Mg, and Al are always less than 1 wt. %, except for the standard deviation of Fe in trellis-textured Fe-Ti oxide intergrowths, which is 1.5 wt. %. Analyses of the single trellis-textured Fe-Ti oxide intergrowth show the largest variability, with standard deviations that range from 0.1 wt. % for Mg ($\bar{x}_{Mg}$ = 1 wt. %), Al ($\bar{x}_{Al}$ = 2.1 wt. %), and Mn ($\bar{x}_{Mn}$ = 0.6 wt. %), and up to 1.5 wt. % for Fe ($\bar{x}_{Fe}$ = 64.6 wt. %). Standard deviations for the analyses of the cloth-textured Fe-Ti oxide intergrowth without thick trellis lamellae are all less than 0.3 wt. % ($\bar{x}_{Mg}$ = 1.3 wt. %, $\bar{x}_{Al}$ = 2.2 wt. %, $\bar{x}_{Ti}$ = 8.3 wt. %, $\bar{x}_{Mn}$ = 0.7 wt. %, $\bar{x}_{Fe}$ = 62.3 wt. %), and those of the cloth-textured Fe-Ti oxide intergrowth with thick trellis lamellae are all less than 0.1 wt. % ($\bar{x}_{Mg}$ = 0.7 wt. %, $\bar{x}_{Al}$ = 1.9 wt. %, $\bar{x}_{Ti}$ = 6.9 wt. %, $\bar{x}_{Mn}$ = 0.5 wt. %, $\bar{x}_{Fe}$ = 64.7 wt. %).

3.4.4 Trace-element chemistry of Fe-Ti oxide intergrowths

3.4.4.1 Representativeness of laser ablation analyses

As with the EDS analyses of the different textural types of Fe-Ti oxide intergrowths, typical traverse lengths (~ 300 μm) may not be representative of the Fe-Ti oxide intergrowth. To identify the ideal sampling strategy, spot size and ablation volume were varied to test the representativeness of analyses. Long traverses on the scale of 1 to 3 mm in length were ablated in multiple areas of Fe-Ti oxide intergrowths in an effort to maximize the amount of magnetite and lamellae sampled. These long traverses were integrated i) as a whole and ii) as multiple individual shorter traverses. Characterization of how the trace-element composition of a Fe-Ti oxide intergrowth varies with respect to the length of the laser traverse and the chosen analysis location within a grain is important because, if these Fe-Ti oxide intergrowths are to be used as a vectoring tool for mineralization, as has been

previously proposed (Dare et al., 2014a), than the analyses must be simple, time efficient, and a protocol must be used that minimizes sampling bias.

When composition of Fe-Ti oxide intergrowths obtained using long and short traverse lengths are compared, the majority of trace elements define a 1:1 line (Fig. 3.16). Of the trace-element concentrations acquired, Si, Ca, Cu, Cd, and Pb show the greatest deviations around the 1:1 line (Fig. 3.16). This is likely because these elements often exhibit spikes in the laser ablation spectra. Because these spikes are not associated with silicate or sulfide inclusions, or cracks in the Fe-Ti oxide intergrowths, they were included in the integration. Accordingly, for this study, shorter traverses are used for sampling instead of longer traverses, because the amount of each phase incorporated during analysis does not affect the accuracy of the data and the time required for analysis will be considerably shortened, allowing for a larger, more spatially diverse dataset to be compared. Because of the way in which analyses were carried out, analyses incorporate magnetite and all intergrown phases (i.e., ulvöspinel, ilmenite, spinel, baddeleyite), and therefore approaches the bulk composition of the high temperature Fe-Ti oxide solid solution.

3.4.4.2 Trace-element composition of Fe-Ti oxide intergrowths

In laser ablation spectra of cloth-textured Fe-Ti oxide intergrowths, the counts per second of most elements are proportional with Ti except for the HFSE (Zr, Hf, Nb, Ta) (Fig. 3.17a) and Zn (not shown). The counts per second of the HFSE fluctuate over approximately an order of magnitude, but do not correlate with other elements (Fig. 3.17a). The counts per second of Zn fluctuate over less than an order of magnitude, but correlate with the counts per second of Al (not shown). In laser ablation spectra of trellis-textured Fe-Ti oxide intergrowths, the counts per second of the HFSE and Sc track with Ti and they increase when thick trellis lamellae are intersected (Fig. 3.17b). The counts per second of Ga typically decrease as trellis ilmenite are intersected (Fig. 3.17b). Most other elements do not show any variation when lamellae are intersected. The counts per second of Si and Cu show significant spikes in spectra from laser ablation traverses that intersect fractures and thick ilmenite lamellae, but they do not correlate with other elements (Fig. 3.17a).

The overall bulk composition of cloth-, intermediate-, and trellis-textured Fe-Ti oxide intergrowths are indistinguishable (Table 3.3, Fig. 3.18). Transition metals range from less than 100 ppm (as low as 0.1 ppm) for Y, the HFSE (Zr, Hf, Nb, Ta), W, Sc, Cu, and Mo to concentrations up to a wt. % for V and Cr (Fig. 3.18). The main-group elements always occur in concentrations less than 100 ppm, with Pb and Ge always occurring in concentrations less than 10 ppm (Fig. 3.18). Chromium, Ni, Mo, Cu, Ta, Nb, and W consistently show the largest variability amongst all of the transition metals and range over 4 to 5 orders of magnitude (Fig. 3.18).

A comparison of the composition of the different textural types of Fe-Ti oxide intergrowths within individual samples illustrates that different elements exhibit different trends between the textural types. Overall, the HFSE are positively correlated with Ti, but within a given sample there is no consistency in the change in their concentration (i.e., direction of vector) from cloth- to intermediate- or trellis-textured Fe-Ti oxide intergrowths (i.e., their concentrations either increase or decrease from one to the other) (Fig. 3.19). Most elements with single oxidation states (e.g., Sc, Zn, Co, Ni, Cr) exhibit no correlation with Ti and no consistent trends between textural types of Fe-Ti oxide intergrowths (Fig. 3.19). Some elements with single oxidation statse, such as Ga and Cu, however, typically exhibit statistically (> 2 S.E.) higher concentrations in intermediate- and trellis-textured Fe-Ti oxide intergrowths relative to cloth varieties (Fig. 3.19). These enrichments are typically less than an order of magnitude (single-digit to tens of ppm) (Fig. 3.19). Elements that can potentially exist in more than one valence state (Ge, W, Mo, Sn, V) show no correlation with Ti (Fig. 3.19). Of these elements, Ge, W, Mo, and Sn typically have higher concentrations in intermediate- and trellis-textured Fe-Ti oxide intergrowths compared to cloth varieties, whereas V typically shows no consistent trend (Fig. 3.19). These enrichments are less than an order of magnitude (single-digit ppm) (Fig. 3.19).

3.5 Discussion

3.5.1 Previously proposed models for the formation of magnetite-ilmenite intergrowths

Although no solid solution between magnetite and ilmenite has been demonstrated, the mechanism that causes the common intergrowth of magnetite and ilmenite is still unresolved. Many studies that dealt with Fe-Ti oxide intergrowths were limited by the analytical techniques available at the time and so were focused primarily on textural characterization and major-element chemistry. Four distinct models have been proposed over the past half century to explain the common occurrence of ilmenite lamellae within magnetite: i) vacancy relaxation (Ramdohr, 1955), ii) Fe-enrichment (Haselton and Nash, 1975), iii) reduction of magnetite (El Goresy et al., 1972; Haggerty, 1977, 1972), and iv) oxy-exsolution (Buddington and Lindsley, 1964; Verhoogen, 1962).

The first two models explain magnetite-ilmenite intergrowths by direct exsolution of ilmenite from titanomagnetite. The vacancy relaxation model (model i) involves the exsolution of ilmenite when a spinel that contains vacancies (Lattard, 1995) becomes stoichiometric at lower temperatures via the mechanism (Lattard, 1995):

$$Fe_{2-2x}Ti_{1-x}\square O_4 \rightleftarrows 4xFeTiO_3 + (1-3_x)Fe_2TiO_4 \qquad \text{eq. 3.1}$$

The Fe-enrichment model (model ii) involves a decrease in Ti^{3+} solubility with decreasing temperature. As Ti^{3+} exsolves out of titanomagnetite, it oxidizes to Ti^{4+}, generating ilmenite, and Fe^{2+} is reduced to metallic Fe^0 via the mechanism (Haselton and Nash 1975):

$$[9FeTiO_3 + Ti_2^{3+}O_3] + 3Fe_2TiO_4 \rightleftarrows 14FeTiO_3 + Fe^0 \qquad \text{eq. 3.2}$$

The other two models, (iii) and (iv), involve conversion of the ulvöspinel component in the magnetite-ulvöspinel solid solution to ilmenite. The reduction model (iii) involves the diffusion of Fe and Ti to the {111} planes of the magnetite-ulvöspinel solid solution followed by exsolution of ilmenite and metallic Fe^0 via the mechanism (Haggerty, 1977, modified from 1972):

$$x(Fe^{2+}Fe_2^{3+}O_4 + Fe^{2+}Ti_2O_4)_{Usp\ ss} \rightleftarrows y(Fe^{2+}Fe_2^{3+}O_4 + Fe^{2+}Ti_2O_4)_{Usp\ ss} + Fe^{2+}TiO_3 + Fe^0 + 0.5O_2 \quad \text{eq. 3.3}$$

where x = Ti > Fe^{3+} and y = Ti < Fe^{3+}

The oxy-exsolution model (iv) has been the most commonly invoked mechanism to interpret the intergrowth between magnetite and ilmenite in terrestrial environments. This model involves the conversion of ulvöspinel to ilmenite by oxidation of some Fe^{2+} to Fe^{3+} by interaction with a fluid (Verhoogen, 1962):

$$3Fe_2^{2+}TiO_4 + \frac{1}{2}O_2 \rightleftarrows 3Fe^{2+}TiO_3 + Fe_2^{3+}Fe^{2+}O_4 \quad \text{eq. 3.4}$$

The widespread application of this model is based on the fact that it incorporates the well-documented extensive solid solution between magnetite and ulvöspinel (Buddington and Lindsley, 1964; Lindsley, 1963, 1962; Vincent et al., 1957), but does not require the presence of ɣ-$FeTiO_3$, the unidentified polymorph of ilmenite, or the occurrence of metallic Fe^0 (discussed below).

3.5.2 Evidence for fluid-induced oxidation

3.5.2.1 Can any of the proposed mechanisms for magnetite-ilmenite intergrowth formation be ruled out?

The vacancy-relaxation (i), Fe-enrichment (ii), and subsolidus reduction (iii) models were proposed for lunar rocks where fO_2 is much lower than on Earth (Haggerty, 1977, 1972; Lattard, 1995; Papike et al., 2005). These models can be unequivocally rejected for three reasons. a) Models (ii) and (iii) require metallic Fe as a reaction product, but terrestrial environments, specifically mafic-ultramafic plutons, are too oxidizing for metallic Fe^0 to be stable (El Goresy et al., 1972; Haggerty, 1977, 1972; Haselton and Nash, 1975). b)

Models (i) and (ii) involve the oxidation of Ti^{3+} to Ti^{4+}. Although the existence of Ti^{3+} in minerals of terrestrial origin has been suggested (Waychunas, 1987), Ti typically occurs as Ti^{4+} in terrestrial environments (Papike et al., 2005). c) Since Ti^{3+} is less common in terrestrial environments, spinel are stoichiometric and do not contain the vacancies required for model (i) (Lattard, 1995).

Although little experimental or natural evidence exists for the direct exsolution of ilmenite from an Fe-Ti oxide solid solution in terrestrial environments (see above), it cannot be ruled out entirely (cf. Vincent et al. 1957; Lattard 1995). Consequently, using textural and compositional evidence, the following discussion will address the mechanism of formation of magnetite-ilmenite intergrowths. The discussion will focus on discriminating between oxidation of ulvöspinel or direct exsolution of ilmenite.

3.5.2.2 Mineralogical and textural evidence for oxidation

The major-element composition of the various Fe-Ti oxide intergrowths supports the oxidation model because, according to the model (equation 4), the only variation in the major-element composition of the various intergrowth types should be the bulk Fe^{3+}:Fe^{2+} ratio; the ratio should be higher for trellis-textured Fe-Ti oxide intergrowths compared to intermediate and cloth varieties. Additionally, the concentrations of Fe_{tot}, Ti, Mg, and Al should be similar amongst the various textural types of Fe-Ti oxide intergrowths, as would be expected if they crystallized from the same high-temperature magnetite-ulvöspinel solid solution. The compositional data for the Fe-Ti oxide intergrowths demonstrate that, amongst different samples and within individual samples (data points and arrows, respectively, on Fig. 3.14), cloth-textured Fe-Ti oxide intergrowths consistently have lower Fe^{3+}:Fe^{2+} ratios than the trellis varieties, with the intermediate varieties exhibiting intermediate ratios. Additionally, amongst the sample population, the bulk major-element composition of cloth- and trellis-textured Fe-Ti oxide intergrowths, and all of the intermediate varieties are indistinguishable with respect to their Fe, Ti, Al, and Mg content (Fig. 3.13) and, within a given sample, the variability in the Ti and Al content of the different textural types is minimal (typically < 2 wt. %) (Fig. 3.15).

The presence of intermediate-textured Fe-Ti oxide intergrowths also supports the oxidation model for a number of reasons. Firstly, if the ulvöspinel and ilmenite lamellae in magnetite formed by exsolution from different Fe-Ti oxide compositions (i.e., along the mt-usp$_{ss}$ in the former and mt-ilm$_{ss}$ in the latter), than the mineralogy and texture of the resulting Fe-Ti oxide intergrowths should be discrete rather than continuous (i.e., cloth-textured ulvöspinel in the former and trellis-textured ilmenite in the latter, with no intermediates). Although end-member varieties of Fe-Ti oxide intergrowths do exist in the Eastern Gabbro (Figs. 3.5a,b and 3.7a,b,c,d), a continuum of intermediate textures also exists from "cloth-like" intermediate-textured Fe-Ti oxide intergrowths (Fig. 3.9b,d) to "trellis-like" intermediate-textured Fe-Ti oxide intergrowths (Fig. 3.9c,e). This continuum includes i) mixtures in which a given grain of magnetite contains variable amounts of intermixed ulvöspinel and ilmenite (Fig. 3.9d,e,f), which are often heterogeneously distributed throughout a crystal (Fig. 3.9a) and ii) localized mixtures in which trellis and blebby ilmenite occur around fractures, grain boundaries, silicate inclusions, and thick trellis lamellae in grains that are mainly cloth-textured Fe-Ti oxide intergrowths (Figs. 3.7e,f and 3.10a,b,c,d).

Secondly, if cloth ulvöspinel and trellis ilmenite that are hosted by the same crystal of intermediate-textured Fe-Ti oxide intergrowth were exsolved from the same, compositionally homogenous Fe-Ti oxide solid solution, than both lamellae types should be homogenously distributed throughout the crystal, but this is typically not the case as demonstrated by the grain-scale (i) and localized (ii) mixtures described above. Thirdly, intermediate-textured Fe-Ti oxide intergrowths commonly exhibit linear features that cut obliquely across the cloth network (Fig. 3.9d), which may represent the early stages of oxidation marked by the reorientation of the ulvöspinel from the {100} plane of magnetite to the {111} plane (cf. Speczik et al., 1988; von Gruenewaldt et al., 1985). Additionally, in the vicinity of trellis lamellae in cloth-texture Fe-Ti oxide intergrowths, the cloth network typically becomes discontinuous, or absent altogether in cases where the trellis lamellae are closely spaced, such that the area adjacent to the trellis lamellae represents end-member magnetite (Fig. 3.9a,f). This has been suggested by numerous authors (e.g.,

Duchesne, 1970; von Gruenewaldt et al., 1985) to represent subsolvus diffusion of Fe and Ti from ulvöspinel to form ilmenite. Lastly, ilmenite lamellae and anhedral blebs are often concentrated along fractures in cloth-textured intergrowths (Figs. 3.7e, 3.10d), around thick trellis lamellae in cloth-textured intergrowths (Fig. 3.10a), and along grain boundaries of cloth-textured intergrowths (Figs. 3.7e, 3.10a). All of these areas are sites of weaknesses in the Fe-Ti oxide intergrowth through which an oxidizing fluid could have infiltrated and more efficiently interacted with the cloth-textured Fe-Ti oxide intergrowth to convert ulvöspinel to ilmenite, as suggested by Haggerty (1976) and von Gruenwaldt et al. (1985).

These mineralogical and textural characteristics indicate that, at least in the Eastern Gabbro, the intermediate- and trellis-textured Fe-Ti oxide intergrowths formed by the oxidation of a magnetite-ulvöspinel solid solution. They do not, however, refute the possibility that, under specific conditions, ilmenite may exsolve directly from an Fe-Ti oxide solid solution to generate magnetite-ilmenite intergrowths.

Coarse, anhedral crystals of ilmenite are known to crystallize from magmas (e.g., ilmenite-dominated Fe-Ti deposits). Buddington and Lindsley (1964), Vincent and Philips (1954), and Wright (1961), however, have suggested, based on Fe and Ti mass balance, that some crystals of ilmenite may be the result of oxy-exsolution from magnetite-ulvöspinel solid solutions. They proposed that such oxy-exsolution of ilmenite occurs at the highest degrees of oxidation and Fe-Ti diffusion (i.e., high *T*). If the ilmenite crystals in the Eastern Gabbro formed by oxy-exsolution from a magnetite-ulvöspinel solid solution, the ilmenite crystals should only occur in trellis-textured Fe-Ti oxide intergrowths, which represent a high degree of magnetite-ulvöspinel oxidation. In the Eastern Gabbro, however, large ilmenite crystals commonly occur associated with unoxidized cloth-textured Fe-Ti oxide intergrowths. Consequently, the ilmenite crystals associated with Fe-Ti oxide intergrowths in the Eastern Gabbro are interpreted to have crystallized prior to the Fe-Ti oxide intergrowths rather than having oxy-exsolved from them.

3.5.2.3 Compositional evidence

There are no published data from any setting on the trace-element chemistry of the various textural types of Fe-Ti oxide intergrowths described above. Variations in trace elements, however, can potentially provide important insights into the mechanisms that produce these diverse textures. Because small variations in optimal site radius (< 0.01 pm) can lead to significant changes in compatibility (Blundy and Wood, 2003), the trace-element chemistry of the Fe-Ti oxide intergrowths may provide a record of oxidation because different oxidation states of elements may be preferentially incorporated into, or excluded from, the different textural varieties of Fe-Ti oxide intergrowths that represent different degrees of oxidation.

According to the oxidation model (equation 4), ulvöspinel is oxidized to form magnetite and ilmenite by the conversion of 30% of its Fe^{2+} to Fe^{3+} ($6Fe^{2+}_{usp} \rightleftarrows 4Fe^{2+}_{mt,ilm} + 2Fe^{3+}_{mt}$). Consequently, as Fe^{3+} sites are generated, the number of Fe^{2+} sites decreases proportionally, but the number of Ti^{4+} sites remains unchanged, albeit moving from ulvöspinel to ilmenite. Accordingly, the compatibility of elements in the Fe-Ti oxide intergrowths after oxidation will principally be controlled by the change in the Fe^{2+} : Fe^{3+} ratio, as well as any changes in oxidation state of multivalent elements.

The compatibility of elements in magnetite, ulvöspinel, and ilmenite has been assessed by comparing their ionic radii and valence to that of tetrahedrally- and/or octahedrally-coordinated Fe^{2+}, Fe^{3+}, and Ti^{4+} (Fig. 3.20). According to Goldschmidt (1962), an element can substitute for another element in a mineral if their ionic radii and charge are within ±15% and ±1 charge of each other; the colored fields in Figure 3.20 illustrate this range in ionic radius and charge for tetrahedrally- and octahedrally-coordinated Fe^{2+}, Fe^{3+}, and Ti^{4+}. In magnetite, Fe^{2+} occurs exclusively in octahedral coordination, whereas Fe^{3+} occurs in both tetrahedral and octahedral coordination. In both ulvöspinel and ilmenite, Fe^{2+} and Ti^{4+} occur in octahedral coordination.

The divalent (Cu^{2+}, Ni^{2+}, Zn^{2+}, Co^{2+}) and trivalent metals (Sc^{3+}, Cr^{3+}, Ga^{3+}) will readily substitute into the Fe-Ti oxides for $^{IV}Fe^{2+}$ or $^{VI}Fe^{2+}$, and $^{VI}Fe^{3+}$, respectively (Fig. 3.20). These preferences for the Fe^{2+} and Fe^{3+} sites are important given that the oxidation

mechanism (equation 4) caused a decrease in the number of Fe^{2+} and an increase in the number of Fe^{3+} sites in the oxidized Fe-Ti oxide intergrowths relative to the reduced intergrowths. Because some of the elements measured in the Fe-Ti oxides can occur in multiple oxidation states at terrestrially-relevant fO_2 conditions (Ge, W, Mo, Sn, V), changes in their concentration as a result of the transformations during oxidation of the intergrowths will depend on whether or not they were oxidized and by how much, as well as their compatibility with the $^{VI}Fe^{3+}$ and $^{VI}Ti^{4+}$ sites (Fig. 3.20). Thus, the concentration of multivalent elements in trellis-textured compared to cloth-textured Fe-Ti oxide intergrowths could be i) higher, if the elements were present in the oxidizing fluid in an oxidation state that was compatible with the oxides, ii) lower, if oxidation resulted in an element becoming incompatible, or iii) the same in both textural varieties, if the elements were not present in the fluid, but the fO_2 was such that the elements in the Fe-Ti oxide intergrowths remained compatible.

The concentration of V exhibits no systematic variation amongst the various textural types of Fe-Ti oxide intergrowths (Fig. 3.19). All of the terrestrially-relevant oxidation states of V (V^{3+}, V^{4+}, and V^{5+}) can readily substitute for $^{VI}Ti^{4+}$ and/or $^{VI}Fe^{3+}$ (Fig. 3.20), and so are all relatively compatible in the Fe-Ti oxide minerals. The lack of variation, therefore, suggests that V was not present in the oxidized fluid, consistent with the relative immobility of V in surficial environments (Agnieszka and Barbara, 2012) and in hydrothermally-altered oceanic basalts (Humphris and Thompson, 1978). The concentration of Ge in intermediate- and trellis-textured Fe-Ti oxide intergrowths is systematically higher than its concentration in the cloth variety (Fig. 3.19). The predominant oxidation states of Ge under terrestrial conditions are +2 and +4. Of these, Ge^{4+} is more common in hydrothermal fluids and is the principal oxidation state in silicates, sulfides, oxides, and hydroxides (Höll et al., 2007; Wood and Samson, 2006); it has been suggested, however, that Ge^{2+} occurs in some environments (Cook et al., 2015). The higher concentration of Ge in trellis- compared to cloth-textured intergrowths suggests that the oxidized fluid carried Ge in its tetravalent oxidation state and that Ge^{4+} was added to the oxy-exsolved ilmenite via substitution for $^{VI}Ti^{4+}$ (Fig. 3.20). Similarly, the statistically (> 2 S.E.) and systematically higher Sn concentrations in intermediate- and trellis-textured Fe-Ti oxide intergrowths compared to

the cloth variety (Fig. 3.19) indicates that Sn was present in the oxidized fluid in its 4+ oxidation state. This is because Sn^{4+} is compatible in all of the Fe-Ti oxides and substitutes for $^{VI}Ti^{4+}$ and/or $^{VI}Fe^{3+}$, whereas Sn^{2+} is highly incompatible in all of the Fe-Ti oxides (Fig. 3.20). This is consistent with the recent study of Schmidt (2018) in which Sn^{4+} was identified as being the predominant oxidization state of Sn in hydrothermal fluids over a wide range of temperatures, pressures and fO_2. A coupled substitution with a divalent metal is required for Sn^{4+} to enter the $^{VI}Fe^{3+}$ site in magnetite, however, no correlation between Sn^{4+} and a divalent metal is observed (not shown). This lack of correlation indicates that Sn^{4+} mainly substituted for $^{VI}Ti^{4+}$ in ilmenite. In their most oxidized valences, W^{6+} and Mo^{6+} behave incompatibly in all of the Fe-Ti oxides (Fig. 3.20), yet their concentrations are systematically higher in intermediate- and trellis-textured Fe-Ti oxide intergrowths compared to the cloth variety (Fig. 3.19). Although the oxidation state of Mo in magnetite, ulvöspinel, and ilmenite at variable fO_2 conditions has not been determined (e.g., by X-ray absorption near edge structure [XANES] or electron energy loss spectroscopy [EELS]), Mo^{4+} and Mo^{6+} are thought to be the dominant oxidation states in a silicate melt at NNO, and Mo^{3+} and Mo^{4+} at the graphite-methane buffer (cf. Tacker and Candela, 1987). Likewise, there is similar debate over the prevalent oxidation state of W in terrestrial environments; although W^{6+} is the common oxidation state of W in most minerals (e.g., scheelite, $CaWO_4$) (O'Neill et al., 2008) and in granitic melts (Che et al., 2013; Farges et al., 2006; O'Neill et al., 2008), W^{4+} has been demonstrated to be the dominant species in a haplobasaltic melt at very reduced conditions where W metal is stable (Ertel et al., 1996). Accordingly, the statistically (> 2 S.E.) and systematically higher concentrations of Mo and W in intermediate- and trellis-textured Fe-Ti oxide intergrowths compared to the cloth variety suggests that they were present in the oxidized fluid and that they occurred in their 4+ and/or 5+ oxidation states, which are compatible in oxy-exsolved ilmenite via substitution for $^{VI}Ti^{4+}$ (Fig. 3.20).

Copper exhibits statistically significant (> 2 S.E.) enrichments in intermediate- and trellis-textured Fe-Ti oxide intergrowths compared to cloth varieties (Fig. 3.19). The typical oxidation states of Cu in terrestrial environments are 1+ and 2+, with Cu^{1+} being the common valence state of Cu in chalcopyrite (Klekovkina et al., 2014; Pearce et al., 2006),

the main Cu sulfide mineral in the Eastern Gabbro. There is ample evidence in the Eastern Gabbro for the mobilization of Cu by hydrothermal fluids. Brzozowski et al. (2017) found that chalcopyrite that had replaced pyrrhotite and those that are intergrown with hydrous silicates have the same trace-element composition as primary chalcopyrite, including their PGE content. They suggested that this was the result of dissolution of primary chalcopyrite followed by local (centimeter-scale) precipitation as secondary chalcopyrite. This indicates that Cu and PGE were mobilized on a local scale. Although an oxidizing fluid is not required to mobilize PGE at magmatic temperatures (Blaine et al., 2011; 600-1250°C; Hanley et al., 2005c), Gammons (1996, 1995) and Wood (2002) determined that, at submagmatic temperatures (25 to 300°C), PGE ± Cu are only mobile under highly oxidizing and/or acidic conditions. Although the number of Fe^{2+} sites in the Fe-Ti oxide intergrowths is decreased during oxidation, a proportional number of Fe^{3+} sites are generated. Therefore, the systematically higher Cu concentration in trellis-textured intergrowths suggests that Cu was present in the oxidized fluid in its 2+ oxidation state and that it behaved compatibly in the oxide assemblage via substitution for $^{VI}Fe^{2+}$ and/or $^{VI}Fe^{3+}$ (Fig. 3.20). Gallium, which preferentially substitutes for $^{VI}Fe^{3+}$ and/or $^{VI}Ti^{4+}$ (Fig. 3.20), exhibits statistically-significant (> 2 S.E.) enrichments in intermediate- and trellis-textured Fe-Ti oxide intergrowths compared to cloth varieties (Fig. 3.19). This systematic enrichment in Ga in the oxidized intergrowths suggests that Ga was present in the oxidized fluid.

The divalent metals Zn, Co, and Ni, and the trivalent metals Sc and Cr largely show no systematic enrichment or depletion between cloth- and trellis-textured Fe-Ti oxide intergrowths (Fig. 3.19). Because the divalent and trivalent metals behave compatibly in magnetite, ulvöspinel, and ilmenite (Fig. 3.20), this suggests that they were either not present in significant concentrations in the oxidized fluid and/or that the concentration of Zn, Co, and Ni were unaffected by the decrease in $^{VI}Fe^{2+}$ sites during oxidation.

The HFSE do not exhibit systematic enrichment or depletion in concentration amongst the textural-types of Fe-Ti oxide intergrowths (Fig. 3.19). Because the HFSE will preferentially substitute for $^{VI}Ti^{4+}$ in ulvöspinel and ilmenite (Fig. 3.20), they behave

relatively compatibly in these minerals. Therefore, the lack of systematic change in their concentration suggests that they were not added to or removed from the Fe-Ti oxide intergrowths by the oxidized fluid, consistent with their relative immobility (Corfu and Davis, 1991; Floyd and Winchester, 1978).

3.5.2.4 An alternative to oxygen in water as the oxidizing agent

Verhoogen (1962) and Buddington and Lindsley (1964) both suggested that the oxidizing agent that converted ulvöspinel to ilmenite was a hydothermal fluid. It is unlikely, however, that oxygen would have been the oxidizing agent because crustal fluids have very low pO_2, less than 10^{-21} atm at 550°C 1 kbar (Chou, 1987). This would require an unreasonable amount of water to have interacted with the Fe-Ti oxide intergrowths to generate the large amount of ilmenite lamellae present in the Eastern Gabbro. If the Eastern Gabbro experienced such a high fluid:rock ratio, the rocks should be intensely and uniformly altered, which is not the case (Good et al., 2015). Given that CO_2 has been identified as a common component of fluid inclusions from the Marathon deposit (Smoke et al., 2013), an alternative oxidizing agent is C^{4+}, which would have been reduced to C^{4-}, forming CH_4 via a modified reaction of equation 4:

$$9Fe_2^{2+}TiO_4 + 0.75CO_2 + 1.5H_2O \leftrightharpoons 9Fe^{2+}TiO_3 + 3Fe_2^{3+}Fe^{2+}O_4 + 0.75CH_4 \quad \text{eq. 3.5}$$

This reaction can also be written using HCO_3^- instead of CO_2:

$$9Fe_2^{2+}TiO_4 + 0.75HCO_3^- + 0.75H_2O + 0.75H^+ \leftrightharpoons 9Fe^{2+}TiO_3 + 3Fe_2^{3+}Fe^{2+}O_4 + 0.75CH_4 \quad \text{eq. 3.6}$$

Carbon dioxide has previously been identified as the predominant component in the vapor phase of secondary apatite-hosted fluid inclusions at the Marathon deposit (Smoke et al., 2013). At Marathon and Four Dams, the vapor phase of pyroxene-hosted fluid inclusions is CH_4 (Fig. 3.12). Carbon dioxide- and methane-rich fluid inclusions are common in mafic

rocks, including those that host Ni-Cu-PGE mineralization (e.g., Stillwater Complex) (Ballhaus and Stumpfl, 1986; Hanley et al., 2005b, 2005a; Kerr, 2013; Larsen et al., 1992; Molnár et al., 1997; Zhitova et al., 2016). Additionally, most mafic rocks, either fresh or altered, contain magnetite-ilmenite intergrowths rather than magnetite-ulvöspinel intergrowths. The fact that both CO_2 and CH_4 occur in fluid inclusions in the Eastern Gabbro, and many Ni-Cu-PGE deposits, supports the proposed models for C-mediated oxidation of ulvöspinel to magnetite and ilmenite. One of the advantages of this oxidation model is its ability to generate magnetite-ilmenite intergrowths and CH_4 without generating hydrous alteration.

3.5.3 Fe-Ti oxide intergrowths as a record of oxidation history

The continuum of textures from cloth- to intermediate- to trellis-textured Fe-Ti oxide intergrowths can be used to track the oxidation history of the rocks that host the intergrowths. Duchesne (1970) outlined a series of end-member textures (cf. Fig. 3 in Duchesne, 1970) that may be expected to form as a result of different rates and temperatures of oxidation relative to the magnetite-ulvöspinel solvus. In their description, however, none of the intermediate-textured Fe-Ti oxide intergrowths or trellis-textured intergrowths without thick trellis ilmenite were described. The figure published by Duchesne (1970) has been modified (Fig. 3.21) to include the intermediate- and trellis-textured Fe-Ti oxide intergrowths at the positions, relative to the magnetite-ulvöspinel solvus and relative to the other textural varieties of Fe-Ti oxide intergrowths, at which they are thought to have formed.

Apart from fine trellis ilmenite lamellae within the cloth network (1b in Fig. 3.21), all of the subsolvus textures have been observed in the Fe-Ti oxide intergrowths hosted in the Eastern Gabbro. The occurrence of cloth-, intermediate-, and trellis-textured Fe-Ti oxide intergrowths throughout the Eastern Gabbro suggests that the oxides experienced variable degrees of oxidation at different rates of Fe-Ti diffusion.

3.5.4 Variation in degree of oxidation throughout the Eastern Gabbro

In the Eastern Gabbro, it is uncommon for all of the Fe-Ti oxide intergrowths in a given suite of rocks to be of a single textural variety (Fig. 3.11). The relative proportion of cloth-, intermediate-, and trellis-textured Fe-Ti oxide intergrowths in a given suite of rocks, therefore, can be used as a proxy for their degree of fluid-induced oxidation (i.e., a higher proportion of trellis-textured Fe-Ti oxide intergrowths equates to a greater degree of oxidation). The Marathon Series must have experienced a much greater degree of postcumulus, fluid-induced oxidation compared to the metabasalt and Layered Series as trellis-textured Fe-Ti oxide intergrowths are more common in the former (Fig. 3.11b). In fact, trellis-textured Fe-Ti oxide intergrowths are absent altogether in the Layered Series, suggesting these rocks experienced the least amount of oxidation (Fig. 3.11b).

Different mineralized zones and occurrences also underwent variable degrees of oxidation as a result of fluid flux. Layered Series mineralization only hosts cloth-textured Fe-Ti oxide intergrowths (Fig. 3.11c). This suggests that Layered Series mineralization experienced the lowest degree of fluid-induced oxidation compared to the other mineralized zones and occurrences. The Layered Series mineralization is secondary and associated with actinolite and albite that has replaced pyroxene and plagioclase, respectively, suggesting that the Layered Series experienced some degree of fluid flux (Good et al., 2015). Yet, because trellis-textured oxides are absent, it is unlikely that the oxygen in water acted as the oxidizing agent, providing support for the proposed model that C in CO_2 was the oxidizing agent. The other mineralized occurrences are all hosted in Marathon Series rocks and contain a distinctly greater abundance of trellis-textured Fe-Ti oxide intergrowths compared to cloth varieties. Based on the proportion of trellis- to cloth-textured Fe-Ti oxide intergrowths, the mineralized occurrences throughout the Eastern Gabbro can be listed from lowest to highest degree of fluid-induced oxidation as i) Redstone and Four Dams, ii) magnetite-apatite-clinopyroxene cumulate, iii) W Horizon and Area 41, and iv) Main and Footwall Zone (Fig. 3.11c). The relatively high degree of oxidation that is observed in the W Horizon is consistent with the recent work of Ames et al. (2017), who interpreted the

association of PGM with millerite and secondary magnetite in the W Horizon as the result of oxidation of Fe^{2+} to Fe^{3+}.

3.5.5 Implications for the use of Fe-Ti oxide chemistry as petrogenetic and exploration tools

Many of the discrimination diagrams that distinguish magnetite that formed in different mineral deposits (Boutroy et al., 2014; e.g., Ni-Cu-PGE; Dupuis and Beaudoin, 2011), during different stages of magma evolution (e.g., primitive vs. evolved; Dare et al., 2014b), or that crystallized from different media (e.g., silicate melt vs. hydrothermal fluid vs. sulfide melt; Dare et al., 2012; Nadoll et al., 2014) include a number of elements that were determined in this study, many of which are mobile, and some of which can occur in multiple oxidation states. Because it is more common for magnetite to contain lamellae of ilmenite rather than ulvöspinel in most magmatic environments (Buddington and Lindsley, 1964), oxidation of Fe-Ti oxide intergrowths must be a common process. Therefore, an understanding of how the trace-element chemistry of Fe-Ti oxide intergrowths varies as a result of oxidation from cloth-textured to trellis-textured varieties is potentially important. Some of these studies described the presence of ilmenite and spinel lamellae in magnetite, and attributed the ilmenite to oxy-exsolution from a magnetite-ulvöspinel solid solution. None of these studies, however, discussed how this oxidation process could have affected the trace-element composition of the Fe-Ti oxide intergrowths. Consequently, the compositions used to develop discriminant diagrams and other petrogenetic indicators may not solely reflect magmatic processes, but also postcumulus oxidation.

The only elements that show statistically-significant variations that resulted from oxidation of Fe-Ti oxide intergrowths are Sn, W, Mo, Cu, Ge, and Ga (Fig. 3.19). In general, however, these differences are small and in the range of tens of ppm (Fig. 3.19). Additionally, none of the discrimination diagrams developed by Dupuis and Beaudoin (2011) incorporated the multivalent elements Sn and Mo and only the discriminant diagram for VMS deposits incorporated Cu. Consequently, postcumulus oxidation of Fe-Ti oxide

intergrowths should not have affected the accuracy, and hence the usefulness, of these discrimination diagrams.

3.6 Conclusion

The reliability of applying Fe-Ti oxides for mineral deposit exploration and igneous petrogenesis may depend on an understanding of the supra- and subsolidus processes that could have modified their chemistry. Most magmatic magnetite contain lamellae of ilmenite, and it is generally understood that such exsolution redistributes elements that were once present in a homogenous magnetite-ulvöspinel solid solution at high temperature. The mechanism by which magnetite-ilmenite intergrowths form, however, is not well understood, nor is the effect of this redistribution on Fe-Ti oxide chemistry and, ultimately, its impact on their usefulness for exploration and petrogenesis.

i. Two mineralogically- and texturally-distinct end-member varieties of Fe-Ti oxides occur throughout the Eastern Gabbro: a) cloth-textured magnetite-ulvöspinel intergrowths and b) trellis-textured magnetite-ilmenite intergrowths. A continuous series of textures also occur that are mineralogically and texturally intermediate to the cloth and trellis varieties.

ii. Mineralogical, textural, and chemical evidence suggest that magnetite-ilmenite intergrowths develop through oxidation of ulvöspinel. Given the occurrence of CO_2 and CH_4 in apatite- and pyroxene-hosted fluid inclusions in the Eastern Gabbro, it is proposed that CO_2 rather than O_2 was the main oxidizing agent in such systems, where the C in CO_2 was reduced to form CH_4:

$$9Fe_2^{2+}TiO_4 + 0.75CO_2 + 1.5H_2O \leftrightharpoons 9Fe^{2+}TiO_3 + 3Fe_2^{3+}Fe^{2+}O_4 + 0.75CH_4$$

This oxidation model can generate magnetite-ilmenite intergrowths and CH_4 without generating hydrous alteration, features that are characteristic of many mafic rocks, including those that host Ni-Cu-PGE mineralization.

iii. Variable distribution of these textural varieties of Fe-Ti oxides throughout the Eastern Gabbro suggests that different rock types and mineralized occurrences experienced different degrees of fluid-induced oxidation.

iv. Trellis-textured intergrowths are consistently enriched in Ge, Mo, W, Sn, Cu, and Ga compared to cloth-textured intergrowths, indicating that the oxidized fluid carried these metals. Because these compositional differences are minor and because petrogenetic discrimination diagrams that employ Fe-Ti oxide chemistry typically do not include these elements (Dupuis and Beaudoin, 2011), the compositional changes that accompanied oxidative conversion of ulvöspinel to magnetite + ilmenite do not interfere with their reliability as petrogenetic indicators or exploration vectors.

3.7 References

Agnieszka, J., Barbara, G., 2012. Chromium, nickel and vanadium mobility in soils derived from fluvioglacial sands. J. Hazard. Mater. 237–238, 315–322.

Ballhaus, C.G., Stumpfl, E.F., 1986. Sulfide and platinum mineralization in the Merensky Reef: evidence from hydrous silicates and fluid inclusions. Contrib. Mineral. Petrol. 94, 193–204.

Blaine, F.A., Linnen, R.L., Holtz, F., Bruegmann, G.E., 2011. The effect of Cl on Pt solubility in haplobasaltic melt: Implications for micronugget formation and evidence for fluid transport of PGEs. Geochim. Cosmochim. Acta 75, 7792–7805.

Blundy, J., Wood, B., 2003. Partitioning of trace elements between crystals and melts. Earth Planet. Sci. Lett. 210, 383–397.

Boutroy, E., Dare, S.A.S., Beaudoin, G., Barnes, S.-J., Lightfoot, P.C., 2014. Magnetite composition in Ni-Cu-PGE deposits worldwide: application to mineral exploration. J. Geochem. Explor. 145, 64–81.

Brzozowski, M., Samson, I., Gagnon, J., Good, D., Linnen, R., 2017. On the controls of low- and high-Cu/Pd mineralization in the Eastern Gabbro, Canada: evidence from

sulfide textures, S/Se ratios, and PGE contents, in: SGA 14th Biennial Meeting. Quebec City, Canada, pp. 423–426.

Buddington, A.F., Lindsley, D.H., 1964. Iron-titanium oxide minerals and synthetic equivalents. J. Petrol. 5, 310–357.

Burke, E.A.J., 2001. Raman microspectrometry of fluid inclusions. Lithos, Fluid Inclusions: Phase Relationships - Methods - Applications. A Special Issue in honour of Jacques Touret 55, 139–158.

Cao, Y., 2017. Cu-Pd mineralization and exploration geochemistry of the Eastern Gabbro, Coldwell Alkaline Complex, ON, Canada (PhD Dissertation). Western University, London, Ontario.

Charlier, B., Namur, O., Bolle, O., Latypov, R., Duchesne, J.-C., 2015. Fe–Ti–V–P ore deposits associated with Proterozoic massif-type anorthosites and related rocks. Earth-Sci. Rev. 141, 56–81.

Che, X.D., Linnen, R.L., Wang, R.C., Aseri, A., Thibault, Y., 2013. Tungsten solubility in evolved granitic melts: An evaluation of magmatic wolframite. Geochim. Cosmochim. Acta 106, 84–98.

Chou, I.-M., 1987. Oxygen buffer and hydrogen sensor techniques at elevated pressures and temperatures, in: Ulmer, G.C., Barnes, H.L. (Eds.), Hydrothermal Experimental Techniques. John Wiley and Sons, New York, pp. 61–99.

Cook, N.J., Etschmann, B., Ciobanu, C.L., Geraki, K., Howard, D.L., Williams, T., Rae, N., Pring, A., Chen, G., Johannessen, B., Brugger, J., 2015. Distribution and Substitution Mechanism of Ge in a Ge-(Fe)-Bearing Sphalerite. Minerals 5, 117–132.

Corfu, F., Davis, D.W., 1991. Comment on “Archean hydrothermal zircon in the Abitibi greenstone belt: constraints on the timing of gold mineralization” by J.C. Claoué-Long, R.W. King and R. Kerrich. Earth Planet. Sci. Lett. 104, 545–552.

Dare, S.A., Barnes, S.-J., Beaudoin, G., 2011. Evolution of trace element concentrations in magnetite from a fractionating magmatic sulphide liquid: an example from the Sudbury (Canada) Ni-Cu-PGE deposits, in: 11th Biennial SGA Meeting: Let’s Talk

Ore Deposits, The Society for Geology Applied to Mineral Deposits. Antofagasta, Chile, pp. 621–623.

Dare, S.A.S., Ames, D.E., Lightfoot, P.C., Barnes, S.-J., Beaudoin, G., 2014a. Mineral chemistry and supporting databases for TGI4 project on "Trace elements in Fe-oxides from fertile and barren igneous complexes: Investigating their use as a vectoring tool in the intrusions that host Ni-Cu-PGE deposits". Geological Survey of Canada Open File No. 7538.

Dare, S.A.S., Barnes, S.-J., Beaudoin, G., 2012. Variation in trace element content of magnetite crystallized from a fractionating sulfide liquid, Sudbury, Canada: Implications for provenance discrimination. Geochim. Cosmochim. Acta 88, 27–50.

Dare, S.A.S., Barnes, S.-J., Beaudoin, G., Méric, J., Boutroy, E., Potvin-Doucet, C., 2014b. Trace elements in magnetite as petrogenetic indicators. Miner. Deposita 49, 785–796.

Dare, S.A.S., Barnes, S.-J., Méric, J., Néron, A., Beaudoin, G., Boutroy, E., 2013. The use of trace elements in Fe-oxides as provenance and petrogenetic indicators in magmatic and hydrothermal environments, in: 12th SGA Biennial Meeting 2013. Uppsala, Sweden, pp. 256–259.

Downs, R.T., 2006. The RRUFF project: an integrated study of the chemistry, crystallography, Raman and infrared spectroscopy of minerals, in: 19th General Meeting of the International Mineralogical Association. Kobe, Japan.

Duchesne, J.-C., 1972. Iron-titanium oxide minerals in the Bjerkrem-Sogndal massif, South-Western Norway. J. Petrol. 13, 57–81.

Duchesne, J.-C., 1970. Microtextures of Fe-Ti oxide minerals in the South-Rogaland anorthositic complex (Norway). Ann. Société Géologique Belg. 935, 527–544.

Dupuis, C., Beaudoin, G., 2011. Discriminant diagrams for iron oxide trace element fingerprinting of mineral deposit types. Miner. Deposita 46, 319–335.

El Goresy, A., Taylor, L.A., Ramdohr, P., 1972. Fra Mauro crystalline rocks: Mineralogy, geochemistry and subsolidus reduction of the opaque minerals, in: Lunar and Planetary Science Conference Proceedings. pp. 333–349.

Ertel, W., O'Neill, H.S.C., Dingwell, D.B., Spettel, B., 1996. Solubility of tungsten in a haplobasaltic melt as a function of temperature and oxygen fugacity. Geochim. Cosmochim. Acta 60, 1171–1180.

Farges, F., Linnen, R.L., Brown, G.E., 2006. Redox and speciation of tin in hydrous silicate glasses: A comparison with Nb, Ta, Mo and W. Can. Mineral. 44, 795–810.

Floyd, P.A., Winchester, J.A., 1978. Identification and discrimination of altered and metamorphosed volcanic rocks using immobile elements. Chem. Geol. 21, 291–306.

Gammons, C.H., 1996. Experimental investigations of the hydrothermal geochemistry of platinum and palladium: V. Equilibria between platinum metal, Pt (II), and Pt (IV) chloride complexes at 25 to 300 C. Geochim. Cosmochim. Acta 60, 1683–1694.

Gammons, C.H., 1995. Experimental investigations of the hydrothermal geochemistry of platinum and palladium: IV. The stoichiometry of Pt (IV) and Pd (II) chloride complexes at 100-300°C. Geochem. Cosmochem. Acta 59, 1655–1667.

Goldschmidt, V.M., 1962. Geochemistry, International series of monographs on physics (Oxford, England). Clarendon Press, Oxford.

Good, D.J., Epstein, R., McLean, K., Linnen, R., Samson, I., 2015. Evolution of the Main Zone at the Marathon Cu-PGE Sulfide Deposit, Midcontinent Rift, Canada: Spatial Relationships in a Magma Conduit Setting. Econ. Geol. 110, 983–1008.

Groschner, C., Lan, S., Wise, A., Leary, A., Lucas, M.S., Park, C., Laughlin, D.E., Diaz-Michelena, M., McHenry, M.E., 2013. The Role of Atmosphere on Phase Transformations and Magnetic Properties of Ulvöspinel. IEEE Trans. Magn. 49, 4273–4276.

Haggerty, S.E., 1977. Apollo 14: Oxide, metal and olivine mineral chemistries in 14072 with a bearing on the temporal relationships of subsolidus reduction, in: Lunar and Planetary Science Conference Proceedings. pp. 1809–1829.

Haggerty, S.E., 1976. Oxidation of Opaque Mineral Oxides in Basalts, in: Rumble, D. (Ed.), Oxide Minerals, Reviews in Mineralogy. Mineralogical Society of America, p. 706.

Haggerty, S.E., 1972. Apollo 14: Subsolidus redcution and compositional variations of spinels, in: Proceedings of the Third Lunar Science Conference. pp. 305–332.

Hanley, J.J., Mungall, J.E., Pettke, T., Spooner, E.T.C., Bray, C.J., 2005a. Ore metal redistribution by hydrocarbon–brine and hydrocarbon–halide melt phases, North Range footwall of the Sudbury Igneous Complex, Ontario, Canada. Miner. Deposita 40, 237–256.

Hanley, J.J., Mungall, J.E., Spooner, E.T.C., Pettke, T., 2005b. Fluid and melt inclusion evidence for platinum-group element transport by high salinity fluids and halide melts below the JM Reef, Stillwater Complex, in: 10th International Platinum Symposium "Platinum-Group Elements-from Genesis to Beneficiation and Environmental Impact." Oulu, Finland, pp. 94–97.

Hanley, J.J., Pettke, T., Mungall, J.E., Spooner, E.T.C., 2005c. The solubility of platinum and gold in NaCl brines at 1.5 kbar, 600 to 800°C: A laser ablation ICP-MS pilot study of synthetic fluid inclusions. Geochim. Cosmochim. Acta 69, 2593–2611.

Haselton, J.D., Nash, W.P., 1975. A model for the evolution of opaques in mare lavas, in: Lunar and Planetary Science Conference Proceedings. pp. 747–755.

Höll, R., Kling, M., Schroll, E., 2007. Metallogenesis of germanium—A review. Ore Geol. Rev. 30, 145–180.

Hu, H., Lentz, D., Li, J.-W., McCarron, T., Zhao, X.-F., Hall, D., 2015. Reequilibration processes in magnetite from iron skarn deposits. Econ. Geol. 110, 1–8.

Humphris, S.E., Thompson, G., 1978. Trace element mobility during hydrothermal alteration of oceanic basalts. Geochim. Cosmochim. Acta 42, 127–136.

Kerr, M.J., 2013. The application of gas chromatography in characterizing bulk fluid inclusion hydrocarbons in the footwall of the Sudbury Igneous Complex and other magmatic, hydrothermal and surficial ore-forming environments (MSc Thesis). Saint Mary's University, Halifax, Nova Scotia.

Klekovkina, V.V., Gainov, R.R., Vagizov, F.G., Dooglav, A.V., Golovanevskiy, V.A., Pen'kov, I.N., 2014. Oxidation and magnetic states of chalcopyrite CuFeS2: A first principles calculation. Opt. Spectrosc. 116, 885–888.

Larsen, R.B., Brooks, C.K., Bird, D.K., 1992. Methane-bearing, aqueous, saline solutions in the Skaergaard intrusion, east Greenland. Contrib. Mineral. Petrol. 112, 428–437.

Lattard, D., 1995. Experimental evidence for the exsolution of ilmenite from titaniferous spinel. Am. Mineral. 80, 968–981.

Lilova, K.I., Pearce, C.I., Gorski, C., Rosso, K.M., Navrotsky, A., 2012. Thermodynamics of the magnetite-ulvöspinel (Fe3O4-Fe2TiO4) solid solution. Am. Mineral. 97, 1330–1338.

Lindsley, D.H., 1963. Equilibrium relations of coexisting pairs of Fe-Ti oxides. Carnegie Inst. Sci. Yearb. 62, 60–66.

Lindsley, D.H., 1962. Investigations in the system FeO-Fe2O3-TiO2. Carnegie Inst. Sci. Yearb. 61, 100–106.

McBride, J., 2015. Assessment Report for Diamond Drilling on the Stillwater Canada Inc. Bermuda Property (Assessment Report No. NTS 42D/16), Assessment Report.

McEnroe, S.A., Robinson, P., Panish, P.T., 2000. Chemical and petrographic characterization of ilmenite and magnetite in oxide-rich cumulates of the Sokndal region, Rogaland, Norway. Nor. Geol. Unders. 436, 49–56.

Molnár, F., Watkinson, D.H., Jones, P.C., Gatter, I., 1997. Fluid Inclusion Evidence for Hyrothermal Enrichment of Magmatic Ore at the Contact Zone of the Ni-Cu-Platinum-Group Element 4b Deposit, Lindsley Mine, Sudbury, Canada. Econ. Geol. 92, 674–685.

Mücke, A., 2003. Magnetite, ilmenite and ulvite in rocks and ore deposits: petrography, microprobe analyses and genetic implications. Mineral. Petrol. 77, 215–234.

Nadoll, P., Angerer, T., Mauk, J.L., French, D., Walshe, J., 2014. The chemistry of hydrothermal magnetite: A review. Ore Geol. Rev. 61, 1–32.

O'Neill, H., Berry, A., Eggins, S., 2008. The solubility and oxidation state of tungsten in silicate melts: Implications for the comparative chemistry of W and Mo in planetary differentiation processes. Chem. Geol. 255, 346–359.

Papike, J.J., Karner, J.M., Shearer, C.K., 2005. Comparative planetary mineralogy: Valence state partitioning of Cr, Fe, Ti, and V among crystallographic sites in olivine, pyroxene, and spinel from planetary basalts. Am. Mineral. 90, 277–290.

Paton, C., Hellstrom, J., Paul, B., Woodhead, J., Hergt, J., 2011. Iolite: Freeware for the visualisation and processing of mass spectrometric data. J. Anal. At. Spectrom. 26, 2508–2518.

Pearce, C.I., Pattrick, R.A.D., Vaughan, D.J., Henderson, C.M.B., van der Laan, G., 2006. Copper oxidation state in chalcopyrite: Mixed Cu d9 and d10 characteristics. Geochim. Cosmochim. Acta 70, 4635–4642.

Ramdohr, P., 1955. Die Erzmineralien und ihre Verwachsung. Akademie Verlag, Berlin.

Ramdohr, P., 1953. Ulvöspinel and its significance in titaniferous iron ores. Econ. Geol. 48, 677–688.

Sage, D., Unser, M., 2003. Teaching image-processing programming in Java. IEEE Signal Process. Mag. 20, 43–52.

Schmidt, C., 2018. Formation of hydrothermal tin deposits: Raman spectroscopic evidence for an important role of aqueous Sn(IV) species. Geochim. Cosmochim. Acta 220, 499–511.

Shaw, C.S.J., 1997. The petrology of the layered gabbro intrusion, eastern gabbro, Coldwell alkaline complex, Northwestern Ontario, Canada: evidence for multiple phases of intrusion in a ring dyke. Lithos 40, 243–259.

Smoke, R., Linnen, R., Samson, I., Good, D., Shahabi Far, M., 2013. Analysis of fluid inclusions from the Marathon Cu-Pd deposit: The role of hydrothermal fluids in mineralization, in: PDAC Student Minerals Colloquium. Toronto, Ontario.

Speczik, S., Wiszniewska, J., Diedel, R., 1988. Minerals, exsolution features and geochemistry of Fe-Ti ores of the Suwalki District (North-East Poland). Miner. Deposita 23, 200–210.

Tacker, R.C., Candela, P.A., 1987. Partitioning of Molybdenum between Magnetite and Melt: A Preliminary Experimental Study of Partitioning of Ore Metals between Silicic Magmas and Crystalline Phases. Econ. Geol. 82, 1827–1838.

Tan, W., Liu, P., He, H., Wang, C.Y., Liang, X., 2016. Mineralogy and Origin of Exsolution in Ti-rich Magnetite From Different Magmatic Fe-Ti Oxide-Bearing Intrusions. Can. Mineral. 54, 539–553.

Verhoogen, J., 1962. Oxidation of iron-titanium oxides in igneous rocks. J. Geol. 70, 168–181.

Vincent, E.A., Phillips, R., 1954. Iron-titanium oxide minerals in layered gabbros of the Skaergaard intrusion, East Greenland: Part I. Chemistry and ore-microscopy. Geochim. Cosmochim. Acta 6, 1–26.

Vincent, E.A., Wright, J.B., Chevalier, R., Mathieu, S., 1957. Heating experiments on some natural titaniferous magnetites. Mineral. Mag. 31, 624–655.

von Gruenewaldt, G., Klemm, D.D., Henckel, J., Dehm, R.M., 1985. Exsolution Features in Titanomagnetites from Massive Magnetite Layers and Their Host Rocks of the Upper Zone, Eastern Bushveld Complex. Econ. Geol. 80, 1049–1061.

Wang, A., Kuebler, K.E., Jolliff, B.L., Haskin, L.A., 2004. Raman spectroscopy of Fe-Ti-Cr-oxides, case study: Martian meteorite EETA79001. Am. Mineral. 89, 665–680.

Waychunas, G.A., 1987. Synchrotron radiation XANES spectroscopy of Ti in minerals: Effects of Ti bonding distances, Ti valence, and site geometry on absorption edge structure. Am. Mineral. 72, 89–101.

Wood, S.A., 2002. The aqueous geochemistry of the platinum-group elements with applications to ore deposits, in: Cabri, L.J. (Ed.), The Geology, Geochemistry, Mineralogy and Mineral Beneficiation of Platinum-Group Elements. Canadian Institute of Mining, Metallurgy and Petroleum, pp. 211–249.

Wood, S.A., Samson, I.M., 2006. The aqueous geochemistry of gallium, germanium, indium and scandium. Ore Geol. Rev. 28, 57–102.

Wright, J.B., 1961. Solid-solution relationships in some titaniferous iron oxide ores of basic igneous rocks. Mineral. Mag. 32, 778–789.

Wright, J.B., 1959. Some further heating experiments on natural titaniferous magnetites. Mineral. Mag. 32, 32–37.

Zhitova, L.M., Kinnaird, J.A., Gora, M.P., Shevko, E.P., 2016. Magmatogene fluids of metal-bearing reefs in the Bushveld Complex, South Africa: Based on research data on fluid inclusions in quartz. Geol. Ore Depos. 58, 58–81.

Zinin, P., Tatsumi-Petrochilos, L., Bonal, L., Acosta, T., Hammer, J., Gilder, S., Fuller, M., 2011. Raman spectroscopy of titanomagnetites: Calibration of the intensity of Raman peaks as a sensitive indicator for their Ti content. Am. Mineral. 96, 1537–1546.

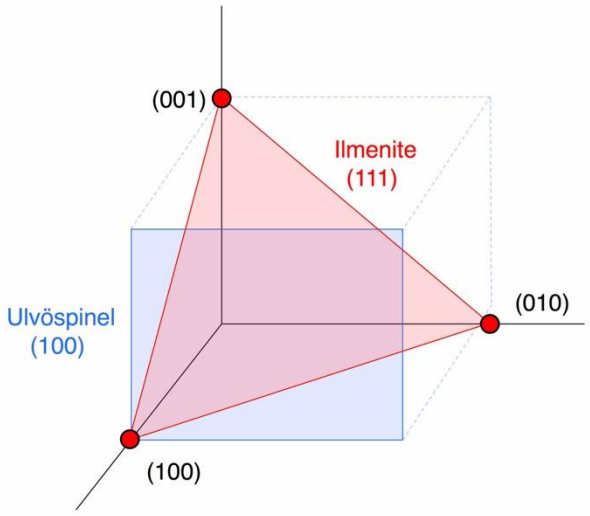

Figure 3.1 Three-dimensional Cartesian plane showing the difference in crystallographic orientation of ulvöspinel {100} and ilmenite {111} in magnetite.

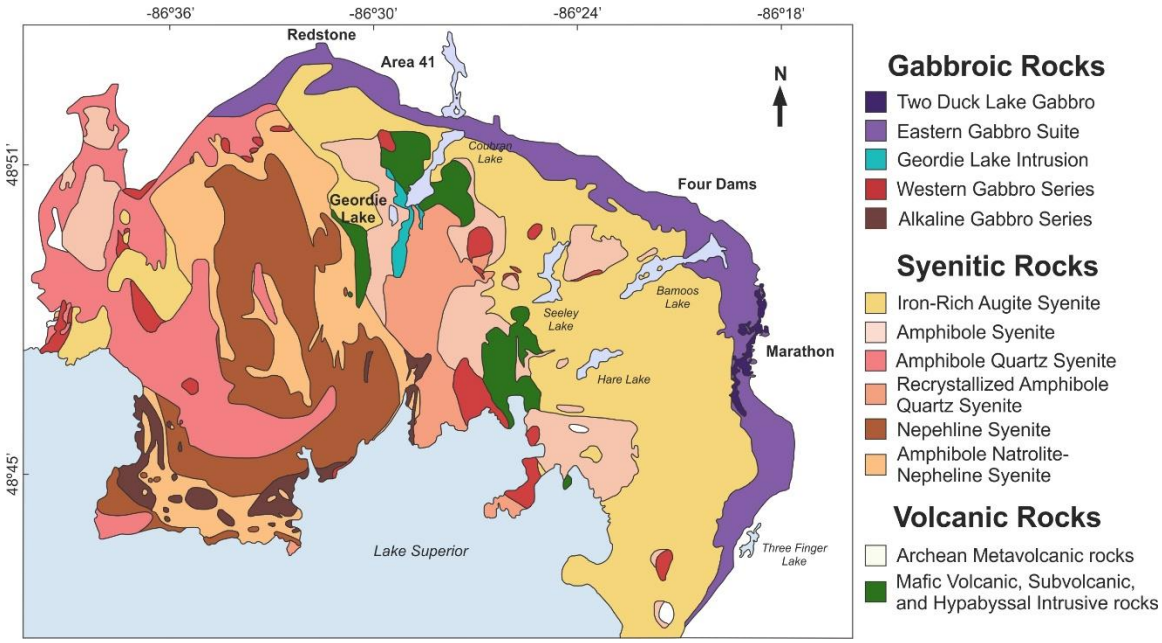

Figure 3.2 Geologic map of the Coldwell Complex highlighting the location of Marathon and Geordie Lake deposits, as well as other mineralized occurrences along the Eastern Gabbro (modified from Good et al., 2015).

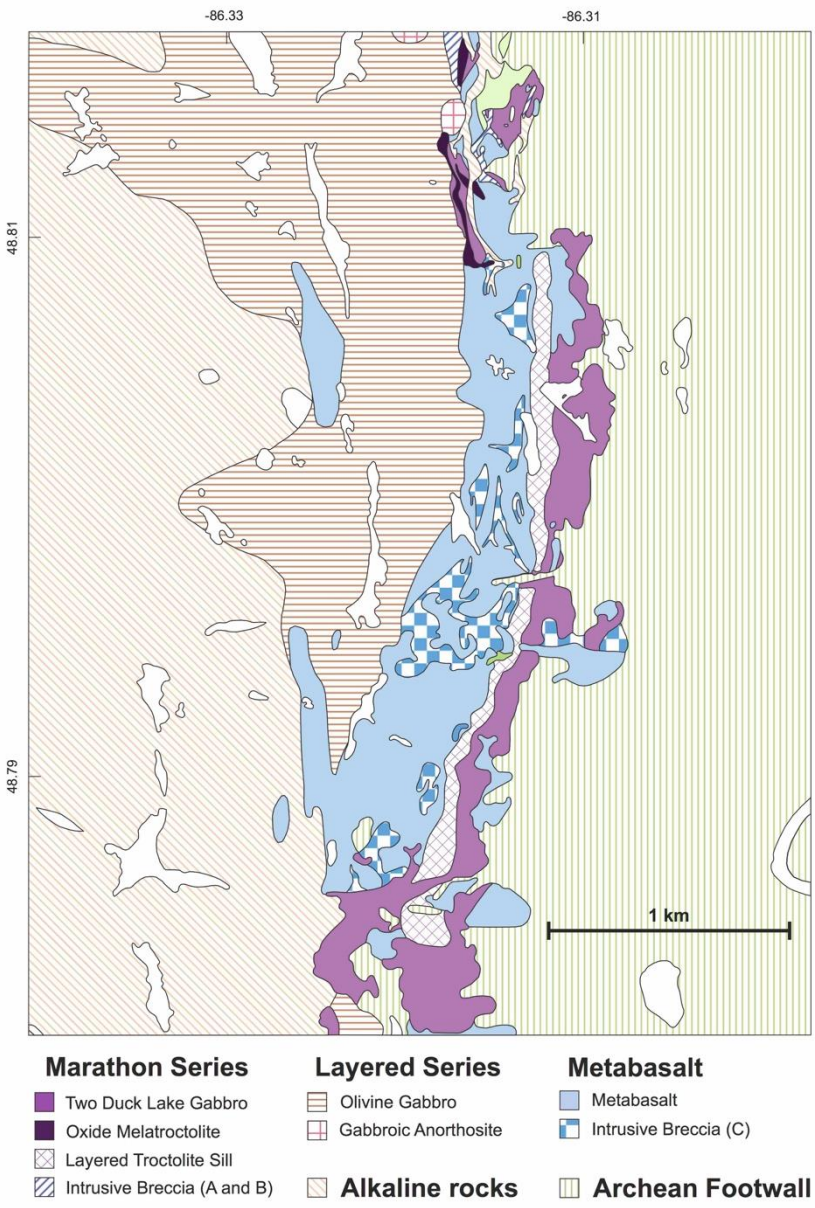

Figure 3.3 Geologic map of the Marathon Cu-PGE deposit illustrating the spatial relationships of each of the rock series (modified from Good et al., 2015).

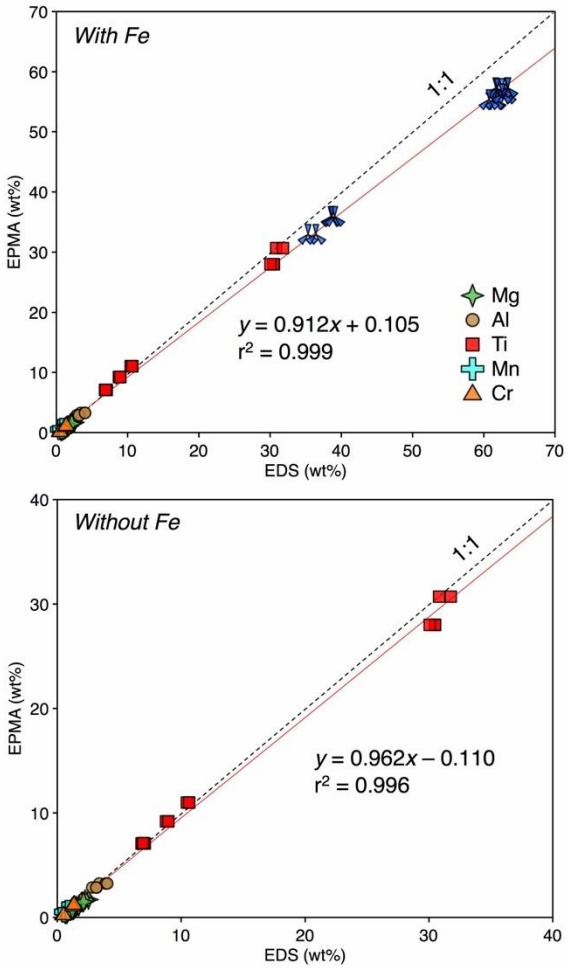

Figure 3.4 Comparison between analyses obtained via EDS and EPMA (wt. %). Analyses included bulk cloth-, intermediate-, and trellis-textured Fe-Ti oxide intergrowths, and ilmenite crystals. Regressions including (top binary) and excluding (bottom binary) Fe were performed. Iron is overestimated by the EDS and skews the regression. When Fe is excluded in the regression, a 1:1 relationship is achieved between EDS and EPMA.

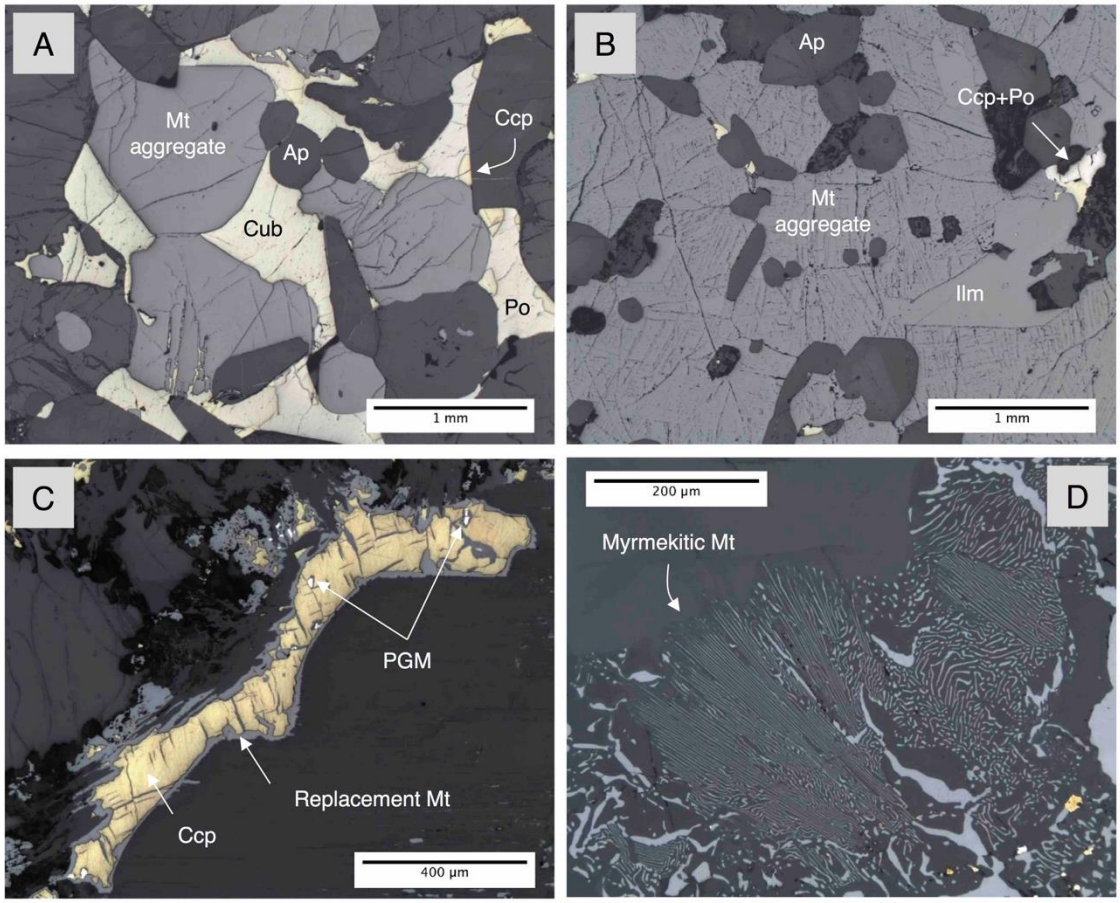

Figure 3.5 Reflected-light images illustrating the dominant types of oxides in the Eastern Gabbro. (A) Fe-Ti oxide intergrowths with ultrafine cloth lamellae. (B) Fe-Ti oxide intergrowths with fine to thick trellis lamellae. (C) Replacement magnetite that rims and intrudes into the cracks of a chalcopyrite grain. (D) Myrmekitic Fe-Ti oxide intergrowth that occurs in an orthopyroxene rim on olivine. Although not visible, the myrmekitic Fe-Ti oxide intergrowth does contain exsolution lamellae. Mt = magnetite, ap = apatite, ccp = chalcopyrite, cub = cubanite, po = pyrrhotite, PGM = platinum-group mineral.

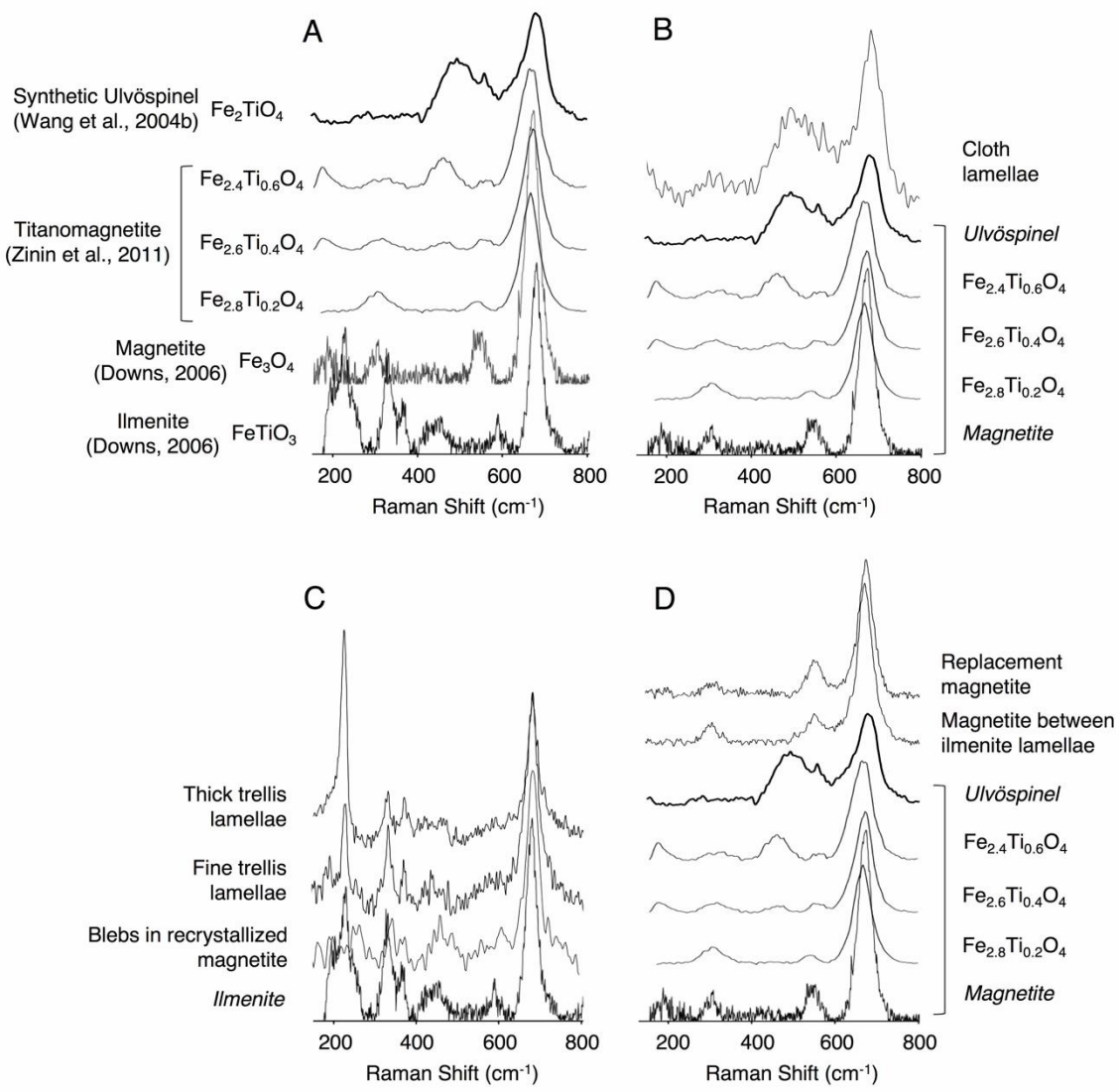

Figure 3.6 (A) Reference Raman spectra for synthetic ulvöspinel (Wang et al., 2004b), titanomagnetite with various proportions of Fe-Ti (Zinin et al., 2011), magnetite (Downs, 2006), and ilmenite (Downs, 2006). (B) Raman spectra for cloth lamellae showing a good match with the ulvöspinel reference spectra. (C) Raman spectra of fine and thick trellis lamellae and anhedral blebs in recrystallized cloth-textured intergrowths showing a good match to the reference spectra for ilmenite. (D) Raman spectra of replacement magnetite and magnetite in between trellis lamellae showing a good match to the magnetite reference spectra.

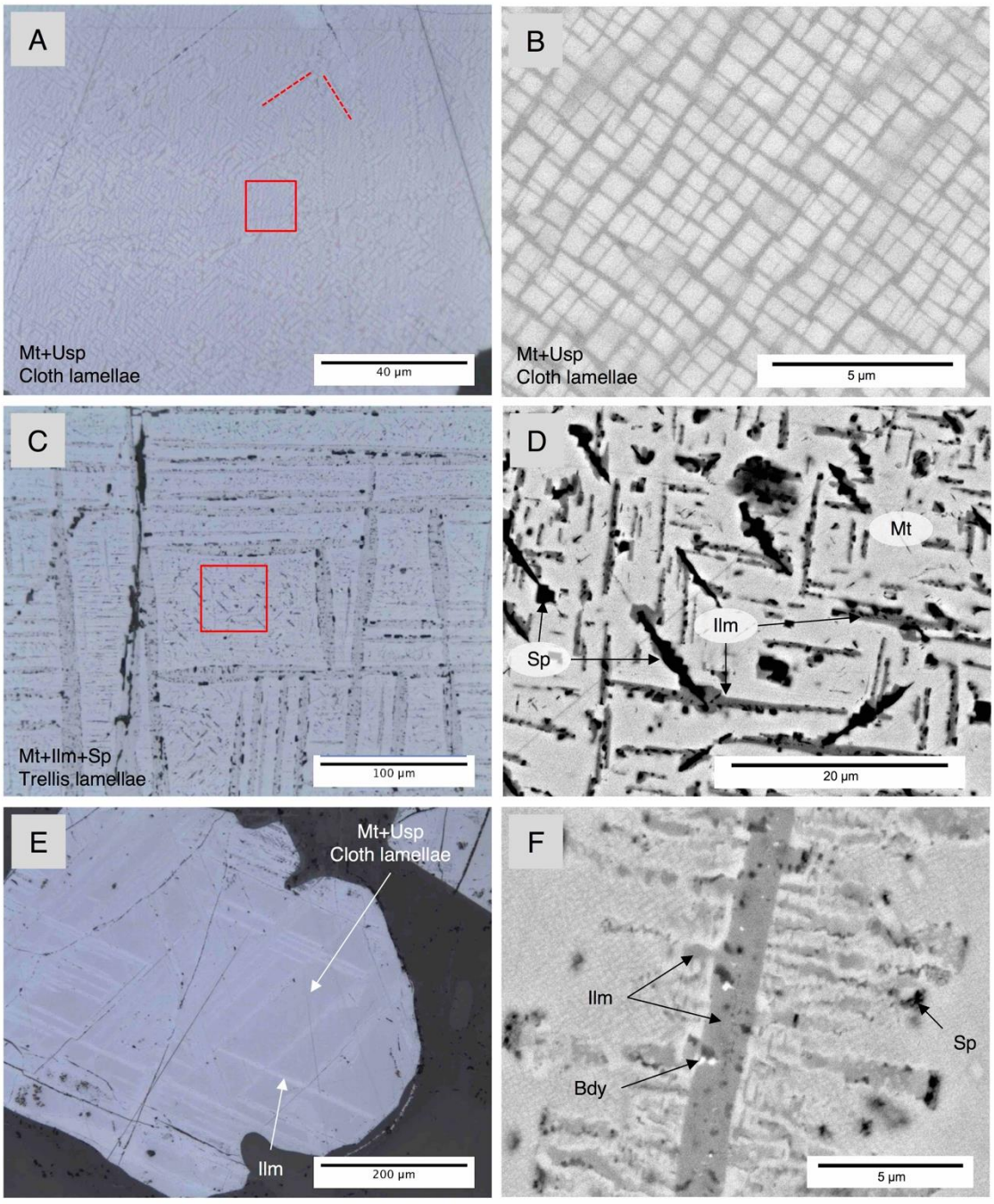
A
Mt+Usp
Cloth lamellae
40 µm
B
Mt+Usp
Cloth lamellae
5 µm
C
Mt+Ilm+Sp
Trellis lamellae
100 µm
D
Mt
Ilm
Sp
20 µm
E
Mt+Usp
Cloth lamellae
Ilm
200 µm
F
Ilm
Sp
Bdy
5 µm

Figure 3.7 (A) Reflected-light image of cloth-textured Fe-Ti oxide intergrowth illustrating the ultrafine ulvöspinel cloth lamellae. (B) High-magnification backscatter electron (BSE) image of cloth-textured Fe-Ti oxide intergrowth illustrating the ultrafine ulvöspinel cloth lamellae. (C) Reflected-light image of trellis-textured Fe-Ti oxide intergrowth with fine and thick trellis lamellae of ilmenite and spinel. (D) BSE image of trellis-textured Fe-Ti oxide intergrowth with fine and thick trellis lamellae of ilmenite and spinel. (E) Reflected-light image of thick trellis lamellae in a cloth-textured Fe-Ti oxide intergrowth. Note the halos surrounding the thick trellis that are brighter than the surrounding cloth-textured intergrowth. Some trellis lamellae extend outwards from fractures in the Fe-Ti oxide intergrowth, extend inwards from the grain boundaries, or are present in the central portion of the intergrowth. (F) High-magnification BSE image of thick trellis lamellae in a cloth-textured Fe-Ti oxide intergrowth. The halo surrounding the thick trellis lamellae contains stringers of ilmenite that extend outwards from the lamellae. Spinel are concentrated at the ends of these stringers. Nano-scale, anhedral grains of baddeleyite occur within the trellis lamellae. Mt = magnetite, usp = ulvöspinel, ilm = ilmenite, bdy = baddeleyite.

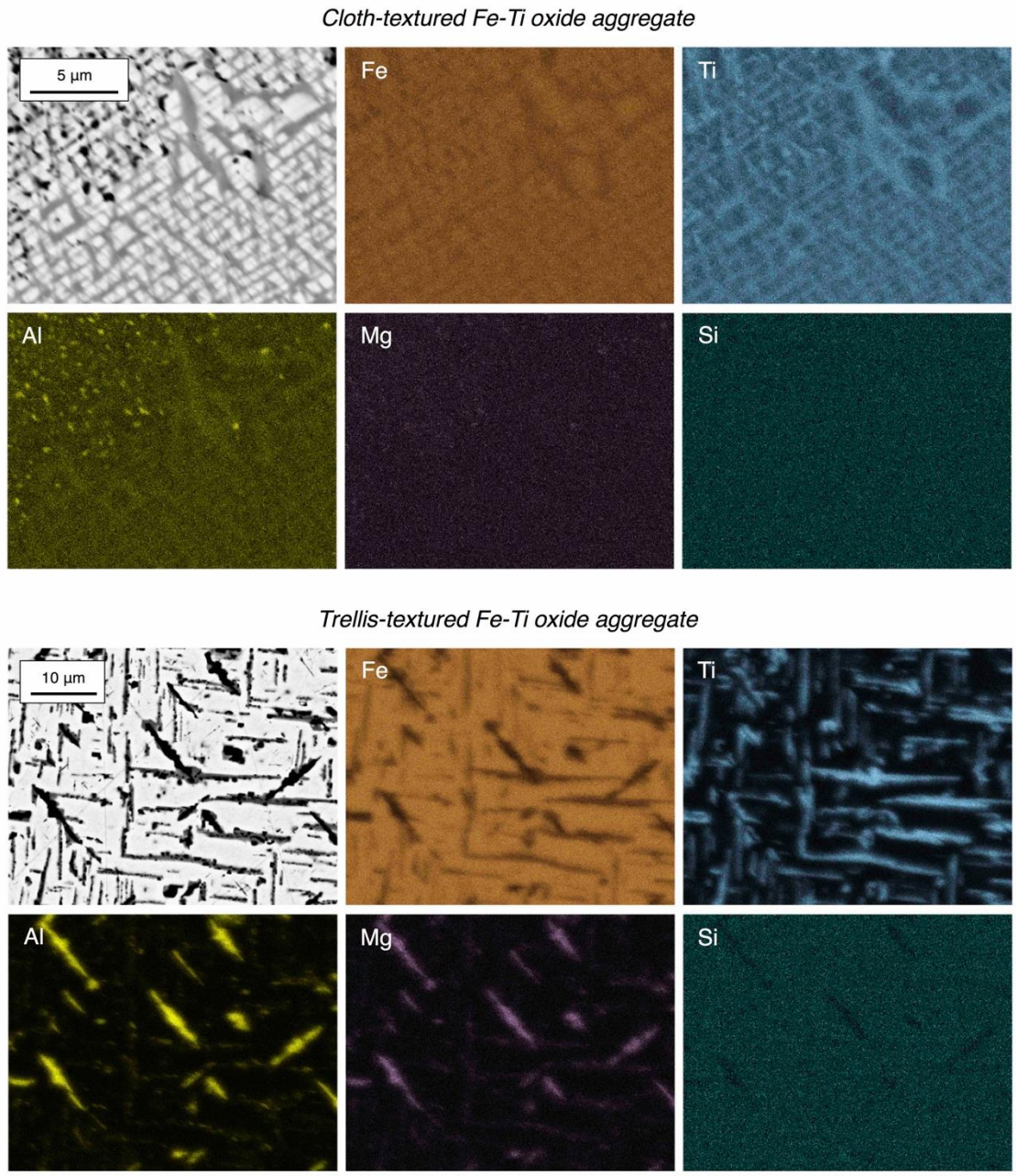

Figure 3.8 Fe-Ti-Al-Mg-Si energy-dispersive spectroscopy (EDS) maps of cloth- and trellis-textured Fe-Ti oxide intergrowths.

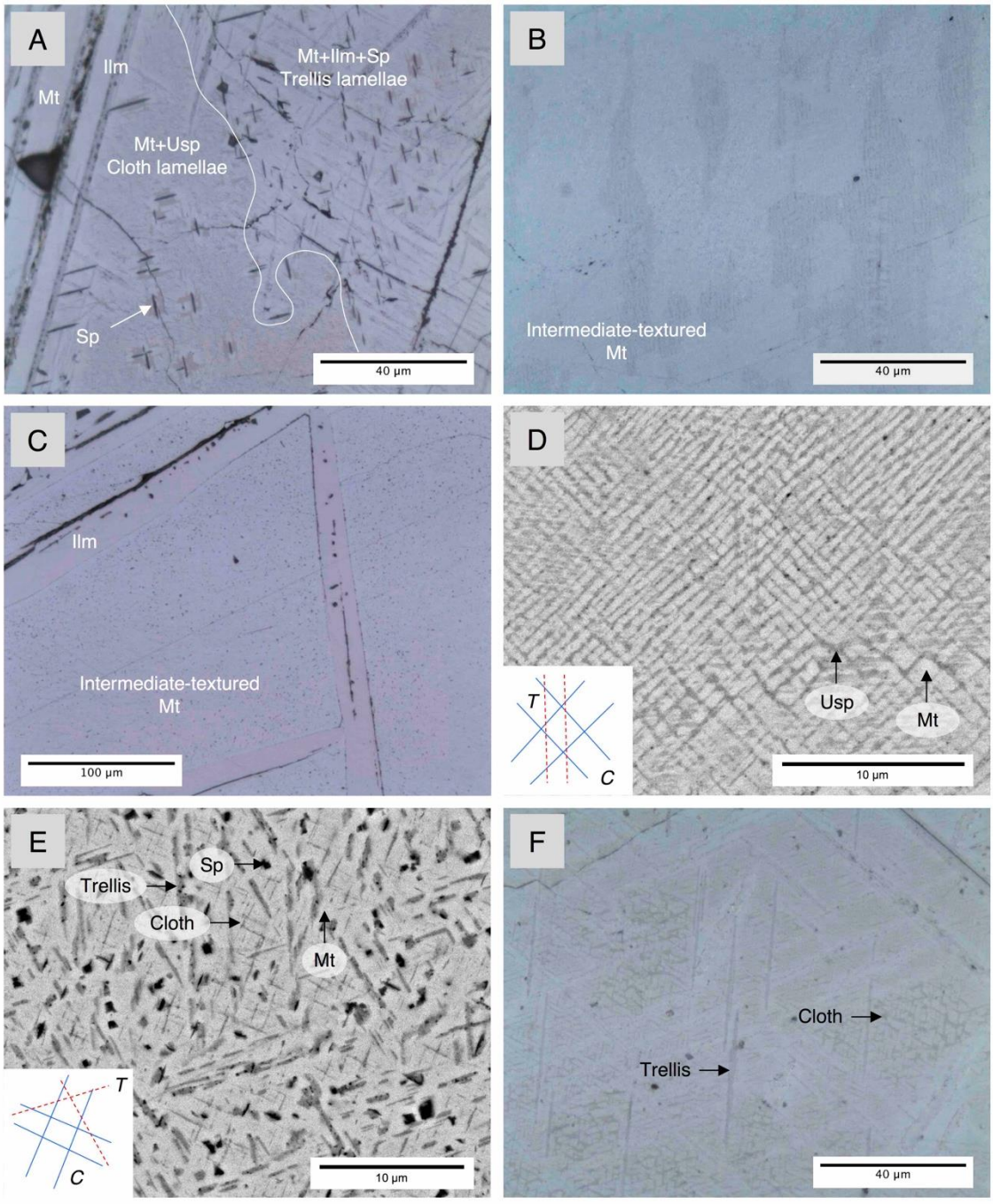
A
Ilm
Mt
Mt+Ilm+Sp
Trellis lamellae
Mt+Usp
Cloth lamellae
Sp
40 µm
B
Intermediate-textured
Mt
40 µm
C
Ilm
Intermediate-textured
Mt
100 µm
D
T
C
Usp
Mt
10 µm
E
Trellis
Sp
Cloth
Mt
T
C
10 µm
F
Cloth
Trellis
40 µm

Figure 3.9 (A) Reflected-light image illustrating the coexistence of cloth- and trellis-textured Fe-Ti oxide intergrowth in association with bladed spinel. The magnetite surrounding the bladed spinel are typically free of cloth lamellae. The cloth lamellae are thicker surrounding this magnetite compared to areas without spinel. (B) Reflected-light image of intermediate-textured Fe-Ti oxide intergrowth (cloth-like). The darker areas of the intergrowth appear to have a cloth texture, whereas the brighter areas appear homogenous in reflected light. (C) Reflected-light image of intermediate-textured Fe-Ti oxide intergrowth (trellis-like) with thick trellis lamellae. The Fe-Ti oxide intergrowth appears homogenous with respect to fine cloth or trellis lamellae under reflected light. (D) High-magnification BSE image of intermediate-textured Fe-Ti oxide intergrowth (cloth-like) with an irregular cloth texture. The inset diagram illustrates the orientation of the cloth lamellae (blue lines) and a set of linear features that cut obliquely across the cloth network (red dashed lines). (E) High-magnification BSE image illustrating the coexistence of cloth and fine trellis lamellae in an intermediate-textured Fe-Ti oxide intergrowth (trellis-like) that appears homogenous in reflected light. The inset diagram illustrates the orientation of the cloth lamellae (blue lines) and trellis lamellae that cut obliquely across the cloth network (red dashed lines). (F) Reflected-light image illustrating the coexistence of cloth and trellis lamellae in an intermediate-textured Fe-Ti oxide intergrowth. Unlike in (E), this mixture of cloth and trellis is readily visible under reflected light. Mt = magnetite, usp = ulvöspinel, ilm = ilmenite.

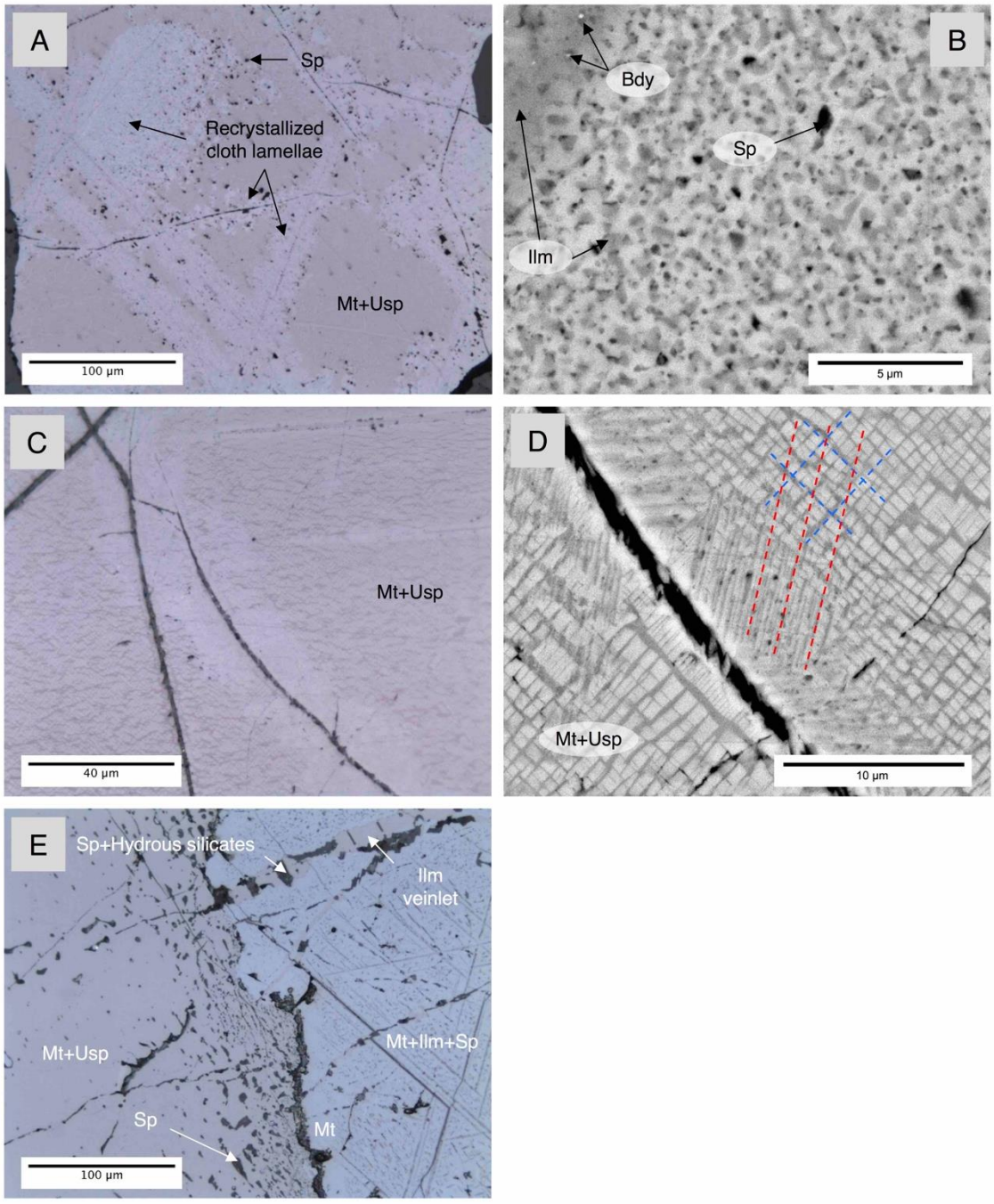
A
Sp
Recrystallized
cloth lamellae
Mt+Usp
100 µm
B
Bdy
Sp
Ilm
5 µm
C
Mt+Usp
40 µm
D
Mt+Usp
10 µm
E
Sp+Hydrous silicates
Ilm
veinlet
Mt+Usp
Mt+Ilm+Sp
Sp
Mt
100 µm

Figure 3.10 (A) Reflected-light image illustrating a cloth-textured Fe-Ti oxide intergrowth that has been recrystallized along grain boundaries, fractures, thick trellis lamellae, and in patches that extend from the lamellae. (B) High-magnification BSE image of a recrystallized cloth-textured Fe-Ti oxide intergrowth. The recrystallized portions contain anhedral blebs of ilmenite and spinel. (C) Reflected-light image showing fractures that cut across a cloth-textured Fe-Ti oxide intergrowth. Around these fractures, a halo is present that appears brighter in reflected light and homogenous with respect to lamellae. (D) High-magnification BSE image of one of these halos illustrating trellis-like lamellae that extend outwards from the fracture and cut obliquely across the cloth network. (E) Reflected-light image of a trellis-textured Fe-Ti oxide intergrowth and an associated ilmenite crystal. Proximal to the ilmenite crystal, trellis lamellae are absent. A spinel-rich rim occurs along the edge of the ilmenite crystal. A veinlet of ilmenite associated with hydrous silicates and spinel crosscuts the trellis-texture intergrowth and intersects the ilmenite crystal. Mt = magnetite, usp = ulvöspinel, ilm = ilmenite, bdy = baddeleyite.

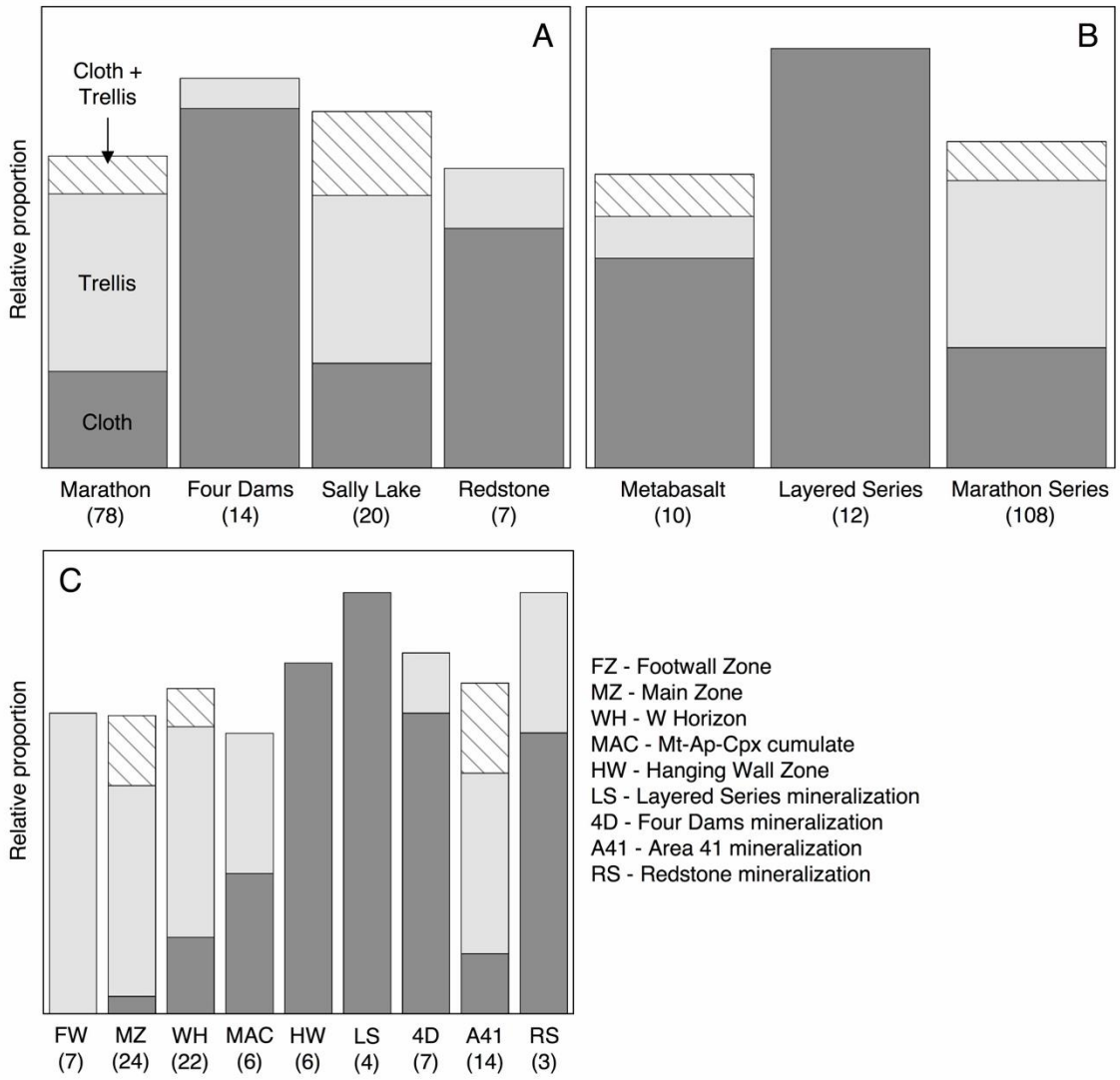

Figure 3.11 Distribution of cloth- and trellis-textured Fe-Ti oxide intergrowths in the various (A) areas, (B) rock series, and (C) mineralized occurrences in the Eastern Gabbro. The numbers in brackets represent the number of thin sections used from each category.

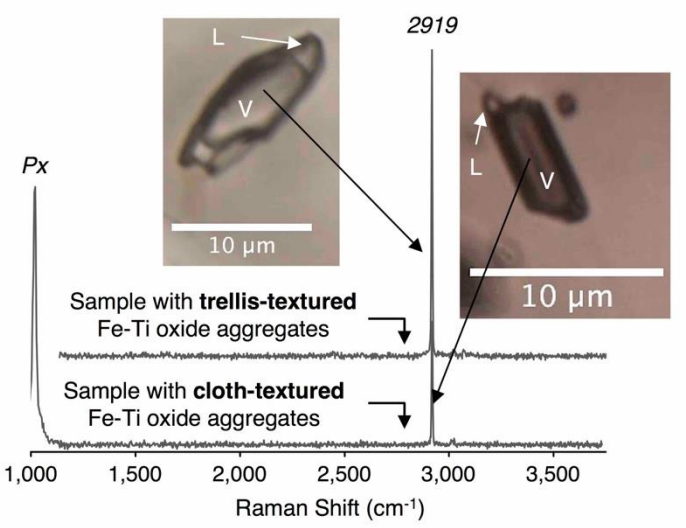

Figure 3.12 Raman spectra of pyroxene-hosted vapor-rich fluid inclusions in thin sections that contain cloth- or trellis-textured Fe-Ti oxide intergrowths.

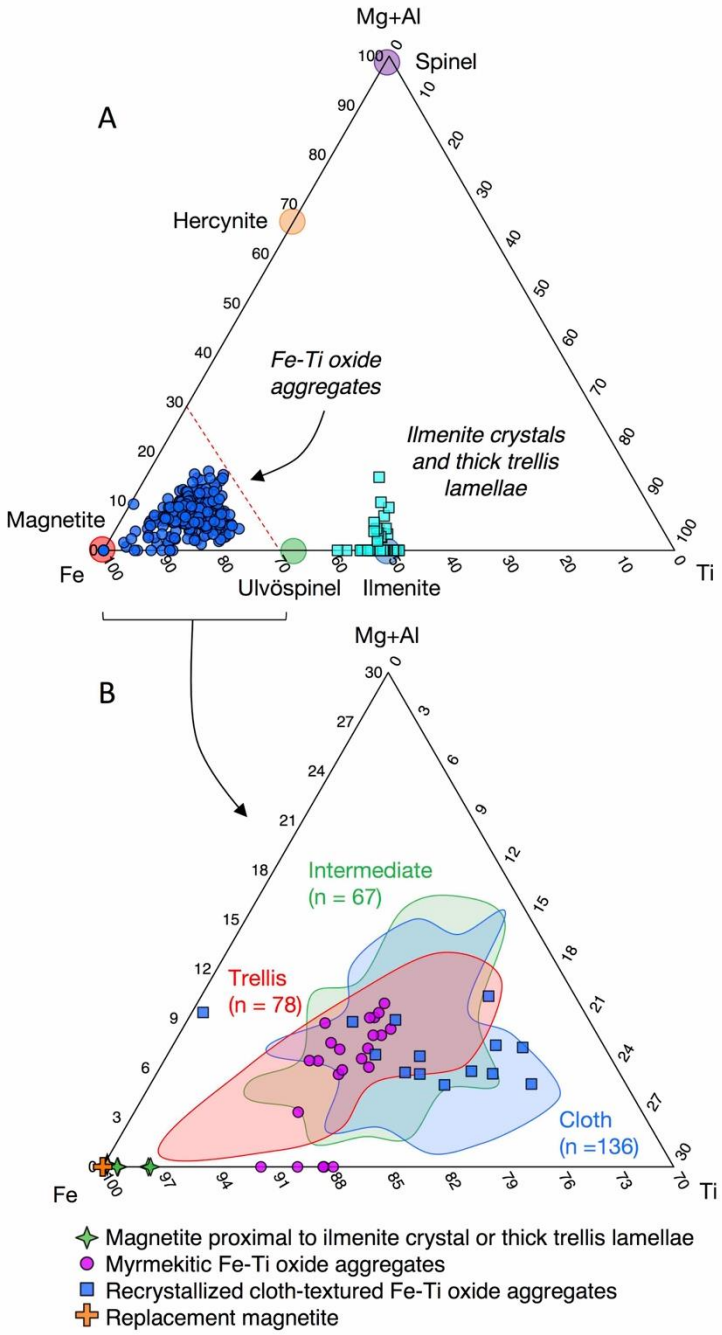

Figure 3.13 Ternary diagrams showing the relative proportions of bulk Fe_{tot}, Ti, and Al+Mg (at. %) in the various Fe-Ti oxide intergrowths and ilmenite crystals and lamellae. Ideal compositions for magnetite, ulvöspinel, ilmenite, hercynite, and spinel are labelled. (A) Complete ternary diagram showing the overall bulk major-element composition of Fe-Ti oxide intergrowths, ilmenite crystals, and thick trellis lamellae. (B) Magnified portion of the above ternary (red dashed line) comparing the bulk major-element composition of cloth-, intermediate-, and trellis-textured Fe-Ti oxide intergrowths, as well as replacement magnetite, myrmekitic Fe-Ti oxide intergrowths, recrystallized patches in cloth-textured Fe-Ti oxide intergrowths, and magnetite adjacent to thick trellis lamellae.

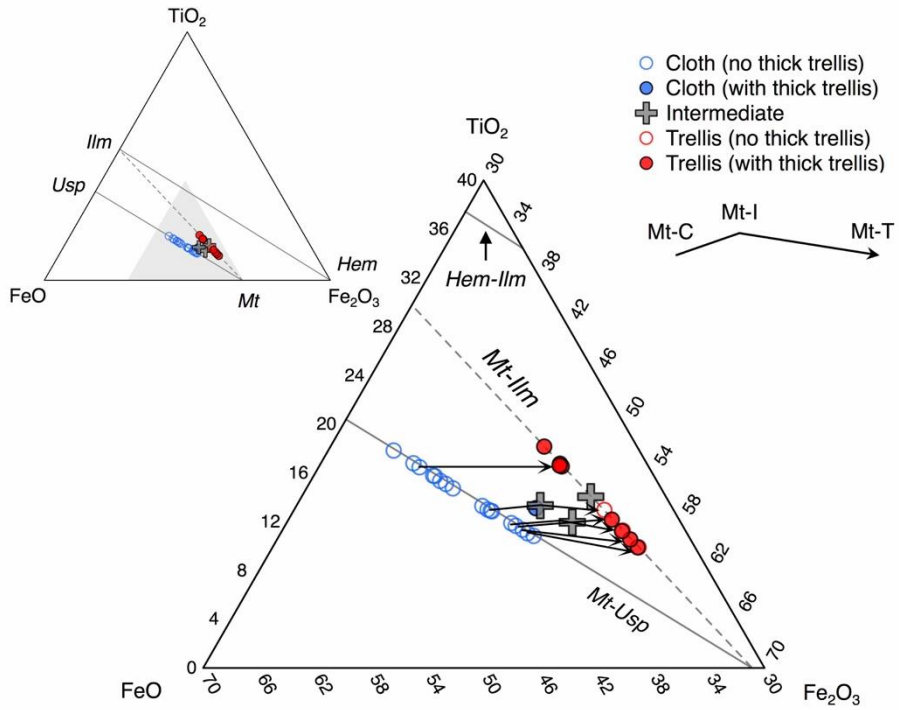

Figure 3.14 Ternary diagram showing the relative proportions of bulk Fe^{2+}, Fe^{3+}, and Ti (wt. %) in cloth-, intermediate-, and trellis-textured Fe-Ti oxide intergrowths. Each arrow represents Fe-Ti oxides from a single thin section, with the start of the arrow representing the average composition of cloth-textured intergrowths and the end of the arrow representing trellis-textured intergrowths. Solid solutions between magnetite-ulvöspinel and ilmenite-hematite are included. A hypothetical solid solution between magnetite and ilmenite is illustrated by the dashed line. Mt = magnetite, usp = ulvöspinel, ilm = ilmenite.

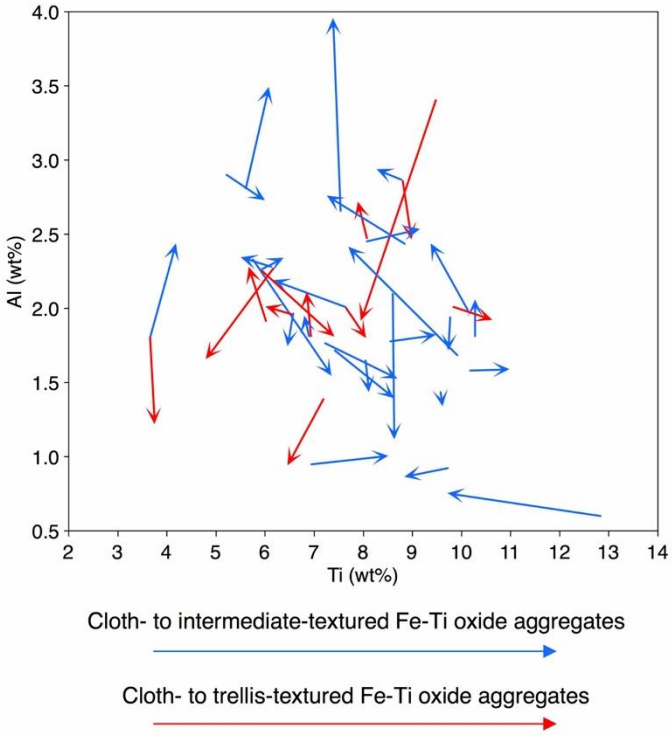

Figure 3.15 Binary vector diagram illustrating the difference in bulk Ti (wt. %) and Al (wt. %) between cloth-, intermediate-, and trellis-textured Fe-Ti oxide intergrowths within a single thin section. Each of the vectors represents a single thin section, with the start of the arrow representing the composition of cloth-textured intergrowths and the end of the arrow representing trellis-textured intergrowths.

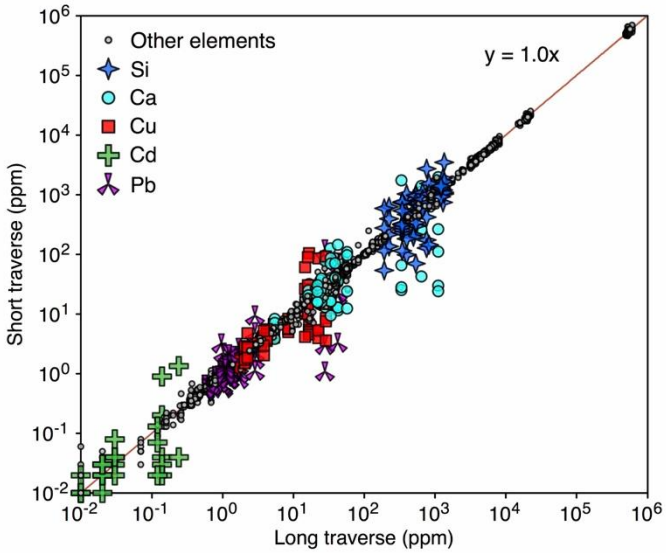

Figure 3.16 Binary diagram comparing trace-element concentrations (ppm) in cloth-textured Fe-Ti oxide intergrowths with thick trellis lamellae and trellis-textured Fe-Ti oxide intergrowths obtained by integrating 1-3 mm-long laser ablation raster analyses and sub-mm portions of these rasters, which mimic typical laser ablation traverse lengths. Note the 1:1 relationship between long and short traverse lengths for the majority of the elements of interest (grey symbols). The colored symbols represent elements that exhibit scatter about the 1:1 line.

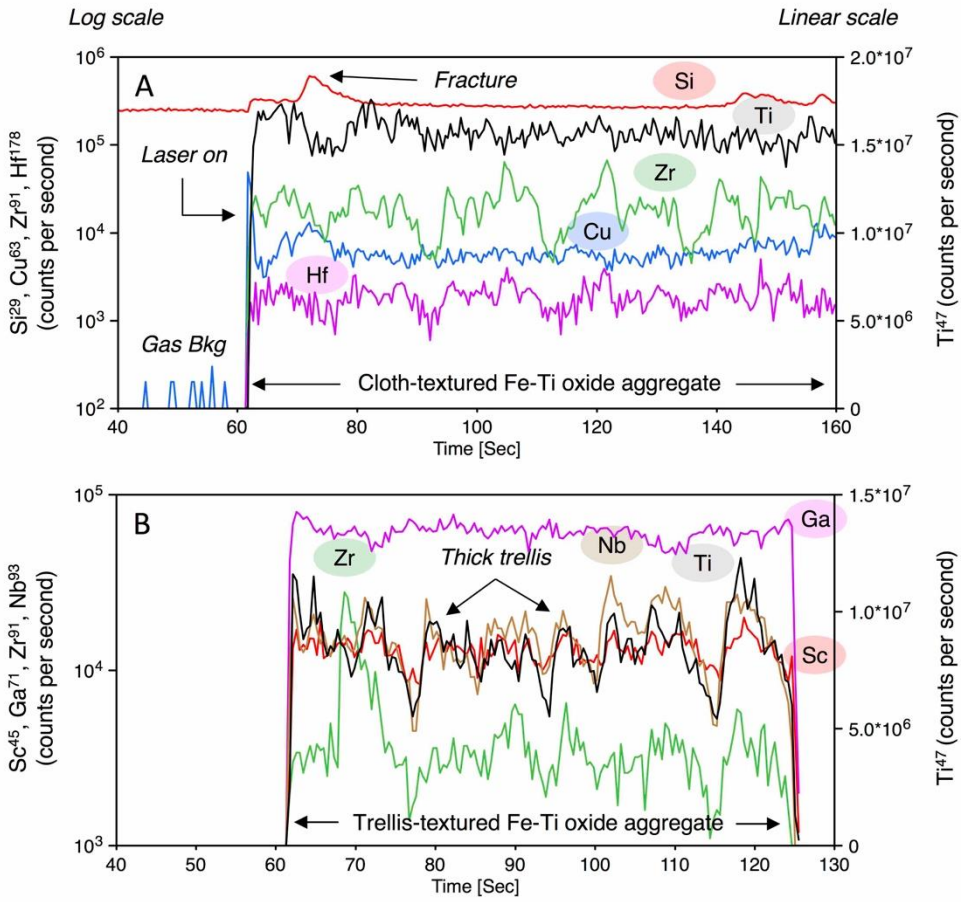

Figure 3.17 Laser ablation spectra for (A) a cloth-textured Fe-Ti oxide intergrowth and (B) a trellis-textured Fe-Ti oxide intergrowth. Note the logarithmic scale for the concentrations.

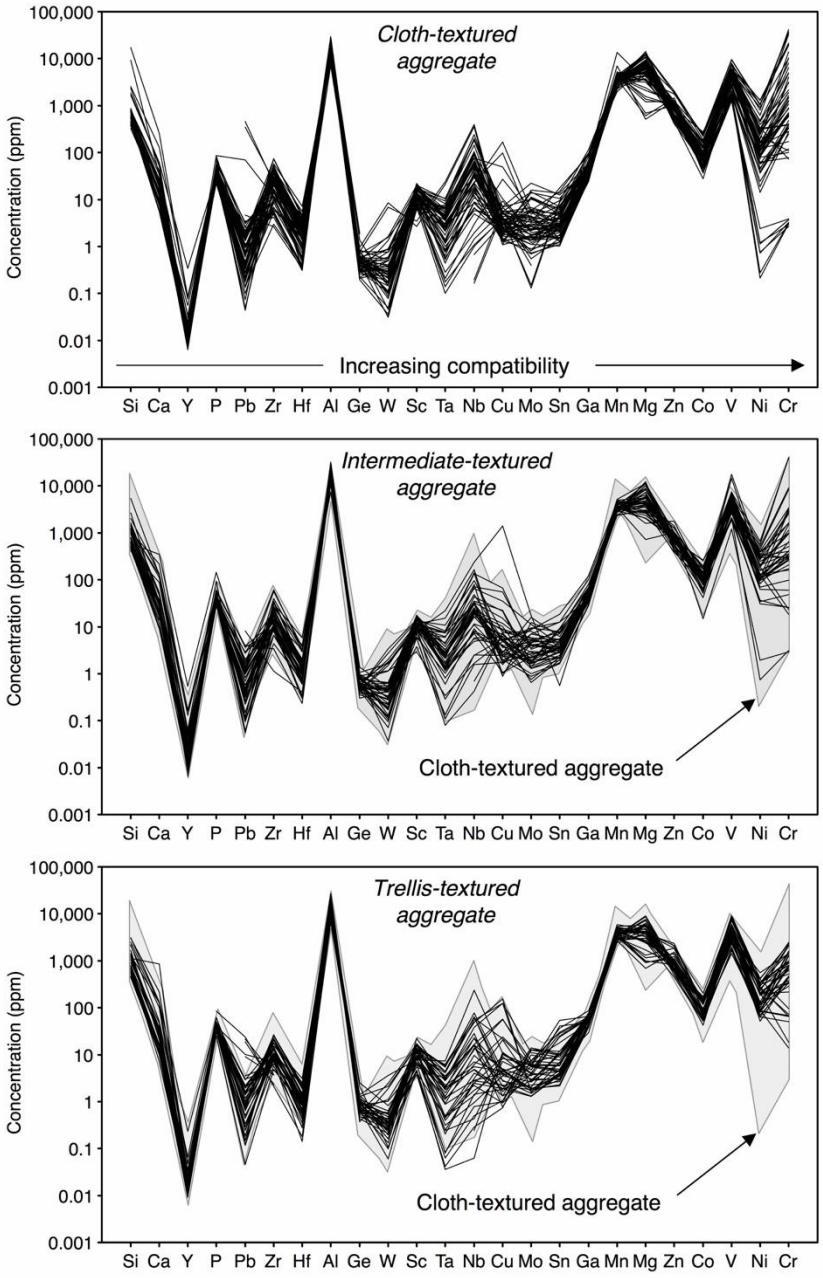

Figure 3.18 Spider diagrams illustrating the minor- to trace-element composition of (A) cloth-textured Fe-Ti oxide intergrowths, (B) intermediate-textured Fe-Ti oxide aggregates, and (C) trellis-textured Fe-Ti oxide intergrowths. The elements are listed in order of increasingly compatibility into magnetite. The grey field on (B) and (C) represents the composition of cloth-textured Fe-Ti oxide intergrowths.

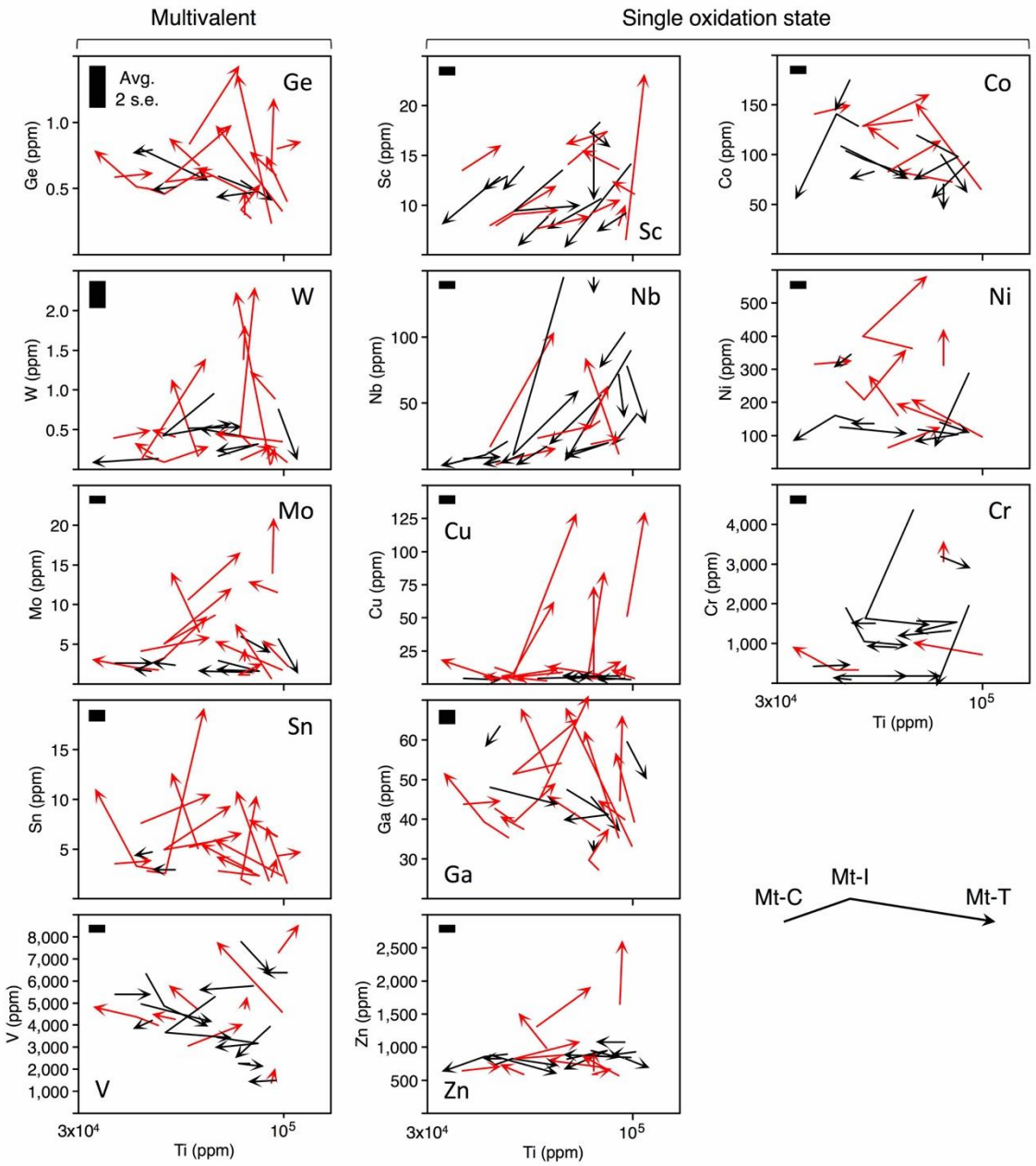

Figure 3.19 Binary vector diagrams illustrating the difference in composition between cloth-, intermediate-, and trellis-textured Fe-Ti oxide intergrowths within a single thin section. Each vector represents a single thin section. The start of the arrow represents the average composition of cloth-textured intergrowths within a single thin section and the end of the arrow represents the average composition of trellis-textured intergrowths within a single thin section. Red arrows denote the samples in which trellis-textured intergrowths are enriched in trace elements (y-axis) relative to cloth-textured intergrowths.

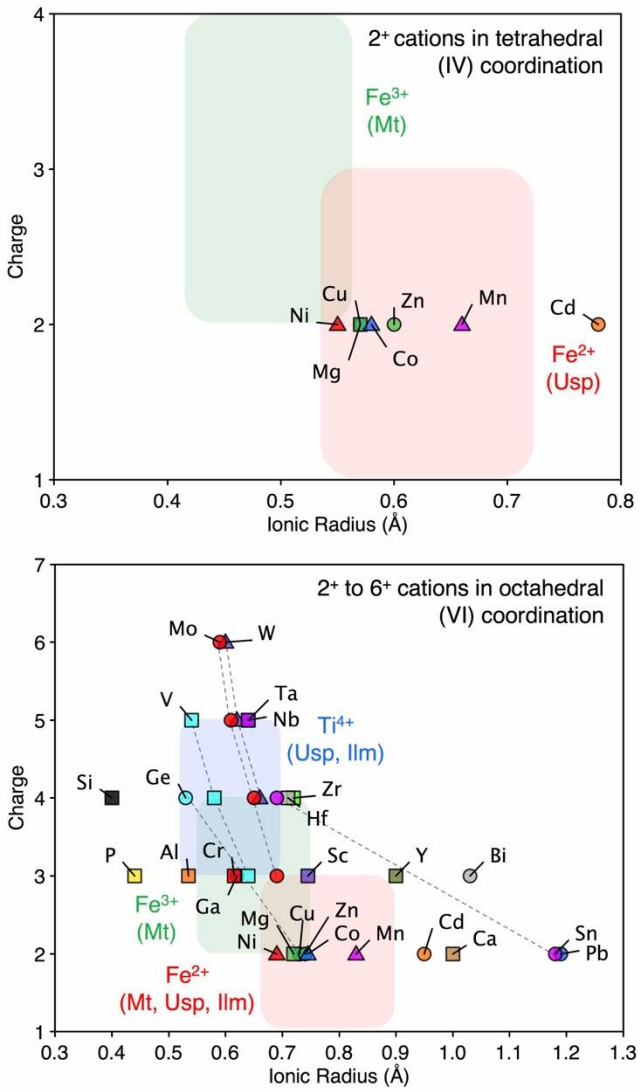

Figure 3.20 Binary diagram comparing the ionic radius and charge of the elements of interest to that of $^{IV}Fe^{2+}$, $^{VI}Fe^{2+}$, $^{IV}Fe^{3+}$, $^{VI}Fe^{3+}$, $^{VI}Ti^{4+}$, which are the building-blocks of magnetite, ulvöspinel, and ilmenite. Dashed lines connect the different valence states of multivalent elements. All ionic radii are from Shannon (1976).

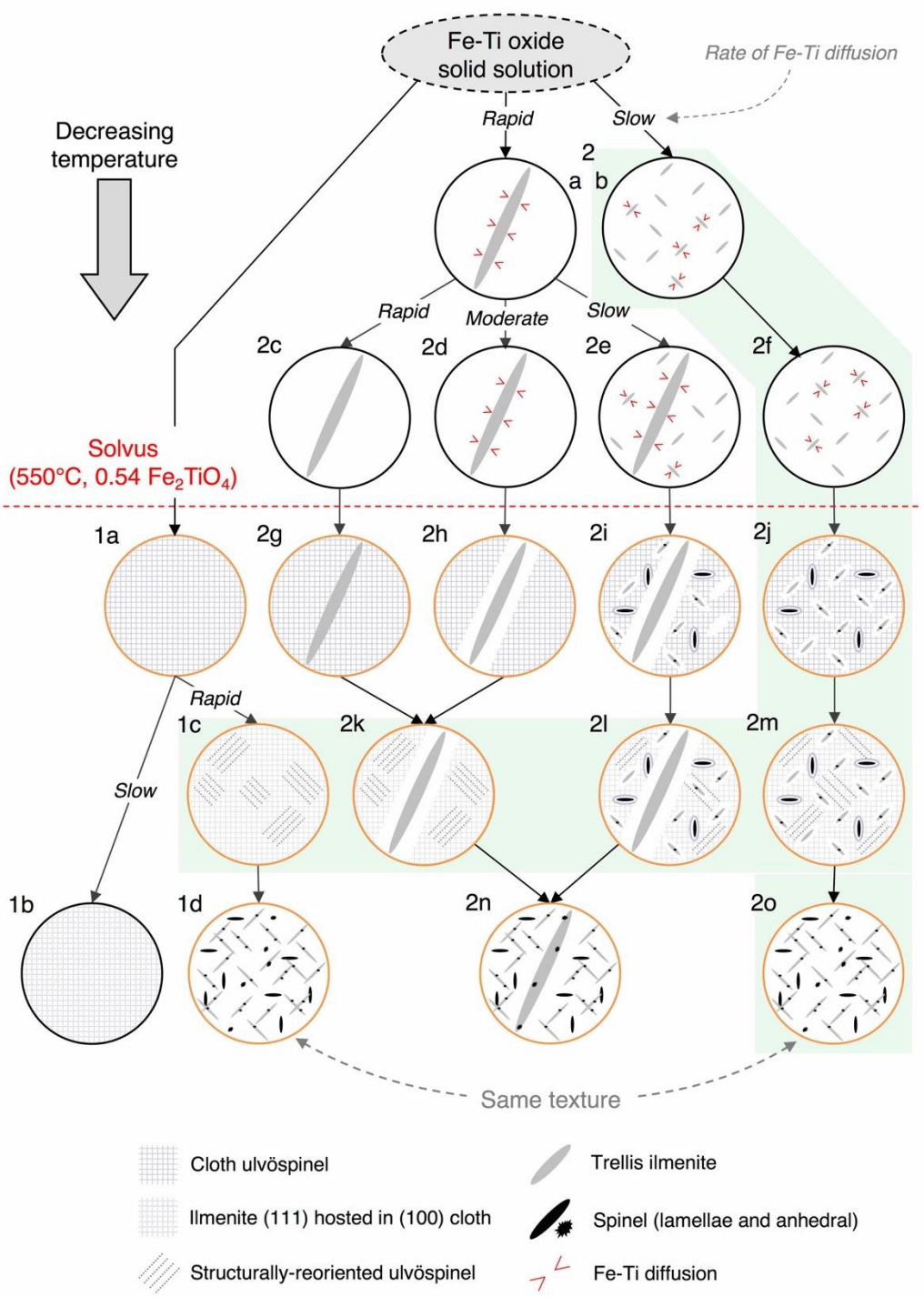
Fe-Ti oxide solid solution
Rate of Fe-Ti diffusion
Rapid
Slow
Decreasing temperature
2
a b
Rapid
Moderate
Slow
2c
2d
2e
2f
Solvus
(550°C, 0.54 Fe2TiO4)
1a
2g
2h
2i
2j
Rapid
1c
2k
2l
2m
Slow
1b
1d
2n
2o
Same texture
Cloth ulvöspinel
Ilmenite (111) hosted in (100) cloth
Structurally-reoriented ulvöspinel
Trellis ilmenite
Spinel (lamellae and anhedral)
Fe-Ti diffusion

Figure 3.21 Cartoon illustrating the variation in Fe-Ti oxide intergrowths developed as a result of supra- and subsolvus fluid-induced oxidation at variable rates of suprasolvus Fe-Ti diffusion (labels in italics, red arrows). The critical temperature of the magnetite-ulvöspinel solvus is 550°C at 0.54 Fe_2TiO_4 (Lilova et al., 2012). This diagram is a modification of figure 3 in Duchesne (1970). The illustrations in the orange circles denote the textures that were observed in the Eastern Gabbro. The illustrations highlighted in green denote those textures that were not described by Duchesne (1970), but were observed in the Fe-Ti oxides in Eastern Gabbro.

Table 3.1 Distribution of thin section samples throughout the Eastern Gabbro

Location	Mineralized zone/occurrence	Rock types	No. of thin sections
Marathon Cu-Pd deposit	Footwall Zone	TDLG	11
	Main Zone	TDLG	29
	W Horizon	TDLG, apatitic clinopyroxenite	26
	Mgt-Ap-Cpx cumulate	TDLG, apatitic clinopyroxenite, oxide melatroctolite	6
	Unmineralized	TDLG, apatitic (olivine) clinopyroxenite, oxide melatroctolite, metabasalt	13
North of the Marathon deposit	Four Dams	Apatitic (olivine) clinopyroxenite, apatitic wehrlite, oxide melatroctolite, metabasalt	8
	Area 41	TDLG, apatitic (olivine) clinpyroxenite, feldspathic clinopyroxenite, oxide melatroctolite, metabasalt	15
	Redstone	TDLG, oxide melatroctolite	3
	Layered Series mineralization	Oxide augite melatroctolite, apatitic olivine clinpyroxenite	4
	Unmineralized	TDLG, olivine gabbro, apatitic clinopyroxenite, feldspathic clinopyroxenite, oxide (augite) melatroctolite	13

**TDLG = Two Duck Lake gabbro*

Table 3.2 Bulk major-element composition of cloth-, intermediate-, and trellis-textured Fe-Ti oxide intergrowths

Fe-Ti oxide intergrowth	Fe (wt. %)			Ti (wt. %)			Mg (wt. %)			Al (wt. %)		
	Avg.	*Min.*	*Max.*	*Avg.*	*Min.*	*Max.*	*Avg.*	*Min.*	*Max.*	*Avg.*	*Min.*	*Max.*
Cloth-textured (n = 136)	63	56	69	9	4	14	1	n.d.	2	2	n.d.	4
Intermediate-textured (n = 67)	64	54	70	8	4	12	1	n.d.	2	2	1	4
Trellis-textured (n = 78)	64	54	74	7	2	11	1	n.d.	2	2	n.d.	3

**n = number of analyses n.d. = not detected*

Table 3.3 Bulk trace-element composition of cloth-, intermediate-, and trellis-textured Fe-Ti oxide intergrowths

	Fe-Ti oxide intergrowth								
	Cloth-textured (n = 63)			Intermediate-textured (n = 46)			Trellis-textured (n = 41)		
ppm	*Avg.*	*Min.*	*Max.*	*Avg.*	*Min.*	*Max.*	*Avg.*	*Min.*	*Max.*
Si	1300	< 30	17000	1200	< 20	12000	1800	< 30	22000
Ca	30	< 4	260	50	< 5	350	70	< 5	860
Y	0.03	< 0.002	0.4	0.04	< 0.002	0.5	0.03	< 0.002	0.2
P	40	< 2	90	40	< 2	150	40	< 1.7	80
Pb	20	0.04	460	1	0.06	8	3	0.05	20
Zr	30	3	70	20	1	60	10	2	30
Hf	2	< 0.005	7	2	0.2	6	1	< 0.005	3
Al	18000	7200	29000	18000	7500	32000	16000	6700	27000
Ge	0.5	< 0.08	2	1	< 0.07	1	0.9	< 0.08	3
W	0.6	< 0.004	9	1	< 0.004	3	0.6	< 0.004	4
Sc	10	< 0.04	20	10	3	20	10	< 0.03	20
Ta	4	< 0.001	20	4	< 0.001	20	2	< 0.001	7
Nb	60	0.2	400	40	0.4	240	20	< 0.001	240
Cu	10	1	170	40	0.9	1400	20	0.7	150
Mo	4	0.1	20	5	0.7	20	5	1	10
Sn	4	< 0.07	20	5	0.6	20	10	2	50
Ga	50	20	120	50	30	120	60	30	90
Mn	3800	2000	14000	3400	2300	5200	3800	2400	5900
Mg	6400	510	14000	5500	730	1200	4200	680	9000

Table 3.3 Continue

	Fe-Ti oxide intergrowth								
	Cloth-textured (n = 63)			Intermediate-textured (n = 46)			Trellis-textured (n = 41)		
ppm	*Avg.*	*Min.*	*Max.*	*Avg.*	*Min.*	*Max.*	*Avg.*	*Min.*	*Max.*
Zn	900	410	100	810	390	1800	940	450	2300
Co	100	30	270	110	20	260	100	40	200
V	4200	1300	9600	4700	1200	18000	4300	1400	9300
Ni	250	0.2	1300	200	0.7	650	200	50	560
Cr	5000	< 0.5	42000	2900	3	40000	840	< 0.5	2400

n = number of analyses Less than values represent minimum detection limits

Chapter 4

Oxide mineralogy and trace-element chemistry as an index to magma evolution and Marathon-type mineralization in the Eastern Gabbro of the Coldwell Complex, Ontario

4.1 Introduction

The past decade has seen a growing interest in the use of magnetite and ilmenite chemistry for petrogenesis (Dare et al., 2014b; Nadoll et al., 2014). The foundation for the use of magnetite chemistry, or the chemistry of any magmatic mineral, as a petrogenetic tool is an understanding that i) mineral chemistry is a reflection of melt chemistry and ii) the chemistry of a mineral will vary systematically during fractional crystallization of a silicate or sulfide melt. Dare et al. (2014b) summarized the variations expected in the composition of magnetite as a function of melt fractionation, noting that magnetite that crystallized from a primitive melt will be enriched in magnetite-compatible elements (e.g., Cr, Ni, V, Co, Mg) and depleted in magnetite-incompatible elements (e.g., Zn, Ga, HFSE, Sn). Conversely, magnetite that crystallized from an evolved melt will be depleted in compatible elements and enriched in incompatible elements. Much of the work that has been done pertaining to the petrogenesis of mineral deposits has focused on characterizing variations in the most compatible elements into magnetite, namely V and Cr. This was done in an effort to identify primitive magma injection events, magma mixing, and contamination, which can be identified by deviations away from the variations expected by these elements due to fractional crystallization (McCarthy et al., 1985; e.g., McCarthy and Cawthorn, 1983; Namur et al., 2010; Tegner et al., 2006). Very few studies, however, have incorporated multiple compatible and incompatible elements in their interpretations. The use of both compatible and incompatible elements is critical for characterizing magmatic processes, such as fractionation, as they should behave coherently during these processes (Dare et al., 2014b, 2012).

The use of indicator minerals for mineral exploration is not a new concept, and there has recently been an increase in the characterization of Fe-Ti oxide chemistry for potential use in exploration (Boutroy et al., 2014; Dare et al., 2014a; Dupuis and Beaudoin, 2011; Rusk et al., 2009; Ward et al., 2018). Many studies have characterized oxide chemistry in both barren and mineralized rocks, as well as in different styles of mineralization. Dare et al. (2014a) characterized the chemistry of magnetite from a variety of Ni-Cu-platinum group element (PGE) deposits and barren rocks and found that Ni is depleted in magnetite hosted in the mineralized rocks. Magnetite with high Mn/Ti were deemed to be a good proxy for mineralized rock, compared to unmineralized rock, in iron oxide copper gold (IOCG) deposits (Carew et al., 2006; Rusk et al., 2009). Singoyi et al. (2006) and Kamvong et al. (2007) used the Sn/Ga and Al/Co content of magnetite to distinguish magnetite from volcanogenic massive sulfide (VMS), skarn, IOCG, and Pb-Zn deposits. Nadoll et al. (2014, 2012, 2009) identified a number of geochemical differences in magnetite from different hydrothermal deposits in the Mesoproterozoic Belt Supergroup, including Ag-Pb-Zn and sediment-hosted Cu-Ag deposits. Dupuis and Beaudoin (2011) devised a series of discrimination diagrams (e.g., Ni+Cr vs. Si+Mg) to distinguish low-Ti magnetite from a variety of deposits, such as Ni-Cu, VMS, and IOCG. The Ni+Cu vs. Si+Mg diagram was later verified by Boutroy et al. (2014), who compared the composition of primary magnetite crystallized from a sulfide liquid and secondary magnetite from a variety of Ni-Cu-PGE deposits. Studies such as these are becoming increasingly more important as the focus of exploration shifts from surface deposits to deeply buried deposits, which require novel approaches for their discovery.

The aforementioned studies characterized the chemistry of oxides from selected samples that represent end-members with respect to magma evolution (e.g., primitive vs. evolved melts) and mineralization. Although studies such as these are required in order to understand how oxide chemistry varies as a result of different magmatic processes, the results of these studies have not been extensively applied to characterize, in detail, the magmatic evolution of complex igneous suites that formed through multiple batches of magma, and which are variably mineralized.

The Eastern Gabbro is a composite pluton that was emplaced along the eastern and northern margins of the 1.1 Ga Coldwell Complex (Good et al., 2015). It comprises three mafic-ultramafic rock series, which, in order of emplacement, are metabasalt, Layered Series, and Marathon Series. The Marathon Series is host to all of the Cu and Pd mineralization in the Eastern Gabbro and is dominated by the Two Duck Lake gabbro (TDLG), but also hosts a number of magnetite-apatite-clinopyroxene-rich rocks, all of which are thought to be co-genetic (Good et al., 2015). The petrogenetic relationship among the various rock series is still debated (e.g., Good et al., 2015; Shahabi Far, 2016; Cao, 2017) – did they form from successive batches of magma that originated from a single source, did they crystallize from magma batches that were variably-contaminated at depth or during emplacement, or did each of the rock series crystallize from magmas that originated from distinct sources? The model of Good et al. (2015), which is based entirely on whole-rock compositional data (e.g., U, Th, Tb/Yb, Zr/Hf), suggests that the metabasalt, Layered Series, and Marathon Series each formed from magmas that originated from distinct sources. Use of whole-rock chemistry presents problems, however, as the rocks of the Eastern Gabbro are cumulates, such that whole-rock analyses do not represent bulk magma compositions. In situations such as these, the trace-element chemistry of minerals is a better proxy for magma composition as the former reflects magma composition at the time that the mineral crystallized, even if the rocks are cumulates. For example, through integrating variations in plagioclase and pyroxene trace-element chemistry with variations in their texture, Shahabi Far (2016) noted that the Two Duck Lake gabbro could not have crystallized from a single batch of magma, but rather from multiple batches of compositionally-distinct magmas.

This contribution applies the foundational work of previous authors on the behavior of oxide chemistry with magma evolution and mineralization to the development of genetic models for complex igneous suites that are variably mineralized. The Eastern Gabbro represents a good example of such a system because it is composed of variably-mineralized rocks that crystallized from multiple batches of compositionally diverse magmas, which evolved to variable degrees (cf. Good et al., 2015; Shahabi Far, 2016; Cao, 2017). This contribution aims to 1) develop a genetic model for the formation of the Eastern Gabbro

and the various mineralized zones that it hosts, and 2) develop exploration tools for Marathon-type Cu-PGE mineralization. The trace-element chemistry of Fe-Ti oxides hosted in mineralized and barren equivalents of the various rock types from each of the rock series is characterized to assess the following questions: i) did the metabasalt, Layered Series, and Marathon Series crystallize from magmas that originated from a single source or different sources?; ii) how are the rock types of the Marathon Series related to each other?; iii) did the Footwall Zone, Main Zone, and W Horizon, which are all hosted by Marathon Series, crystallize from magmas that originated from the same source?; iv) can Fe-Ti oxide chemistry be used as an indicator of mineralization?

4.2 Geological Setting

4.2.1 Geology of the Coldwell Complex and the Eastern Gabbro

The Eastern Gabbro is a composite pluton that wraps around the northern and eastern margins of the Coldwell Complex, an alkaline pluton that intruded into the North American Midcontinent Rift at circa 1.1 Ga (Good et al., 2015) (Fig. 4.1). The Eastern Gabbro is subdivided into three rock series, which are, from oldest to youngest, metabasalt, Layered Series, and Marathon Series (Good et al., 2015) (Fig. 4.2). The current model suggests that these rock series originated from distinct sources according to whole-rock chemistry (e.g., U, Th, Nb/Ta, Zr/Hf) (Good et al., 2015).

The metabasalts are a package of homogenous and equigranular basalts that were metamorphosed to hornfels grade by the later Layered and Marathon Series magmas. They make up 20 to 30% of the Eastern Gabbro, but lack mineralization. More recently, several units within the metbasalt have been characterized based on variations in trace-element composition (e.g., Nb, Zr) (Good and Dunning, 2018). The Layered Series makes up the majority of the Eastern Gabbro and sits stratigraphically above the metabasalts. It is texturally and compositionally homogenous along the length of the Eastern Gabbro, with an average composition of olivine gabbro. More specifically, the Layered Series consists of two dominant rock types, which include olivine gabbro ± modal layering defined by

variations in the proportion of plagioclase and pyroxene and oxide augite melatroctolite. Secondary Cu mineralization occurs in this series in association with albite and actinolite alteration, but it lacks PGE mineralization. The Marathon Series is the youngest intrusive event and is defined as including all of the mafic to ultramafic rocks that host Cu-PGE mineralization, including the Marathon Cu-Pd deposit. At the Marathon deposit, the Marathon Series is dominated by the Two Duck Lake gabbro (TDLG), a coarse to pegmatitic gabbro that displays an ophitic to subophitic texture. The TDLG intruded the metabasalt package just above the contact with Archean rocks, which, in the vicinity of the Marathon deposit, comprise intermediate pyroclastic metavolcanic rocks. This series also contains a layered troctolite sill, a marker horizon that overlies the Main mineralized zone, and sill- to pod-like bodies of oxide melatroctolite, apatitic clinopyroxenite, and apatitic olivine clinopyroxenite, which are spatially associated with the feeder channels of the Marathon deposit. The oxide melatroctolite has been subdivided into younger and older varieties according to crosscutting relationships. The older oxide melatroctolite is gradational with the Marathon Series gabbros and is thought to have been emplaced at a similar time as the TDLG. The younger oxide melatroctolite crosscuts the TDLG and the older oxide melatroctolite, but has gradational contacts with the pyroxenites. All of the rocks hosted within each of the rock series are thought to be genetically related based to their whole-rock compositions (Good et al., 2015).

4.2.2 Mineralization in the Eastern Gabbro

A number of Cu-PGE occurrences occur along the length of the Eastern Gabbro, the main occurrences being the Marathon Cu-Pd deposit on the eastern margin of the complex, and the Four Dams, Area 41, and Redstone showings, which are located northwest of the Marathon deposit on the northern contact of the Eastern Gabbro (Fig. 4.1). Most research to date has focused on characterizing and understanding the mineralizing processes at the Marathon Cu-PGE deposit (Dahl et al., 2001; Good et al., 2015; Good and Crocket, 1994; Ruthart, 2013; Shahabi Far et al., 2018; Watkinson and Ohnenstetter, 1992). Mineralization at Marathon occurs predominantly in three lenses, which, in stratigraphic order, are termed the Footwall Zone, Main Zone, and W Horizon (Fig. 4.3) (Good et al., 2015).

Mineralization also occurs in irregular sill- to pod-like bodies of oxide-apatite-rich rocks, termed magnetite-apatite-clinopyroxene cumulate. Sulfides consist of disseminated chalcopyrite and pyrrhotite with lesser bornite, cubanite, pentlandite, and pyrite. Sulfides in the Footwall, Main, and Hanging Wall Zones are generally interstitial to silicates and oxides, but also commonly occur intergrown with hydrous silicates. The W Horizon is distinct from these mineralized zones in three ways - it has a lower sulfide content, distinctly lower Cu/Pd, and sulfide assemblages dominated by chalcopyrite + bornite rather than chalcopyrite + pyrrhotite. The magnetite-apatite-clinopyroxene cumulates consist of predominantly chalcopyrite + pyrrhotite and have elevated PGE contents. Less work has been done to characterize the mineralization at Four Dams, Area 41, and Redstone. Most recently, Ames et al. (2016) and Good et al. (2017) characterized, in detail, the platinum group mineral (PGM) assemblages in Area 41. They noted that Area 41 has similar PGM to the Main Zone and W Horizon, but differ in that it also contains PGE-S-As group minerals, Pt-Fe alloys, and Pd-Ge group minerals. Sulfides at these occurrences are dominated by chalcopyrite, pyrrhotite, cubanite and minor bornite (McBride, 2015).

4.3 Sampling and analytical methods

Samples were selected down the length of 13 drill holes from the Marathon Cu-PGE deposit, Four Dams, Area 41, and Redstone, and encompass all of the rock types from each of the three rock series, all 9 of the mineralized occurrences, and barren rock. The majority of samples were selected from the Marathon Series as it hosts the largest variety of rock types and all of the mineralized occurrences. Where possible, different mineralized occurrences hosted within a single lithology were sampled in order to assess the effects of mineralization on oxide chemistry while minimizing the effects that the host rock may have had on the chemistry of the oxides. A representative population of 142 thin sections was used for detailed petrography and a subset of these for major- and trace-element chemistry.

Petrographic studies were done to characterize i) the relationship between oxides, silicates, and sulfides and ii) the various oxy-exsolution textures observed in magnetite. Semi-quantitative major-element chemistry of the oxides was obtained using an FEI Quanta 200

FEG scanning electron microscope (SEM) fitted with an EDAX energy-dispersive spectrometer (EDS) at the Advanced Microscopy and Materials Characterization Facility at the University of Windsor. Analyses were obtained under high vacuum and a voltage of 20 kV. Bulk area analyses, which incorporate both magnetite and exsolution lamellae, were performed to obtain the original composition of the homogenous, high temperature Fe-Ti oxide solid solution prior to any exsolution. Additionally, these bulk area analyses sample a volume of material that is more similar to laser ablation (LA) ICP-MS sampling volumes compared to EDS spot analyses. Major and minor elements (Mg, Al, Si, P, Ca, Ti, V, Cr, Mn, Fe, Co, Ni, Zn, Zr) were also obtained using a JEOL JXA-8530F field-emission electron microprobe (EPMA) at the Earth and Planetary Materials Analysis Laboratory at Western University to determine the accuracy of EDS analyses. Bulk analyses were performed at 15 kV, 50 nA, and spot sizes of 1 μm, 100 μm, and 300 μm. Calibration was achieved using various Astimex and Smithsonian mineral and pure element standards. Corrections were applied to account for overlaps on the Kα and Kβ peaks for V-Ti, Cr-V, Mn-Cr, and Fe-Co. Figure 4.4 illustrates the difference, in weight percent, of Mg, Al, Ti, Cr, Fe, and Mn in titanomagnetite, ilmenite, and end-member magnetite obtained by bulk EDS and EPMA analyses. With the exception of Fe, the difference in all of the elements is < 0.5 wt. %. Therefore, except for Fe, which is overestimated by ~ 6 wt. % by EDS, the major-element concentrations obtained by EDS are accurate and it was the principal method for major-element analysis.

The trace-element chemistry of the oxides was determined using an Agilent 7900 inductively-coupled plasma mass spectrometer coupled with a 193 nm excimer laser at the Element and Heavy Isotope Analytical Laboratory of the University of Windsor. The laser was operated at an energy of 1.5 mJ, repetition rate of 20 Hz, and spot size of 50 μm. A large spot size was used in order to incorporate both magnetite and lamellae, such that the analyses are representative of the homogenous, high temperature Fe-Ti oxide solid solution prior to exsolution. A total of 36 isotopes were measured (^{24}Mg, ^{27}Al, ^{29}Si, ^{31}P, ^{44}Ca, ^{45}Sc, ^{47}Ti, ^{51}V, ^{52}Cr, ^{55}Mn, ^{57}Fe, ^{59}Co, ^{60}Ni, ^{63}Cu, ^{66}Zn, ^{71}Ga, ^{74}Ge, ^{89}Y, ^{91}Zr, ^{92}Zr, ^{93}Nb, ^{95}Mo, ^{101}Ru, ^{103}Rh, ^{105}Pd, ^{111}Cd, ^{120}Sn, ^{178}Hf, ^{181}Ta, ^{182}W, ^{189}Os, ^{193}Ir, ^{195}Pt, ^{197}Au, ^{208}Pb, and ^{209}Bi). Two isotopes of Zr were analyzed to monitor for interferences of VAr on ^{91}Zr and

CrAr on ^{92}Zr. All analyses were referenced to GSE-1G, a synthetic basalt glass produced by the United States Geological Survey (USGS). Titanium was used as the internal standard as it occurs in high abundance in the Fe-Ti oxides from the Eastern Gabbro and can be measured accurately by EDS. The effect of traverse length on the representativeness of bulk magnetite (pre-exsolution) trace-element composition was characterized by Brzozowski et al. (in preparation). They compared the bulk composition of Fe-Ti oxide intergrowths obtained by long rasters (~ 500 s) and typical traverse lengths (~ 100 s) in individual grains of magnetite. Analyses using these two methods yielded nearly identical trace-element concentrations. As a result, analyses in this study consisted of 60 seconds of gas background followed by up to 100 seconds of ablation. Data reduction was completed using the Iolite software package (Paton et al., 2011).

4.4 Results

4.4.1 Oxide minerals in the Eastern Gabbro

Iron-Ti oxides are ubiquitous in all of the rock series of the Eastern Gabbro, making them good candidates for use as petrogenetic and exploration tools. Grain size of these minerals varies from very fine-grained (< 100 μm) in the metabasalt to coarse-grained (> 1 mm) in the Layered and Marathon Series. They are typically disseminated, but can form semi-massive to massive pods in Cu-PGE-mineralized oxide- and apatite-rich cumulate rocks. The oxide- and apatite-rich rocks occur as thin lenses within the Two Duck Lake gabbro, but also crosscut the rocks above (metabasalt) and below the Two Duck Lake gabbro (Good et al. 2015)

4.4.2 Petrography of Fe-Ti oxides

Three broad types of Fe-Ti oxide crystals and intergrowths are present (Brzozowski et al. in preparation) – i) Fe-Ti oxide intergrowths (Fig. 4.5a), ii) replacement magnetite (Fig. 4.5b), and iii) myrmekitic Fe-Ti oxide intergrowths (Fig. 4.5c). Fe-Ti oxide intergrowths are the most common type of oxide assemblage. They comprise a host magnetite phase and

lamellae of ulvöspinel, ilmenite, or both, as well as bladed to anhedral spinel. They are typically associated with coarse crystals of ilmenite, which may occur along the silicate mineral-oxide mineral boundary, within the Fe-Ti oxide intergrowth, or along fractures in the intergrowth (Fig. 4.5a). The Fe-Ti oxide intergrowths can occur interstitially to silicates or as subhedral crystals, depending on their host rock and location (Fig. 4.6). The Fe-Ti oxide intergrowths hosted in metabasalt, olivine gabbro, and TDLG (Marathon) are generally interstitial to plagioclase and olivine (Fig. 4.6). The Fe-Ti oxide intergrowths hosted in the subophitic gabbro northwest of Marathon, melatroctolite, and pyroxenite are generally subhedral, with interstitial plagioclase, pyroxene, ± olivine. In both cases, coarse, euhedral apatite is often present as inclusions within the oxide intergrowths.

Fe-Ti oxide intergrowths can be classified according to the nature of the lamellae hosted by the magnetite (Brzozowski et al., 2017). They are: i) cloth-textured intergrowths, ii) intermediate-textured intergrowths, and iii) trellis-textured intergrowths. Cloth-textured Fe-Ti oxide intergrowths appear relatively homogenous under low-magnification reflected light (Fig. 4.7a), but in high-magnification BSE images, these can be seen to contain a nano-scale (< 1 μm) network of ulvöspinel (Fig. 4.7b). Exsolved spinel is uncommon in cloth-textured Fe-Ti oxide intergrowths, except for those from Redstone and Area 41.

Trellis-textured Fe-Ti oxide intergrowths are characterized by a trellis of fine, bladed and thick, tabular lamellae of ilmenite (Fig. 4.7c, d). Fine and thick trellis lamellae range in width from 1 to 5 μm and 5 to 20 μm, respectively. Unlike the lamellae in cloth-textured intergrowths, lamellae in trellis-textured intergrowths are readily visible in low-magnification reflected light (Fig. 4.7c). Exsolved spinel is ubiquitous in trellis-textured intergrowths and occurs as tabular crystals between thick trellis lamellae and as anhedral crystals concentrated within ilmenite lamellae (Fig. 4.7d). Thick trellis lamellae can also occur within cloth-textured Fe-Ti oxide intergrowths, but they are more heterogeneously distributed throughout the crystal than in trellis-textured intergrowths and are sometimes concentrated along grain boundaries and fractures.

Intermediate-textured intergrowths appear to be homogenous or display a mottled anisotropy in low- to high-magnification reflected light (halo around fracture in Fig. 4.7e). In high-magnification BSE images, they can be seen to consist of magnetite and either i) a cloth network that is interrupted by trellis-like features that cut obliquely across the network (red lines in Fig. 4.7f) or ii) a mixture of cloth lamellae and fine trellis lamellae, with the cloth network occurring in between the trellis lamellae, which are oriented oblique to the cloth network. The latter texture (ii) can also occur as a coarser variety that is readily visible under reflected light. These textures can occur throughout the entire magnetite crystal or locally around fractures (Fig. 4.7e, f), silicate inclusions, thick trellis lamellae, and boundaries of magnetite. The cloth, intermediate, and trellis textural varieties of Fe-Ti oxide intergrowths can all be present in a single thin section and within a single Fe-Ti oxide intergrowth.

Replacement magnetite is much less common than Fe-Ti oxide intergrowths and occur along the boundaries of sulfides, within fractures in sulfides, and in alteration patches/veinlets not directly associated with sulfides (Fig. 4.5b). They do not have ilmenite crystals associated with them and do not host any lamellae. Myrmekitic Fe-Ti oxide intergrowths are the least common type of oxide and are observed as intergrowths with orthopyroxene as rims on olivine (Fig. 4.5c). They host the same lamellar textures as interstitial Fe-Ti oxide intergrowths.

4.4.3 Major-element chemistry of Fe-Ti oxides

Fe-Ti oxide intergrowths exhibit a range of major-element compositions, from Ti-poor (2 wt. %) to Ti-rich (14.5 wt. %) (Fig. 4.8). Iron correlates negatively with Ti and ranges from 54-74 wt. % (Fig. 4.8). Magnesium and Al range from 0.3 wt. % up to 2.5 and 4 wt. %, respectively, and correlate with each other, but not with Fe or Ti (Fig. 4.8). The major-element composition of Fe-Ti oxide intergrowths from metabasalt and Layered Series overlap with the composition from the Marathon Series (Fig. 4.8). Fe-Ti oxide intergrowths hosted in metabasalt and Layered Series, however, are compositionally distinct; Layered

Series intergrowths have higher Ti and lower Fe, Al, and Mg contents than those from metabasalt (Fig. 4.8).

4.4.4 Trace-element chemistry of Fe-Ti oxides

In order to use Fe-Ti oxide chemistry for petrogenesis and mineral exploration, it is critical to understand how their chemistry varies as a function of i) the timing of their crystallization relative to other minerals, ii) their host rock series and rock type, iii) whether they are hosted in mineralized or barren rock, and iv) the mineralized zone in which they are hosted.

Table 4.1 summarizes the range of magnetite-silicate melt partition coefficients (D) that ave previously been determined for basaltic melt compositions, as well as rhyolitic and andesitic compositions for some elements (e.g., Mo), and vary as a function of T and fO_2. Partition coefficients for Cr, V, Mg, Mn, Ga, W, Ni, Co, and Zn are consistently greater than 1 (i.e., these elements are compatible in magnetite), whereas values for Ge and Al are consistently less than 1 (i.e., they are incompatible) (Table 4.1). The HFSE can either be compatible or incompatible, but D values are predominantly less than 1 (Table 4.1). Similarly, Sc, Mo, Pb, and Cu can have D values greater or less than 1, with most values for Sc, Mo, and Pb being greater than 1, and most values for Cu being less than 1. The partition coefficient for Sn was estimated by Dare et al. (2014b) to be around 1. Therefore, Cr, V, Mg, Mn, Ga, W, Ni, Co, Zn, Sc, Mo, and Pb magnetite-compatible, whereas the HFSE, Ge, Al, and Cu are magnetite-incompatible.

4.4.4.1 Timing of Fe-Ti oxide crystallization

Cobalt, V, Ni, and Cr are compatible in magnetite, pyroxene, and olivine (Table 4.1) and should behave in a predictable manner in magnetite as a result of pyroxene and olivine crystallization. In the Layered Series, where magnetite has crystallized before pyroxene (oxide augite melatroctolite), magnetite generally has higher concentrations of V, Ni, Cr, and, to an extent, Co than where magnetite has crystallized after pyroxene (olivine gabbro)

(Figs. 4.6, 4.9). In the Marathon Series, there is no correlation between Fe-Ti oxide chemistry and the timing of magnetite crystallization relative to olivine and pyroxene in the various rock types (Fig. 4.9).

4.4.4.2 Rock series and rock types

The composition of Fe-Ti oxide intergrowths hosted in metabasalt and Layered Series fall within the range of compositions of those from the Marathon Series (Fig. 4.10a). Relative to intergrowths hosted in metabasalt, those hosted in the Layered Series are enriched in the incompatible elements Zr, Hf, Ge, Ta, and Nb, and depleted in the compatible elements Co, V, Ni, Cr, and Zn (Fig. 4.10a). Elements that are moderately compatible and/or incompatible (W, Sc, Cu, Mo, Sn, Ga, Mn, Mg) exhibit similar concentrations in Fe-Ti oxide intergrowths hosted in metabasalt and Layered Series (Fig. 4.10a).

Relative to primitive mantle, all Fe-Ti oxide intergrowths are enriched in some compatible elements (W, Mo, Sn, Ga, Mn, Zn, V, and Ti), but depleted in others (Mg and Ni) (Fig. 4.10b). Similarly, intergrowths are enriched in some incompatible elements (Ta and Nb), but depleted in others (P) relative to primitive mantle (Fig. 4.10b). The most notable correlations between the different rock series are: i) intergrowths from the Layered Series are enriched in the incompatible elements Zr and Hf, and depleted in the compatible elements Cu and Cr, ii) intergrowths hosted in metabasalt are enriched in the compatible element Co, iii) and most intergrowths hosted in Marathon Series are depleted in the compatible element Cr (Fig. 4.10b).

4.4.4.2.1 Element-element binary diagrams

Depending on the rock series, elements may correlate positively, negatively, or show no correlation with respect to Ni concentration (Fig. 4.11). In the metabasalt, both compatible (V, Cr, Co, Sn, Ga, Cu, and Pb) and some incompatible (Ge and Cu) elements exhibit positive correlations with Ni; other incompatible elements (HFSE) exhibit negative correlations with Ni (Fig. 4.11). In the Layered and Marathon Series, Ni and Cr are

positively correlated, whereas the other compatible and incompatible elements exhibit no correlation with Ni (Fig. 4.11). Further, Fe-Ti oxide intergrowths in the Layered Series exhibit a large variability in Ni, with minor variability in other compatible and incompatible elements, whereas the opposite is true for intergrowths in the metabasalt and Marathon Series (Fig. 4.11).

The dominant rock type in the Marathon Series is a subophitic gabbro, and it occurs throughout the length of the Eastern Gabbro. At the Marathon deposit, this gabbro is called the Two Duck Lake gabbro (TDLG). The TDLG and subophitic gabbro to the northwest of Marathon differ in that the sequence of crystallization is different (cf. Sequence of Crystallization).

As a whole, the compatible elements (Cr, V, Co, and Ga) in Fe-Ti oxide intergrowths from the various rock types in the Marathon Series exhibit a positive correlation with Ni (Fig. 4.12). When individual rock types are considered, these elements only exhibit positive correlations with Ni for those intergrowths hosted in apatitic clinopyroxenite and oxide melatroctolite (Fig. 4.12). The incompatible (HFSE, Cu) and moderately compatible elements (Sc, Mo, W, Sn, Pb) do not correlate with Ni (Fig. 4.12). The concentrations of Cr, V, and Co vary over significant ranges for all rock types, but are greatest for intergrowths hosted by apatitic clinopyroxenite (~ 3 orders of magnitude) compared to the other rock types (1 to 2 orders of magnitude) (Fig. 4.12, Table 4.2). The concentration of the moderately compatible elements (Sn, Mo, W, Pb) range over ~ 1 order of magnitude, whereas the incompatible elements (HFSE, Cu) range over 1 to 4 orders of magnitude (Fig. 4.12, Table 4.2).

4.4.4.2.2 Ratio-element binary diagrams

On Ni/element vs. element binary diagrams, Fe-Ti oxide intergrowths from the Marathon Series define hyperbolic trends for both compatible (W, Sc, Mn, Pb, Mg, Mo, Sn, Ga, Zn, Co, Cr) and incompatible (HFSE, Cu, Ge) elements, where both compatible and incompatible elements show large ranges in concentration, as do Ni/element ratios (Fig.

4.13). Conversely, Fe-Ti oxide intergrowths from the metabasalt and the Layered Series do not exhibit hyperbolic trends, but rather define five different types of data arrays (Fig. 4.13). i) Chromium exhibits a large range in concentration in intergrowths from metabasalt, with minor variability in Ni/Cr, whereas intergrowths from Layered Series exhibit minor variability in both Cr and Ni/Cr (Fig. 4.13, Tables 4.2 and 4.3). ii) The opposite is true for Cu and Pb; intergrowths from the metabasalt exhibit minor variability in Cu and Pb concentration, but a large range in Ni/Cu and Ni/Pb, whereas intergrowths from Layered Series exhibit minor variability in Cu, Pb, Ni/Cu, and Ni/Pb (Fig. 4.13, Tables 4.2 and 4.3). iii) Fe-Ti oxide intergrowths from metabasalt exhibit minor variability in HFSE, W, Sc, and Mn concentration, but a large range in their Ni/element ratios, whereas intergrowths from Layered Series exhibit the opposite trend (Fig. 4.13, Tables 4.1 and 4.2). iv) Fe-Ti oxide intergrowths from both metabasalt and Layered Series exhibit a large range in Mg concentration, but only minor variability in Ni/Mg (Fig. 4.13, Tables 4.1 and 4.2). v) Lastly, in both the metabasalt and Layered Seires, there is little variability in the concentration of Mo, Sn, Ga, Zn, and Co, and their Ni/element ratios (Fig. 4.13, Tables 4.1 and 4.2).

In the Marathon Series, intergrowths from TDLG (Marathon), and to a lesser extent the apatitic clinopyroxenite, define hyperbolic trends for both compatible and incompatible elements (i.e., large variability in both Ni/element ratio and the element concentration) (Fig. 4.14). In contrast, intergrowths from the other rock types (subophitic gabbro, apatitic olivine clinpyroxenite, oxide melatroctolite), typically exhibit variations in only one of these variables (i.e., either Ni/element ratio or the element concentration) (Fig. 4.14). For the element most compatible in magnetite (Cr), intergrowths from the subophitic gabbro northwest of Marathon exhibit large variability in Ni/Cr , but only minor variability in Cr, whereas intergrowths from apatitic clinopyroxenite exhibit large variability in Cr, but only minor variability in Ni/Cr (Fig. 4.14, Tables 4.2 and 4.3). Intergrowths from oxide melatroctolite and apatitic olivine clinopyroxenite exhibit minor variability in both Cr and Ni/Cr (Fig. 4.14, Tables 4.1 and 4.2). In contrast, the elements that are most incompatible in magnetite (HFSE, Al), as well as some moderately compatible elements (Sc, Mo, Mg), exhibit the opposite trends (Fig. 4.14, Tables 4.1 and 4.2). With respect to Cu, W, and Sn,

which range from moderately compatible to incompatible, intergrowths from apatitic clinopyroxenite exhibit large variability in Ni/element ratio and minor variability in the element concentration, whereas intergrowths from the other rock types exhibit minor variability in both Ni/element ratio and element concentration (Fig. 4.14, Tables 4.1 and 4.2). The moderately compatible element Pb largely exhibits the same trends as Cu, W, and Sn, except for the intergrowths hosted in the subophitic gabbro northwest of Marathon, which exhibit large variability in Ni/Pb and minor variability in Pb (Fig. 4.13, Tables 4.1 and 4.2).

4.4.4.3 Mineralized zones at the Marathon Cu-Pd deposit

Fe-Ti oxide intergrowths from the three mineralized zones in the Marathon deposit have distinctly different trace-element compositions. Only those Fe-Ti oxide intergrowths hosted in the Two Duck Lake gabbro are compared here because i) the composition of Fe-Ti oxide intergrowths correlate with the host rock type (Fig. 4.12), and ii) most of the mineralization in the Marathon deposit is hosted by the TDLG. The distinct differences between the three mineralized zones apply to both compatible and incompatible elements (Fig. 4.15). Some compatible elements (Ni, Sc), as well as most incompatible elements (HFSE, Al) have the lowest concentrations in intergrowths from the Footwall Zone and highest concentrations in intergrowths from the W Horizon (Fig. 4.15). Intergrowths from the Main Zone have intermediate concentrations of these elements (Fig. 4.15). In contrast, other compatible elements (Zn, Mn, Ga, Sn, Pb) always occur in highest concentrations in intergrowths from the Footwall Zone relative to intergrowths in both the Main Zone and W Horizon, in which these metals occur in similar concentrations (Fig. 4.15).

4.4.4.4 Petrogenetic and mineral exploration diagrams

Dupuis and Beaudoin (2011) developed a series of discrimination diagrams to distinguish between Ti-poor magnetite (< 2 wt. % Ti) from various magmatic-hydrothermal mineral deposits. The composition of Fe-Ti oxide intergrowths from mineralized zones in the Eastern Gabbro fall outside of the compositional fields for Ni-Cu deposits and

volcanogenic massive sulfide (VMS) deposits, but fall within the compositional field for Fe-Ti and V deposits (at least for the discrimination diagram that includes the Ca, Al, and Mn content of magnetite) (Fig. 4.16). Although the Ti contents of the intergrowths in the Eastern Gabbro are all greater than 2 wt. % (3.5 to 10.5 wt. %), there is no correlation between their Ti concentration and proximity to the compositional fields (Fig. 4.16). This is an important detail because it demonstrates that the parameters that define the compositional fields in the discrimination diagrams are not controlled by the Ti content of oxides.

Dare et al. (2014a) suggested that the Ni content of magnetite can be used to identify mineralized rock in that magnetite from mineralized rock is depleted in Ni compared to magnetite from barren rock. Ward et al. (2018) used a Ni vs. Cr/V diagram to distinguish mineralized from barren rock based on the Ni content of magnetite, and to distinguish magnetite from mafic and ultramafic rocks based on its Cr/V. According to their diagram, magnetite from mineralized rock has higher Ni (> 300 ppm) than magnetite from barren rock, which contrasts with the work of Dare et al. (2014a). In addition, magnetite from mafic rocks has a lower Cr/V (< 0.022) than magnetite from ultramafic rocks. Such differences are not evident in the Marathon Series rocks. The Ni content of Fe-Ti oxide intergrowths hosted by mineralized Marathon Series overlaps significantly with the Ni contents of intergrowths hosted by barren Marathon Series (Fig. 4.17). The same is true for other chalcophile elements, such as Cu, Co, and Zn (Fig. 4.17). Intergrowths from unmineralized metabasalt contain higher Ni and Co contents than those from mineralized Marathon Series, whereas intergrowths from unmineralized Layered Series contain lower Ni and Co contents (Fig. 4.17). The Zn and Cu contents of intergrowths from all of these rock types are largely similar (Fig. 4.17). On the Ni vs. Cr/V diagram, intergrowths from both unmineralized and mineralized rock fall within the compositional fields for both mineralized and barren rock, with the majority of intergrowths having compositions that fall within the barren field (Fig. 4.18). Additionally, all of the intergrowths from the Marathon Series pyroxenites fall within the field for mafic rocks, whereas intergrowths from the gabbros and troctolites from the metabasalt, Layered Series, and Marathon Series span the fields for both mafic and ultramafic rocks (Ni. vs. Cr/V).

4.5 Discussion

4.5.1 Basis for petrogenetic interpretations

According to the Rayleigh fractional crystallization model, the concentration of elements compatible in a mineral will be highest in the first crystals to crystallize from a silicate melt and lowest in the last crystals to crystallize (Fig. 4.19). The concentration of elements incompatible in a mineral, on the other hand, will be lowest in the first crystals to crystallize from a silicate melt and highest in the last crystals to crystallize as the elements become concentrated in the residual melt (Fig. 4.19). In primitive melts, small degrees of fractionation yield large changes in the concentration of compatible elements in the crystallizing mineral, whereas the concentration of incompatible elements are relatively unaffected (Fig. 4.19) (Rollinson, 1993). In evolved melts, however, the opposite is observed (Fig. 4.19). This concept is critical for the interpretations made below on the origins of the rock series and rock types in the Eastern Gabbro.

The dominant minerals in the rocks of the Eastern Gabbro are olivine, pyroxene, plagioclase, Fe-Ti oxide intergrowths, and apatite. Because the intergrowths crystallized at different times relative to these minerals in different rock types, the composition of the intergrowths will, in part, have been controlled by the crystallization of these minerals and the compatibility of elements in them. Table 4.1 summarizes the behavior of the elements of interest in these minerals relative to a basaltic melt. During fractional crystallization, the concentration of Ga will have been controlled by plagioclase, Al by plagioclase and pyroxene, Mg, Cr, Mn, Co, and Ni by pyroxene and olivine, Sc and V by pyroxene, and P by apatite. In addition, magnetite may have been important as all of these elements, apart from Al, are compatible in it.

4.5.2 Origin of the rock series

The most recent model for the genesis of the Eastern Gabbro (Good et al., 2015), envisages a conduit system that comprised multiple sills and chambers, analogous to the idealized

model presented by Barnes et al. (2015) for Ni-Cu-PGE deposits. Based on differences in whole-rock chemistry (e.g., U, Th), Ce/Y, and Nb/Zr, the various rock types were subdivided into three distinct rock series (metabasalt, Layered Series, Marathon Series) that crystallized from magmas that originated from different sources (Good et al., 2015). Contamination via assimilation of country rock locally or at depth was ruled out as a possibility for causing these variations based on εNd values that are consistent with mantle values.

4.5.2.1 Metabasalt and Layered Series

Fe-Ti oxide intergrowths in the Layered Series are depleted in compatible elements and enriched in incompatible elements relative to intergrowths in the metabasalt (Figs. 4.10a, 4.11). This suggests that the metabasalt crystallized from a more primitive magma compared to the Layered Series. Intergrowths in the Layered Series exhibit a large range in Ni, Cr, and V concentrations (i.e., the elements most compatible in Fe-Ti oxides, Table 4.1), but only minor variability in the concentration of all of the other elements (Figs. 4.10a, 4.11, Table 4.2). This suggests that the Layered Series experienced low degrees of fractional crystallization. Intergrowths hosted in the metabasalt, however, generally show the opposite, with only minor variability in concentration of the elements most compatible in Fe-Ti oxides and significant variability in the elements most incompatible in Fe-Ti oxides (e.g., HFSE, Ge, Cu) (Figs. 4.10a, 4.11, Table 4.2). Because the metabasalt crystallized from a relatively primitive melt, this compositional variability cannot be due to fractional crystallization (cf. Fig. 4.19). Rather, it is more likely that the metabasalt samples belong to different metabasaltic units, which crystallized from magmas with distinct trace-element composition (Good and Dunning, 2018)

The compatibility of elements in fractionating minerals can be used to assess which minerals controlled the composition of the melt from which the oxides crystallized. Apatite, plagioclase, pyroxene, olivine, and sulfides are the dominant minerals present in the Eastern Gabbro. Of these minerals, P is only compatible in apatite, Ga in plagioclase, Sc and V in pyroxene, Cr, Mn, Co, and Ni in pyroxene and olivine, and Cu in sulfides

(Table 4.1). If fractionation of these minerals controlled the composition of the melt from which the oxides crystallized, the oxides should be depleted in these elements relative to primitive mantle. Fe-Ti oxide intergrowths from metabasalt and Layered Series only show a minor depletion in P, they are enriched in Ga and V, and Sc shows no enrichment or depletion relative to primitive mantle (Fig. 4.10b). This suggests that fractionation of apatite, plagioclase, and pyroxene likely did not play a major role in controlling the composition of the intergrowths in these rock series. Only Mg, Ni, Cr, and Cu show large depletions in the intergrowths relative to primitive mantle with Mg, Ni, and Cu being depleted in most intergrowths from both rock series, and Cr only being depleted in aggregates from the Layered Series (Fig. 4.10b). Magnesium, Ni, and Cr are compatible in pyroxene and olivine. Given that pyroxene fractionation did not affect the composition of the intergrowths, the depletion of these elements was likely the result of olivine fractionation. The depletion in Cu could only be the result of sulfide liquation.

Given that the Layered Series crystallized from a more evolved melt than the metabasalt and that it crosscuts the metabasalt, the two could not have originated from the same source. The distinct trends exhibited by Fe-Ti oxide intergrowths from the metabasalt and Layered Series on Ni/element vs. element diagrams are also consistent with their crystallization from melts that originated from different magma sources (Fig. 4.13). The lack of hyperbolic correlations exhibited by the intergrowths from these rock series on these diagrams suggests that these rocks did not crystallize from magmas that underwent significant degrees of magma mixing (Faure and Mensing, 2004; Langmuir et al., 1978) (Fig. 4.13). These interpretations are in agreement with those of Good et al. (2015) who suggested that these two rock series are genetically distinct. This is in contrast, however, to the model proposed by Shaw (1997), in which the Layered Series was interpreted to have formed from multiple batches of compositionally distinct magmas. This interpretation was based, in part, on distinct major-element variations in the cumulus minerals. Trace elements, however, are more sensitive to crystal fractionation and, although they exhibit noticeable variations in Fe-Ti oxides in the Layered Series, they are not consistent with emplacement of multiple batches of compositionally distinct magmas.

4.5.2.2 Marathon Series

Fe-Ti oxide intergrowths from the Marathon Series exhibit minor variability in Ni concentration, but significant variations in the concentration of other elements, particularly the elements that are most compatible (e.g., Cr) and incompatible (e.g., HFSE) in Fe-Ti oxides (Fig. 4.11, Table 4.2). Additionally, none of the compatible or incompatible elements exhibit distinct correlations with Ni (Fig. 4.11). In a Rayleigh fractional crystallization model, the magma from which the Marathon Series crystallized could not therefore have experienced either high or low degrees of fractional crystallization, similar to the metabasalts and Layered Series (cf. Fig. 4.19). Rather, it is more likely that the rocks of the Marathon Series crystallized from a variety of magmas that had experienced both high or low degrees of fractionation. The latter is indicated by the large variations in Ni/element ratios that correlate hyperbolically with the denominator element concentration (Fig. 4.13, Table 4.3). Typically, trends such as these are interpreted to result from mixing of multiple magmas with different compositions (Faure and Mensing, 2004; Langmuir et al., 1978). Because Fe-Ti oxide intergrowths in the Marathon Series exhibit large ranges in both compatible and incompatible element concentrations (Figs. 4.11, 4.13), the different batches of magmas that mixed likely represented different stages of evolution.

Just as described for the metabasalt and Layered Series, fractionation of apatite, pyroxene, and plagioclase likely did not play a major role in controlling the composition of the melt from which the Fe-Ti oxide intergrowths crystallized. Rather, the consistent depletion in Mg, Ni, and Cr in the intergrowths relative to primitive mantle likely resulted from fractionation of olivine (Fig. 4.10b). Although the Marathon Series hosts significant Cu and PGE sulfide mineralization, which, according to Shahabi Far et al. (2018), liquated at depth, the Fe-Ti oxide intergrowths are not depleted in Cu relative to primitive mantle. The enrichment in some intergrowths in Cu relative to primitive mantle (Fig. 4.10b) may be explained by mixing between primitive melts in which sulfides did not fractionate (i.e., enriched in Cu) and evolved melts in which sulfides did fractionate (i.e., depleted in Cu). These interpretations are consistent with the detailed work of Shahabi Far (2016) who interpreted a number of mineral textures and compositional variations in plagioclase and

pyroxene at Marathon as evidence for injection of primitive magma from a distinct source. Alternatively, if only a small volume of sulfide liquated from a large volume of silicate melt, the Cu content of the silicate melt would not be significantly affected. Consequently, oxides that crystallized from this melt would not be depleted in Cu.

The above interpretations are supported by compositional variations exhibited by Fe-Ti oxide intergrowths when compared to their timing of crystallization relative to other silicates. Depending on when the Fe-Ti oxide intergrowths crystallized relative to olivine, pyroxene, and plagioclase will affect their concentration of Co, V, Ni, and Cr. All of these elements behave compatibly in olivine and pyroxene relative to a basaltic melt, with Ni and Co being more compatible in olivine than pyroxene, and Cr and V being more compatible in pyroxene than olivine (Table 4.1). Therefore, crystallization of olivine and/or pyroxene prior to the Fe-Ti oxide intergrowths would decrease the concentration of these elements in the melt, and hence their concentration in the intergrowths. None of these elements are compatible in plagioclase and so crystallization of plagioclase prior to the Fe-Ti oxide intergrowths would have the opposite effect on the concentration of these elements in the melt and the intergrowths (i.e., their concentration would increase in the Fe-Ti oxide intergrowths if plagioclase crystallized before them).

In the Layered Series, intergrowths that crystallized after olivine, pyroxene, and plagioclase (olivine gabbro) have lower concentrations of Co, V, Ni, and Cr compared to intergrowths that crystallized with olivine, but before pyroxene and plagioclase (oxide augite melatroctolite) (Fig. 4.9). This is consistent with the fact that crystallization of olivine and pyroxene prior to the intergrowths would have depleted the melt in these elements, such that later-crystallized intergrowths would have been depleted in these elements. Therefore, the variation in Co, V, Ni, and Cr in Fe-Ti oxide intergrowths hosted in different rocks of the Layered Series can be explained by fractional crystallization of a melt that originated from a single source.

In the Marathon Series, intergrowths that crystallized with olivine, but before pyroxene and plagioclase (subophitic gabbro northwest of Marathon, oxide melatroctolite) should

have the highest concentration of V and Cr compared to the intergrowths that crystallized with pyroxene (TDLG, clinopyroxenites). These intergrowths, however, have the lowest concentration of these elements, as well as Ni and, to a lesser extent Co (Fig. 4.9). The intergrowths that crystallized after olivine, but with pyroxene (clinopyroxenites) should have the lowest concentration of Co, V, Ni, and Cr since they would have been sequestered in the earlier-formed olivine and pyroxene. The concentration of these elements in the intergrowths, however, are similar to or greater than their concentration in intergrowths that crystallized with olivine and before pyroxene (subophitic gabbro northwest of Marathon, oxide melatroctolite) (Fig. 4.9). Compatible element variations such as these cannot be explained solely by fractional crystallization of a magma. Again, a possible mechanism that could enrich the Co, V, Ni, and Cr contents in the Fe-Ti oxide intergrowths hosted in some of the Marathon Series rocks is injection of and re-equilibration with primitive magma.

Several studies have used variations in V and Cr in magnetite and ilmenite as indicators of re-equilibration with more primitive magma. Some of these studies invoked magma chamber replenishment (e.g., Charlier et al., 2010; Namur et al., 2010; Song et al., 2013), whereas others invoked different mechanisms, such as magma convection (e.g., McCarthy and Cawthorn, 1983; Tegner et al., 2006). Normal and reverse trends in the Cr content of ilmenite from the Allard Lake ilmenite deposit had been suggested by Charlier et al. (2010) to result from three processes, including normal crystal fractionation (normal fractionation trend), replenishment of the magma chamber with more primitive magma (reverse fractionation trend), and magma hybridization. Large- and small-scale cyclical reversals in the fractionation trend of plagioclase An%, pyroxene Mg#, olivine Fo%, magnetite Cr, and $(^{87}Sr/^{86}Sr)_{564}$, as well as the disappearance of cumulus apatite, Ca-pyroxene, and Fe-Ti oxides in the Sept Iles layered intrusion was suggested by Namur et al. (2010) to result from periodic replenishment of the magma chamber with primitive basaltic magma. Song et al. (2013) suggested that periodic reversals in the Cr contents of magnetite through the cyclic unit of the Lower Zone of the Panzhihua intrusion resulted from episodic magma chamber replenishment with primitive magma. Cawthorn and McCarthy (1980) and McCarthy and Cawthorn (1983) interpreted cycles of rapid depletion in Cr followed by

sudden increases in the Cr content of magnetite in a drill hole through the magnetite layer of the Rustenberg Layered Suite of the Bushveld Complex to result from convective recharge. The sudden increases in the Cr content of magnetite was attributed to the input of undepleted, or primitive, magma into the zone of crystallization by convection cells. Tegner et al. (2006) suggested that the cyclicity in olivine appearance, plagioclase An%, pyroxene Mg%, and possibly the V_2O_5 content of magnetite in the Main and Upper Zones of the Bushveld Complex resulted from mixing of evolved cumulates with more primitive residual melt in a fractionating magma sheet due to density inversions resulting from magnetite crystallization.

Earlier studies by Good and Crocket (1994) and Dahl et al. (2001) have suggested that the heterogeneity observed throughout the Eastern Gabbro is due to injection of multiple batches of magma. Recently, Good et al. (2015) built upon this by proposing a conduit model for the Marathon Cu-PGE deposit. A characteristic feature of conduit-style deposits is the replenishment of magma chambers by multiple batches of magma, which has been demonstrated for a number of Ni-Cu-PGE deposits, including Voisey's Bay (Li and Naldrett, 1999; Ripley and Li, 2011), Partridge River (Ripley et al., 2007; Thériault et al., 2000), Eagle (Ding et al., 2012; Ripley and Li, 2011), Noril'sk (Arndt et al., 2003; Naldrett, 1992), and South Kawishiwi (Gál et al., 2013, 2011). Accordingly, the enrichment in Co, V, Ni, and Cr in the Fe-Ti oxide intergrowths which crystallized late relative to silicate minerals (TDLG, pyroxenite) compared to those that crystallized early (subophitic gabbro northwest of Marathon, oxide melatroctolite) is consistent with injection of more primitive magma. The compositional homogeneity of the Layered Series throughout the Eastern Gabbro (Good et al., 2015) and the consistent behavior of Fe-Ti oxide chemistry with fractional crystallization suggests that the Layered Series did not experience significant, if any, reinjection of primitive magma.

4.5.3 Origin of the rock types of the Marathon Series

The Marathon Series is the youngest intrusive series in the Eastern Gabbro and is host to significant Cu and PGE mineralization (Good et al., 2015). All of the rocks hosted within

this series are considered to be co-genetic even though this has not been rigorously demonstrated (Good et al., 2015). The metabasalts, Layered Series, and Marathon Series were all classified by Good et al. (2015) as genetically-distinct rock series according to notably different whole-rock HFSE ratios (e.g., Nb/Zr). Yet, the average Nb/Zr of the various rock types hosted in the Marathon Series span a range from 3.53 for the older oxide melatroctolite to 11.9 for the younger oxide melatroctolite, with the TDLG and apatitic olivine clinopyroxenite having average ratios of 3.63 and 7.54, respectively (Good et al., 2015). The range in these ratios within the Marathon Series is similar to or greater than the differences in the ratios between the rock series (metabasalt = 1.1, Layered Series = 6.8-11.3). Therefore, if one accepts that the HFSE content of the various Marathon Series rocks have not been modified by some other processes, than these distinct ratios might reflect crystallization from or interaction among magmas that originated from different magmatic sources.

Fe-Ti oxide intergrowths in the various Marathon Series rocks crystallized at different times relative to primary silicates, suggesting the composition of the melts from which they crystallized were different. Fe-Ti oxide intergrowths in the clinopyroxenites crystallized with pyroxene, after olivine, and before plagioclase (Fig. 4.6). Fe-Ti oxide intergrowths in Two Duck Lake gabbro and subophitic gabbro northwest of Marathon crystallized at different times with respect to these silicates. In the TDLG, intergrowths crystallized with pyroxene, but after olivine and plagioclase crystallized, whereas in subophitic gabbro northwest of Marathon, intergrowths crystallized with olivine, but before pyroxene and plagioclase crystallized (Fig. 4.6). Intergrowths in the oxide melatroctolite crystallized at the same time relative to other silicates as those in the subophitic gabbro northwest of Marathon (Fig. 4.6). None of the gabbros and pyroxenites can be related via fractional crystallization of a single batch of magma because i) Fe-Ti oxide intergrowths in the Marathon Series exhibit large variability (relative to metabasalt and Layered Series) in both compatible and incompatible elements (Figs. 4.11, 4.12), which, according to the Rayleigh fractional crystallization model (cf. Fig. 4.19), can only occur at either low or high degrees of fractionation, respectively, and ii) these rock types cross cut each other, with the older oxide melatroctolite being the oldest, followed by the TDLG, the clinopyroxenites, and

finally the younger oxide melatroctolite (Good et al., 2015). Additionally, several lines of evidence suggest that at least some of the Marathon Series rocks, particularly the TDLG and apatitic clinopyroxenite, experienced late input of more primitive melt. Fe-Ti oxide intergrowths in the TDLG and apatitic clinopyroxenite have Co, V, Ni, and Cr concentrations that are variably enriched compared to intergrowths hosted in the subophitic gabbro northwest of Marathon, oxide melatroctolite, and apatitic olivine clinopyroxenite (Fig. 4.9). If the Marathon Series rocks didn't experience late input of more primitive melt, than the Fe-Ti oxide intergrowths in the subophitic gabbro northwest of Marathon, oxide melatroctolite, and apatitic olivine clinopyroxenite should have higher concentrations of these elements compared to those in the TDLG and apatitic clinopyroxenite according to the timing of their crystallization relative to olivine and pyroxene (Fig. 4.6). Input of primitive melt would have acted to refertilize the Marathon Series melts in Co, V, Ni, and Cr, which were previously removed by crystallization of olivine and pyroxene. This is consistent with the hyperbolic trends that are always exhibited by the composition of Fe-Ti oxide intergrowths from TDLG and sometimes by intergrowths from apatitic clinopyroxenite on Ni/element vs. element diagrams, but the lack of such trends in the other rock types (Fig. 4.14).

These interpretations require that the resident TDLG and apatitic clinopyroxenite magmas mixed with an influx of primitive magma to a greater degree than the resident magmas from which the subophitic gabbro northwest of Marathon, oxide melatroctolite, and apatitic olivine clinopyroxenite crystallized. These differences may reflect the timing and location of emplacement of these individual batches of magma. The oxide melatroctolite was one of the first Marathon Series rock types to be emplaced into the Eastern Gabbro (Good et al., 2015) and, as such, would have had ample opportunity to interact with new batches of magma. Yet, Fe-Ti oxide intergrowths from these rocks do not record evidence of significant mixing. This is likely because these rocks occur in pod-like bodies that are, to some degree, isolated from the main Marathon Series intrusion and would not have readily interacted with new batches of melt (Fig. 4.3). Conversely, the apatitic olivine clinopyroxenite was one of the last rock types to be emplaced into the Marathon Series pluton (Good et al., 2015). Their emplacement at the end of the intrusive history may not

have been followed by any subsequent batches of primitive magma (i.e., the magma from which they crystallized would not have been refertilized). According to McBride (2015), the TDLG, which makes up the majority of the Marathon Series (Good et al. 2015), is contiguous between Marathon and the areas to the northwest, and was emplaced after the oxide melatroctolite, but before the apatitic olivine clinopyroxenite. The relatively early emplacement of the subophitic gabbro into the main chamber that hosts the Marathon Series (Fig. 4.3) would have allowed the magma from which it crystallized to interact with any new influxes of primitive melt that were injected into the chamber. Yet, as with the oxide melatroctolite, Fe-Ti oxide intergrowths from the subophitic gabbro northwest of Marathon do not record any significant input of primitive melt. Brzozowski et al. (2017) interpreted the depleted whole-rock Cu/Pd and sulfide S/Se relative to mantle values, and the higher cubanite/chalcopyrite ratio in the mineralized zones to the north of Marathon (i.e., Four Dams Main Zone, Area 41, and Redstone) to be a result of these sulfides having experienced lower R factors (silicate/sulfide mass ratio; Campbell and Naldrett, 1979) than sulfides in the mineralized zones in the Marathon deposit. High R factors are typically achieved through the interaction of sulfides with successive batches of primitive melt (Maier, 2005). Therefore, the low R factors experienced by the gabbroic magmas in the northern mineralized occurrences also suggest that magma mixing was not important in this part of the Eastern Gabbro.

4.5.4 Origin of massive Fe-Ti oxides

Massive Fe-Ti oxides in the oxide melatroctolite occur in pods and consist predominantly of Fe-Ti oxide intergrowths and apatite with lesser olivine and pyroxene. They have been subdivided into older and younger varieties according to their crosscutting relationships and mineralogy. The older oxide melatroctolite consists predominantly of Fe-Ti oxide intergrowths, olivine, pyroxene, and apatite and, based on crosscutting relationships, are coeval with the Two Duck Lake gabbro. The younger oxide melatroctolite, which crosscuts all of the Marathon Series rocks, is different in that it lacks olivine and pyroxene. The different crosscutting relationships between these two varieties of oxide melatroctolite indicates that they crystallized from different batches of magma. As discussed in the

previous section, since the magmas from which the oxide melatroctolites crystallized likely did not experience significant refertilization by mixing with primitive melt, the lower concentrations of compatible elements in the younger oxide melatroctolite indicate that it likely crystallized from a more evolved melt compared to the older oxide melatroctolite (Figure 4.12).

The concentration of P in a mafic melt has a strong control on the stability of magnetite and the abundance of magnetite that crystallizes (Toplis et al., 1994). Under relatively oxidized conditions (FMQ+1), the abundance of magnetite that crystallizes from a mafic melt increases as the P content of the melt decreases (Toplis et al., 1994). The concentration of Fe and Ti in mafic melts also increases with degree of fractionation as a result of olivine, pyroxene, and plagioclase crystallization (Best, 2002). Accordingly, if significant amounts of P is removed from the melt by, for example, apatite crystallization, this would induce magnetite crystallization. If this melt had also undergone a notable amount of fractionation, than it would also be enriched in Fe and Ti and result in crystallization of significant quantities of Ti-rich magnetite. This could explain the crystallization of the oxide melatroctolites since i) they contain significant quantities of apatite and ii) the apatite crystallized early relative to the Fe-Ti oxide intergrowths (Fig. 4.6).

4.5.5 Magnetite chemistry as an exploration tool in the Eastern Gabbro

Relative to Fe-Ti oxide intergrowths hosted in the Main Zone and W Horizon, intergrowths hosted in Footwall Zone are notably enriched in the moderately compatible elements Mn, Ga, Sn, and Pb and depleted in the incompatible elements Sc, Al, and the HFSE, and the compatible element Ni (Fig. 4.15). Fe-Ti oxide intergrowths hosted in the W Horizon, however, are relatively enriched in Ni and the incompatible HFSE, Sc, and Al compared to intergrowths hosted in the other zones (Fig. 4.15). These variations cannot be due to fractional crystallization of a single melt because the highly incompatible elements (HFSE, Al) exhibit the same trend as the highly compatible element Ni. Accordingly, these variations are likely due to variations in the composition of the melts from which each of the mineralized zones crystallized. This is consistent with the interpretations of Shahabi

Far (2016) and Ames et al. (2017) based on mineralogical and compositional (Mg/Fe, V, Ni, Sc) variations in pyroxenes in the various zones, and the larger diversity of PGM in the W Horizon compared to the Footwall Zone and Main Zone, respectively.

Dare et al. (2014a) suggested that the Ni content of magnetite can be used as an indicator of fertility. They noted that magnetite from mineralized plutons are depleted in Ni compared to magnetite from barren plutons as a result of sulfide saturation. Ward et al. (2018) characterized the opposite relationship, whereby magnetite from mineralized rock contains higher Ni contents than magnetite from barren rock; they noted that magnetite from mineralized rock contains > 300 ppm Ni. The Ni concentration of Fe-Ti oxide intergrowths hosted by mineralized Marathon Series is indistinguishable from those hosted by barren Marathon Series (Fig. 4.17). Intergrowths from unmineralized metabasalt and Layered Series have higher and lower concentrations, respectively, compared to mineralized Marathon Series (Fig. 4.17). This large variability in Ni contents between intergrowths from barren and mineralized rock, along with the inconsistent relationship of Ni between mineralized and barren rock described by Dare et al. (2014a) and Ward et al. (2018), emphasizes the fact that the Ni content of Fe-Ti oxides is not a robust indicator of mineralization, at least not in Ni-depleted systems, such as the Eastern Gabbro. Cobalt exhibits a similar relationship to Ni, whereas the other chalcophile elements (Cu and Zn) are largely similar between mineralized and barren rock (Fig. 4.17). This suggests that not only the Ni content, but the chalcophile element content of oxides as a whole are not robust indicators of mineralization, and that other factors need to be considered, such as the timing of sulfide liquation relative to oxide crystallization.

The chalcophile element content of Fe-Ti oxides depends, in part, on the timing of their crystallization relative to sulfide liquation. If mineralized and barren Marathon Series crystallized from different batches of magma with sulfide only having liquated in some of those batches, than two scenarios are possible. i) If Fe-Ti oxides crystallized before sulfide liquated, the concentration of chalcophile elements in the oxides hosted in the barren and fertile Marathon Series would be similar. ii) If Fe-Ti oxides crystallized after sulfides liquated, the concentration of chalcophile elements in oxides hosted in fertile Marathon

Series would be depleted relative to barren Marathon Series, in which sulfide did not liquate. A third scenario (iii) is possible if sulfide liquated in all of the batches of magma from which the Marathon Series crystallized. In this scenario, regardless if Fe-Ti oxides crystallized before or after sulfide liquation, their concentration of chalcophile elements would be similar. Because there is no difference in chalcophile element concentration between barren and fertile Marathon Series, scenario (i) or (iii) are the only possibilities. Of these two, scenario (iii) is more likely because it has been suggested, based on multiple S isotopes ($\Delta^{33}S$, $\Delta^{36}S$), that sulfide probably liquated at depth prior to significant crystallization of the magma (Shahabi Far et al., 2018).

4.5.6 Are previously-developed discrimination diagrams reliable?

Dupuis and Beaudoin (2011) developed a number of binary diagrams that can sequentially be used to distinguish magnetite and hematite hosted by different types of magmatic and hydrothermal sulfide deposits. The compositional fields for each of the deposits were generated using magnetite and hematite in which no minor or trace element (Zn, Cu, Ni, Mn, Cr, V, K, Ca, Ti, Al, Si, Mg) occurred in concentrations greater than 2 wt. %. They also included magnetite from Cr, V, and Fe-Ti deposits, which inherently have high concentrations (> 2 wt. %) of Cr, V, and Ti, respectively. Although the primary Fe-Ti oxide intergrowths in the Eastern Gabbro have Ti contents that are consistently greater than 2 wt. % (Fig. 4.8), there is no correlation between their Ti contents and the elements used in the discrimination diagrams (Fig. 4.16). The high concentration of Ti in the Fe-Ti oxide intergrowths, therefore, should not affect the reliability of these discriminant diagrams.

As mentioned above, the diagrams developed by Dupuis and Beaudoin (2011) need to be used sequentially to discriminate magnetite from different magmatic-hydrothermal sulfide deposits. The composition of magnetite are first tested to characterize if they originate from Ni-Cu-PGE deposits (Fig. 4.16a). Those magnetite that fall outside of the Ni-Cu-PGE field are than tested to characterize if they originate from VMS deposits (Fig. 4.16b). Lastly, those magnetite that fall outside of the VMS field are than tested to characterize if they

originate from IOCG, Kiruna, BIF, porphyry Cu, skarn, or Fe-Ti-V deposits (Fig. 4.16c, d).

Based on 172 analyses of magnetite from 15 Ni-Cu-PGE deposits, Dupuis and Beaudoin (2011) characterized magnetite to be enriched in Ni and Cr compared to all other magmatic and hydrothermal sulfide deposits (Fig. 4.16a). It is well-established that the mineralization at Marathon, and the other occurrences north of Marathon, principally represent the concentration of metals by an immiscible sulfide liquid (Good et al., 2015; Ruthart, 2013; Shahabi Far et al., 2018). Yet, on the Ni+Cr vs. Si+Mg diagram of Dupuis and Beaudoin (2011), the composition of Fe-Ti oxide intergrowths from mineralized areas of the Eastern Gabbro consistently have Si+Mg contents greater than the Ni-Cu field and Ni+Cr contents that span a range of concentrations from less than to greater than the Ni-Cu field (Fig. 4.16a). The Si contents of Fe-Ti oxide intergrowths from the Eastern Gabbro are similar to the concentrations in magnetite from the Ni-Cu-PGE deposits used by Dupuis and Beaudoin (2011) (Table 4.2). The Mg contents, however, are notably higher in the former compared to the latter (Table 4.2). Accordingly, the compositional field for Ni-Cu-PGE deposits could be modified to incorporate Fe-Ti oxide intergrowths from Marathon-type mineralization, which exhibit lower Ni, higher Cr, and higher Mg compared to the magnetite from Ni-Cu-PGE deposits used to generate the compositional field. The Ni+Cr limits would need to be extended to lower (0.01 wt. %) and higher values (4.5 wt. %), and the Si+Mg limits would need to be extended to higher values, up to 2.6 wt. % (Fig. 4.16a).

Because these discriminant diagrams are designed to be used for mineral exploration, it is often not known what mineral deposit type might be found in a given environment. Since the majority of the Fe-Ti oxide intergrowths from the Eastern Gabbro have compositions that lie outside of the Ni-Cu-PGE field, than according to the model by Dupuis and Beaudoin (2011), they should be tested to see if they plot within the field for other mineral deposits. The composition of all of the Fe-Ti oxide intergrowths plot outside of the compositional field for VMS deposits (Fig. 4.16b), but plot within the compositional field for Fe-Ti, V deposits on the Ca+Al+Mn vs. Ti+V diagram (Fig. 4.16c).

This example illustrates two important aspects regarding these discrimination diagrams. The first point is that the compositional field that discriminates magnetite from Ni-Cu-PGE deposits could be modified to incorporate Fe-Ti oxide intergrowths hosted by Marathon-type Cu-PGE deposits. The second point is that these discrimination diagrams are not reliable in discerning magnetite hosted in different types of sulfide deposits as they mistakenly characterize the magmatic Cu-PGE mineralization in the Eastern Gabbro as an Fe-Ti and V deposit.

Ward et al. (2018) developed the Ni vs. Cr/V diagram to distinguish mineralized and barren mafic and ultramafic rocks. They suggested that magnetite from mineralized rock have Ni concentrations > 300 ppm and that ultramafic rocks have Cr/V < 0.022. The Ni content of Fe-Ti oxides from mineralized and barren rock largely lie within the field for barren rock on Figure 4.18. This diagram was developed using magnetite-ilmenite intergrowths, but is based on trace-element data of the magnetite between the ilmenite lamellae. The concentration of Ni in ilmenite is lower than the bulk content in magnetite-ulvöspinel-ilmenite intergrowths in the Eastern Gabbro (not shown). Because ilmenite lamellae were incorporated into the laser ablation analyses in this study, the bulk Ni content of the Fe-Ti oxide intergrowths would be lower than if just the magnetite in between the lamellae were analyzed (i.e., the Ni content is diluted). Accordingly, all of the data points on Figure 4.18 should be moved to higher Ni values. In either case, the discriminant diagram does not accurately distinguish oxides from barren and mineralized rock given the large overlap in Ni contents of oxides from mineralized and barren rock in the Eastern Gabbro. Nor does it accurately distinguish magnetite from mafic and ultramafic rocks based on Cr/V content given that magnetite from mafic (gabbros and melatroctolites) and ultramafic rocks (pyroxenites) in the Eastern Gabbro have indistinguishable Cr/V (Fig. 4.18). Again, the diagrams were developed using data from magnetite between exsolution lamellae. The Cr/V content of ilmenite from the Eastern Gabbro is similar to bulk Cr/V content of magnetite-ulvöspinel-ilmenite intergrowths, and so incorporation of the lamellae should not have modified this ratio. Therefore, in Ni-depleted systems similar to the Eastern Gabbro, the Ni vs. Cr/V diagram may not accurately distinguish between mineralized and barren mafic and ultramafic rocks.

4.6 Conclusion

The past decade has seen a growing interest in the use of magnetite and ilmenite chemistry for petrogenesis and mineral exploration. Most of these studies, however, characterized the chemistry of oxides in rocks that represent end-members with respect to magma evolution and mineralization. Although studies such as these are required in order to understand how oxide chemistry varies as a result of different magmatic processes, the outcomes need to be applied to more complex systems to assess their robustness.

i. The metabasalt, Layered Series, and Marathon Series all crystallized from compositionally distinct magmas that experienced different magmatic histories prior to intrusion. The metabasalt and Layered Series magmas experienced little to no magma mixing, with the Layered Series having crystallized from a more evolved melt than the metabasalt. The Marathon Series crystallized from a mixture of several magma batches, some of which were more evolved than others.

ii. The various rock types of the Marathon Series cannot be related by fractional crystallization of a single batch of magma. Rather, the magmas from which the rock types crystallized had to have mixed to variable degrees with a late input of more primitive melt. The degree of this mixing was controlled by the location and timing of emplacement of the magmas from which the different rock types crystallized, with the Two Duck Lake gabbro and apatitic clinopyroxenite having mixed with the primitive melt the most. The oxide melatroctolite, which exhibited the least amount of mixing, likely formed as a result of P removal through apatite crystallization, which induced crystallization of Fe-Ti oxides.

iii. The Footwall Zone, Main Zone, and W Horizon of the Marathon Cu-Pd deposit could not have formed from a single batch of evolving magma, but rather multiple compositionally distinct magmas.

iv. Fe-Ti oxide intergrowths exhibit no compositional difference between those hosted in barren and mineralized rock. This is likely because sulfide liquated at depth in all of the batches of magma from which the Marathon Series crystallized.

v. Previously developed discrimination diagrams should be used with caution in Ni-depleted systems like the Eastern Gabbro to circumvent erroneous interpretations. Additionally, to include Marathon-type Cu-Pd mineralization, the compositional field for Ni-Cu-PGE deposits in the discrimination diagrams of Dupuis and Beaudoin (2011) can be extended.

4.7 References

Aigner-Torres, M., Blundy, J., Ulmer, P., Pettke, T., 2007. Laser Ablation ICPMS study of trace element partitioning between plagioclase and basaltic melts: an experimental approach. Contrib. Mineral. Petrol. Heidelb. 153, 647–667.

Ames, D.E., Kjarsgaard, I.M., Good, D.J., McDonald, A.M., 2016. Ore mineralogy of Cu-PGE mineralized gabbros, Coldwell Alkaline Complex, Midcontinent rift: supporting databases, scanning electron microscope, and mineral chemistry. Geological Survey of Canada Open File No. 8006.

Arndt, N.T., Czamanske, G.K., Walker, R.J., Chauvel, C., Fedorenko, V.A., 2003. Geochemistry and Origin of the Intrusive Hosts of the Noril'sk-Talnakh Cu-Ni-PGE Sulfide Deposits. Econ. Geol. 98, 495–515.

Baker, M.B., Wyllie, P.J., 1992. High-pressure apatite solubility in carbonate-rich liquids: Implications for mantle metasomatism. Geochim. Cosmochim. Acta 56, 3409–3422.

Barnes, S.J., Cruden, A.R., Arndt, N., Saumur, B.M., 2015. The mineral system approach applied to magmatic Ni-Cu-PGE sulphide deposits. Ore Geol. Rev. 76, 296–316.

Beattie, P., 1994. Systematics and energetics of trace-element partitioning between olivine and silicate melts: Implications for the nature of mineral/melt partitioning. Chem. Geol., Trace-element Partitioning with Application to Magmatic Processes 117, 57–71.

Best, M.G., 2002. Igneous and Metamorphic Petrology, 2nd edition. ed. Wiley-Blackwell, Malden, MA.

Bindeman, I.N., Davis, A.M., 2000. Trace element partitioning between plagioclase and melt: investigation of dopant influence on partition behavior. Geochim. Cosmochim. Acta 64, 2863–2878.

Bindeman, I.N., Davis, A.M., Drake, M.J., 1998. Ion Microprobe Study of Plagioclase-Basalt Partition Experiments at Natural Concentration Levels of Trace Elements. Geochim. Cosmochim. Acta 62, 1175–1193.

Bougault, H., Hekinian, R., 1974. Rift Valley in the Atlantic Ocean near 36°50′N: petrology and geochemistry of basaltic rocks. Earth Planet. Sci. Lett. 24, 249–261.

Boutroy, E., Dare, S.A.S., Beaudoin, G., Barnes, S.-J., Lightfoot, P.C., 2014. Magnetite composition in Ni-Cu-PGE deposits worldwide: application to mineral exploration. J. Geochem. Explor. 145, 64–81.

Brunet, F., Chazot, G., 2001. Partitioning of phosphorus between olivine, clinopyroxene and silicate glass in a spinel lherzolite xenolith from Yemen. Chem. Geol. 176, 51–72.

Brzozowski, M., Samson, I., Gagnon, J., Good, D., Linnen, R., 2017. On the controls of low- and high-Cu/Pd mineralization in the Eastern Gabbro, Canada: evidence from sulfide textures, S/Se ratios, and PGE contents, in: SGA 14th Biennial Meeting. Quebec City, Canada, pp. 423–426.

Brzozowski, M.J., Samson, I.M., Gagnon, J.E., Good, D.J., Linnen, R.L., 2017. Textural and chemical characteristics of oxide minerals as a record of psotmagmatic processes in the Eastern Gabbro, Coldwell Complex, NW Ontario, in: GAC-MAC. Kingston, Canada.

Campbell, I.H., Naldrett, A.J., 1979. The influence of silicate: sulfide ratios on the geochemistry of magnetic sulfides. Econ. Geol. 74, 1503–1506.

Carew, M.J., Mark, G., Oliver, N.H.S., Pearson, N., 2006. Trace element geochemistry of magnetite and pyrite in Fe oxide (±Cu-Au) mineralised systems: Insights into the geochemistry of ore-forming fluids, in: Goldschmidt. p. A83.

Cawthorn, R.G., McCarthy, T.S., 1980. Variations in Cr content of magnetite from the upper zone of the Bushveld Complex — evidence for heterogeneity and convection currents in magma chambers. Earth Planet. Sci. Lett. 46, 335–343.

Charlier, B., Namur, O., Malpas, S., de Marneffe, C., Duchesne, J.-C., Auwera, J.V., Bolle, O., 2010. Origin of the giant Allard Lake ilmenite ore deposit (Canada) by fractional crystallization, multiple magma pulses and mixing. Lithos 117, 119–134.

Dahl, R., Watkinson, D.H., Taylor, R.P., 2001. Geology of the Two Duck Lake Intrusion and the Marathon Cu-PGE Deposit, Coldwell Complex, Northern Ontario. Explor. Min. Geol. 10, 51–65.

Dale, I.M., Henderson, P., 1972. The partitioning of transition elements in phenocryst bearing basalts and the implications about melt structure, in: International Geological Congress. pp. 105–111.

Dare, S.A.S., Ames, D.E., Lightfoot, P.C., Barnes, S.-J., Beaudoin, G., 2014a. Mineral chemistry and supporting databases for TGI4 project on "Trace elements in Fe-oxides from fertile and barren igneous complexes: Investigating their use as a vectoring tool in the intrusions that host Ni-Cu-PGE deposits". Geological Survey of Canada Open File No. 7538.

Dare, S.A.S., Barnes, S.-J., Beaudoin, G., 2012. Variation in trace element content of magnetite crystallized from a fractionating sulfide liquid, Sudbury, Canada: Implications for provenance discrimination. Geochim. Cosmochim. Acta 88, 27–50.

Dare, S.A.S., Barnes, S.-J., Beaudoin, G., Méric, J., Boutroy, E., Potvin-Doucet, C., 2014b. Trace elements in magnetite as petrogenetic indicators. Miner. Deposita 49, 785–796.

Ding, X., Ripley, E.M., Li, C., 2012. PGE geochemistry of the Eagle Ni–Cu–(PGE) deposit, Upper Michigan: constraints on ore genesis in a dynamic magma conduit. Miner. Deposita 47, 89–104.

Duke, J.M., 1976. Distribution of the Period Four Transition Elements among Olivine, Calcic Clinopyroxene and Mafic Silicate Liquid: Experimental Results. J. Petrol. 17, 499–521.

Dunn, T., 1987. Partitioning of Hf, Lu, Ti, and Mn between olivine, clinopyroxene and basaltic liquid. Contrib. Mineral. Petrol. 96, 476–484.

Dupuis, C., Beaudoin, G., 2011. Discriminant diagrams for iron oxide trace element fingerprinting of mineral deposit types. Miner. Deposita 46, 319–335.

Esperança, S., Carlson, R.W., Shirey, S.B., Smith, D., 1997. Dating crust-mantle separation: Re-Os isotopic study of mafic xenoliths from central Arizona. Geology 25, 651–654.

Faure, G., Mensing, T.M., 2004. Mixing Theory, in: Isotopes: Principles and Applications. Wiley, p. 928.

Forsythe, L.M., Nielsen, R.L., Fisk, M.R., 1994. High-field-strength element partitioning between pyroxene and basaltic to dacitic magmas. Chem. Geol., Trace-element Partitioning with Application to Magmatic Processes 117, 107–125.

Gál, B., Molnár, F., Guzmics, T., Mogessie, A., Szabó, C., Peterson, D.M., 2013. Segregation of magmatic fluids and their potential in the mobilization of platinum-group elements in the South Kawishiwi Intrusion, Duluth Complex, Minnesota — Evidence from petrography, apatite geochemistry and coexisting fluid and melt inclusions. Ore Geol. Rev. 54, 59–80.

Gál, B., Molnár, F., Peterson, D.M., 2011. Cu-Ni-PGE Mineralization in the South Filson Creek Area, South Kawishiwi Intrusion, Duluth Complex: Mineralization Styles and Magmatic and Hydrothermal Processes. Econ. Geol. 106, 481–509.

Good, D.J., Cabri, L.J., Ames, D.E., 2017. PGM Facies variations for Cu-PGE deposits in the Coldwell Alkaline Complex, Ontario, Canada. Ore Geol. Rev. 90, 748-771.

Good, D.J., Crocket, J.H., 1994. Genesis of the Marathon Cu-Platinum-Group Element Deposit, Port Coldwell Alkalic Complex, Ontario: A Midcontinent Rift-Related Magmatic Sulfide Deposit. Econ. Geol. 89, 131–149.

Good, D. J., Dunning, G., 2018. Geochronology of mafic rocks in the Coldwell Complex, Midcontinent Rift: Age constraints on magma evolution in relation to Cu-PGE, in: Resources for Future Generations, Vancouver, Canada.

Good, D.J., Epstein, R., McLean, K., Linnen, R., Samson, I., 2015. Evolution of the Main Zone at the Marathon Cu-PGE Sulfide Deposit, Midcontinent Rift, Canada: Spatial Relationships in a Magma Conduit Setting. Econ. Geol. 110, 983–1008.

Hart, S.R., Dunn, T., 1993. Experimental cpx/melt partitioning of 24 trace elements. Contrib. Mineral. Petrol. 113, 1–8.

Hauri, E.H., Wagner, T.P., Grove, T.L., 1994. Experimental and natural partitioning of Th, U, Pb and other trace elements between garnet, clinopyroxene and basaltic melts. Chem. Geol., Trace-element Partitioning with Application to Magmatic Processes 117, 149–166.

Higuchi, H., Nagasawa, H., 1969. Partition of trace elements between rock-forming minerals and the host volcanic rocks. Earth Planet. Sci. Lett. 7, 281–287.

Irvine, T.N., Kushiro, I., 1976. Partitioning of Ni and Mg between olivine and silicate liquids. Yearb. Carnegie Inst. Wash. 75, 668–675.

Jenner, G.A., Foley, S.F., Jackson, S.E., Green, T.H., Fryer, B.J., Longerich, H.P., 1994. Determination of partition coefficients for trace elements in high pressure-temperature experimental run products by laser ablation microprobe-inductively coupled plasma-mass spectrometry (LAM-ICP-MS). Geochim. Cosmochim. Acta 57, 5099–5103.

Johnson, K.T.M., 1998. Experimental determination of partition coefficients for rare earth and high-field-strength elements between clinopyroxene, garnet, and basaltic melt at high pressures. Contrib. Mineral. Petrol. 133, 60–68.

Johnson, K.T.M., 1994. Experimental cpx/ and garnet/melt partitioning of REE and other trace elements at high pressures : petrogenetic implications. Mineral. Mag. 58, 454–455.

Johnson, K.T.M., Kinzler, R.J., 1989. Partitioning of REE, Ti, Zr, Hf, and Nb between clinopyroxene and basaltic liquid: an ion microprobe study. EOS Trans. Am. Geophys. Union 70, 1388.

Jones, R.H., Layne, G.D., 1997. Minor and trace element partitioning between pyroxene and melt in rapidly cooled chondrules. Am. Mineral. 82, 534–545.

Kamvong, T., Zaw, K., Siegele, R., 2007. PIXE/PIGE microanalysis of trace elements in hydrothermal magnetite and exploration significant: a pilot study, in: 15th Australian Conference on Nuclear and Complementary Techniques of Analysis and 9th Vacuum Society of Australia Congress. University of Melbourne, Melbourne, Australia.

Keleman, P.B., Dunn, J.T., 1992. Depletion of Nb relative to other highly incompatible elements by melt/rock reaction on the upper mantle. EOS Trans. Am. Geophys. Union 73, 656–657.

Kloeck, W., Palme, H., 1988. Partitioning of siderophile and chalcophile elements between sulfide, olivine, and glass in a naturally reduced basalt from Disko Island, Greenland, in: Proceedings of the Lunar and Planetary Science Conference. pp. 471–483.

Kravuchuk, I.K., Chernysheva, I., Urosov, S., 1981. Element distribution between plagioclase and groundmass as an indicator for crystallization conditions of the basalts in the southern vent of Tolbachik. Geochem. Int. 17, 18–24.

Langmuir, C.H., Vocke, R.D., Hanson, G.N., Hart, S.R., 1978. A General Mixing Equation with Applications to Icelandic Basalts. Earth Planet. Sci. Lett. 37, 380–392.

La Tourrette, T.Z., Burnett, D.S., Bacon, C.R., 1991. Uranium and minor-element partitioning in Fe-Ti oxides and zircon from partially melted granodiorite, Crater Lake, Oregon. Geochim. Cosmochim. Acta 55, 457–469.

Leeman, W.P., Lindstrom, D.J., 1978. Partitioning of Ni2+ between basaltic and synthetic melts and olivines—an experimental study. Geochim. Cosmochim. Acta, Experimental trace element geochemistry 42, 801–816.

Leeman, W.P., Scheidegger, K.F., 1977. Olivine/liquid distribution coefficients and a test for crystal-liquid equilibrium. Earth Planet. Sci. Lett. 35, 247–257.

Lemarchand, F., Villemant, B., Calas, G., 1987. Trace element distribution coefficients in alkaline series. Geochim. Cosmochim. Acta 51, 1071–1081.

Li, C., Naldrett, A.., 1999. Geology and petrology of the Voisey's Bay intrusion: reaction of olivine with sulfide and silicate liquids. Lithos 47, 1–31.

Luhr, J.F., Carmichael, I.S.E., Varekamp, J.C., 1984. The 1982 eruptions of El Chichón Volcano, Chiapas, Mexico: Mineralogy and petrology of the anhydrite-bearing pumices. J. Volcanol. Geotherm. Res. 23, 69–108.

Malvin, D.J., Drake, M.J., 1987. Experimental determination of crystal/melt partitioning of Ga and Ge in the system forsterite-anorthite-diopside. Geochim. Cosmochim. Acta 51, 2117–2128.

Matsui, Y., Onuma, N., Nagasawa, H., Higuchi, H., Banno, S., 1977. Crystal structure control in trace element partition between crystal and magma. Tectonics 100, 315–324.

McBride, J., 2015. Assessment Report for Diamond Drilling on the Stillwater Canada Inc. Bermuda Property (Assessment Report No. NTS 42D/16), Assessment Report.

McCallum, I.S., Charette, M.P., 1978. Zr and Nb partition coefficients: Implications for the genesis of mare basalts, KREEP and sea floor basalts. Geochim. Cosmochim. Acta, Experimental trace element geochemistry 42, 859–869.

McCarthy, T.S., Cawthorn, R., 1983. The Geochemistry of Vanadiferous Magnetite in the Bushveld Complex: Implications for Crystallization Mechanisms in Layered Complexes. Miner. Deposita 18, 505–518.

McCarthy, T.S., Cawthorn, R.G., Wright, C.J., McIver, J.R., 1985. Mineral layering in the Bushveld Complex; implications of Cr abundances in magnetite from closely spaced magnetitite and intervening silicate-rich layers. Econ. Geol. 80, 1062–1074.

McKenzie, D., O'Nions, R.K., 1991. Partial Melt Distributions from Inversion of Rare Earth Element Concentrations. J. Petrol. 32, 1021–1091.

Mysen, B.O., 1978. Experimental determination of nickel partition coefficients between liquid, pargasite, and garnet peridotite minerals and concentration limits of behavior according to Henry's law at high pressure and temperature. Am. J. Sci. 278, 217–243.

Nabalek, P.I., 1980. Nickel partitioning between olivine and liquid in natural basalts: Henry's Law behavior. Earth Planet. Sci. Lett. 48, 293–302.

Nadoll, P., Angerer, T., Mauk, J.L., French, D., Walshe, J., 2014. The chemistry of hydrothermal magnetite: A review. Ore Geol. Rev. 61, 1–32.

Nadoll, P., Mauk, J.L., Hayes, T.S., Koenig, A.E., Box, S.E., 2012. Geochemistry of magnetite from hydrothermal ore deposits and host rocks of the Mesoproterozoic Belt Supergroup, United States. Econ. Geol. 107, 1275–1292.

Nadoll, P., Mauk, J.L., Hayes, T.S., Koenig, A.E., Hofstra, A.H., Box, S.E., 2009. Geochemistry of magnetite from hydrothermal ore deposits and their host rocks in the Proterozoic Belt Supergroup, USA, in: Smart Science for Exploration and Mining, Proc 10th Biennial Meeting, Townsville. pp. 129–131.

Naldrett, A.J., 1992. A model for the Ni-Cu-PGE ores of the Noril'sk region and its application to other areas of flood basalt. Econ. Geol. 87, 1945–1962.

Namur, O., Charlier, B., Toplis, M.J., Higgins, M.D., Liegeois, J.P., Vander Auwera, J., 2010. Crystallization Sequence and Magma Chamber Processes in the Ferrobasaltic Sept Iles Layered Intrusion, Canada. J. Petrol. 51, 1203–1236.

Nash, W.P., Crecraft, H.R., 1985. Partition coefficients for trace elements in silicic magmas. Geochim. Cosmochim. Acta 49, 2309–2322.

Nielsen, R.L., Gallahan, W.E., Newberger, F., 1992. Experimentally determined mineral-melt partition coefficients for Sc, Y and REE for olivine, orthopyroxene, pigeonite, magnetite and ilmenite. Contrib. Mineral. Petrol. 110, 488–499.

Nikogosyan, I.K., Sobolev, A.V., 1997. Ion-microprobe analysis of melt inclusions in olivine: experience in estimating the melt-olivine distribution coefficients of impurity elements. Geokhimiya 149–157.

Paster, T.P., Schauwecker, D.S., Haskin, L.A., 1974. The behavior of some trace elements during solidification of the Skaergaard layered series. Geochim. Cosmochim. Acta 38, 1549–1577.

Paton, C., Hellstrom, J., Paul, B., Woodhead, J., Hergt, J., 2011. Iolite: Freeware for the visualisation and processing of mass spectrometric data. J. Anal. At. Spectrom. 26, 2508–2518.

Ripley, E.M., Li, C., 2011. A review of conduit-related Ni-Cu-(PGE) sulfide mineralization at the Voisey's Bay Deposit, Labrador, and the Eagle Deposit, northern Michigan. Rev. Econ. Geol. 17, 181–197.

Ripley, E.M., Taib, N.I., Li, C., Moore, C.H., 2007. Chemical and mineralogical heterogeneity in the basal zone of the Partridge River Intrusion: implications for the origin of Cu–Ni sulfide mineralization in the Duluth Complex, midcontinent rift system. Contrib. Mineral. Petrol. 154, 35.

Rollinson, H., 1993. Using Geochemical Data: Evaluation, Presentation, Interpretation. Longman.

Rusk, B.G., Oliver, N.H.S., Zhang, D., Brown, A., Lilly, R., Jungmann, D., 2009. Compositions of Magnetite and Sulfide from Barren and Mineralized IOCG Deposits in the Eastern Succession of the Mt Isa Inlier, Australia, in: 2009 Portland GSA Annual Meeting.

Ruthart, R., 2013. Characterization of High-PGE Low-Sulphur Mineralization at the Marathon PGE-Cu Deposit, Ontario (MSc). University of Waterloo.

Seifert, S., O'Neill, H.S.C., Brey, G., 1988. The partitioning of Fe, Ni and Co between olivine, metal, and basaltic liquid: An experimental and thermodynamic investigation, with application to the composition of the lunar core. Geochim. Cosmochim. Acta 52, 603–616.

Shaw, C.S.J., 1997. The petrology of the layered gabbro intrusion, eastern gabbro, Coldwell alkaline complex, Northwestern Ontario, Canada: evidence for multiple phases of intrusion in a ring dyke. Lithos, 40, 243-259.

Shahabi Far, M., 2016. The magmatic and volatile evolution of gabbros hosting the Marathon PGE-Cu deposit: evolution of a conduit system (PhD Dissertation). University of Windsor, Windsor.

Shahabi Far, M., Samson, I.M., Gagnon, J.E., Good, D.J., Linnen, R.L., Layne, G.D., Wing, B.A., 2018. Identifying externally derived sulfur in conduit-type Cu–platinum-group element deposits: The importance of multiple sulfur isotope studies. Geology.

Singoyi, B., Danyushevsky, L., Davidson, G.J., Large, R., Zaw, K., 2006. Determination of trace elements in magnetites from hydrothermal deposits using the LA ICP-MS technique, in: SEG Keystone Conference. Denver, USA.

Skulski, T., Minarik, W., Watson, E.B., 1994. High-pressure experimental trace-element partitioning between clinopyroxene and basaltic melts. Chem. Geol., Trace-element Partitioning with Application to Magmatic Processes 117, 127–147.

Sobolev, A.V., Migdisov, A.A., Portnyagin, M.V., 1996. Incompatible Element Partitioning between Clinopyroxene and Basalt Liquid Revealed by the Study of Melt Inclusions in Minerals from Troodos Lavas, Cyprus 4, 11.

Song, X.-Y., Qi, H.-W., Hu, R.-Z., Chen, L.-M., Yu, S.-Y., Zhang, J.-F., 2013. Formation of thick stratiform Fe-Ti oxide layers in layered intrusion and frequent replenishment of fractionated mafic magma: Evidence from the Panzhihua intrusion, SW China: Magnetite deposits in layered insutrions. Geochem. Geophys. Geosystems 14, 712–732.

Tacker, R.C., Candela, P.A., 1987. Partitioning of Molybdenum between Magnetite and Melt: A Preliminary Experimental Study of Partitioning of Ore Metals between Silicic Magmas and Crystalline Phases. Econ. Geol. 82, 1827–1838.

Tegner, C., Cawthorn, R.G., Kruger, F.J., 2006. Cyclicity in the Main and Upper Zones of the Bushveld Complex, South Africa: Crystallization from a Zoned Magma Sheet. J. Petrol. 47, 2257–2279.

Thériault, R.D., Barnes, S.-J., Severson, M.J., 2000. Origin of Cu-Ni-PGE Sulfide Mineralization in the Partridge River Intrusion, Duluth Complex, Minnesota. Econ. Geol. 95, 929–943.

Toplis, M.J., Corgne, A., 2002. An experimental study of element partitioning between magnetite, clinopyroxene and iron-bearing silicate liquids with particular emphasis on vanadium. Contrib. Mineral. Petrol. 144, 22–37.

Toplis, M.J., Libourel, G., Carroll, M.R., 1994. The role of phosphorus in crystallisation processes of basalt: An experimental study. Geochim. Cosmochim. Acta 58, 797–810.

Vannucci, R., Bottazzi, P., Wulff-Pedersen, E., Neumann, E.-R., 1998. Partitioning of REE, Y, Sr, Zr and Ti between clinopyroxene and silicate melts in the mantle under La Palma (Canary Islands): implications for the nature of the metasomatic agents. Earth Planet. Sci. Lett. 158, 39–51.

Ward, L.A., Holwell, D.A., Barry, T.L., Blanks, D.E., Graham, S.D., 2018. The use of magnetite as a geochemical indicator in the exploration for magmatic Ni-Cu-PGE sulfide deposits: A case study from Munali, Zambia. J. Geochem. Explor. 188, 172–184.

Watkinson, D.H., Ohnenstetter, D., 1992. Hydrothermal Origin of Platinum-Group Mineralization in the Two Duck Lake Intrusion, Coldwell Complex, Northwestern Ontario. Can. Mineral. 30, 121–136.

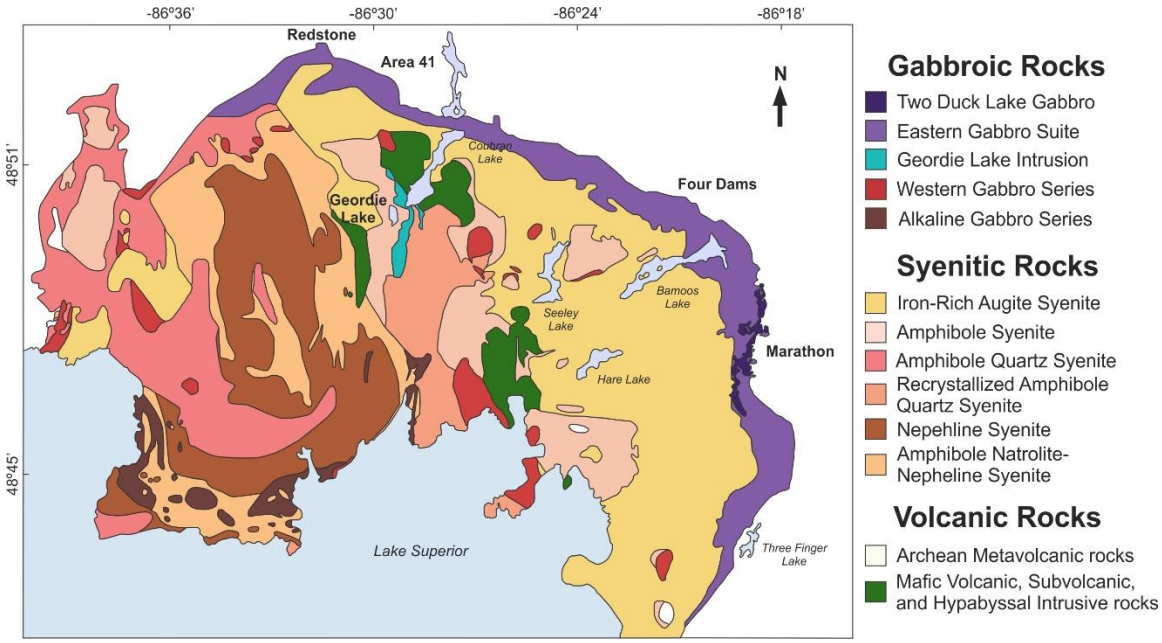

Figure 4.1 A geologic map of the Colwell Complex showing the location of the various mineralized deposits that occur along the Eastern Gabbro (modified after Good et al., 2015).

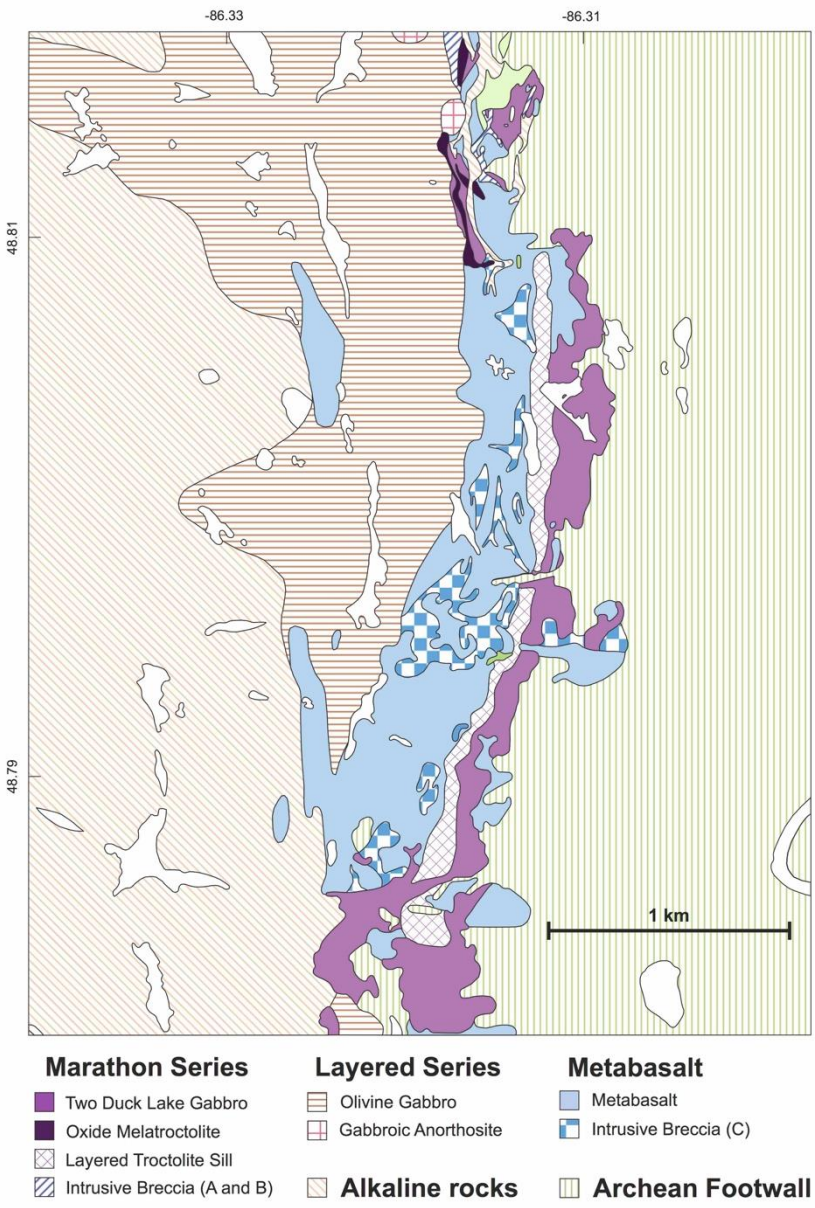

Figure 4.2 A geologic map of the Marathon Cu-Pd deposit showing the locations of, and relationships between, the three gabbroic series: metabasalt, Layered Series, Marathon Series (modified after Good et al., 2015).

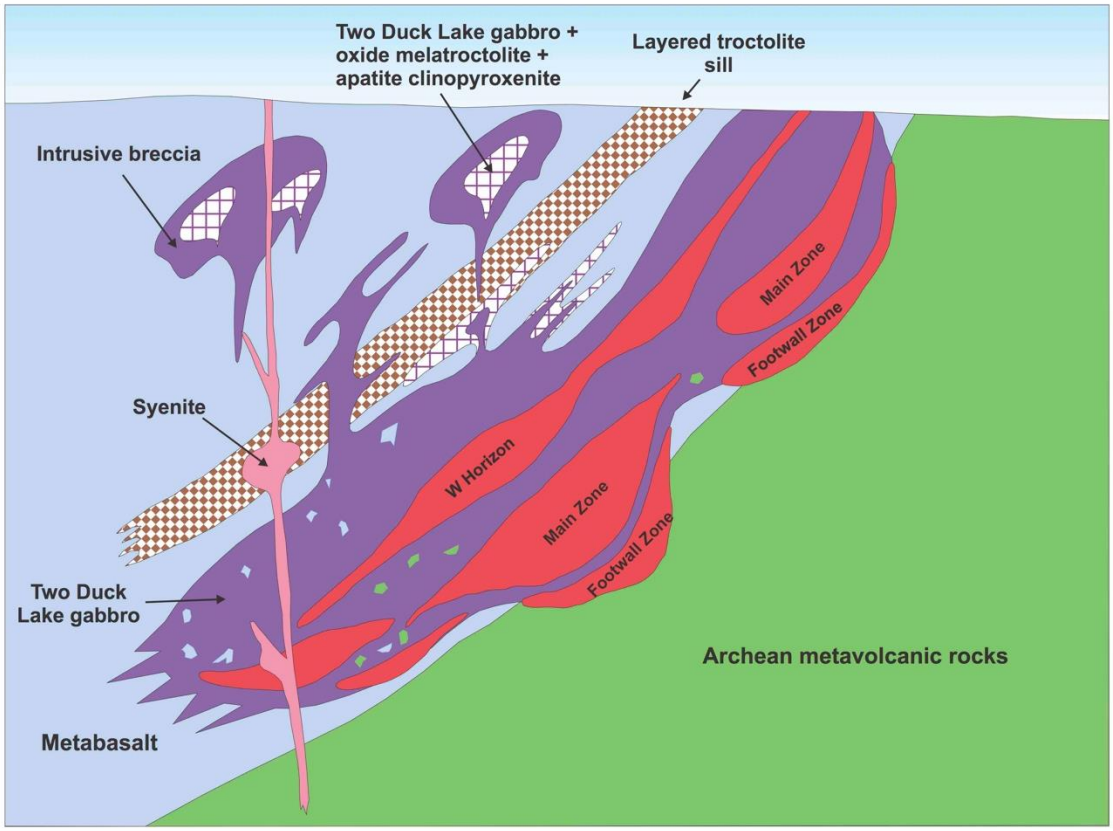

Figure 4.3 A cross-section of the Marathon deposit showing the location of the Footwall Zone, Main Zone, and W Horizon (modified after Shahabi Far, 2016).

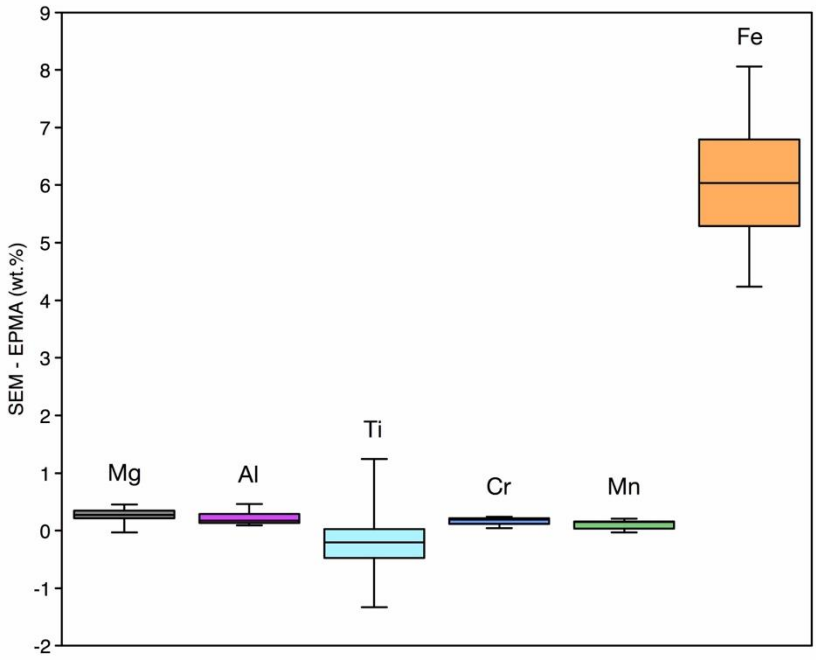

Figure 4.4 Box-whisker diagram illustrating the difference in major-element composition of Fe-Ti oxide intergrowths obtained by energy- and wavelength-dispersive spectroscopy. Note that Fe is consistently overestimated by energy-dispersive spectroscopy.

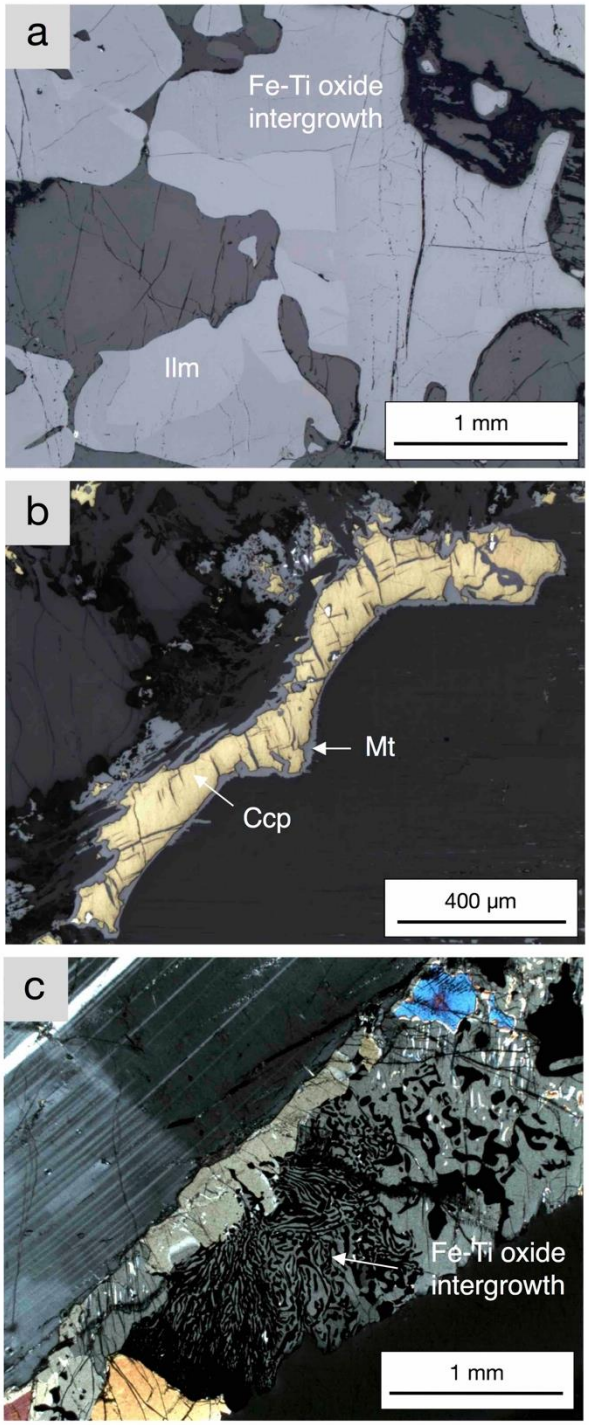

Figure 4.5 Reflected-light images of a) Fe-Ti oxide intergrowths with crystals of ilmenite and b) magnetite that occurs as a rim and as protrusions throughout a chalcopyrite grain. c) A cross-polarized image that illustrates the occurrence of myrmekitic Fe-Ti oxides in orthopyroxene. Mt = magnetite, ilm = ilmenite, ccp = chalcopyrite.

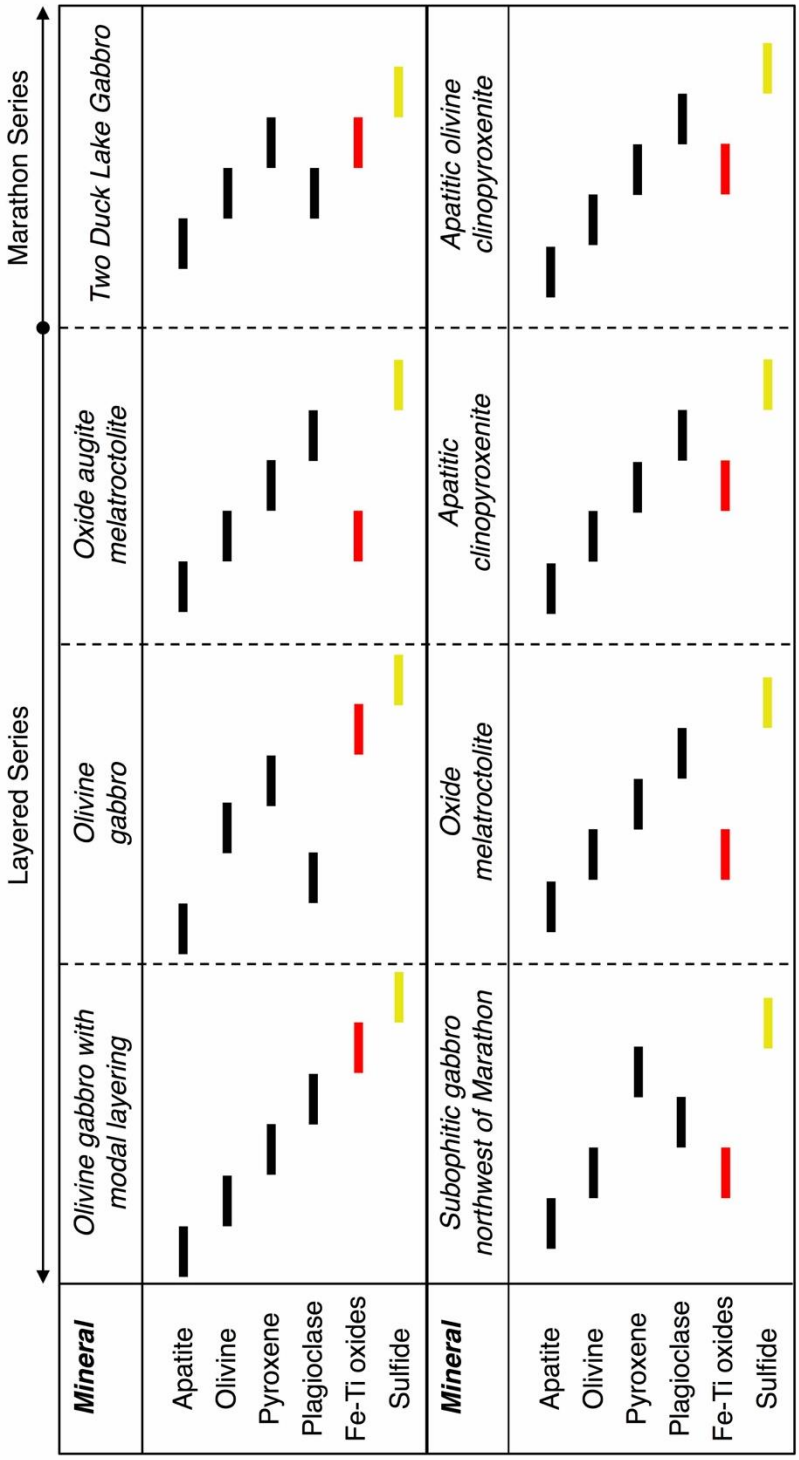

Figure 4.6 Schematic diagram illustrating the relative sequence of crystallization of apatite, olivine, pyroxene, plagioclase, magnetite, and sulfides in the various Layered Series and Marathon Series rock types. The location of Fe-Ti oxides and sulfides are denoted in red and yellow, respectively.

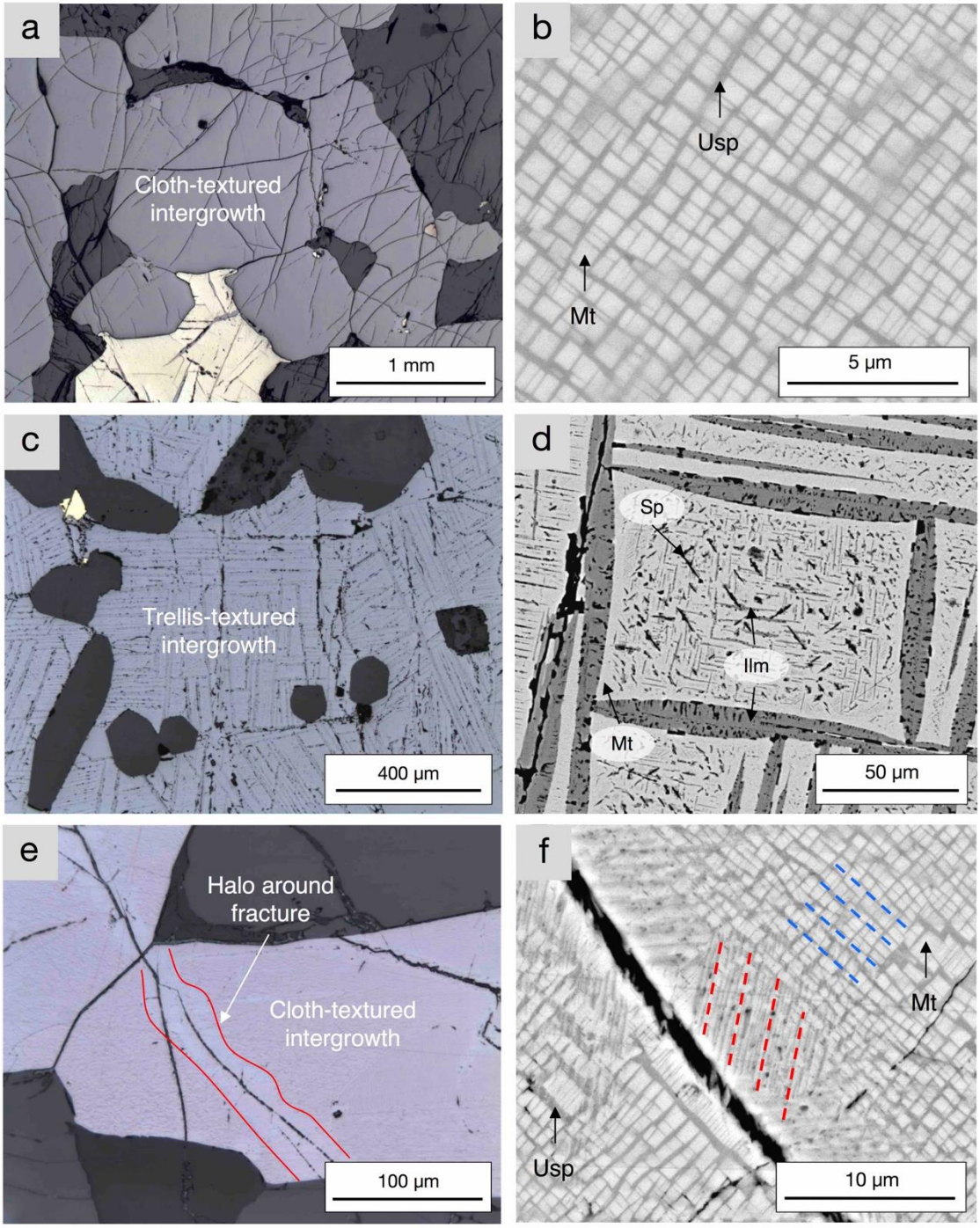
a
Cloth-textured intergrowth
1 mm
b
Usp
Mt
5 µm
c
Trellis-textured intergrowth
400 µm
d
Sp
Ilm
Mt
50 µm
e
Halo around fracture
Cloth-textured intergrowth
100 µm
f
Mt
Usp
10 µm

Figure 4.7 (A) Low-magnification reflected-light image of cloth-textured Fe-Ti oxide intergrowths. Note the homogeneity of these intergrowths under low-magnification. (B) High-magnification backscatter electron (BSE) image of a cloth-textured Fe-Ti oxide intergrowth illustrating the sub-micron scale intergrowth of magnetite and ulvöspinel. (C) Low-magnification reflected-light image of a trellis-textured Fe-Ti oxide intergrowth. Note that thick trellis lamellae of ilmenite are readily visible at this scale. (D) High-magnification BSE images of a trellis-textured Fe-Ti oxide intergrowth in which both fine and thick trellis lamellae of ilmenite are visible, along with spinel. (E) Low-magnification reflected-light image of a cloth-textured Fe-Ti oxide intergrowth with a fracture cutting across the grain. Note the halo surrounding the fracture that appears brighter in reflected light than the surrounding cloth intergrowth. (F) High-magnification BSE image of a halo surrounding a facture in a cloth-textured intergrowth. Note the trellis-like lamellae that extend outwards from the fracture. The blue lines depict the orientation of the cloth network and the red lines depict the orientation of the trellis lamellae around the fracture. Mt = magnetite, usp = ulvöspinel, ilm = ilmenite, sp = spinel.

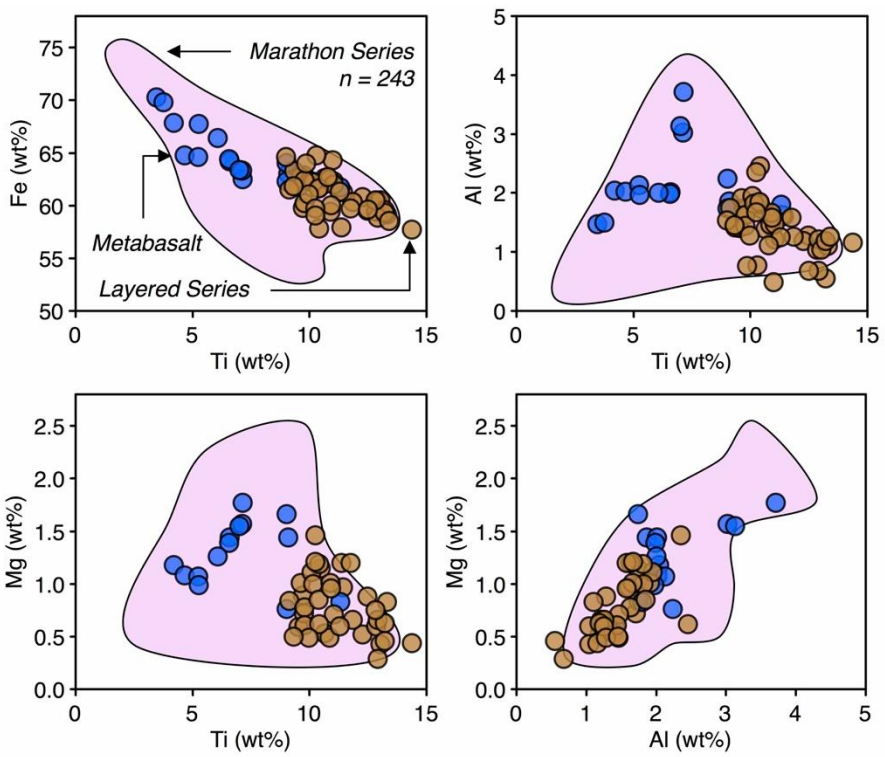

Figure 4.8 Binary diagrams illustrating variations in the major-element composition of Fe-Ti oxide intergrowths hosted by metabasalt, Layered Series, and Marathon Series. The number of data points (n) in the field for Marathon Series is noted.

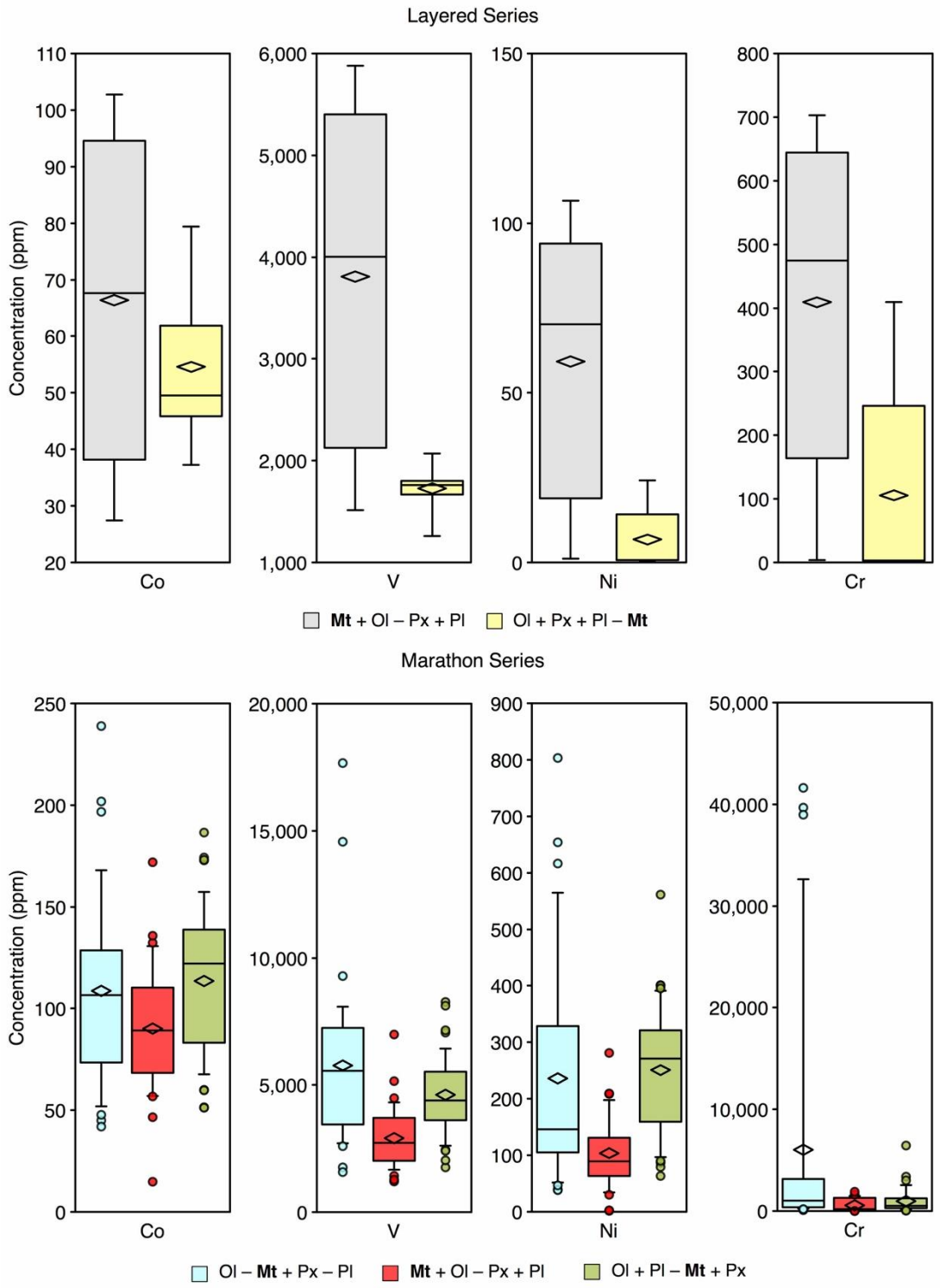
Layered Series
Concentration (ppm)
Co
V
Ni
Cr
Mt + Ol – Px + Pl
Ol + Px + Pl – Mt
Marathon Series
Concentration (ppm)
Co
V
Ni
Cr
Ol – Mt + Px – Pl
Mt + Ol – Px + Pl
Ol + Pl – Mt + Px

Figure 4.9 Box-whisker diagrams illustrating the range of concentration of Co, V, Ni, and Cr in Fe-Ti oxide intergrowths from the Layered and Marathon Series that crystallized at different times relative to silicates. With respect to the timing of oxide crystallization, the rock types include i) Mt+Ol – Px+Pl: *subophitic gabbro NW of Marathon*, *oxide melatroctolite, oxide augite melatroctolite*, ii) Ol – Mt+Px – Pl: *apatitic olivine clinopyroxenite, apatitic clinopyroxenite*, iii) Ol+Pl – Mt+Px: *TDLG*, and iv) Ol+Px+Pl – Mt: *olivine gabbro*. Mt = magnetite, ol = olivine, px = pyroxene, pl = plagioclase.

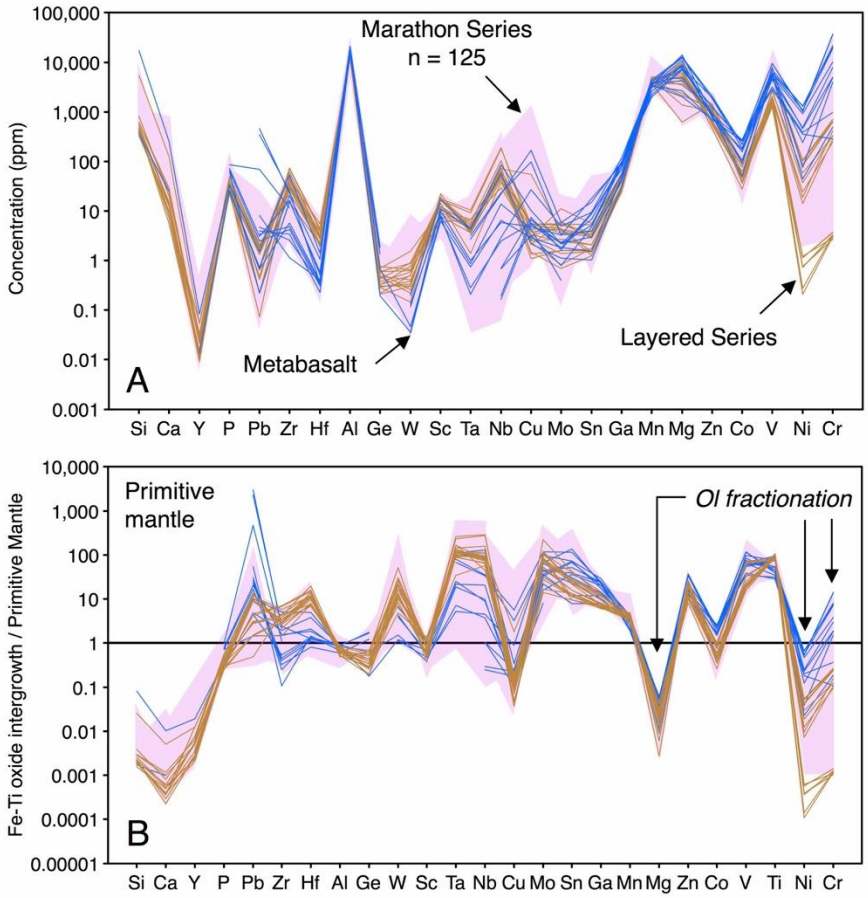

Figure 4.10 Spider diagrams illustrating (A) the bulk composition of Fe-Ti oxide intergrowths hosted by metabasalt, Layered Series, and Marathon Series and (B) the bulk composition of Fe-Ti oxide intergrowths normalized to primitive mantle. The purple field represents the bulk composition of Fe-Ti oxide intergrowths hosted by Marathon Series. The elements are listed in order of increasing compatibility into magnetite. The number of data points (n) in the field for Marathon Series is noted.

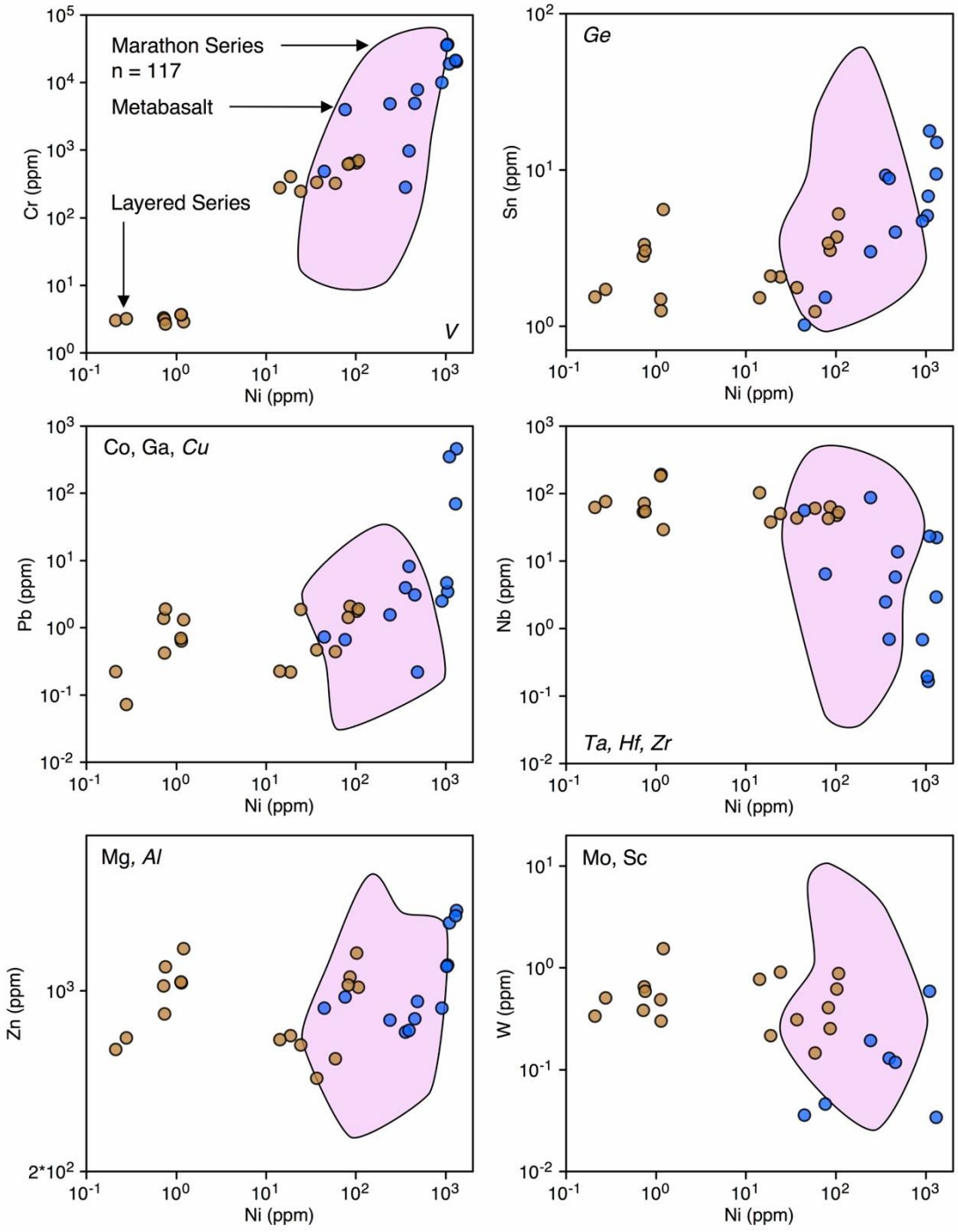

Figure 4.11 Binary diagrams illustrating variations in minor to trace elements as a function Ni content in Fe-Ti oxide intergrowths hosted by metabasalt, Layered Series, and Marathon Series. The elements noted in the corners of the diagrams denote the elements that exhibit similar trends to those plotted on the y-axes. The purple field represents the composition of Fe-Ti oxide intergrowths hosted by Marathon Series. The number of data (n) points in the field for Marathon Series is noted.

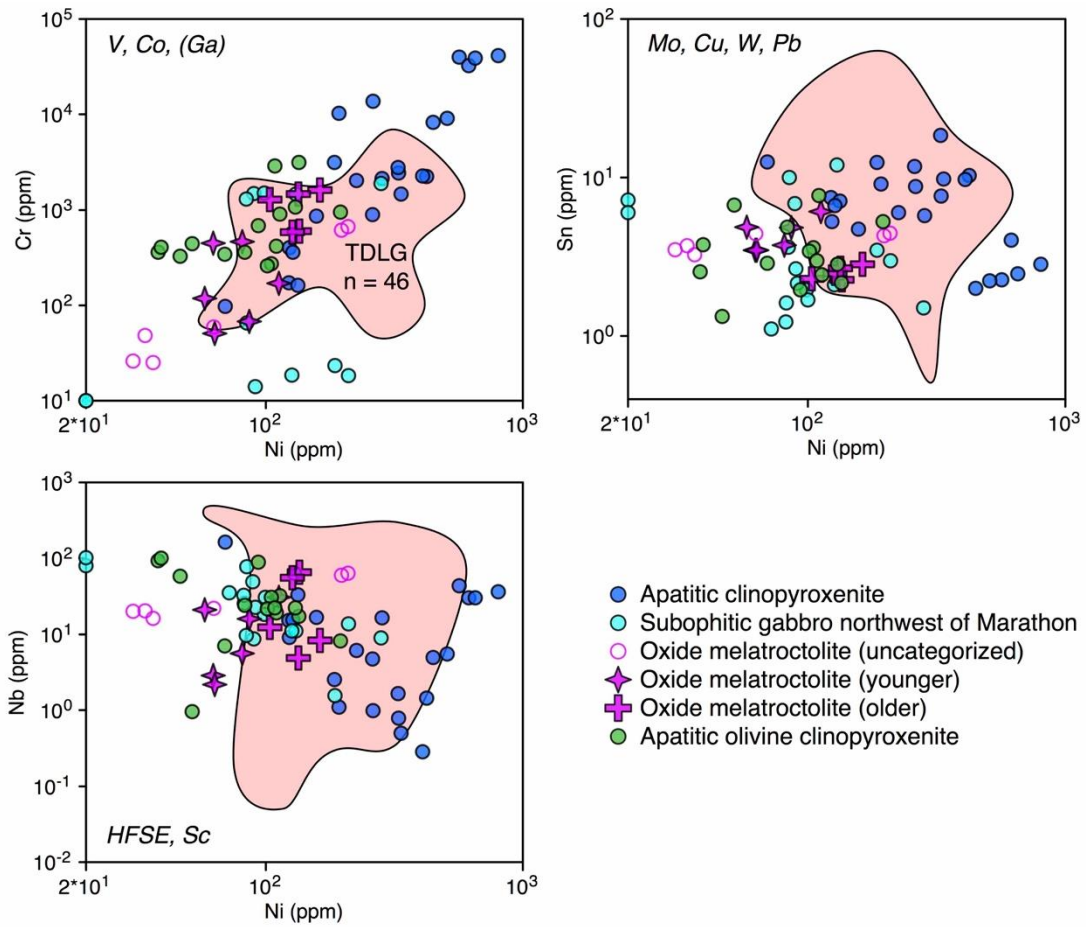

Figure 4.12 Binary diagrams illustrating variations in minor to trace elements as a function Ni content in Fe-Ti oxide intergrowths hosted by the various rock types of the Marathon Series. The elements noted in the corners of the diagrams denote the elements that exhibit similar trends to those plotted on the y-axes. The red field represents the composition of Fe-Ti oxide intergrowths hosted by Two Duck Lake gabbro. The number of data (n) points in the field for TDLG is noted.

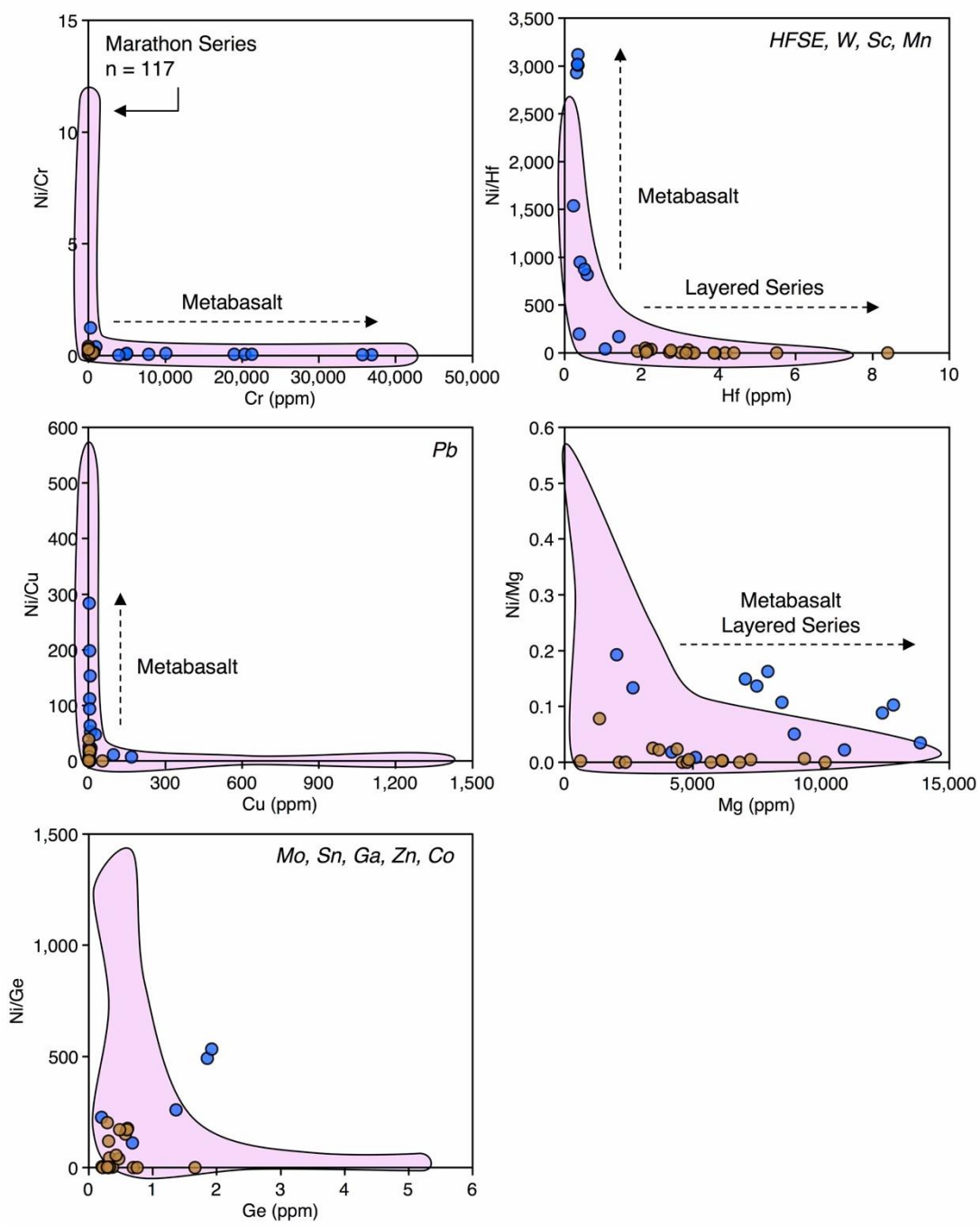

Figure 4.13 Ratio-element binary diagrams illustrating variations in element/Ni values relative to Ni in Fe-Ti oxide intergrowths hosted by metabasalt, Layered Series, and Marathon Series. The elements noted in the corners of the diagrams denote the elements that exhibit similar trends to those plotted on the x-axes. The purple field represents the composition of Fe-Ti oxide intergrowths hosted by Marathon Series. The dashed arrows represent the dominant compositional trends exhibited by oxides hosted by each of the rock series. The number of data (n) points in the field for Marathon Series is noted.

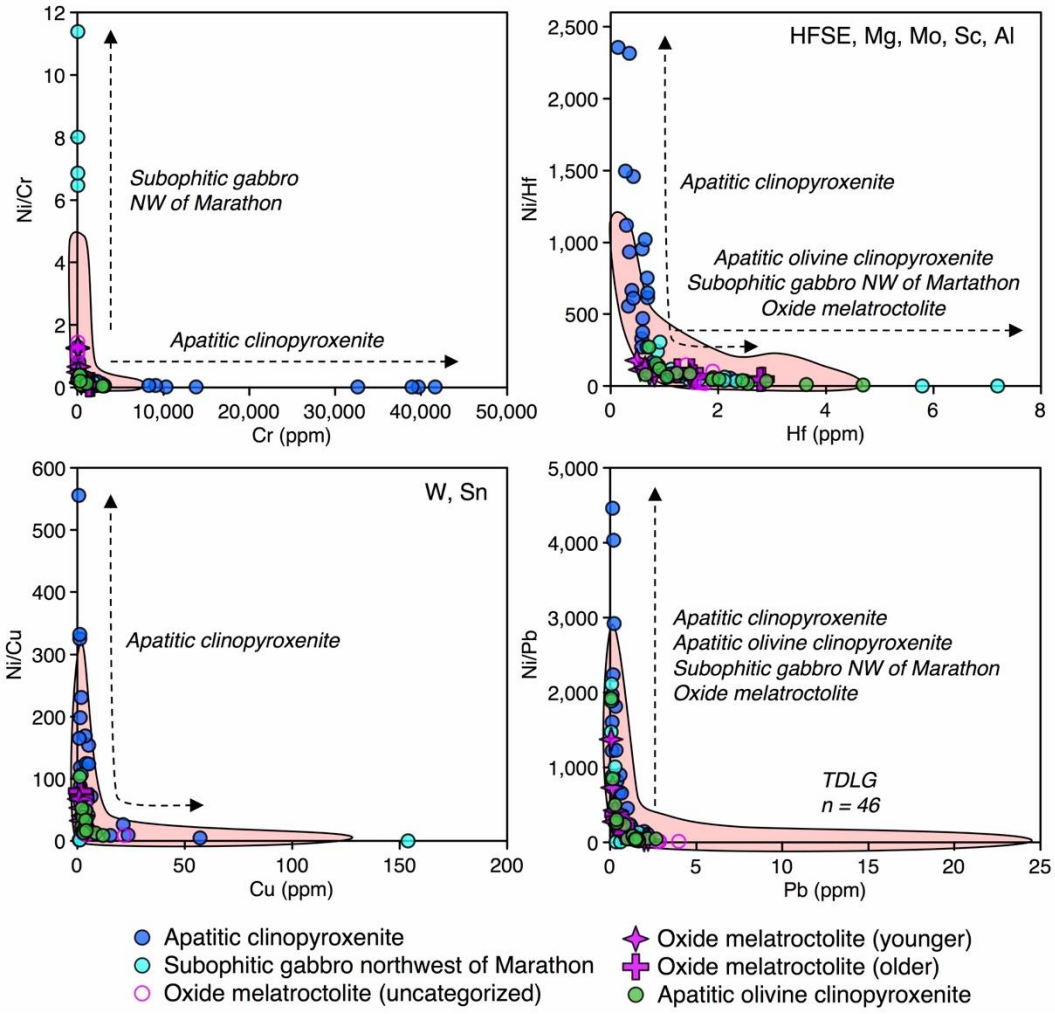

Figure 4.14 Ratio-element binary diagrams illustrating variations in element/Ni values relative to Ni in Fe-Ti oxide intergrowths hosted by the various rock types of the Marathon Series. The elements noted in the corners of the diagrams denote the elements that exhibit similar trends to those plotted on the x-axes. The red field represents the composition of Fe-Ti oxide intergrowths hosted by Two Duck Lake gabbro located in the Marathon deposit. The dashed arrows represent the dominant compositional trends exhibited by oxides hosted by each of the rock types. The number of data (n) points in the field for TDLG is noted.

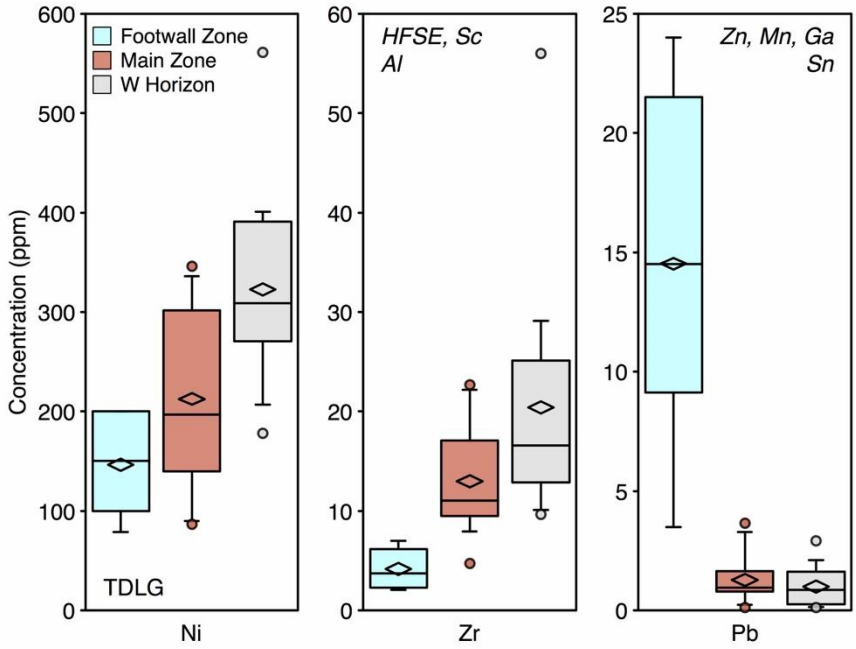

Figure 4.15 Box-whisker diagrams illustrating the variation in trace-element concentration in Fe-Ti oxide intergrowths hosted by Footwall Zone, Main Zone, and W Horizon mineralization. The elements noted in the corners of the diagrams denote the elements that exhibit similar trends among mineralized zones as the plotted element.

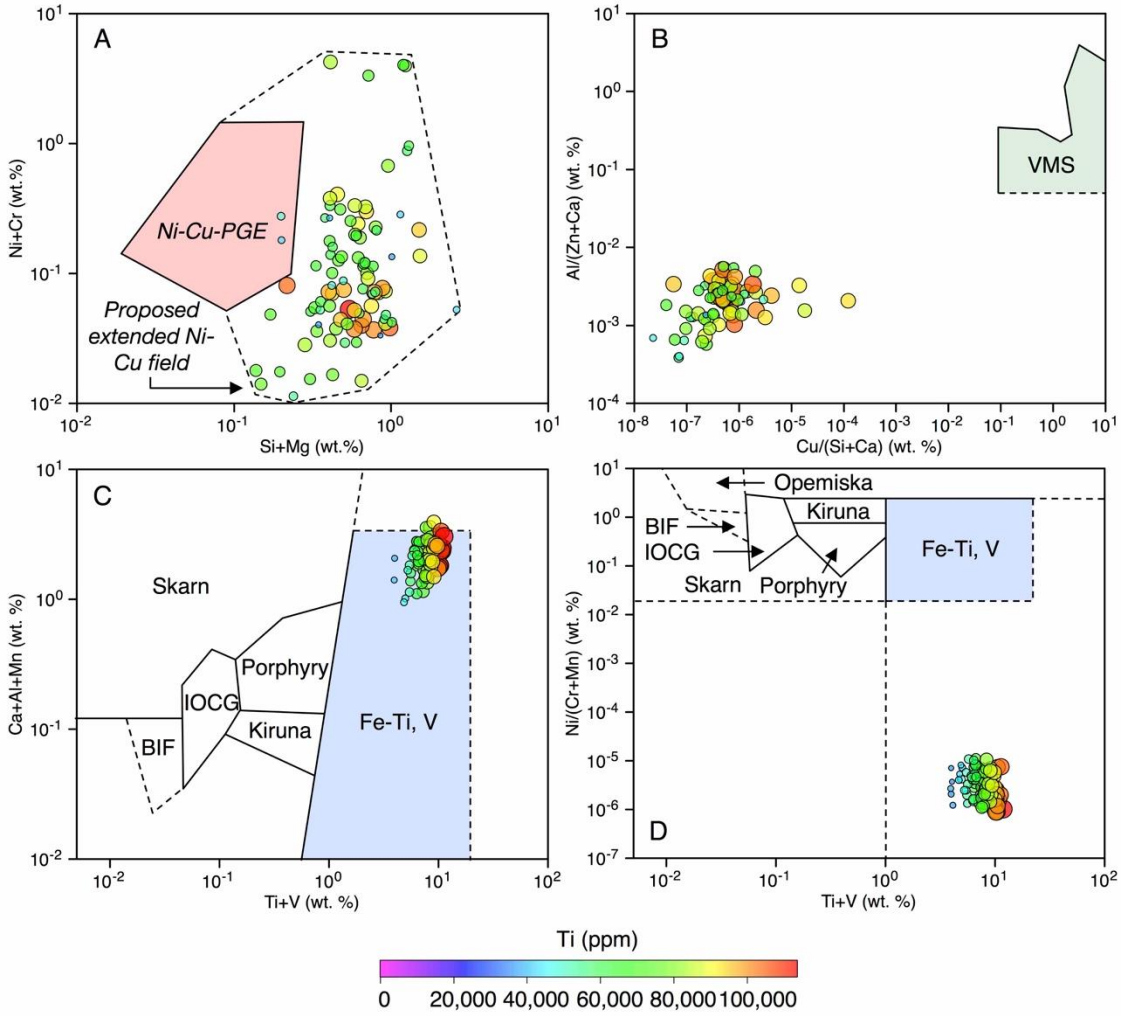

Figure 4.16 Binary diagrams illustrating the variation in (A) Ni+Cu and Si+Mg, (B) Al/(Zn+Ca) and Cu/(Si+Ca), (C) Ca+Al+Mn and Ti+V, and (D) Ni/(Cr+Mn) and Ti+V contents of Fe-Ti oxide intergrowths hosted by mineralized Marathon Series rocks. The Ti content of the Fe-Ti oxide intergrowths is denoted by the size and color of the symbols. These diagrams are modified from Dupuis and Beaudoin (2011).

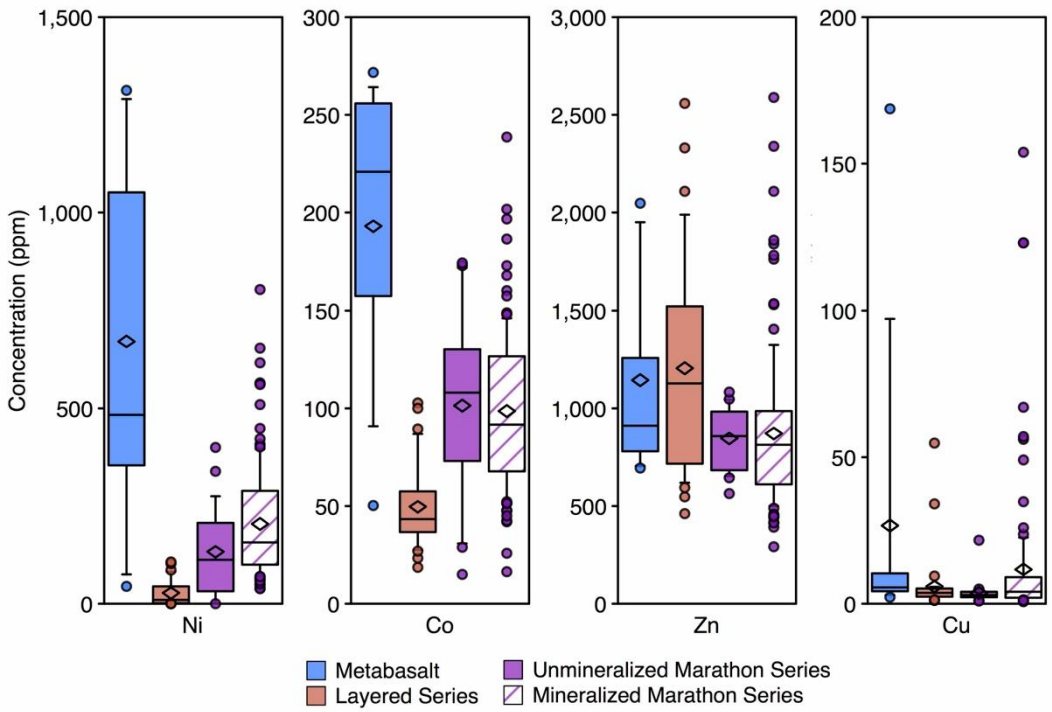

Figure 4.17 Box-whisker diagram illustrating the variation in Cu, Zn, Co, and Ni content of Fe-Ti oxide intergrowths hosted by unmineralized metabasalt, Layered Series, and Marathon Series, and mineralized Marathon Series rocks.

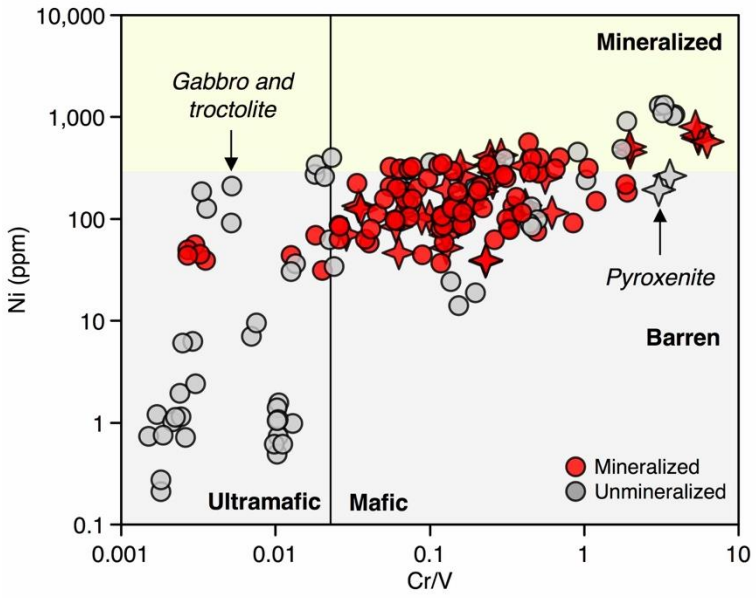

Figure 4.18 Binary diagram illustrating the variation in Ni and Cr/V contents of Fe-Ti oxide intergrowths from unmineralized metabasalt, Layered Series, and Marathon Series, and mineralized Marathon Series. The circles and stars represent mafic (gabbros and troctolites) and ultramafic rocks (pyroxenites), respectively. The grey and red data points represent unmineralized and mineralized rock, respectively. The diagram is modified from Ward et al. (2018).

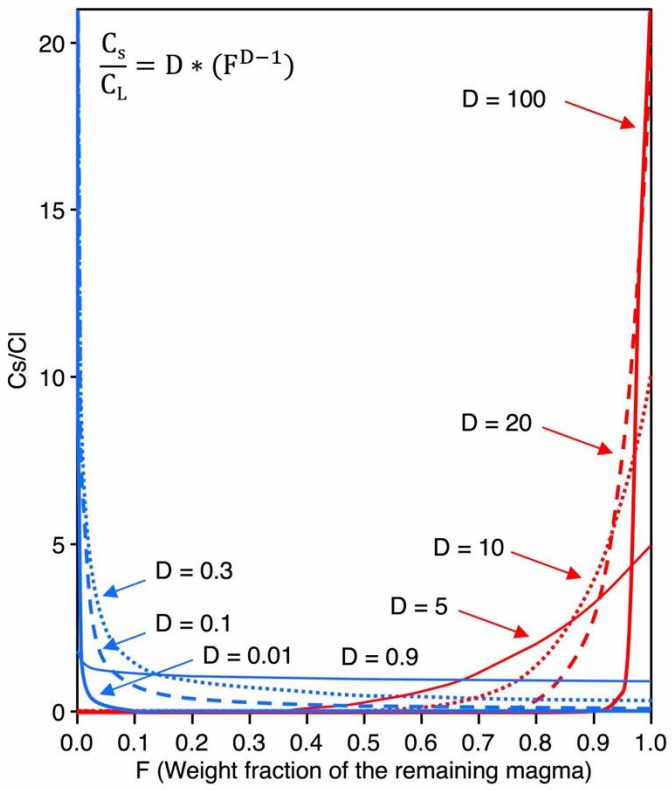

Figure 4.19 A model illustrating the variation in concentration of variably-compatible and-incompatible elements in a mineral as a function of the degree of fractional crystallization of that mineral from a melt. The blue and red lines represent the trends expected from elements that have mineral/melt partition coefficients less than 1 and greater than 1, respectively.

Table 4.1 Mineral/basaltic melt partition coefficients for plagioclase, clinopyroxene, olivine, apatite, and magnetite

Element	Plagioclase	References	Clinopyroxene	References	Olivine	References
Mg	0.028 - 0.053	*1, 2, 3*	-	-	1.96 - 8	*29, 30, 31, 32*
Al	1.63	*4*	0.1 - 0.37	*10*	0.0101 - 0.0222	*29*
P	0.065 - 0.429	*1, 5*	0.004 - 0.05	*11, 12*	0.1	*11*
Sc	0.016 - 1.458	*3, 5*	0.808 - 3.3	*7, 13, 14, 15, 16, 17*	0.12 - 0.38	*7, 15, 29, 30, 32, 34*
V	0.01 - 0.27	*5, 6*	0.22 - 6.18	*6, 13, 16, 17, 18, 19*	0.088 - 0.09	*6, 18*
Cr	0.02 - 0.191	*3, 5, 6*	1.66 - 36	*6, 13, 14, 15, 17, 18, 19*	0.63 - 5.2	*6, 18, 29, 30, 32, 35*
Mn	0.016 - 0.184	*2, 3, 4, 5, 7*	0.55 - 1.6	*6, 7, 14, 15, 18, 20*	0.5 - 1.75	*6, 7, 15, 18, 20, 29, 30, 32*
Co	0.026 - 1.03	*2, 5, 6, 7*	0.68 - 2.08	*6, 7, 14, 15, 18*	1.1 - 6.3	*6, 7, 15, 18, 29, 30, 32, 36*
Ni	0.06 - 1.16	*5, 6*	1.2 - 10	*6, 15, 18, 21*	1.35 - 48	*6, 15, 18, 21, 30, 32, 36, 38, 39, 40*
Cu	0.004 - 0.17	*6, 7*	0.071 - 0.36	*6, 7, 13*	0.023 - 0.55	*6, 7, 30*
Zn	0.11 - 0.18	*2, 6, 7*	0.41 - 0.5	*6, 7, 14*	0.8 - 1.8	*6, 7, 30*
Ga	1.7	*7*	0.25 - 0.74	*7, 13*	0.04 - 0.25	*7, 30*
Ge	-	-	-	-	-	-
Zr	0.0022 - 0.0146	*1, 3, 5, 8*	0.001 - 1.53	*8, 13, 16, 17, 19, 22, 23, 24, 25, 26, 27, 28*	-	-
Nb	0.002 - 0.139	*3, 5, 8, 9*	0.004 - 0.119	*8, 9, 13, 16, 17, 23, 25, 26, 27, 28*	0.01	*9*
Mo	-	-	-	-	-	-
Sn	-	-	-	-	-	-
Hf	0.01 - 0.153	*3, 9*	0.004 - 0.44	*9, 13, 16, 17, 19, 20, 23, 25, 28*	0.01	*9*
Ta	0.042 - 0.17	*3*	0.011 - 0.261	*26*	-	-
W	-	-	-	-	-	-

Table 4.1 Continued

Element	Apatite	References	Magnetite	References
Mg	-	-	1 - 10.3	*41, 42*
Al	-	-	0.12 - 0.29	*41, 42*
P	-	-	0.0018 - 0.0050	*41, 42*
Sc	0.22	*7*	0.67 - 5.76	*34, 43*
V	-	-	0.02 - 6.85	*34*
Cr	-	-	153	*44*
Mn	0.13	*7*	1.4	*43*
Co	0.03	*7*	3.4	*43*
Ni	-	-	31 - 65	*34*
Cu	0.28	*7*	0.42	*43*
Zn	0.25	*7*	2.6	*43*
Ga	0.25	*7*	2	*43*
Ge	-	-	0.11	*45*
Zr	-	-	0.02 - 1.78	*34*
Nb	-	-	0.01 - 1.8	*34*
Mo	-	-	0.21 - 16	*6, 47*
Sn	-	-	1	*33*
Hf	-	-	0.16	*43*
Ta	-	-	0.23	*43*
W	-	-	2.3	*37*

**Partition coefficients are primarily for mineral-basalt melt. Few partition coefficients are from silicate melts of other basaltic composition (e.g., basalt-andesite)*

***References**: 1 - Bindeman and Davis (2000), 2 - Kravuchuk et al. (1981), 3 - Aignertorres et al. (2007), 4 - Higuchi and Nagasawa (1969), 5 - Bindeman et al. (1998), 6 - Bougault and Hekian (1974), 7 - Paster et al. (1974), 8 - McCallum and Charette (1978), 9 - McKenzie and O'Nions (1991), 10 - Jones and Layne (1997), 11 - Brunet and Chazot (2001), 12 - Baker and Wyllie (1992), 13 - Hart and Dunn (1993), 14 - Matsui et al. (1977), 15 - Dale and Henderson (1972), 16 - Jenner et al. (1994), 17 - Harui et al. (1994), 18 - Duke (1976) , 19 - Skulski et al. (1994), 20 - Dunn (1987), 21 - Mysen (1978), 22 - Sobolev et al. (1996), 23 - Johnson and Kinzler (1989), 24 - Vannucci et al. (1998), 25 - Johnson (1998), 26 - Forsythe et al. (1994), 27 - Keleman and Dunn (1992), 28 - Johnson (1994), 29 - Beattie (1994), 30 - Kloeck and Palme (1988), 31 - Higuchi and Nagasawa (1969), 32 - Leeman and Scheidegger (1977), 33 - Dare et al. (2012), 34 - Nielsen et al. (1992), 35 - Nikogosian and Sobolev (1997), 36 - Seifert et al. (1988), 37 - Luhr et al. (1984), 38 - Leeman and Lindstrom (1978), 39 - Irvine and Kushiro (1976), 40 - Nabalek (1980), 41 - Toplis and Corgne (2002), 42 - Latourrette et al. (1991), 43 - Lemarchand et al. (1987), 44 - Esperança et al. (1997), 45 - Malvin and Drake (1987), 46 - Nash and Crecraft (1985), 47 - Tacker and Candela (1987)*

Table 4.2 Composition of Fe-Ti oxide aggregates hosted in the various rock types of the Eastern Gabbro

Rock Series	Rock Type			Si ppm	Ca ppm	Y ppm	P ppm	Pb ppm	Zr ppm	Hf ppm	Al ppm	Ge ppm
Metabasalt	Metabasalt	*n = 13*	*Mean*	7400	140	0.03	50	70	10	0.5	19000	1
			Min.	< 49	< 10	< 0.006	< 4	0.2	1	< 0.02	14000	< 0.2
			Max.	17000	260	0.08	90	460	50	1	21000	2
Layered Series	Olivine gabbro	*n = 10*	*Mean*	990	28	0.02	30	0.9	30	3	16000	0.4
			Min.	330	< 6	0.009	20	0.07	20	2	11000	0.2
			Max.	5400	130	0.06	40	2	50	6	19000	0.8
	Oxide augite melatroctolite	*n = 8*	*Mean*	530	14	0.02	40	1	50	3	16000	0.4
			Min.	390	< 5	0.01	30	0.4	20	2	12000	0.2
			Max.	820	29	0.03	50	2	70	4	20000	0.6
Marathon Series	Two Duck Lake gabbro	*n = 65*	*Mean*	2000	80	0.04	40	3	10	2	17000	0.8
			Min.	< 40	< 6	< 0.002	< 2	0.1	2	< 0.005	8100	< 0.09
			Max.	22000	860	0.5	150	20	60	4	29000	3
	Subophitic gabbro northwest of Marathon	*n = 18*	*Mean*	650	29	0.04	50	0.7	20	2	19000	0.6
			Min.	410	< 6	< 0.002	30	0.04	4	0.7	7500	0.2
			Max.	1700	89	0.3	90	2	60	7	28000	1
	Apatitic clinopyroxenite	*n = 23*	*Mean*	1100	46	0.03	40	0.6	9	0.7	17000	0.8
			Min.	460	< 7	< 0.002	30	0.09	3	0.1	6700	0.4
			Max.	3100	130	0.2	60	2	10	2	32000	1
	Apatitic olivine clinopyroxenite	*n = 15*	*Mean*	600	18	0.02	30	1	30	2	18000	0.5
			Min.	390	< 4	0.008	30	0.05	8	0.7	12000	0.3
			Max.	1100	38	0.04	40	3	70	5	25000	0.9
	Oxide melatroctolite	*n = 17*	*Mean*	750	35	0.03	40	1	20	1	16000	0.7
			Min.	390	< 5	0.009	30	0.05	5	0.5	7100	0.3
			Max.	1400	220	0.2	50	4	50	3	24000	1

Table 4.2 Continued

Rock Series	Rock Type			W ppm	Sc ppm	Ta ppm	Nb ppm	Cu ppm	Mo ppm	Sn ppm	Ga ppm	Mn ppm
Metabasalt	Metabasalt	*n = 13*	*Mean*	0.2	9	2	20	30	2	7	70	3300
			Min.	< 0.02	< 0.09	< 0.008	0.2	2	0.4	< 0.1	30	2000
			Max.	0.6	20	4	90	170	6	20	120	4400
Layered Series	Olivine gabbro	*n = 10*	*Mean*	0.7	20	5	60	8	4	3	30	4000
			Min.	0.2	10	1	30	1	1	2	20	3000
			Max.	2	20	7	100	50	10	6	50	4700
	Oxide augite melatroctolite	*n = 8*	*Mean*	0.4	10	6	90	4	4	3	40	4200
			Min.	0.1	6	4	40	1	0.7	1	30	3300
			Max.	0.9	20	10	190	6	5	5	60	5100
Marathon Series	Two Duck Lake gabbro	*n = 65*	*Mean*	1	10	4	60	40	6	10	50	3700
			Min.	< 0.005	< 0.05	< 0.002	< 0.001	1	1	0.6	30	2400
			Max.	9	20	20	400	1400	20	50	90	7100
	Subophitic gabbro northwest of Marathon	*n = 18*	*Mean*	0.6	10	3	30	10	3	4	40	3600
			Min.	0.04	7	0.1	2	0.9	0.5	1	30	2300
			Max.	2	20	7	100	150	10	10	60	5400
	Apatitic clinopyroxenite	*n = 23*	*Mean*	0.4	9	2	20	7	6	7	60	3900
			Min.	< 0.006	3	0.04	0.3	0.7	0.1	2	40	2700
			Max.	2	20	20	160	60	10	20	120	14000
	Apatitic olivine clinopyroxenite	*n = 15*	*Mean*	0.3	10	3	40	4	4	4	40	3700
			Min.	0.08	6	0.3	1	1	1	1	30	2700
			Max.	0.5	20	6	100	10	5	8	70	5000
	Oxide melatroctolite	*n = 17*	*Mean*	0.4	10	3	30	4	4	4	40	3600
			Min.	0.2	7	0.9	2	0.9	1	2	30	2400
			Max.	0.6	20	7	70	20	20	6	70	4400

Table 4.2 Continued

Rock Series	Rock Type			Mg *ppm*	Zn *ppm*	Co *ppm*	V *ppm*	Ti *ppm*	Ni *ppm*	Cr *ppm*
Metabasalt	Metabasalt	*n = 13*	*Mean*	8000	1100	190	6000	65000	670	13000
			Min.	2000	690	50	2800	35000	40	280
			Max.	14000	2000	270	9600	110000	1300	37000
Layered Series	Olivine gabbro	*n = 10*	*Mean*	5000	860	50	1700	110000	7	110
			Min.	610	590	40	1300	96000	0.2	3
			Max.	10000	1500	80	2100	110000	20	410
	Oxide augite melatroctolite	*n = 8*	*Mean*	4900	970	70	3800	110000	60	410
			Min.	1400	460	30	1500	91000	1	4
			Max.	9300	1400	100	5900	130000	110	700
Marathon Series	Two Duck Lake gabbro	*n = 65*	*Mean*	5100	860	110	4600	65000	240	970
			Min.	510	390	40	1800	35000	60	< 0.6
			Max.	11000	2300	190	8300	100000	560	6400
	Subophitic gabbro northwest of Marathon	*n = 18*	*Mean*	6500	740	90	2900	84000	110	650
			Min.	730	450	10	1200	55000	2	< 0.7
			Max.	14000	1000	170	7000	97000	280	1900
	Apatitic clinopyroxenite	*n = 23*	*Mean*	5400	970	130	6500	66000	330	9400
			Min.	680	420	40	2600	41000	70	100
			Max.	13000	1800	240	18000	89000	800	42000
	Apatitic olivine clinopyroxenite	*n = 15*	*Mean*	5800	800	80	4700	87000	90	850
			Min.	2800	560	40	1600	60000	40	260
			Max.	8700	940	150	7600	100000	200	3100
	Oxide melatroctolite	*n = 17*	*Mean*	3900	810	90	3000	72000	100	490
			Min.	1200	410	60	1400	54000	30	30
			Max.	8700	1800	130	4500	87000	210	1600

** n = number of analyses Less than values represent minimum detection limits*

Table 4.3 Ni/element ratios of Fe-Ti oxide aggregates hosted in the various rock types of the Eastern Gabbro

Rock Series	Rock Type		Ni/Y	Ni/P	Ni/Pb	Ni/Zr	Ni/Hf	Ni/Al	Ni/Ge
Metabasalt	Metabasalt	*Mean*	52000	8	290	120	1500	0.03	320
		Min.	2900	2	3	2	40	0.002	110
		Max.	150000	20	2200	390	3100	0.06	530
Layered Series	Olivine gabbro	*Mean*	390	0.3	20	0.3	3	0.0004	20
		Min.	10	0.007	0.4	0.006	0.06	0.00001	0.7
		Max.	1500	0.8	80	1	9	0.001	60
	Oxide augite melatroctolite	*Mean*	3300	1	50	2	20	0.004	120
		Min.	50	0.04	2	0.02	0.3	0.00009	3
		Max.	8400	2	130	4	50	0.007	200
Marathon Series	Two Duck Lake gabbro	*Mean*	17000	6	540	20	230	0.01	400
		Min.	720	2	8	3	10	0.005	50
		Max.	53000	10	2700	100	1100	0.03	1100
	Subophitic gabbro northwest of Marathon	*Mean*	6300	2	640	8	90	0.005	250
		Min.	7	0.06	4	0.04	0.3	0.0003	3
		Max.	21000	7	2100	40	310	0.01	1300
	Apatitic clinopyroxenite	*Mean*	22000	8	1200	50	760	0.02	480
		Min.	1800	2	100	6	60	0.007	120
		Max.	88000	20	4500	210	2400	0.06	1400
	Apatitic olivine clinopyroxenite	*Mean*	5700	3	300	5	80	0.006	190
		Min.	1900	1	20	0.5	8	0.002	70
		Max.	12000	5	1900	20	270	0.009	290
	Oxide melatroctolite	*Mean*	6200	3	270	9	80	0.006	160
		Min.	280	0.8	10	2	20	0.002	70
		Max.	14000	6	1400	30	180	0.01	390

Table 4.3 Continued

Rock Series	Rock Type		Ni/W	Ni/Sc	Ni/Ta	Ni/Nb	Ni/Cu	Ni/Mo	Ni/Sn
Metabasalt	Metabasalt	*Mean*	7200	70	1000	1100	80	370	100
		Min.	1200	4	10	0.8	8	40	40
		Max.	38000	190	6100	6400	280	1200	200
Layered Series	Olivine gabbro	*Mean*	20	0.4	2	0.1	2	3.1	3
		Min.	0.5	0.01	0.05	0.003	0.01	0.1	0.1
		Max.	90	1	10	0.5	7	10	10
	Oxide augite melatroctolite	*Mean*	170	7	10	1	20	30	20
		Min.	2	0.07	0.1	0.006	0.2	0.3	0.8
		Max.	400	20	20	2	40	80	50
Marathon Series	Two Duck Lake gabbro	*Mean*	820	30	400	100	60	80	60
		Min.	9	10	3	0.2	0.2	4	3
		Max.	2900	60	3600	1800	300	240	530
	Subophitic gabbro northwest of Marathon	*Mean*	910	8	180	10	40	80	50
		Min.	2	0.3	0.3	0.02	0.6	0.2	0.3
		Max.	5600	20	1700	120	110	510	190
	Apatitic clinopyroxenite	*Mean*	1800	40	1400	170	130	300	80
		Min.	30	6	5	0.4	5	10	6
		Max.	8400	110	9700	1400	560	2000	280
	Apatitic olivine clinopyroxenite	*Mean*	520	9	60	9	30	30	30
		Min.	130	2	6	0.4	9	10	8
		Max.	1700	30	190	50	100	70	60
	Oxide melatroctolite	*Mean*	270	8	40	9	40	40	30
		Min.	80	2	20	2	9	6	9
		Max.	680	20	80	30	80	120	60

Table 4.3 Continued

Rock Series	Rock Type		Ni/Ga	Ni/Mn	Ni/Mg	Ni/Zn	Ni/Co	Ni/V	Ni/Cr
Metabasalt	Metabasalt	*Mean*	8	0.2	0.09	0.6	3	0.1	0.2
		Min.	1	0.01	0.009	0.05	0.8	0.008	0.02
		Max.	10	0.5	0.2	1	6	0.2	1
Layered Series	Olivine gabbro	*Mean*	0.2	0.002	0.001	0.01	0.1	0.004	0.2
		Min.	0.008	0.00006	0.00004	0.0004	0.004	0.0001	0.05
		Max.	0.8	0.005	0.005	0.04	0.3	0.01	0.4
	Oxide augite melatroctolite	*Mean*	1	0.02	0.02	0.06	0.8	0.01	0.2
		Min.	0.04	0.0002	0.0002	0.001	0.03	0.0007	0.1
		Max.	2	0.03	0.08	0.1	1	0.02	0.3
Marathon Series	Two Duck Lake gabbro	*Mean*	5	0.07	0.06	0.3	2	0.05	0.8
		Min.	1	0.01	0.01	0.06	0.7	0.02	0.05
		Max.	10	0.1	0.2	0.8	8	0.2	5
	Subophitic gabbro northwest of Marathon	*Mean*	3	0.03	0.02	0.2	1	0.04	3
		Min.	0.05	0.0006	0.002	0.002	0.05	0.002	0.06
		Max.	8	0.09	0.06	0.6	3	0.08	10
	Apatitic clinopyroxenite	*Mean*	6	0.09	0.1	0.4	2	0.06	0.2
		Min.	2	0.03	0.02	0.1	1	0.01	0.01
		Max.	10	0.2	0.5	1	4	0.1	0.8
	Apatitic olivine clinopyroxenite	*Mean*	2	0.03	0.02	0.1	1	0.02	0.2
		Min.	0.8	0.01	0.006	0.06	0.5	0.009	0.04
		Max.	3	0.04	0.04	0.2	2	0.04	0.4
	Oxide melatroctolite	*Mean*	2	0.03	0.03	0.1	1	0.03	0.6
		Min.	0.8	0.007	0.006	0.05	0.3	0.01	0.08
		Max.	4	0.05	0.07	0.3	2	0.07	1

Chapter 5

On the mechanisms for low sulfide, high precious metal and high sulfide, low precious metal mineralization in the Eastern Gabbro, Coldwell Complex: Evidence from textural associations, S/Se values, and PGE concentrations of sulfides

5.1 Introduction

The concentration of platinum-group elements (PGE) in sulfides has been used to assess mineralization and post-mineralization processes in a wide range of Ni-Cu-PGE deposits (e.g., Barnes et al., 2006; Dare et al., 2014, 2011, 2010; Duran et al., 2016; Godel and Barnes, 2008; Prichard et al., 2013). There are a number of issues, however, that arise from using PGE concentrations to infer mineralization mechanisms. These include the accurate determination of PGE concentrations in sulfides by laser ablation ICP-MS due to the deficiency of well-developed and characterized PGE-bearing sulfide standards; spectral interferences on PGE (e.g., Ni and Cu argides on ^{101}Ru, ^{103}Rh, and ^{105}Pd); and the lack of understanding of how PGE behave in hydrothermal fluids at magmatic temperatures (800-900°C) (cf. Hanley, 2005). Interpretations of mineralizing processes, therefore, should not be made strictly on the basis of PGE concentration in sulfides, but should incorporate other geochemical proxies, such as S/Se values, as demonstrated by Holwell et al. (2015).

Given that mantle S/Se values range from 2850 to 4350 (Eckstrand and Hulbert, 1987), whole-rock and mineral S/Se values have been used to track magmatic and post-magmatic processes in a number of Ni-Cu-PGE deposits (e.g., Barnes et al., 2009, 2001; Holwell et al., 2015; Maier and Barnes, 2010; Prichard et al., 2013; Queffurus and Barnes, 2014; Ripley, 1990; Ripley et al., 2002; Smith et al., 2016; Theriault and Barnes, 1998). The usefulness of S/Se values to monitor such processes stems from the notion that i) S and Se behave similarly during partial melting of the mantle (Hattori et al., 2002), ii) Se has a high sulfide/silicate partition coefficient ($D^{sul/sil}$) in the range of 345 to 1770 (Barnes et al., 2009; Patten et al., 2013; Peach et al., 1990), and iii) S and Se behave differently during hydrothermal alteration, with S typically being more mobile than Se (Howard, 1977; Smith

et al., 2016; Yamamoto, 1976). As a result, S/Se values can be used to characterize changes in R factor (e.g., Theriault and Barnes, 1998), early segregation of sulfides (e.g., Barnes et al., 2009), S loss (e.g., Godel and Barnes, 2008; Schissel et al., 2002), and contamination by rocks with high S/Se values (e.g., Eckstrand et al., 1989).

The Eastern Gabbro of the Coldwell Complex, Canada hosts several disseminated Cu-PGE occurrences, including the Marathon Cu-Pd deposit. At the Marathon deposit, mineralization occurs in texturally, mineralogically, and geochemically distinct lenses that are termed, in order of increasing distance from the footwall contact, as Footwall Zone, Main Zone, and W Horizon. Based on variations in whole-rock Cu and Pd, and textural variations in sulfides, several models have been proposed to explain the formation of the Footwall Zone and Main Zone: i) a magmatic model (Good et al., 2015; Good and Crocket, 1994), ii) a hydrothermal model (Dahl et al., 2001; Watkinson and Dahl, 1988; Watkinson and Jones, 1996; Watkinson and Ohnenstetter, 1992), iii) a zone-refining model (Barrie et al., 2002), and iv) a hybrid magmatic-hydrothermal model (Samson et al., 2008). For the W Horizon, a multistage dissolution upgrading model (Kerr and Leitch, 2005) was proposed to explain the extreme enrichment of PGE (Cu/Pd > 3) relative to the Main Zone (Cu/Pd 1,000-20,000) (Good, 2010; Good et al., 2015; Ruthart, 2013). Despite the differences between the zones, the trace-metal composition of sulfides hosted in the various mineralized zones at Marathon and the other mineralized occurrences along the Eastern Gabbro has not been studied in detail. Additionally, with the exception of the preliminary work of Samson et al. (2008), no studies have characterized variations in trace-metal chemistry of the sulfides in different textural associations, and so the role of hydrothermal fluids in the redistribution of metals throughout the Eastern Gabbro has not been assessed.

Using trace-element concentrations, S/Se values, and PGE concentrations of sulfides from the various zones at Marathon (Footwall Zone, Main Zone, W Horizon), and other zones of mineralization around the margin of the Coldwell Complex, this study aims to i) assess the processes that led to the distinct types of mineralization in the Eastern Gabbro, ii) characterize the role of multistage dissolution upgrading in the formation of high-PGE, low S mineralization in the W Horizon, and iii) address the role of hydrothermal fluids in the

redistribution of base metals, PGE, and main-group elements (e.g., As, Sb, Te) throughout the Eastern Gabbro

5.2 Geology and mineralization

5.2.1 Coldwell Complex

The Proterozoic Coldwell Complex is a composite pluton located on the northeastern shore of Lake Superior (Fig. 5.1) (Walker et al., 1993). It was emplaced into the Archean Schreiber-Hemlo greenstone belt along the northern edge of the North American Midcontinent rift. Age determinations for various phases of the Coldwell Complex are bracketed between 1108 ± 1 Ma (Heaman and Machado, 1992) and 1105.3 $\pm$ 0.6 Ma (Good and Dunning, 2018). The Coldwell Complex is the largest alkaline intrusion in North America (582 km^2) and consists of three intrusive centers (I, II, III) (Currie, 1980; Mitchell and Platt, 1982). Center I is the oldest intrusive phase and consists of syenodiorite, layered ferroaugite-amphibole syenite, syenite and the Eastern Gabbro Suite which includes the gabbroic host pluton for the Marathon Cu-PGE deposit (Walker et al., 1993), as well as numerous other Cu-PGE occurrences.

5.2.2 Eastern Gabbro Suite

The Eastern Gabbro occurs along the eastern and northern margins of the Coldwell Complex (Fig. 5.1). It has been subdivided into three rock units according to crosscutting relationships, geochemistry, and petrographic characteristics (Good et al., 2015). From oldest to youngest these units are metabasalt, Layered Series, and Marathon Series (Fig. 5.2). The metabasalt typically occurs at the base of the Eastern Gabbro and consists of basalt flows and sills that were metamorphosed to hornfels grade by the later injection of large volumes of Layered and Marathon Series magma (Good et al., 2015). This unit contains no Cu-PGE mineralization. The Layered Series makes up the majority of the Eastern Gabbro and, at the Marathon deposit, crosscuts the metabasalt package. Although the Layered Series exhibits similar textures throughout the Eastern Gabbro, a recent

investigation by Cao et al. (2016) identified subtle but distinct variations in the whole-rock composition of this unit. It is dominated by olivine gabbro with modal layering that is defined by variations in the proportion of plagioclase and pyroxene, and contains substantial oxide augite melatroctolite. Mineralization in the Layered Series is limited to secondary Cu mineralization associated with albite and actinolite alteration.

The Marathon Series is the youngest of the mafic intrusive events and is defined as comprising all of the mafic and ultramafic rocks that host Cu-PGE mineralization (Good et al., 2015). At the Marathon deposit, it is dominated by the Two Duck Lake gabbro, a coarse-grained to pegmatitic subophitic gabbro. The Two Duck Lake gabbro intruded the metabasalt package just above the contact with Archean country rocks, which, in the vicinity of the Marathon deposit, comprise intermediate pyroclastic metavolcanic rocks (Good et al., 2015; Walker et al., 1993). Other minor units in the Marathon Series include sill- to pod-like bodies of oxide melatroctolite, apatitic clinopyroxenite, and apatitic olivine clinopyroxenite (Good et al., 2015).

5.2.3 Mineralization in the Eastern Gabbro

Mineralized zones in the Eastern Gabbro are subdivided into two groups based on their location. Group one occurs within the Marathon deposit. Mineralized zones in group two are located to the northwest of the Marathon deposit.

Mineralization in the Marathon deposit occurs in three lenses that are texturally, mineralogically, and geochemically distinct from one another, although the host rock types are comparable. In order of increasing distance from the footwall, these lenses are termed Footwall Zone, Main Zone, and W Horizon (Fig. 5.3) (Good et al., 2015). The Footwall Zone occurs at the base of the Two Duck Lake gabbro, at the contact with the Archean country rocks. The Main Zone is the thickest and most continuous zone of mineralization and occurs above the Footwall Zone. It is thickest in the northern portion of the deposit. The W Horizon occurs above the Main Zone, closer to the contact with the metabasalts.

The W Horizon only occurs in the southern half of the deposit and overlies Main Zone type mineralization.

Sulfides in the Footwall Zone comprise semi-massive to net-textured pyrrhotite with lesser chalcopyrite (Samson et al., 2008; Watkinson and Ohnenstetter, 1992). In the Main Zone, sulfides are dominated by disseminated chalcopyrite and pyrrhotite, with lesser cubanite and bornite, all of which occur interstitial to primary silicates, oxides, and apatite. Sulfides in the W Horizon are also disseminated and distinguished from those in the Main Zone by a lower modal abundance of sulfides and hydrous silicates, a different suite of PGM, a distinctly higher proportion of bornite and lower proportion of pyrrhotite, lower S concentrations, and noticeably lower Cu/Pd values (Ames et al., 2017, 2016; Good et al., 2017; Good, 2010; Ruthart, 2013).

Mineralized zones to the northwest of the Marathon deposit include Four Dams, Area 41, and Redstone (Fig. 5.1). These zones were discovered within the past twelve years and contain disseminated chalcopyrite with lesser pyrrhotite and minor bornite (McBride, 2015). Mineralization at Area 41 was described by Good et al. (2017) and Ames et al. (2016). Mineralization at Area 41 and Four Dams was described by Cao (2017). Area 41 mineralization was subdivided into three types by Cao (2017) based on Cu/Pd ratios. Type I mineralization has Cu/Pd > 100,000 with Pt+Pd values between 0.008 and 0.03, type II mineralization has Cu/Pd between 2,500 and 15,000 with Pt+Pd values between 0.1 and 0.9, and type III mineralization has Cu/Pd < 2,500 with Pt+Pd values between 1 and 4.

A small pod of semi-massive chalcopyrite plus pyrrhotite hosted by clinopyroxene-olivine-apatite cumulate is located outside of the Complex margin at an undisclosed location. This pod contains Pd grades of up to 100 ppm and is characterized by Cu/Pd values near 500.

5.3 Methods

A total of 65 thin sections from mineralized intervals at Marathon, and 26 from mineralized intervals at Four Dams, Area 41, and Redstone were investigated petrographically.

Samples from Area 41 encompass types I, II, and III mineralization, along with type IV mineralization, which was previously undocumented and is characterized by Cu/Pd between 15,000 and 100,000 with Pt+Pd values between 0.04 and 0.1. These samples encompass the range of textural varieties of sulfides within these deposits and occurrences and, cumulatively, are representative of the different styles of mineralization that occur throughout the Eastern Gabbro.

Raman spectroscopy was used to aid in the identification of sulfide phases that were difficult to analyze using energy- and wavelength-dispersive spectroscopy (EDS and WDS). Spectra were collected using a WiTec confocal Raman spectrometer fitted with a 532 nm laser at the University of Windsor. Raman spectra were acquired using a laser energy of 2 mW and represent averages of 5 spectra acquired over a period of 20 s. The major-element composition (S, Fe, Cu, Ni) of sulfides (bornite, chalcopyrite, cubanite, pentlandite, pyrrhotite, pyrite) were primarily obtained using a FEI Quanta 200 FEG scanning electron microscope equipped with an EDAX EDS x-ray detector at the Advanced Microscopy and Materials Characterization Facility at the University of Windsor. Sulfides in a total of 66 thin sections (420 analyses) were analyzed using an accelerating voltage of 20 kV, beam current of 206 μA, and counting times of 30 s. A series of 5 replicate analyses were conducted on a bornite, chalcopyrite, pyrrhotite, and pentlandite crystal. The standard deviation on the concentrations of each of S, Fe, Cu, Zn, Ni, and Co in each of the sulfides is less than 0.25 wt. %. To assess the accuracy of the data obtained by EDS, the S, Fe, Cu, Zn, Ni, and Co concentrations in the various sulfide minerals were also obtained from a subset of thin sections (n = 4) using a JEOL JXA-8530F field-emission electron microprobe (EPMA) at the Earth and Planetary Materials Analysis Laboratory at Western University. Analyses were obtained at an accelerating voltage of 15 kV, probe current of 20 nA, and a spot size of 1 μm. A correction was applied to Co due to an overlap with the Fe peak. The average % instrumental error of S is 0.66%, Fe is 1.18%, Cu in chalcopyrite, bornite, and cubanite is 0.72%, Ni in pentlandite is 0.69%, and Co in pentlandite is 2.46%. Figure 5.4 compares the concentrations in wt. % of S, Fe, Cu, Ni, and Co obtained by EDS and EPMA. The elemental concentrations obtained by EDS and EPMA are nearly identical, as they plot on a 1:1 line with an r^2 of 0.996. Given these

results, EDS was the primary means by which the major-element compositions of sulfides were obtained in this study. The samples for which EPMA data were collected were analyzed during each EDS session for quality control of the major-element data obtained.

Trace-metal concentrations for sulfides from 66 samples (462 analyses) were obtained at the Element and Heavy Isotope Analytical Laboratory at the University of Windsor using an Agilent 7900 Inductively-Coupled Plasma Mass Spectrometer coupled with a 193-nm excimer laser. The laser was operated at an energy of 1.5 to 2.5 mJ, repetition rate of 20 Hz, spot size of 25 μm, and raster speed of 5 μm/s. Analyses represent traverses across the surface of sulfide grains and included 30 seconds of gas background and up to 120 seconds of ablation and signal collection. The masses analyzed were ^{29}Si, ^{33}S, ^{34}S, ^{47}Ti, ^{51}V, ^{57}Fe, ^{59}Co, ^{60}Ni, ^{63}Cu, ^{65}Cu, ^{66}Zn, ^{68}Zn, ^{75}As, ^{77}Se, ^{78}Se, ^{82}Se, ^{101}Ru, ^{103}Rh, ^{105}Pd, ^{106}Pd, ^{107}Ag, ^{108}Pd, ^{111}Cd, ^{118}Sn, ^{120}Sn, ^{123}Sb, ^{125}Te, ^{185}Re, ^{189}Os, ^{193}Ir, ^{194}Pt, ^{197}Au, ^{206}Pb, ^{207}Pb, ^{208}Pb, and ^{209}Bi. Silicon was used to monitor for silicate mineral contamination. Interferences on S, Cu, Zn, Se, Pd, Sn, and Pb were monitored by analyzing multiple isotopes of these elements. Micron-scale inclusions of platinum-group minerals (PGM) were included in the integration as there is evidence that they were exsolved from the host sulfides (see Discussion). Three external standards were used for calibration. MASS-1 is a pressed polymetallic powder (Fe-Zn-Cu-S) developed by the United States Geological Survey that was used to calculate the concentrations of Co, Cu, Zn, As, Se, Ag, Cd, Sn, Sb, Se, and Bi. With the exception of Cu and Zn, which occur in concentrations of 10 to 20 wt. % in MASS-1, these elements are present in concentrations < 100 ppm (Wilson et al., 2002). The synthetic pyrrhotite standard Po725 (Sylvester et al., 2005) was used to calculate the concentrations of PGE and Au, which are present in concentrations of < 50 ppm in the standard. Although NIST610 is a synthetic silicate glass, it was used to calculate the concentration of Ti, Te, and Pb in sulfides as they are not present in any of the sulfide standards available. The concentration of these elements, therefore, are semi-quantitative. Iron was used as the internal standard.

^{105}Pd, ^{106}Pd, ^{108}Pd and ^{103}Rh have argide interferences with ^{65}Cu, ^{66}Zn, ^{68}Zn, and ^{63}Cu, respectively. Pure Cu (99.9999%) and Zn (99.9985%) foils from Alfa Aesar were analyzed

to determine the amount of $^{63}Cu^{40}Ar$, $^{65}Cu^{40}Ar$, $^{66}Zn^{40}Ar$ and $^{68}Zn^{40}Ar$ generated during laser microsampling. Sphalerite from the East Kemptville Sn-polymetallic greisen was also analyzed to compare the Zn-argide ratio obtained from a pure Zn metal to that obtained in a PGE-free mineral. The Zn metal and sphalerite were ablated using the same conditions at which the samples were ablated. Copper, however, did not ablate at these conditions and so the laser energy was increased to 4.1 mJ. Table 5.1 provides the average counts per second of the various Cu, Zn, Rh, and Pd isotopes measured on the pure metals, as well as their isotope/argide ratios. The percentage of these argides generated during analyses were all < 0.01% of the counts for Cu and Zn. The average isotope/argide ratio was used to correct Cu- and Zn-argide interferences on Rh and Pd. Rhodium is not used in any interpretations given the high concentration of Cu in chalcopyrite, cubanite, and bornite, which cause inaccuracies in the correction. ^{106}Pd rather than ^{105}Pd was used to calculate the concentration of Pd because the concentration of Zn in all of the sulfides of interest is much lower than the concentration of Cu.

The majority of trace metals in sulfides exhibit the same variations in their laser ablation spectra as their major elements (Cu, Fe, S), suggesting that they occur in solid solution in the sulfide (Fig. 5.5). Spectra from analyses of chalcopyrite, bornite, and cubanite grains that appear homogenous in reflected light commonly contain coincident peaks for Co, Ni, Zn, and Cd (Fig. 5.5). The peaks for Co and Ni could be the result of incorporation of micron-sized crystals of pyrrhotite and pentlandite that are not visible at the surface, given that these sulfides are the principal hosts of Co and Ni. The numerous peaks for Zn, Cd, and Co are the result of incorporation of micron-sized sphalerite crystals disseminated throughout the chalcopyrite grains; these are visible using high-magnification reflected light and backscatter electron (BSE) imaging. Given that the aims of this study require characterization of the composition of the different sulfides, regions of the laser ablation spectra in which these peaks are absent were chosen for integration, when possible. The peaks in Co and Ni were easily avoided during integration of the laser ablation spectra. The peaks for Zn, Cd, Co, however, typically occur throughout the spectra and could not always be excluded from the integration region. As such, regions with the least number of peaks were chosen for integration. Although Pd was commonly close to the detection limit in

most sulfides, apart from pentlandite, (Fig. 5.5), Pd peaks were present in some laser ablation spectra that were often coincident with peaks for main-group elements (e.g., Fig. 5.5); these peaks are likely the result of incorporation of micron-sized inclusions of PGM during laser sampling. These PGM are incorporated during integration as there is evidence that these PGM exsolved from the sulfides (see Discussion). Pentlandite commonly contains Pd in solid solution as its signal consistently tracks with Fe and Ni (Fig. 5.5).

5.4 Results

5.4.1 Sulfide mineralogy and textures

5.4.1.1 Sulfide mineralogy

Disseminated sulfides occur interstitial to silicates and oxides in all of the mineralized zones, except for the Footwall Zone, where the sulfides are net-textured to semi-massive. The main sulfide minerals include chalcopyrite, cubanite, bornite, pyrrhotite, and pentlandite. The relative proportions of these sulfides varies between zones. Chalcopyrite occurs in all of the mineralized zones, but is least abundant in the Marathon Footwall Zone and most abundant in the Main Zone. Pyrrhotite is present in all mineralized zones except for the W Horizon and Four Dams occurrences. Pyrrhotite is most abundant in the Footwall Zone, Area 41, and Redstone occurrences. The W Horizon is the only mineralized zone that contains abundant bornite. Cubanite is present in all of the mineralized zones, except for the W Horizon, but occurs in greatest abundance at Four Dams.

Sulfides can occur as monomineralic grains or as multi-mineral aggregates in a variety of textural associations. Some sulfides occur interstitial to, and in equilibrium with, primary silicates, whereas others are interstitial to primary silicates, but display disequilibrium textures with other sulfides and/or hydrous silicates (typically tremolite-actinolite and chlorite).

5.4.1.2 Sulfide assemblages that are characterized by equilibrium textures

Sulfide assemblages that exhibit equilibrium textures are common in all of the mineralized zones and exhibit planar or curved, equilibrium boundaries with each other, as well as with silicates and other minerals (Fig. 5.6b). Bornite or cubanite commonly occur as fine blebby to wormy (bornite) (Fig. 5.6a) and tabular (cubanite) (Fig. 5.6c) exsolution phases in chalcopyrite, but can occur as monomineralic grains and as grains associated with other sulfides (Fig. 5.6a). Pentlandite, although uncommon, can occur as fine- to medium-grained euhedral crystals within pyrrhotite and Cu-rich sulfides (Fig. 5.6b), or as exsolution flames within pyrrhotite (Fig. 5.6b). It is not uncommon for pentlandite crystals to be partially replaced by magnetite, pyrrhotite, marcasite, and/or pyrite along fractures or their boundaries. Cobalt-rich pentlandite is rare, and occurs as skeletal pseudomorphs in chalcopyrite and cubanite (Fig. 5.6d) or as blebby exsolution lamellae. Troilite, which was confirmed using Raman spectroscopy, occurs as regular arrays of wavy exsolution lamellae in pyrrhotite hosted in all of the mineralized zones, but is not abundant. Chalcopyrite can extend outwards from sulfide grains/aggregates as thin films along grain boundaries, fractures, and cleavage planes. Chalcopyrite and pyrrhotite commonly occur as elongated grains along the cleavage planes of plagioclase and within Ca-rich rims on plagioclase in contact with sulfide grains (Fig. 5.6e). Partial to complete replacement of chalcopyrite by magnetite (Fig. 5.6f) has been observed in all of the mineralized zones excluding the Footwall Zone, and is most abundant in Four Dams, Area 41, and Redstone.

5.4.1.3 Sulfide assemblages that are characterized by disequilibrium textures

Interstitial sulfide assemblages that exhibit disequilibrium textures comprise the replacement of pyrrhotite or pyrite by chalcopyrite and the intergrowth of predominantly chalcopyrite with secondary hydrous minerals. Where pyrrhotite has been replaced by chalcopyrite, the pyrrhotite commonly occurs as optically-continuous islands that exhibit ragged boundaries with a matrix of chalcopyrite, indicating that these islands of pyrrhotite are remnants of fewer larger crystals (Fig. 5.7a). Where sulfides are intergrown with hydrous silicates, the hydrous silicates typically comprise tremolite-actinolite ± chlorite

that have partially to completely replaced pyroxene and, to a lesser degree, olivine, plagioclase, and magnetite. Chalcopyrite is the most common sulfide intergrown with these hydrous silicates, but bornite, cubanite, pyrrhotite, and pentlandite occur in some chalcopyrite crystals or aggregates. A number of textural varieties of sulfide-hydrous silicate intergrowths have been identified: i) aligned, euhedral actinolite blades protruding from altered pyroxene into sulfides, where actinolite in the sulfides has the same orientation as the actinolite-pyroxene pseudomorph (Fig. 5.7d), ii) aligned, euhedral actinolite blades within sulfides, but which are not associated with altered pyroxene (Fig. 5.7b), iii) randomly-oriented, euhedral actinolite blades within sulfides (Fig. 5.7c), and iv) sulfides within pyroxene that has been partially to completely replaced by hydrous silicates (Fig. 5.7e). Magnetite and calcite can also occur in the sulfide-actinolite assemblages in which the actinolite is aligned (i and ii). In each of these variants, it is common for euhedral actinolite crystals to occur isolated within the sulfides. In some instances, chalcopyrite cuts across individual actinolite crystals. Rarely, chalcopyrite has been observed as a rim along the boundary of alteration patches within altered silicates (Fig. 5.7e). Where magnetite-ilmenite aggregates have been altered, ilmenite lamellae are unaffected, but the magnetite is replaced by hydrous silicates ± chalcopyrite (Fig. 5.7f). These textural associations are common in all of the mineralized zones, except for the W Horizon.

5.4.2 Trace-metal concentrations in sulfides

The following sections compare the trace-element composition of i) the various sulfide minerals, ii) equilibrium and disequilibrium chalcopyrite, and iii) chalcopyrite hosted in the various mineralized zones throughout Eastern Gabbro. The data are illustrated in Figures 5.8 through 5.10, with median, minimum, and maximum concentrations of trace elements in sulfides summarized in Table 5.2.

5.4.2.1 Distribution of metals among sulfides

Figure 5.8 plots the concentrations of metals analyzed in equilibrium (colored fields) and disequilibrium (colored data points) sulfides vs. cobalt for all of the mineralized zones.

Cobalt is plotted on the x-axis on Figure 5.8 because it is an MSS-compatible element, and so its concentration is distinctly different between Fe-rich and Cu-rich sulfides. The concentration of Co is higher in Fe-rich sulfides compared to Cu-rich sulfides; its concentration is highest in pentlandite and lowest in bornite. Zinc concentrations are highest in the Cu-rich sulfides and exhibit a continuum of values, being lowest in bornite and extending to the highest values in cubanite. Noble metals (PGE, Au, Ag) in sulfides display large ranges in concentration of over 2 to 3 orders of magnitude. Of the noble metals, Pd, Ru, Ag, and Au are consistently present in detectable concentrations in all sulfides from all mineralized occurrences studied. Roughly 75% of the pentlandite grains analyzed have Pd, Ru, Ir, and Au concentrations that are higher than, and distinguishable from, their concentration in other sulfide minerals. The concentration of Pd is similar in chalcopyrite, cubanite, bornite, and pyrrhotite. Ruthenium concentrations are highest in pentlandite, followed by bornite, chalcopyrite and cubanite, and pyrrhotite. Silver concentrations are similar in all sulfides. Gold concentrations are highest in bornite and pentlandite, and occur in similar concentrations in the other sulfides. Iridium occurs in the lowest detectable concentrations in chalcopyrite and cubanite, and was undetectable in bornite. Platinum concentrations are highest in chalcopyrite and pyrrhotite, whereas Os concentrations are highest in pyrrhotite. Apart from Sn and Se, the concentrations of main-group elements are typically less than 1 ppm. All of the main-group elements, except for Se, exhibit a large range in concentration (up to 4 orders of magnitude). Their concentrations are indistinguishable between sulfides.

5.4.2.2 Comparison of sulfides in different textural associations

Apart from Pt, the entire population of disequilibrium chalcopyrite has trace-element compositions that completely overlap with the composition of equilibrium chalcopyrite (Fig. 5.8). In many disequilibrium chalcopyrite crystals, Pt occurs in higher concentrations (up to 1.4 ppm) than equilibrium chalcopyrite crystals (up to 0.2 ppm) (Fig. 5.8). Figure 5.9 is a vector diagram that compares the concentration of metals in equilibrium (start of the vector) and disequilibrium (end of the vector) chalcopyrite hosted within a single thin section. On a sample-by-sample basis, there are differences in the concentration of trace

elements in equilibrium and disequilibrium chalcopyrite (Fig. 5.9). Apart from Zn and Ag, which exhibit differences of hundreds and tens of ppm, respectively, these differences are generally minor and range from sub-ppm to tens of ppm. No elements exhibit a systematic variation in concentration between equilibrium and disequilibrium chalcopyrite pairs (Fig. 5.9). Rather, the concentration of elements in disequilibrium chalcopyrite can either be greater than or less than those in equilibrium chalcopyrite.

5.4.2.3 Variations in S/Se value

The relationships between whole-rock Pt+Pd recalculated to 100% sulfide and whole-rock S/Se have been demonstrated to be useful in differentiating between magmatic and post-magmatic processes that generated or modified mineralization in numerous Ni-Cu-PGE deposits (Queffurus and Barnes, 2015). For the purpose of this study, this diagram was modified to use whole-rock Cu/Pd values rather than Pt+Pd recalculated to 100% sulfide because: i) the sulfide content of mineralized occurrences in the Eastern Gabbro is relatively low (ranges from 0.05 wt. % S in the W Horizon to 3 wt. % S in the Footwall Zone; Shahabi Far, 2016), such that they can readily be affected by subsolidus S loss caused by alteration (Barnes and Lightfoot, 2005), ii) rocks of the Eastern Gabbro contain a significant amount of olivine and minimal Ni-sulfides, such that a significant proportion of Ni will be hosted in olivine rather than sulfides (Barnes and Lightfoot, 2005), iii) this method does not assume that all of the Pt and Pd is in sulfides, and iv) the Cu/Pd values are more diagnostic of the various mineralized zones and occurrences along the Eastern Gabbro than Pt and Pd alone (Good et al. 2017).

The concentration of Se does not vary among sulfide phases (Fig. 5.8, Table 5.2) and shows no notable variation between sulfides hosted in different textural associations (Fig. 5.9). Therefore, all sulfides in all textural associations are used in Figures 5.10 and 5.11. Samples from the Marathon deposit span a continuous range of Cu/Pd, from the Footwall Zone, which has the highest Cu/Pd, to the W Horizon, which has the lowest Cu/Pd values (Fig. 5.10, Table 5.3). The Footwall Zone and Main Zone samples have Cu/Pd values that

largely fall within the mantle range, whereas most samples from the W Horizon are enriched in Pd relative to the mantle (Fig. 5.10).

Disseminated sulfides from the Footwall Zone and Footwall-Main Zone transition consistently have S/Se values that are higher than the mantle range, with semi-massive sulfides from the Footwall Zone ranging from 21,000 to 300,000 (Fig. 5.10, Table 5.3). Sulfides from the Main Zone have S/Se values that straddle the mantle range (Fig. 5.10, Table 5.3). Of 105 sulfide analyses from the Main Zone, 33% have S/Se values less than the mantle range, 51% have values higher than the mantle range, and 16% have values within the mantle range (Fig. 5.10).

Sulfides from the W Horizon have S/Se values that are predominantly lower than the mantle range (Fig. 5.10, Table 5.3). Of 65 sulfide analyses from the W Horizon, 78% have S/Se values that are lower than the mantle range, 8% have ratios higher than the mantle range, and 14% have values within the mantle range (S/Se). They can be subdivided into three populations (I, II, and III) based on differences in the Cu/Pd and S/Se values relative to mantle values. Those in population I and II have S/Se values (300 to 1,800) less than the mantle range and occur in rocks with moderate (population I, ~ 700) and low (population II, ~ 30) Cu/Pd values (Fig. 5.10). Those in population III have S/Se values (600 to 16,000) that span a continuous range from values below the mantle range to values higher than the mantle range and occur in rocks with Cu/Pd values (~ 140) intermediate to the those of population I and II (Fig. 5.10). In terms of their whole-rock Pd concentrations, rocks from population II have the highest average concentrations (~ 57 ppm), those from population I the lowest (~ 6 ppm), and those from population 3 intermediate to these (~ 37 ppm). Whole-rock S/Se values for 58 W Horizon samples reported by Ruthart (2013) are plotted on Figure 5.10 for comparison with the S/Se values obtained from sulfide minerals. The whole-rock values largely overlap with the S/Se values of sulfides in population I and II (Fig. 5.10).

The Cu/Pd values of the samples chosen from mineralized zones northwest of the Marathon deposit span a continuous range from below to above the mantle range (Fig. 5.11, Table

5.3). All of the samples from mineralization types I and IV at Area 41, Four Dams, and Redstone mineralized zones have Cu/Pd values that are consistently higher than the mantle range, whereas those from mineralization type II have ratios that fall within the mantle range, and those from type III have ratios that fall below the mantle range (Fig. 5.11, Table 5.3). The S/Se value of the sulfides is relatively constant among all of these mineralized zones (Fig. 5.11, Table 5.3). Of 141 sulfide analyses from these zones, 77% have S/Se values less than mantle values, 8% have values above the mantle range, and 15% have mantle S/Se values (Fig. 5.11). The Cu/Pd values of the chalcopyrite-rich pod (~ 500) are notably lower than mantle values, whereas the S/Se values are consistently greater than mantle values (Fig. 5.11, Table 5.3).

5.4.2.4 Numerical modelling of sulfide compositions

The composition of a fractionating sulfide liquid and the resulting MSS and ISS was modelled for sulfides in the Eastern Gabbro in a similar fashion to the work of Duran et al. (2017) for sulfides in the Noril'sk-Talnakh mining district. Sulfide liquid compositions were modelled here using the closed-system R factor model of Campbell and Naldrett (1979):

$$C^{sul} = \frac{[C_o^{sil} D_i^{sul/sil}(R+1)]}{(R + D_i^{sul/sil})} \qquad \text{eq. 5.1}$$

where C_o^{sil} is the concentration of an element in the original silicate melt, C^{sul} is the concentration of an element in the sulfide liquid, $D_i^{sul/sil}$ is the sulfide liquid/silicate melt partition coefficient for a given element *i*, and *R* is the R factor (silicate melt/sulfide liquid mass ratio). A closed-system model was used as the modelled composition of sulfides are similar to those obtained using simple open-system models (Kerr and Leitch, 2005). R factors of 100, 1,000, and 10,000 were used in the calculations as these values cover the range of R factors that sulfides in the Footwall Zone and Main Zone are thought to have experienced (Good et al., 2017). The starting silicate melt composition was taken as the average of the Wolf Camp basalts that have Cu/Pd within the range of mantle values. These

basalts are thought to be the extrusive equivalent of the Geordie Lake gabbro and are likely cogenetic with the rocks that make up the Marathon Series (Good et al., 2017a). Crystallization of the sulfide liquid to form monosulfide solid solution (MSS) and residual Cu-rich liquid was modelled using Rayleigh fractional crystallization equations (after Rollinson, 1993). The equation for MSS composition during crystallization is:

$$C^{mss} = C_o^{sul} D_i^{mss/sul} [F^{\left(D_i^{mss/sul}-1\right)}] \qquad \text{eq. 5.2}$$

The equation for residual Cu-rich liquid composition during crystallization is:

$$C^{liq} = C_o^{sul} [F^{\left(D_i^{mss/sul}-1\right)}] \qquad \text{eq. 5.3}$$

where C_o^{sul} is the original concentration of an element in the sulfide liquid at a given R factor, C^{mss} is the concentration of an element in MSS, C^{liq} is the concentration of an element in the residual Cu-rich liquid, $D_i^{mss/sul}$ is the MSS/sulfide liquid partition coefficient for element *i*, and *F* is the proportion of sulfide liquid remaining. The composition of intermediate solid solution (ISS) that crystallized from the residual Cu-rich liquid was modelled using equation 5.2 and ISS/sulfide liquid partition coefficients. Maximum sulfide liquid/silicate melt, MSS/sulfide liquid, and ISS/sulfide liquid partition coefficients were used (Barnes and Ripley, 2016 and references therein). Table 5.4 summarizes the sulfide liquid/silicate melt, MSS/sulfide liquid, and ISS/sulfide liquid partition coefficients used.

The concentrations of key base, precious, and main-group metals, namely Pd, Ru, Au, Co, Zn, and Sn, in MSS that crystallized from a sulfide liquid under different R factors, as well as their concentration in the residual Cu-rich liquid and the ISS that crystallized from it, were modelled using Rayleigh fractional crystallization (the data points on Fig. 5.13). The starting point for the modelled composition of ISS in the Footwall Zone and Main Zone was taken as 70% MSS crystallization and R factors between 100 and 1,000 for the Footwall Zone, and 60% MSS crystallization and R factors between 1,000 and 10,000 for

the Main Zone. The starting point for the modelled composition of ISS in the W Horizon was taken as 30% MSS crystallization and an R factor greater than 10,000. The percent MSS crystallization used in the model is based on the ratio of pyrrhotite to chalcopyrite in each of the mineralized zones, which was estimated by Good et al. (2017) using whole-rock Cu and S. The R factor used in the model is based on estimates by Good et al. (2017) using whole-rock Cu and Pd concentrations and the Cu/Pd vs. Pd diagram of Barnes et al. (1993). The measured concentrations of these metals in chalcopyrite from the Footwall Zone, Main Zone, and W Horizon are illustrated by the colored fields on Figure 5.13.

The modelled concentrations of Pd, Ru, and Au in ISS (light grey data points) exhibit low variability (less than an order of magnitude) with respect to degree of crystallization of the residual Cu-rich liquid (Fig. 5.13a,b). The modelled concentrations of Zn and Sn, however, exhibit a large range in concentration with degree of crystallization (Fig. 5.13c,d). The concentration of Zn decreases by up to 3 orders of magnitude from 0% crystallization (F = 1) to 100% crystallization (F = 0) of the residual Cu-rich liquid, whereas the concentration of Sn increases by less than an order of magnitude (Fig. 5.13c,d).

Chalcopyrite from all of the mineralized zones in the Marathon deposit are depleted in Pd, Au, and Sn relative to their modelled concentrations in ISS, regardless of degree of crystallization of the residual Cu-rich liquid (Fig. 5.13a,b,d). The measured concentration of Ru in chalcopyrite from all of the mineralized zones is greater than the modelled concentration in ISS (Fig. 5.13a). Of these mineralized zones, chalcopyrite from the Footwall Zone exhibits the greatest degree of enrichment relative to ISS (Fig. 5.13a). The measured concentrations of Zn in chalcopyrite from all of the mineralized zones at the Marathon deposit are similar to the modelled concentrations in ISS that crystallized from the residual Cu-rich liquid at various F values; Footwall Zone chalcopyrite overlaps with ISS between F = 1 to 0.4, Main Zone chalcopyrite overlaps with ISS between F = 1 to 0.5, and W Horizon chalcopyrite overlaps with ISS from F = 1 to 0.1 (Fig. 5.13c).

5.5 Discussion

5.5.1 Hydrothermal redistribution of metals

A number of studies have noted the involvement of fluids in the redistribution of base and noble metals in the Marathon Cu-PGE deposit. Watkinson and Ohnenstetter (1992) suggested that fluids played a role in the mineralizing process based on several lines of evidence. These include: i) the predominance of PGM in coarse to pegmatitic gabbro that contains abundant F- and Cl-bearing mica and apatite, ii) the occurrence of PGM near partially-digested footwall xenoliths, in assemblages of hydrous minerals (e.g., chlorite, amphibole, epidote) and veinlets that crosscut partially replaced primary minerals, iii) the chemical zonation of some PGM (e.g., hollingworthite [(Rh,Pt,Pd)AsS]) (Ohnenstetter et al., 1991), iv) the presence of PGM in saline fluid inclusions in quartz and epidote (Watkinson and Jones, 1996), and v) the replacement of pyrrhotite by chalcopyrite and cubanite. Based on these textural and chemical features, they proposed that Cu- and PGE-bearing fluids, which were either derived from the magma and/or by the digestion of Archean metavolcanic footwall rocks, augmented the concentration of these metals in sulfides and that PGM were precipitated upon changes in fluid composition that resulted from alteration of magnetite by chlorite, and pyrrhotite by chalcopyrite and cubanite (Dahl et al., 2001; Watkinson and Ohnenstetter, 1992). The presence of late-stage, metal-rich fluids in the Marathon deposit was suggested by Shahabi Far et al. (2015) based on the occurrence of sulfides in Ca-rich overgrowths on plagioclase associated with biotite and hornblende, late cavities containing sulfides, biotite, hornblende, and carbonate, late apatite associated with assemblages of hornblende, biotite, carbonate, and sulfide, and the occurrence of fluid inclusions in replacement rims on late apatite. Accordingly, Shahabi Far (2016) suggested that metals (Cu, PGE) were remobilized throughout the deposit by this late-stage fluid based on the occurrence of high Cl/F, S, and metal concentrations in late apatite compared to primary apatite in the Footwall Zone, the association of late apatite with chalcopyrite, the replacement of sulfides by hydrous silicates, the replacement of pyrrhotite by chalcopyrite, and the replacement of exsolution lamellae in pyroxene by sulfides.

Experimentally-determined MSS/sulfide liquid partition coefficients ($D^{MSS/Sul}$) for base metals, the noble metals, and the main-group elements (Fleet et al., 1993; Helmy et al., 2010; Liu and Brenan, 2015; Mungall et al., 2005), along with their distribution among natural sulfides (e.g., Dare et al., 2011) suggest that the Ir-group PGE (IPGE; Ir, Os, Ru) and Co partition into MSS, whereas the Pt-group PGE (PPGE; Pt, Pd), Au, Ag, Zn, and the main-group elements (As, Sn, Sb, Te, Pb, and Bi) prefer to remain in the Cu-rich residual sulfide melt and either partition into ISS or form discrete phases (e.g., PGM). Selenium prefers the Cu-rich residual sulfide melt, but has a D close to 1 ($D_{Se}^{MSS/ISS} \sim 0.6$) (Cafagna and Jugo, 2016; Liu and Brenan, 2015). Therefore, if equilibrium chalcopyrite-pyrrhotite-pentlandite assemblages have a magmatic origin, as suggested by their rounded sulfide-silicate and sulfide-sulfide grain boundaries (Fig. 5.6a-c), than their chemistry should reflect that expected by MSS-ISS partitioning. If chalcopyrite that has replaced pyrrhotite (Fig. 5.7a) and that is commonly intergrown with hydrous silicates (Fig. 5.7b-f) has a hydrothermal origin, than the composition of chalcopyrite in these assemblages should deviate from that expected by MSS-ISS partitioning as they would not have crystallized from a fractionating sulfide liquid in equilibrium with the silicate melt, but rather precipitated from a hydrothermal fluid. In addition, the chalcopyrite may have inherited some of the chemical characteristics of the pyrrhotite that they replaced, as has been suggested by Djon and Barnes (2012) to account for the elevated concentration of IPGE in pyrite that replaced pyrrhotite in the Lac des Iles deposit.

5.5.1.1 Origin of sulfides that exhibit equilibrium textures

Of the noble metals, the IPGE were rarely detected in sulfides from the various mineralized zones throughout the Eastern Gabbro (Table 5.2). Although some of the PGM in the Eastern Gabbro contain IPGE, they are largely Pd- and Pt-bearing (Ames et al., 2017, 2016; Good et al., 2017). The low concentrations of IPGE in sulfides, therefore, cannot be entirely due to exsolution of PGM that contain IPGE. The low concentration of IPGE in the sulfides is more likely due to the original silicate magma having low concentrations of these metals, possibly due to early olivine fractionation at depth and sequestration of the IPGE (Liu et al., 2016). This is consistent with previous suggestions that olivine fractionated early

relative to pyroxene and sulfides at Marathon (Good and Crocket, 1994; Shahabi Far, 2016).

In the equilibrium assemblages, the Cu-rich sulfides are enriched in Zn and depleted in Co, Ru, and Ir relative to pyrrhotite and pentlandite, whereas the PPGE (apart from Pd in pentlandite), Au, Ag, and main-group elements occur in similar concentrations in all sulfides (Fig. 5.8). This distribution of metals is reflective of MSS-ISS partitioning and their magmatic origin. The similarly low concentration of PPGE, Au, Ag, and main-group elements among all sulfides that exhibit equilibrium textures can be explained by the exsolution of Pt- and Pd-rich PGM and Au-Ag alloys from the Cu-rich sulfides as the temperature of the system decreased (Barnes et al., 2008; Barnes and Lightfoot, 2005; Barnes and Ripley, 2016). Exsolution of PGM and alloys would have decreased the concentration of PPGE, Au, Ag, and the main-group elements in the sulfides, but would not have affected the concentration of base metals, such as Cu and Zn, as observed (Fig. 5.8). During laser ablation of the Cu-rich sulfides, many of these PGM would not have been included in the analyses as they may not have been intersected during laser sampling, resulting in concentrations in sulfides that do not reflect the original concentration of Pd, Pt, Au, and Ag. Post-cumulus modification of the noble metal concentrations of sulfides by exsolution of PGM is consistent with numerous lines of evidence. i) The concentration of Pd, Au, and Sn in chalcopyrite are lower than their modelled concentrations in ISS (Fig. 5.13a,b,d), suggesting that they exsolved as Sn-bearing PGM (e.g., Ames et al., 2017, 2016; Good et al., 2017). ii) Platinum-group minerals have been observed optically (Fig. 5.6a) and interpreted to be present in some laser ablation spectra based on coincident peaks in PGE and main-group elements (Fig. 5.5). iii) Ames et al. (2017, 2016) and Good et al. (2017) documented abundant Pd- and Pt-rich PGM and Au-Ag alloys in the Main Zone, W Horizon, and Area 41, many of which were associated with sulfides. The common occurrence of PGM within sulfides suggests that at least some of the PGM formed by exsolution from sulfides.

The enrichment of Pd in pentlandite (Fig. 5.8) has been observed in other Ni-Cu-PGE deposits (Ballhaus and Ryan, 1995; Cabri, 1994; Chai et al., 1993; Czamanske et al., 1992;

Li and Naldrett, 1993; Paktunc et al., 1990). Although it is known that pentlandite exsolves from MSS (Holwell and McDonald, 2010), the enrichment of Pd in pentlandite has been used to suggest that it may exsolve from ISS rather than MSS (e.g., Peregoedova and Ohnenstetter, 2002 and references therein), since ISS is the dominant host of the PPGE. The enrichment of Pd in pentlandite, however, does not necessitate that it exsolved from ISS rather than MSS because, if the Pd-rich pentlandite exsolved from ISS, than it should contain lower concentrations of IPGE than pyrrhotite, which exsolved from MSS (Dare et al., 2010). This is not the case, however, with some pentlandite even hosting more IPGE than pyrrhotite (Fig. 5.8). Rather, the enrichment of Pd in pentlandite can be ascribed to diffusion of small amounts of Pd from MSS and larger amounts from ISS into pentlandite at high temperature (~ 400-650°C) (Dare et al., 2010). For diffusion to have occurred, however, MSS and ISS could not have separated. This is consistent with previous work by Good et al. (2015), who suggested that the fractionation of MSS from ISS did not play an important role in the concentration of metals in the Marathon deposit based on the coherent behavior whole-rock PGE.

Copper and Zn are enriched in ISS over MSS, as expected by their MSS/sulfide liquid partition coefficients (Fig. 5.8). The low Zn concentrations observed in W Horizon sulfides compared to sulfides in all of the other mineralized zones are similar to those expected in ISS that crystallized to variable degrees (F = 1 to 0.1) from residual Cu-rich liquid (Fig. 5.13c).

This distribution of base metals, noble metals, and main-group elements among the equilibrium sulfides, therefore, is consistent with a magmatic origin. That is, they formed through fractionation of MSS and ISS followed by subsequent exsolution.

5.5.1.2 Origin of sulfides that exhibit disequilibrium textures

The occurrence of sulfide-hydrous mineral intergrowths has been described in numerous magmatic Ni-Cu-PGE deposits (e.g., Djon and Barnes, 2012; Gál et al., 2011; Hinchey and Hattori, 2005; Holwell et al., 2006; Hutchinson and Kinnaird, 2005; Li et al., 2007, 2004;

Liu et al., 2016; Park et al., 2004; Polovina et al., 2004), but no studies have noted the replacement of pyrrhotite by chalcopyrite. These textures clearly do not represent equilibrium assemblages. The chalcopyrite-hydrous silicate intergrowths can be interpreted in several ways. Some workers have interpreted these intergrowths largely as the replacement of magmatic sulfides by hydrous silicates (Djon and Barnes, 2012; Holwell et al., 2006; Li et al., 2004; Liu et al., 2016; Park et al., 2004). An alternative interpretation is that they represent hydrothermal sulfides that precipitated with hydrous silicates from a metal-rich fluid. A few studies have suggested a similar process, in which some of the intergrowths result from redeposition of Cu, Fe, and S (as secondary chalcopyrite) that was remobilized by the replacement of magmatic chalcopyrite (Li et al., 2007, 2004). The interpretation that the hydrous silicates replaced the sulfides was based largely on elevated concentrations of Cu in the hydrous silicates that replaced the chalcopyrite relative to those that were isolated from sulfides (Li et al., 2007, 2004). It might also be expected, however, that the concentration of Cu in hydrous silicates that precipitated from a Cu-rich fluid would also be elevated. The Cu concentration of hydrous silicates, therefore, cannot be used to uniquely describe the origin of these intergrowths and, as such, another approach is required to assess their origin.

Chalcopyrite has no cleavage, so actinolite that has replaced chalcopyrite should exhibit no preferred orientation. Yet, in many examples from the Eastern Gabbro, the actinolite that occur as inclusions in sulfides are aligned in a preferred orientation that is the same as their orientation in the pyroxene which they have replaced (Fig. 5.7d). These sulfide-hydrous silicate intergrowths, therefore, cannot be interpreted as the replacement of magmatic chalcopyrite by actinolite, but rather the replacement of pyroxene by actinolite and secondary chalcopyrite via the interaction of pyroxene with a Cu-rich fluid. In contrast, the sulfides that contain inclusions of randomly-oriented actinolite crystals (Fig. 5.7c) could represent the replacement of magmatic sulfides by actinolite. This is consistent with the common occurrence of these sulfides interstitial to primary silicates with which they often share equilibrium boundaries, and the occurrence of individual actinolite crystals that crosscut multiple sulfides in an assemblage, including chalcopyrite, bornite, and pyrrhotite.

Where magnetite is replaced by hydrous silicates (Fig. 5.7f), chalcopyrite can occur intergrown with the hydrous silicates between unaltered lamellae of ilmenite. This indicates that the chalcopyrite had to have formed after oxyexsolution of ilmenite, a late-stage, volatile-induced post-cumulus process (cf. Chapter 3; Buddington and Lindsley, 1964) that occurs at temperatures below those at which sulfide liquids completely crystallize; this rejects the possibility that this chalcopyrite crystallized from a sulfide melt. This interpretation is similar to that presented by Shahabi Far (2016), who interpreted chalcopyrite intergrown with hydrous silicates within replaced lamellae hosted in pyroxene as having precipitated from a hydrothermal fluid.

The occurrence of fine-grained chalcopyrite within pyroxene that has been partially to completely replaced by hydrous silicates (Fig. 5.7e) also suggests that these intergrowths cannot be magmatic in origin. If these chalcopyrite grains were magmatic, than they would represent larger crystals that were hosted within pyroxene prior to alteration. Although primary sulfide blebs do occur within pyroxene, they are typically fine-grained. Additionally, the occurrence of chalcopyrite restricted to alteration patches indicates that they cannot be magmatic in origin (Fig. 5.7e). These observations indicate that the chalcopyrite that occurs intergrown with hydrous silicates that have replaced pyroxene and magnetite must be hydrothermal in origin.

Two possible interpretations exist to account for the replacement of pyrrhotite by chalcopyrite. The first possibility is the resorption of pyrrhotite through its interaction with a late-stage Cu-rich sulfide liquid, followed by crystallization of magmatic chalcopyrite from this liquid. The second possibility is the replacement of pyrrhotite by a Cu-rich hydrothermal fluid. Resorption of pyrrhotite by a late-stage Cu-rich sulfide liquid is unlikely for a number of reasons. Firstly, these textures are dissimilar to classic resorption textures, that is, the pyrrhotite typically does not exhibit smooth, rounded embayments (e.g., Ginibre et al., 2007; Murphy et al., 2000; Ruprecht and Wörner, 2007; Shahabi Far, 2016), but rather the chalcopyrite-pyrrhotite boundaries are ragged (Fig. 5.7a). Secondly, the temperature of a residual liquid would be too low to resorb MSS. Lastly, introduction of a Cu-rich sulfide liquid of different composition would not be limited to the resorption

of only pyrrhotite. Other sulfides (e.g., pentlandite, chalcopyrite, cubanite) that were also out of equilibrium with the new sulfide liquid should also show evidence of resorption, but this was not observed. Therefore, a hydrothermal origin for chalcopyrite that has replaced pyrrhotite is preferred. Additional evidence for a hydrothermal origin of replacement chalcopyrite includes the common association with pyroxene and titanomagnetite that has been replaced by chalcopyrite and hydrous silicates (Fig. 5.7f).

5.5.1.3 Mobility of metals in the Eastern Gabbro

Few studies have made a direct comparison between the composition of magmatic and hydrothermal sulfides (e.g., Keays et al., 1982; Lesher and Keays, 2002). None of the comparisons were made between sulfides hosted in the same deposit or even the same type of deposit. This makes it difficult to compare how metals behave during magmatic and hydrothermal mineralizing processes as different deposit types (e.g., Ni-Cu-PGE vs. volcanogenic massive sulfide) will be characterized by different metal abundances. The coexistence of magmatic and hydrothermal sulfides at the scale of a thin section in this study provides an opportunity to directly compare the composition of sulfides that crystallized from a fractionating sulfide melt to those that precipitated from high-temperature hydrothermal fluids.

Hydrothermal chalcopyrite is, overall, compositionally similar to magmatic chalcopyrite (Fig. 5.8). Although magmatic and hydrothermal chalcopyrite pairs (i.e., those that occur in the same thin section) do show differences in base metal, noble metal, and main-group element concentrations, the differences are neither systematic nor very large (i.e., they are smaller than the variation observed among magmatic chalcopyrite within an individual thin section) (Fig. 5.9). The compositional similarity between the magmatic and hydrothermal chalcopyrite can be explained through dissolution of magmatic chalcopyrite in one location followed by the transport and precipitation of the metals as secondary chalcopyrite in another location. This is similar to what was suggested by Farrow and Watkinson (1992), Farrow (1994), Watkinson (1994), Farrow and Watkinson (1996), and Everest (1999) to explain the vein-type deposits in the footwall of the Sudbury Igneous complex, and Li et

al. (2004) and Li et al. (2007) to explain the sulfide-hydrous silicate intergrowths in the Bushveld Complex and Great Dyke. This model is also similar to that proposed by Shahabi Far (2016) for metal remobilization in the Eastern Gabbro. According to these models, secondary chalcopyrite would have precipitated from a fluid that was carrying similar metals as those hosted in magmatic chalcopyrite and in similar concentrations. Because the Cu/Pd values of both the Footwall Zone and Main Zone are similar, and both lie within the range of mantle values (Fig. 5.10), Cu could not have been removed from or added to these zones. It is more likely that redistribution of metals only occurred locally within a given mineralized zone. Therefore, it is suggested that the remobilized metals originated from magmatic chalcopyrite that had been replaced by hydrous silicates (Fig. 5.7c) and was redeposited as replacement chalcopyrite (Fig. 5.7a) or as chalcopyrite intergrown with hydrous silicates (Fig. 5.7d-f). Small-scale remobilization of base metals, noble metals, and main-group elements is reasonable given that numerous studies, both experimental and empirical, have documented their mobility (Hanley et al., 2005; Liu and McPhail, 2005; Mountain and Wood, 1988; Pan and Wood, 1994; Wood, 2002). Additionally, several examples of base metal, noble metal (preferentially Pd and Au), and main-group element (e.g., As) mobility in Ni-Cu-PGE systems have been described (Barnes and Liu, 2012; Boudreau et al., 2014; Gál et al., 2013; Holwell et al., 2017; Liu et al., 2016), with the most recent examples being from the Miitel and Sarah's Find komatiite (Le Vaillant et al., 2016, 2015).

5.5.2 Insights from S/Se values

As is the case for many Ni-Cu-PGE deposits, the PGE concentration of sulfides in the Eastern Gabbro has been modified by exsolution of PGM (cf. Ames et al., 2017, 2016; Good et al., 2017), and so are not an accurate proxy for R factor. The S/Se value of sulfides, however, is a better proxy for mineralization and post-cumulus processes because the Se concentration of sulfides in the Eastern Gabbro has not been modified by the exsolution of PGM since PGE-selenides have not been identified (Ames et al., 2017, 2016; Good et al., 2017). In fact, there are no known occurrences of Pt or Pd selenides that have directly crystallized from an evolving sulfide melt (Helmy and Fonseca, 2017), with the only

known occurrences of such PGM being associated with hydrothermal veins and oxidized weathered ores (Cabral et al., 2002; Prichard et al., 2013) that likely precipitated from low-temperature fluids (Forster et al., 2016).

The S/Se values of sulfides can record the effects of numerous supra- and subsolidus processes, including variations in R factor, contamination by S-rich rocks, early segregation of sulfide liquid, MSS-ISS fractionation, low- to high-temperature hydrothermal alteration, and metamorphism (Queffurus and Barnes, 2015; Smith et al., 2016). A number of these processes, however, can be ruled out as having had an effect on the S/Se values of sulfides in the Eastern Gabbro. Good et al. (2015) suggested that fractionation of MSS and ISS did not play a significant role in the concentration of metals in the Marathon deposit given the coherent behavior between Pd-Ir, Pd-Rh, and Pd-Pt throughout the Footwall Zone, Main Zone, and W Horizon. This is supported by the enrichment of pentlandite in Pd (Fig. 5.8) via diffusion from ISS and MSS, which requires that MSS and ISS did not separate. At least at Marathon, the possibility that S/Se was affected by early segregation of sulfide liquid seems unlikely given that Cu/Pd values of most Main Zone and Footwall Zone samples are within the mantle range (Fig. 5.10) (Barnes et al., 1993; Good et al., 2015). If sulfide liquid segregated at depth, Cu/Pd values (and S/Se) of the current sulfide assemblage would be greater than the mantle range due to the preferential removal of Pd over Cu (Fig. 5.14). Selenium likely remained immobile during any postcumulus processes given that i) the Se concentration of magmatic and hydrothermal chalcopyrite are indistinguishable (Figs. 5.8, 5.9), suggesting that Se remained in the sulfides during the hydrothermal event, similar to what was observed by Smith et al. (2016) in pyrite and millerite that replaced pyrrhotite, and ii) PGM-selenides associated with alteration assemblages that contain hematite are absent, suggesting that the saline, acidic, and oxidizing conditions required for Se mobility, at least at low temperatures (100 to 300ºC), were not present (Prichard et al., 2013). Effects due to regional metamorphism can be ruled out because there is no evidence for metamorphism in the Marathon Series. The only processes that remain that could have modified the S/Se value of sulfides are contamination by rocks that host variable S/Se values, variations in R factor, and suprasolidus S loss (e.g., multistage dissolution upgrading).

Contamination of a silicate melt by S- or Se-rich rocks can lead to deviations in the S/Se value relative to mantle values only if the S/Se value of the contaminant is significantly different from mantle values (Queffurus and Barnes, 2015; Smith et al., 2016). For this reason, interpretations of S/Se values are typically made in conjunction with S isotopic data. Sulfur/Se ratios higher than the mantle range typically occur in pyrite- and pyrrhotite-bearing sedimentary rocks and their incorporation into the silicate melt will yield a sulfide liquid with S/Se values higher than the mantle range (Queffurus and Barnes, 2015; Stanton, 1972). Ratios lower than the mantle range can occur in S-poor and Se-rich sedimentary rocks, such as the Aguablanca black slates (Piña et al., 2008) or low S/Se metamorphic rocks that lost S as a result of devolatilization (Piña et al., 2008; Queffurus and Barnes, 2015; Stanton, 1972).

Due to the high sulfide liquid/silicate melt partition coefficients of Pd ($D_{PGE}^{sul/sil}$ = 10^3 to > 10^5) (Campbell and Naldrett, 1979; Kerr and Leitch, 2005) and Se ($D_{Se}^{sul/sil}$ = 323 to 1,700) (Brenan, 2015; Patten et al., 2013; Peach et al., 1990), variations in R factor will yield a steep, positive slope on a Cu/Pd vs. S/Se diagram. Sulfides that experienced high R factors will have Cu/Pd and S/Se values lower than the mantle range, whereas sulfides that experienced low R factors will have Cu/Pd values at the higher end of the mantle range (Fig. 5.14) (Queffurus and Barnes, 2015). Because of the difference in D between Pd and Se, variations in R factor will yield a greater change in Cu/Pd than S/Se. This is consistent with the variations in these ratios observed among numerous other Ni-Cu-PGE deposits that have been demonstrated to have experienced variable R factors (Fig. 5.14).

5.5.3 Variability in R factor and segregation of sulfides in the Eastern Gabbro

5.5.3.1 Marathon Cu-PGE deposit

Samples from the mineralized zones in the Marathon deposit exhibit a wide range of Cu/Pd values from ~ 30 in the W Horizon to ~ 13,000 in the Footwall Zone (Fig. 5.10), suggesting that these zones experienced a wide range of R factors. Good et al. (2017) suggested that

sulfides in the W Horizon experienced higher R factors than the Footwall Zone and Main Zone, as well as a greater range of R factors (i.e., a more dynamic environment) based on a steeper negative slope defined by the W Horizon compared to the Footwall Zone and Main Zone on a Cu/Pd vs. Pd diagram. Based on the large diversity of PGM that occur in the W Horizon (e.g., PGE-sulfides, PGE-arsenides), Ames et al. (2017) suggested that the W Horizon formed by intrusion into the Eastern Gabbro as late-stage magma pulses that were enriched in PGE as a result of early sulfide liquation with high R factors in a staging chamber at depth. It is well-established that extreme enrichment in PGE can only be achieved via high R factors given the very high sulfide liquid/silicate melt partition coefficients of PGE (10^3 to > 10^5) (Campbell and Naldrett, 1979; Kerr and Leitch, 2005). Dynamic, conduit-type settings that involve injection of multiple pulses of magma are often employed to explain the high and often-times variable R factors experienced by sulfides in many Ni-Cu-PGE deposits (Barnes et al., 2015), including the Marathon deposit (Good et al., 2017; Shahabi Far, 2016).

The Cu/Pd values of the Footwall Zone and Main Zone samples fall within the range of mantle values, with the Footwall Zone typically having higher values than the Main Zone (Fig. 5.10). As discussed by Good et al. (2017), this suggests that these zones experienced moderate R factors. If these zones experienced moderate R factors, than individual sulfide minerals in these zones should have S/Se values within the mantle range (cf. Fig. 5.14). This is largely the case for the sulfides in the Main Zone, apart from a few sulfides that have S/Se values that are distinctly higher than the mantle range (Fig. 5.10). Sulfides hosted in the Footwall Zone, however, have S/Se values that are consistently higher than the mantle range (Fig. 5.10). The inconsistency between the Cu/Pd and S/Se value suggests that some other process besides R factor likely affected the S/Se value of the sulfides, which will be discussed in detail below.

The Cu/Pd values of the W Horizon samples are always lower than mantle values and span a similar range exhibited by numerous other PGE deposits, including the JM Reef of the Stillwater Complex and Merensky Reef of the Bushveld Complex (Fig. 5.12). The low Cu/Pd values correspond with S/Se values that are also largely lower than mantle values,

but exhibit a large range compared to other PGE deposits (Fig. 5.12). The relationship between Cu/Pd and S/Se values suggests that the W Horizon experienced high R factors, greater than those experienced by the Footwall Zone and Main Zone. Variations in R factor alone, however, cannot explain the large range in S/Se values exhibited by W Horizon sulfides (cf. Fig. 5.14), suggesting that some other processes must have modified the S/Se value of the sulfides. In the Eastern Gabbro, the two dominant processes that could have generated S/Se values that are lower than the mantle range are i) contamination by low S/Se rocks or ii) suprasolidus S loss (Fig. 5.14). Suprasolidus S loss is more likely the cause for the low S/Se values because, as will be discussed in detail below, the Marathon deposit, including the W Horizon, was contaminated by high S/Se sedimentary rocks rather than low S/Se rocks.

Sulfur loss in the W Horizon has been previously proposed. Good (2010) and Ruthart (2013) suggested that the W Horizon formed from sulfide liquids that experienced high R factors that resulted from multistage dissolution upgrading (Kerr and Leitch, 2005). Multistage dissolution upgrading refers to the dissolution of some mass of sulfide liquid by the influx of S-undersaturated silicate melt (i.e., suprasolidus S loss). The new PGE introduced into the system by successive pulses of silicate melt, along with the PGE recycled into the magma by dissolution of sulfide would allow the mass of sulfide liquid that was not dissolved to interact with this metal-enriched silicate melt (i.e., higher R factor). This would allow the sulfide liquid to become enriched in PGE to much higher concentrations than possible in a closed-system R factor model (Campbell and Naldrett, 1979, p. 1979; Kerr and Leitch, 2005). Additionally, Ruthart (2013) was able to accurately model the metal tenors of the W Horizon using this model and R factors ranging from 100 to 250,000.

Suprasolidus S loss might also account for the unique sulfide assemblage of chalcopyrite and bornite that is observed in the W Horizon. Sulfide assemblages containing bornite are not typical magmatic assemblages because crystallization of MSS and ISS results in a sulfide liquid with a Cu/Fe ratio near unity, such that the resulting sulfide assemblage would consist of pyrrhotite, pentlandite, and chalcopyrite (Tsujimura and Kitakaze, 2004;

Wohlgemuth-Ueberwasser et al., 2013; Yund and Kullerud, 1966). Even the most Cu-rich deposits (e.g., Noril'sk) are dominated by chalcopyrite and lack bornite (Cawthorn and Meyer, 1993). Several mechanisms have been proposed to account for the formation of bornite in sulfide assemblages, including i) fractional crystallization of MSS from the Cu-rich liquid (Naldrett et al., 1982; Wohlgemuth-Ueberwasser et al., 2013), ii) oxidation of the sulfide liquid, and iii) suprasolidus S loss. Of the three mechanisms, fractional crystallization of MSS at the Marathon deposit seems unlikely given the coherent behavior of bulk rock PGE as discussed by Good et al. (2015).

Ames et al. (2017) and Shahabi Far (2016) suggested that the bornite in the W Horizon resulted from oxidation of the sulfide liquid (cf. Wohlgemuth-Ueberwasser et al., 2013). Oxidation of the FeS and NiS components of a sulfide liquid to FeO, Fe_2O_3, and NiO causes an increase in its Cu/S ratio, which subsequently depresses its liquidus and solidus temperatures, allowing sulfide liquids to fractionate past the ISS stability field and eventually solidify to a Cu-rich assemblage that contains bornite and millerite (Ballhaus et al., 2001; Fonseca et al., 2008; Kaiser and Elliott, 1986; Kress, 2007, 2000, 1997; Moretti and Baker, 2008; Naldrett, 1969; Wohlgemuth-Ueberwasser et al., 2013). The FeO and NiO components that were formed either stabilize magnetite or enter into Fe-rich silicates (Wohlgemuth-Ueberwasser et al., 2013). Although the abundance of Fe-Ti oxides in the W Horizon relative to the Footwall Zone and Main Zone is inconsistent with the model (i.e., the abundance of magnetite is similar among the mineralized zones), this model could explain the occurrence of bornite and millerite in the W Horizon and the higher concentration of Ni in magnetite (cf. Chapter 4) and olivine (Ruthart, 2013) from the W Horizon compared to the Footwall Zone and Main Zone.

Although the oxidation model cannot be ruled out, it is also possible that S loss also played a role in generating bornite. Because bornite has a lower proportion of S compared to chalcopyrite, removal of S from the sulfide liquid can result in higher Cu/S values capable of crystallizing bornite. This is consistent with the S/Se values of sulfides in the W Horizon, which are consistently less than mantle values (Fig. 5.10).

5.5.3.2 Mineralized occurrences northwest of the Marathon deposit

Samples from the mineralized zones northwest of the Marathon deposit exhibit a continuous and wide range of Cu/Pd values that extend from values lower than mantle (~ 270) to values that are significantly higher than mantle (~ 350,000) (Fig. 5.11). Samples from mineralization type II at Area 41 have Cu/Pd within the mantle range and low S/Se that partly overlap with the Main Zone (Fig. 5.11), suggesting the system experienced moderate to low R factors comparable to the Main Zone. Samples from the mineralization type III have low (enriched) Cu/Pd and low S/Se relative to mantle. These values overlap with the W Horizon (Fig. 5.11) and suggest that the system experienced moderate to high R factors comparable to the W Horizon (Good et al., 2017).

Samples from Four Dams, mineralization types I and IV at Area 41, and Redstone are similar with high Cu/Pd and low S/Se (Fig. 5.11). The high Cu/Pd could not have been generated by low R factors because even at R factors of 100, the Cu/Pd of a sulfide liquid is still within the mantle range (cf. Barnes et al., 1993). The high Cu/Pd could have been generated by i) addition of externally-derived Cu or ii) removal of Pd by early sulfide segregation. Addition of externally-derived Cu is unlikely because Cu/Pd values in these areas show a negative correlation with Pd on Cu/Pd vs. Pd binary diagrams (not shown). If external Cu was added to these zones, whole-rock Cu/Pd values would increase, but whole-rock Pd values would be unaffected (i.e., there would be no correlation). It is more likely, therefore, that sulfides in these zones had formed from a Pd depleted magma, presumably due to a prior episode of sulfide segregation. This process, however, should also have increased the S/Se above the mantle range (cf. Fig. 5.14). Because the S/Se of the low PGE zones northwest of the Marathon deposits are lower than the mantle range, than an alternative process, such as S loss of contamination by a low S/Se source, must have occurred. This is discussed below.

If mineralization type III at Area 41 experienced moderate to high R factors, than sulfide S/Se values should be similar to, or slightly lower than, the mantle and correlate positively with Cu/Pd (cf. Fig. 5.14). This is largely the case, with sulfides having S/Se values that

are distinctly lower than the mantle range (as low as ~ 1,200) (Fig. 5.11). In contrast, if mineralization types I and IV at Area 41, Four Dams, and Redstone experienced low R factors, than sulfide S/Se values should be slightly higher than the mantle range (cf. Fig. 5.14). Most of the sulfides, however, have S/Se values (as low as ~ 1,100) that are consistently lower than the mantle range (Fig. 5.11). In addition, sulfide S/Se values in these zones exhibit no correlation with Cu/Pd values. These relationships suggest that a process other than variations in R factor modified the S/Se value of the sulfides.

Although R factor may not have played a large role in generating the characteristic Cu/Pd and S/Se values at Four Dams, mineralization types I and IV at Area 41, and Redstone, it is likely that these zones experienced lower R factors than mineralization types II and III at Area 41 and all of the mineralized zones at the Marathon deposit. A unique feature that is common to the low PGE occurrences northwest of Marathon is the high abundance of cubanite relative to chalcopyrite. Variations in the proportion of cubanite and chalcopyrite have been noted in other Ni-Cu-PGE deposits (e.g., Naldrett et al., 2000; Ripley and Alawi, 1986). Given silicate melts with similar Cu concentrations, Ripley and Alawi (1986) suggested that variations in R factor can produce sulfide assemblages that are either dominated by chalcopyrite or by cubanite based on the partitioning behaviors of Cu and Fe into the sulfide liquid. High R factors result in sulfide liquids with high Cu/Fe ratios, whereas low R factors result in low Cu/Fe ratios, which crystallize into assemblages dominated either by chalcopyrite or cubanite, respectively (Naldrett et al., 2000; Ripley and Alawi, 1986). The rocks that host mineralization at Marathon and in the occurrences northwest of Marathon occur in the same rock series (Good et al., 2015). If the composition of the original sulfide liquids that formed the mineralized zones at Marathon and the northern occurrences was similar, than variations in R factor could explain the differences in mineralogy of their Cu-rich sulfide assemblage. Accordingly, based on the sulfide mineralogy, sulfides in the northern occurrences would have experienced lower R factors than sulfides at Marathon, consistent with the difference in their Cu/Pd and S/Se values.

5.5.4 Contamination in the Eastern Gabbro

5.5.4.1 Marathon deposit

Shahabi Far et al. (2018) noted that the $\Delta^{33}S$ values for sulfides from each of the mineralized zones at Marathon were consistently negative, with sulfides in the Footwall Zone having the most negative values, sulfides in the W Horizon having the least negative values, and sulfides in the Main Zone having values intermediate to these. Shahabi Far et al. (2018) also noted a negative correlation between $\Delta^{33}S$ and $\Delta^{36}S$ that is characteristic of Archean sedimentary rocks. Accordingly, it was interpreted that the magmas that formed the Marathon deposit were variably contaminated by Archean sedimentary rocks at depth.

Sedimentary rocks are typically characterized by S/Se values higher than the mantle range. Accordingly, if the Marathon deposit was variably contaminated by Archean sedimentary rocks at depth, with the Footwall Zone having experienced the highest degree of contamination and W Horizon the lowest degree, than the S/Se values of their sulfides should be greatest for the Footwall Zone sulfides (and above the mantle range) and lowest for the W Horizon sulfides (but still above the mantle range).

Sulfides from the Footwall Zone have the highest S/Se values of all of the mineralized zones at Marathon; they range from 6,000 to 300,000 and are consistently higher than the mantle range (Fig. 5.10). They extend to higher values than those exhibited by sulfides at Kabanga (S/Se values between 39,000 and 42,000), a Ni-Cu deposit that has been described as an extreme example of contamination by externally-derived S (Fig. 5.12) (Maier and Barnes, 2010). Additionally, the high S/Se values in these sulfides have the correspondingly lowest (most negative) $\Delta^{33}S$ values of all the mineralized zones at Marathon (Fig. 5.15). Therefore, the high S/Se values exhibited by Footwall Zone sulfides are consistent with the interpretations made by Shahabi Far et al. (2018), based on multiple S isotopes, that the Footwall Zone experienced the highest degree of contamination out of all of the mineralized zones at Marathon.

Most of the sulfides from the Main Zone have S/Se values (1,400 to 8,000) that straddle the mantle range and do not correlate with Cu/Pd (Fig. 5.10), suggesting that the S/Se

values are not entirely controlled by variable R factors and that this zone experienced minimal modification by suprasolidus processes (e.g., S contamination, S loss). A few samples, however, have S/Se values that are higher than the mantle range, from 10,000 to 19,000, similar to the values exhibited by disseminated Footwall Zone sulfides (Fig. 5.10). As discussed for the Footwall Zone, these high values suggest that the Main Zone likely did experience some degree of contamination by high S/Se sedimentary rock, albeit less than the Footwall Zone, consistent with the less negative $\Delta^{33}S$ of its sulfides compared to that of the Footwall Zone (Fig. 5.15) (Shahabi Far et al., 2018).

The majority of W Horizon sulfides have S/Se and Cu/Pd values that are lower than the mantle, and which are, in general, positively correlated (Fig. 5.10). This suggests that the S/Se values are, at least to some degree, controlled by variability in R factor, as discussed above. The large range in S/Se to values greater than the mantle range, however, suggests that the W Horizon may also have been contaminated by high S/Se rocks. Sulfides from the W Horizon were subdivided into three populations based on S/Se and Cu/Pd values (cf. *Variation in S/Se value*). Sulfides from populations I and II have moderate and low Cu/Pd values, respectively, and have S/Se values that are consistently lower than the mantle range (Fig. 5.10); these populations exhibit no evidence for contamination by high S/Se rocks. Sulfides from population III, however, have Cu/Pd values intermediate to populations I and II, and S/Se values that extend from less than to greater than the mantle range (Fig. 5.10). If sulfides from population III originally had S/Se values similar to populations I and II (Fig. 5.10), as suggested by the lack of population III in the whole-rock S/Se, than the high S/Se values of population III likely record contamination of the silicate melt by high S/Se sedimentary rocks. This interpretation is supported by the fact that sulfides from one sample in population III have a $\Delta^{33}S$ value of -0.06 (Fig. 5.15), which, as discussed above, are indicative of addition of Archean sedimentary S.

5.5.4.2 Mineralized occurrences northwest of Marathon

As discussed above, the high Cu/Pd in the northern occurrences was likely due to segregation of sulfides at depth. This process, however, should also have increased the S/Se

of the sulfides, but this is not observed, indicating that some other processes had to have modified the S/Se of the sulfides.

The presence of bornite in the W Horizon was attributed, in part, to suprasolidus S loss. The fact that bornite is absent in the mineralized zones in the northwest suggests that S loss is likely not the process that generated their low S/Se values. It is more likely that the low S/Se values were generated by contamination of the silicate melt by low S/Se rocks. The country rocks to the Eastern Gabbro are predominantly mafic to felsic metavolcanics and granitoid rocks (Walker et al., 1993). Igneous rocks typically have S/Se values that are similar to mantle values, which, if incorporated into a magma, would not significantly modify the S/Se value of the sulfide liquid that liquates from it (Queffurus and Barnes, 2015; Stanton, 1972). Piña et al. (2008) suggested that devolatilization of igneous rocks during metamorphism, however, can cause S loss and generate bulk S/Se values that are lower than the mantle range. Accordingly, if the metavolcanic country rocks lost S by devolatilization and were subsequently incorporated into the silicate melt that formed the high Cu/Pd mineralized zones northwest of Marathon, the sulfides that liquated from this melt would have S/Se values lower than the mantle range, as is observed (Fig. 5.11).

5.5.5 Semi-massive chalcopyrite-rich pod

The semi-massive chalcopyrite-rich pod represents a unique style of mineralization in the vicinity of the Coldwell Complex. It is dominated by chalcopyrite and contains Pd grades of up to 100 ppm. This pod is characterized by Cu/Pd values lower than the mantle range, similar to the W Horizon, but S/Se values higher than the mantle range, similar to the Footwall Zone and Main Zone (Fig. 5.11). As discussed above, these zones were generated by different suprasolidus processes, with the W Horizon having experienced high R factors and minor contamination, and the Footwall Zone and Main Zone having experienced low R factors and moderate to large degrees of contamination. Accordingly, to generate the ratios observed in the chalcopyrite-rich pod, the sulfides it hosts must have experienced both high R factors, as well as relatively high degrees of contamination by high S/Se rocks (Fig. 5.14). The R factors were likely similar to those experienced by the W Horizon, and

the degree of contamination likely similar to those experienced by the Footwall Zone. This high degree of S contamination may be the reason why the sulfides in the pod are semi-massive.

5.6 Conclusion

Although the platinum-group element content of sulfides has been used to assess mineralizing mechanisms in several Ni-Cu-PGE deposits, there are several issues which plague this approach, including a lack of well-developed LA-ICP-MS sulfide standards, spectral interferences on PGE, and lack of understanding of how PGE behave in hydrothermal fluids at magmatic temperatures. Accordingly, interpretations of mineralizing processes should not be made strictly on the basis of the PGE concentration of sulfides, but should incorporate other geochemical proxies, such as S/Se values, as well as detailed textural characterization. Accordingly, it has been demonstrated that a range of processes acted to generate and modify mineralization in the Eastern Gabbro, illustrating the complex nature of conduit-type Cu-PGE systems.

i. Mineralization at the Marathon Cu-Pd deposit and those northwest of Marathon are mineralogically and chemically (Cu/Pd, S/Se) distinct.
ii. The platinum-group element content of sulfides was modified by the formation of platinum-group minerals prior to crystallization of sulfides and/or exsolution after the crystallization of sulfides.
iii. Base metals, noble metals, and main-group elements were remobilized from primary chalcopyrite by hydrothermal fluids and precipitated as secondary chalcopyrite, which occur as intergrowths with hydrous silicates and as a replacement of pyrrhotite. This mobility occurred locally at the scale of a mineralized zone.
iv. In the Marathon deposit, the sulfide liquid that generated the sulfides in the W Horizon evolved to a greater degree than the sulfide liquid that generated the sulfides in the Footwall Zone and Main Zone.

v. Sulfides in the W Horizon experienced the highest R factors, followed by the Main Zone and the Footwall Zone. The W Horizon also experienced variable amounts of suprasolidus S loss (e.g., multistage dissolution upgrading), which may explain the occurrence of bornite. Sulfides in the mineralized occurrences northwest of Marathon experienced lower R factors than the Marathon deposit, which can also account for the high proportion of cubanite relative to chalcopyrite in these occurrences.

vi. Of the mineralized zones in the Eastern Gabbro, Four Dams, mineralization types I and IV at Area 41, and Redstone are the only zones that exhibit evidence for a prior episode of sulfide segregation.

vii. The mineralized zones at Marathon were contaminated to varying degrees by high S/Se rocks (e.g., Archean sedimentary rocks), with the Footwall Zone having experienced the greatest degree of contamination, and the W Horizon the least. The degree of contamination in the Footwall Zone is similar to that observed at Kabanga, an extreme example of contamination by externally-derived S. In contrast, the occurrences northwest of Marathon were likely contaminated by low S/Se rocks (e.g., metamorphic rocks).

viii. The chalcopyrite-rich pod experienced both high R factors, as well as high degrees of contamination, similar to the W Horizon and Footwall Zone, respectively, at Marathon.

5.7 References

Ames, D.E., Kjarsgaard, I.M., Good, D.J., McDonald, A.M., 2016. Ore mineralogy of Cu-PGE mineralized gabbros, Coldwell Alkaline Complex, Midcontinent rift: supporting databases, scanning electron microscope, and mineral chemistry. Geological Survey of Canada Open File No. 8006.

Ames, D.E., Kjarsgaard, I.M., McDonald, A.M., Good, D.J., 2017. Insights into the extreme PGE enrichment of the W Horizon, Marathon Cu-Pd deposit, Coldwell

Alkaline Complex, Canada: Platinum-group mineralogy, compositions and genetic implications. Ore Geol. Rev. 90, 723–747.

Ballhaus, C., Ryan, C.G., 1995. Platinum-group elements in the Merensky reef. I. PGE in solid solution in base metal sulfides and the down-temperature equilibration history of Merensky ores. Contrib. Mineral. Petrol. 122, 241–251.

Ballhaus, C., Tredoux, M., Späth, A., 2001. Phase Relations in the Fe-Ni-Cu-PGE-S System at Magmatic Temperature and Application to Massive Sulphide Ores of the Sudbury Igneous Complex. J. Petrol. 42, 1911–1926.

Barnes, S.-J., Couture, J.-F., Sawyer, E.W., Bouchaib, C., 1993. Nickel-Copper Occurrences in the Belleterre-Angliers Belt of the Pontiac Subprovince and the Use of Cu-Pd Ratios in Interpreting Platinum-Group Element Distributions. Econ. Geol. 88, 1402–1418.

Barnes, S.-J., Cox, R.A., Zientek, M.L., 2006. Platinum-group element, Gold, Silver and Base Metal distribution in compositionally zoned sulfide droplets from the Medvezky Creek Mine, Noril'sk, Russia. Contrib. Mineral. Petrol. 152, 187–200.

Barnes, S.J., Cruden, A.R., Arndt, N., Saumur, B.M., 2015. The mineral system approach applied to magmatic Ni-Cu-PGE sulphide deposits. Ore Geol. Rev. 76, 296–316.

Barnes, S.-J., Lightfoot, P.C., 2005. Formation of Magmatic Nickel Sulfide Ore Deposits and Processes Affecting Their Copper and Platinum Group Element Contents.

Barnes, S.J., Liu, W., 2012. Pt and Pd mobility in hydrothermal fluids: Evidence from komatiites and from thermodynamic modelling. Ore Geol. Rev. 44, 49–58.

Barnes, S.-J., Prichard, H.M., Cox, R.A., Fisher, P.C., Godel, B., 2008. The location of the chalcophile and siderophile elements in platinum-group element ore deposits (a textural, microbeam and whole rock geochemical study): Implications for the formation of the deposits. Chem. Geol. 248, 295–317.

Barnes, S.-J., Ripley, E.M., 2016. Highly Siderophile and Strongly Chalcophile Elements in Magmatic Ore Deposits. Rev. Mineral. Geochem. 81, 725–774.

Barnes, S.-J., Savard, D., Bédard, L.P., Maier, W.D., 2009. Selenium and sulfur concentrations in the Bushveld Complex of South Africa and implications for formation of the platinum-group element deposits. Miner. Deposita 44, 647–663.

Barnes, S.-J., van Achterbergh, E., Makovicky, E., Li, C., 2001. Proton microprobe results for the partitioning of platinum-group elements between monsulphide solid solution and sulphide liquid. South Afr. J. Geol. 104, 275–286.

Barrie, C.T., MacTavish, P., Walford, P., Chataway, R., MIddaugh, R., 2002. Contact-type and Magnetite Reef-type Pd-Cu Mineralization in Ferroan Olivine Gabbros of the Coldwell Complex, Ontario, in: The Geology, Geochemistry, Mineralogy and Mineral Beneficiation of Platinum-Group Elements: Canadian Institute of Mining, Metallurgy and Petroleum Special. pp. 321–338.

Boudreau, A., Djon, L., Tchalikian, A., Corkery, J., 2014. The Lac Des Iles Palladium Deposit, Ontario, Canada part I. The effect of variable alteration on the Offset Zone. Miner. Deposita 49, 625–654.

Brenan, J.M., 2015. Se–Te fractionation by sulfide–silicate melt partitioning: Implications for the composition of mantle-derived magmas and their melting residues. Earth Planet. Sci. Lett. 422, 45–57.

Buddington, A.F., Lindsley, D.H., 1964. Iron-titanium oxide minerals and synthetic equivalents. J. Petrol. 5, 310–357.

Cabral, A.R., Lehmann, B., Kwitko-Ribeiro, R., Costa, C.H.C., 2002. Palladium and platinum minerals from the Serra Pelada Au-Pd-Pt deposit, Carajas Mineral Province, Northern Brazil. Can. Mineral. 40, 1451–1463.

Cabri, L.J., 1994. Current status of determination of mineralogical balances for platinum-group element-bearing ores. Trans. Inst. Min. Metall.-Sect. B-Appl. Earth Sci. 103, B3–B9.

Cafagna, F., Jugo, P.J., 2016. An experimental study on the geochemical behavior of highly siderophile elements (HSE) and metalloids (As, Se, Sb, Te, Bi) in a mss-iss-pyrite system at 650°C: A possible magmatic origin for Co-HSE-bearing pyrite and the role

of metalloid-rich phases in the fractionation of HSE. Geochim. Cosmochim. Acta 178, 233–258.

Campbell, I.H., Naldrett, A.J., 1979. The influence of silicate: sulfide ratios on the geochemistry of magnetic sulfides. Econ. Geol. 74, 1503–1506.

Cao, Y., 2017. Cu-Pd mineralization and exploration geochemistry of the Eastern Gabbro, Coldwell Alkaline Complex, ON, Canada (PhD Dissertation). Western University, London, Ontario.

Cao, Y.H., Linnen, R.L., Good, D.J., Samson, I.M., Epstein, R., 2016. The application of portable XRF and benchtop SEM-EDS to Cu-Pd exploration in the Coldwell Alkaline Complex, Ontario, Canada. Geochem. Explor. Environ. Anal. 16, 193–212.

Cawthorn, R.G., Meyer, F.M., 1993. Petrochemistry of the Okiep Copper District Basic Intrusive Bodies, Northwestern Cape Province, South Africa. Econ. Geol. 88, 590–605.

Chai, G., Naldrett, A.J., Rucklidge, J.C., 1993. In situ quantitative analyses for PGE and Au in sulfide minerals of the Jinchuan Ni-Cu deposit by accelerator mass spectrometry. Can. Mineral. 31, 19–30.

Currie, K.L., 1980. A conrtibution to the petrology of the Coldwell alkaline complex, northern Ontario. Geol. Surv. Can. Bull. 287.

Czamanske, G.K., Kunilov, V.E., Zientek, M.L., Cabri, L.J., Likhachev, A.P., Calk, L.C., Oscarson, R.L., 1992. A proton-microprobe study of magmatic sulfide ores from the Noril'sk-Talnakh district, SIberia. Can. Mineral. 30, 249–287.

Dahl, R., Watkinson, D.H., Taylor, R.P., 2001. Geology of the Two Duck Lake Intrusion and the Marathon Cu-PGE Deposit, Coldwell Complex, Northern Ontario. Explor. Min. Geol. 10, 51–65.

Dare, S.A.S., Barnes, S.-J., Prichard, H.M., 2010. The distribution of platinum group elements (PGE) and other chalcophile elements among sulfides from the Creighton Ni–Cu–PGE sulfide deposit, Sudbury, Canada, and the origin of palladium in pentlandite. Miner. Deposita 45, 765–793.

Dare, S.A.S., Barnes, S.-J., Prichard, H.M., Fisher, P.C., 2014. Mineralogy and geochemistry of Cu-rich ores from the McCreedy East Ni-Cu-PGE deposit (Sudbury, Canada): Implications for the behavior of platinum group and chalcophile elements at the end of crystallization of a sulfide liquid. Econ. Geol. 109, 343–366.

Dare, S.A.S., Barnes, S.-J., Prichard, H.M., Fisher, P.C., 2011. Chalcophile and platinum-group element (PGE) concentrations in the sulfide minerals from the McCreedy East deposit, Sudbury, Canada, and the origin of PGE in pyrite. Miner. Deposita 46, 381–407.

Djon, M.L.N., Barnes, S.-J., 2012. Changes in sulfides and platinum-group minerals with the degree of alteration in the Roby, Twilight, and High Grade Zones of the Lac des Iles Complex, Ontario, Canada. Miner. Deposita 47, 875–896.

Duran, C.J., Barnes, S.-J., Corkery, J.T., 2016. Trace element distribution in primary sulfides and Fe–Ti oxides from the sulfide-rich pods of the Lac des Iles Pd deposits, Western Ontario, Canada: Constraints on processes controlling the composition of the ore and the use of pentlandite compositions in exploration. J. Geochem. Explor. 166, 45–63.

Duran, C.J., Barnes, S.-J., Pleše, P., Kudrna Prašek, M., Zientek, M. L., Pagé, P., 2017. Fractional crystallization-induced variations in sulfides from the Noril'sk-Talnakh mining district (polar Siberia, Russia). Ore Geol. Rev. 90, 326-351.

Eckstrand, O.R., Grinenko, L.N., Krouse, H.R., Paktunc, A.D., Schwann, P.L., Scoates, R.F.J., 1989. Preliminary Data On Sulphur Isotopes and Se/S Ratios, and the Source of Sulphur in Magmatic Sulphides From the Fox River Sill, Molson Dykes and Thompson Nickel Deposits, northern Manitoba, in: Current Research, Part C. Geological Survey of Canada, Paper 89-1C. pp. 235–242.

Eckstrand, O.R., Hulbert, L.J., 1987. Selenium and the source of sulfur in magmatic nickel and platinum deposits, in: Geological Association of Canada-Mineralogical Association of Canada. Saskatoon, Canada.

Everest, J.O., 1999. The relationship of Cu-Ni-PGE veins in the Levack Gneiss Complex to contact magmatic ore at the McCreedy West mine, Sudbury (MSc Thesis). Carleton, Ottawa, Canada.

Farrow, C.E.G., 1994. Geology, alteration and the role of fluids in Cu-Ni- PGE mineralization of the footwall rocks to the Sudbury Igneous Complex, Levack and Morgan townships, Sudbury district, Ontario (PhD Dissertation). Carleton, Ottawa, Canada.

Farrow, C.E.G., Watkinson, D.H., 1996. Geochemical evolution of the Epidote Zone, Fraser Mine, Sudbury, Ontario: Ni-Cu-PGE remobilization by saline fluids. Explor. Min. Geol. 5, 17–31.

Farrow, C.E.G., Watkinson, D.H., 1992. Alteration and the role of fluids in Ni, Cu and platinum-group element deposition, Sudbury Igneous Complex contact, Onaping-Levack area, Ontario. Mineral. Petrol. 46, 67–83.

Fleet, M.E., Chryssoulis, S.L., Stone, W.E., Weisener, C.G., 1993. Partitioning of platinum-group elements and Au in the Fe- Ni- Cu- S system: experiments on the fractional crystallization of sulfide melt. Contrib. Mineral. Petrol. 115, 36–44.

Fonseca, R.O.C., Campbell, I.H., O'Neill, H.S.C., Fitzgerald, J.D., 2008. Oxygen solubility and speciation in sulphide-rich mattes. Geochim. Cosmochim. Acta 72, 2619–2635.

Forster, H.-J., Bindi, L., Grundmann, G., Stanley, C., 2016. Quijarroite, Cu6HgPb2Bi4Se12, a New Selenide from the El Dragón Mine, Bolivia. Minerals 6, 123.

Gál, B., Molnár, F., Guzmics, T., Mogessie, A., Szabó, C., Peterson, D.M., 2013. Segregation of magmatic fluids and their potential in the mobilization of platinum-group elements in the South Kawishiwi Intrusion, Duluth Complex, Minnesota — Evidence from petrography, apatite geochemistry and coexisting fluid and melt inclusions. Ore Geol. Rev. 54, 59–80.

Gál, B., Molnár, F., Peterson, D.M., 2011. Cu-Ni-PGE Mineralization in the South Filson Creek Area, South Kawishiwi Intrusion, Duluth Complex: Mineralization Styles and Magmatic and Hydrothermal Processes. Econ. Geol. 106, 481–509.

Ginibre, C., Wörner, G., Kronz, A., 2007. Crystal Zoning as an Archive for Magma Evolution. Elements 3, 261–266.

Godel, B., Barnes, S.-J., 2008. Platinum-group elements in sulfide minerals and the whole rocks of the J-M Reef (Stillwater Complex): Implication for the formation of the reef. Chem. Geol. 248, 272–294.

Good, D., Meghji, I., Linnen, R., Samson, I., Cundari, R., 2017a. Cogenetic relationship between the Wolf Camp basalt and the Geordie Lake intrusion, Coldwell Alkaline Complex, Midcontinent Rift, Ontario, in: Institute on Lake Superior Geology 63rd Annual Meeting. Wawa, Ontario.

Good, D.J., 2010. Applying multistage dissolution upgrading and 3D-GIS to exploration at the Marathon Cu-PGE deposit, Canada, in: 11th International Platinum Symposium, Sudbury, Ontario, Canada.

Good, D.J., Cabri, L.J., Ames, D.E., 2017. PGM Facies variations for Cu-PGE deposits in the Coldwell Alkaline Complex, Ontario, Canada. Ore Geol. Rev. 90, 748-771.

Good, D.J., Crocket, J.H., 1994. Genesis of the Marathon Cu-Platinum-Group Element Deposit, Port Coldwell Alkalic Complex, Ontario: A Midcontinent Rift-Related Magmatic Sulfide Deposit. Econ. Geol. 89, 131–149.

Good, D.J., Epstein, R., McLean, K., Linnen, R., Samson, I., 2015. Evolution of the Main Zone at the Marathon Cu-PGE Sulfide Deposit, Midcontinent Rift, Canada: Spatial Relationships in a Magma Conduit Setting. Econ. Geol. 110, 983–1008.

Hanley, J.J., 2005. The Aqueous Geochemistry of the Platinum Group Elements (PGE) in Surficial, Low-T Hydrothermal and High-T Magmatic-Hydrothermal Environments, in: Mungall, J.E. (Ed.), Exploration for Platinum-Group Element Deposits. Mineralogical Association of Canada, Oulu, Finland, pp. 35–56.

Hanley, J.J., Pettke, T., Mungall, J.E., Spooner, E.T.C., 2005. The solubility of platinum and gold in NaCl brines at 1.5 kbar, 600 to 800°C: A laser ablation ICP-MS pilot study of synthetic fluid inclusions. Geochim. Cosmochim. Acta 69, 2593–2611.

Hattori, K.H., Arai, S., Clarke, D.B., 2002. Selenium, tellurium, arsenic and antimony contents of primary mantle sulfides. Can. Mineral. 40, 637–650.

Heaman, L.M., Machado, N., 1992. Timing and origin of midcontinent rift alkaline magmatism, North America: evidence from the Coldwell Complex. Contrib. Mineral. Petrol. 110, 289–303.

Helmy, H.M., Ballhaus, C., Wohlgemuth-Ueberwasser, C., Fonseca, R.O.C., Laurenz, V., 2010. Partitioning of Se, As, Sb, Te and Bi between monosulfide solid solution and sulfide melt – Application to magmatic sulfide deposits. Geochim. Cosmochim. Acta 74, 6174–6179.

Helmy, H.M., Fonseca, R.O.C., 2017. The behavior of Pt, Pd, Cu and Ni in the Se-sulfide system between 1050 and 700°C and the role of Se in platinum-group elements fractionation in sulfide melts. Geochim. Cosmochim. Acta.

Hinchey, J.G., Hattori, K.H., 2005. Magmatic mineralization and hydrothermal enrichment of the High Grade Zone at the Lac des Iles palladium mine, northern Ontario, Canada. Miner. Deposita 40, 13–23.

Holwell, D.A., Adeyemi, Z., Ward, L.A., Smith, D.J., Graham, S.D., McDonald, I., Smith, J.W., 2017. Low temperature alteration of magmatic Ni-Cu-PGE sulfides as a source for hydrothermal Ni and PGE ores: A quantitative approach using automated mineralogy. Ore Geol. Rev.

Holwell, D.A., Keays, R.R., McDonald, I., Williams, M.R., 2015. Extreme enrichment of Se, Te, PGE and Au in Cu sulfide microdroplets: evidence from LA-ICP-MS analysis of sulfides in the Skaergaard Intrusion, east Greenland. Contrib. Mineral. Petrol. 170.

Holwell, D.A., McDonald, I., 2010. A Review of the Behaviour of Platinum Group Elements within Natural Magmatic Sulfide Ore Systems. Platin. Met. Rev. 54, 26–36.

Holwell, D.A., McDonald, I., Armitage, P.E.B., 2006. Platinum-group mineral assemblages in the Platreef at the Sandsloot Mine, northern Bushveld Complex, South Africa. Mineral. Mag. 70, 83–101.

Howard, J.H., 1977. Geochemistry of selenium: formation of ferroselite and selenium behavior in the vicinity of oxidizing sulfide and uranium deposits. Geochim. Cosmochim. Acta 41, 1665–1678.

Hutchinson, D., Kinnaird, A., 2005. Complex multistage genesis for the Ni-Cu-PGE mineralization in the southern region of the Platreef, Bushveld Complex, South Africa. Appl. Earth Sci. 114.

Kaiser, D.L., Elliott, J.F., 1986. Solubility of oxygen and sulfur in copper-iron mattes. Metall. Mater. Trans. B 17, 147–157.

Keays, R.R., Nickel, E.H., Groves, D.I., McGoldrick, P.J., 1982. Iridium and palladium as discriminants of volcanic-exhalative, hydrothermal, and magmatic nickel sulfide mineralization. Econ. Geol. 77, 1535–1547.

Kerr, A., Leitch, A.M., 2005. Self-Destructive Sulfide Segregation Systems and the Formation of High-Grade Magmatic Ore Deposits. Econ. Geol. 100, 311–332.

Kress, V., 2007. Thermochemistry of sulfide liquids III: Ni-bearing liquids at 1 bar. Contrib. Mineral. Petrol. 154, 191–204.

Kress, V., 2000. Thermochemistry of sulfide liquids. II. Associated solution model for sulfide liquids in the system O-S-Fe. Contrib. Mineral. Petrol. 139, 316–325.

Kress, V., 1997. Thermochemistry of sulfide liquids. I. The system OS-Fe at 1 bar. Contrib. Mineral. Petrol. 127, 176–186.

Le Vaillant, M., Barnes, S.J., Fiorentini, M.L., Miller, J., McCuaig, T.C., Muccilli, P., 2015. A hydrothermal Ni-As-PGE geochemical halo around the Miitel komatiite-hosted nickel sulfide deposit, Yilgarn Craton, Western Australia. Econ. Geol. 110, 505–530.

Le Vaillant, M., Saleem, A., Barnes, S.J., Fiorentini, M.L., Miller, J., Beresford, S., Perring, C., 2016. Hydrothermal remobilisation around a deformed and remobilised

komatiite-hosted Ni-Cu-(PGE) deposit, Sarah's Find, Agnew Wiluna greenstone belt, Yilgarn Craton, Western Australia. Miner. Deposita 51, 369–388.

Lesher, C.M., Keays, R.R., 2002. Discrimination between Magmatic and Hydrothermal Ni-Cu-PGE and PGE Mineralization, in: 9th International Platinum Symposium. Stillwater, USA.

Li, C., Naldrett, A.J., 1993. Platinum-group minerals from the Deep Copper Zone of the Strathcona deposit, Sudbury, Ontario. Can. Mineral. 31, 31–44.

Li, C., Ripley, E.M., Merino, E., Maier, W.D., 2004. Replacement of base metal sulfides by actinolite, epidote, calcite, and magnetite in the UG2 and Merensky Reef of the Bushveld Complex, South Africa. Econ. Geol. 99, 0173–0184.

Li, C., Ripley, E.M., Oberthür, T., Miller, J.D., Joslin, G.D., 2007. Textural, mineralogical and stable isotope studies of hydrothermal alteration in the main sulfide zone of the Great Dyke, Zimbabwe and the precious metals zone of the Sonju Lake Intrusion, Minnesota, USA. Miner. Deposita 43, 97.

Liu, W., McPhail, D.C., 2005. Thermodynamic properties of copper chloride complexes and copper transport in magmatic-hydrothermal solutions. Chem. Geol. 221, 21–39.

Liu, Y., Brenan, J., 2015. Partitioning of platinum-group elements (PGE) and chalcogens (Se, Te, As, Sb, Bi) between monosulfide-solid solution (MSS), intermediate solid solution (ISS) and sulfide liquid at controlled fO2–fS2 conditions. Geochim. Cosmochim. Acta 159, 139–161.

Liu, Y., Mungall, J.E., Ames, D.E., 2016. Hydrothermal Redistribution and Local Enrichment of Platinum Group Elements in the Tootoo and Mequillon Magmatic Sulfide Deposits, South Raglan Trend, Cape Smith Belt, New Quebec Orogen. Econ. Geol. 111, 467–485.

Maier, W.D., Barnes, S.-J., 2010. The Kabanga Ni sulfide deposits, Tanzania: II. Chalcophile and siderophile element geochemistry. Miner. Deposita 45, 443–460.

McBride, J., 2015. Assessment Report for Diamond Drilling on the Stillwater Canada Inc. Bermuda Property (Assessment Report No. NTS 42D/16), Assessment Report.

Mitchell, R., Platt, G., 1982. Mineralogy and petrology of nepheline syenites from the Coldwell alkaline complex, Ontario, Canada. J. Petrol. 23, 186–214.

Moretti, R., Baker, D.R., 2008. Modeling the interplay of fO2 and fS2 along the FeS-silicate melt equilibrium. Chem. Geol. 256, 286–298.

Mountain, B.W., Wood, S.A., 1988. Chemical Controls on the Solubility, Transport, and Deposition of Platinum and Palladium in Hydrothermal Solutions: A Thermodynamic Approach. Econ. Geol. 83, 492–510.

Mungall, J.E., Andrews, D.R.A., Cabri, L.J., Sylvester, P.J., Tubrett, M., 2005. Partitioning of Cu, Ni, Au, and platinum-group elements between monosulfide solid solution and sulfide melt under controlled oxygen and sulfur fugacities. Geochim. Cosmochim. Acta 69, 4349–4360.

Murphy, M.D., Sparks, R.S.J., Barclay, J., Carroll, M.R., Brewer, T.S., 2000. Remobilization of andesite magma by intrusion of mafic magma at the Soufriere Hills Volcano, Montserrat, West Indies. J. Petrol. 41, 21–42.

Naldrett, A.J., 1969. A Portion of the System Fe-S-O between 900 and 1080°C and its Application to Sulfide Ore Magmas. J. Petrol. 10, 171–201.

Naldrett, A.J., Asif, M., Krstic, S., Li, C., 2000. The composition of mineralization at the Voisey's Bay Ni-Cu sulfide deposit, with special reference to platinum-group elements. Econ. Geol. 95, 845–865.

Naldrett, A.J., Innes, D.G., Sowa, J., Gorton, M.P., 1982. Compositional variations within and between five Sudbury ore deposits. Econ. Geol. 77, 1519–1534.

Ohnenstetter, D., Watkinson, D.H., Dahl, R., 1991. Zoned hollingworthite from the Two Duck Lake intrusion, Coldwell complex, Ontario. Am. Mineral. 76, 1694–1700.

Paktunc, D., Hulbert, L.J., Harris, D.C., 1990. Partitioning of the platinum-group and other trace elements in sulfides from the Bushveld Complex and Canadian occurrences of Nickel-Copper sulfides. Can. Mineral. 28, 475–488.

Pan, P., Wood, S.A., 1994. Solubility of Pt and Pd sulfides and Au metal in aqueous bisulfide solutions. Miner. Deposita 29, 373–390.

Park, Y.-R., Ripley, E.M., Miller, J.D., Li, C., Mariga, J., Shafer, P., 2004. Stable isotopic constraints on fluid-rock interaction and Cu-PGE-S redistribution in the Sonju Lake Intrusion, Minnesota. Econ. Geol. 99, 325–338.

Patten, C., Barnes, S.-J., Mathez, E.A., Jenner, F.E., 2013. Partition coefficients of chalcophile elements between sulfide and silicate melts and the early crystallization history of sulfide liquid: LA-ICP-MS analysis of MORB sulfide droplets. Chem. Geol. 358, 170–188.

Peach, C.L., Mathez, E.A., Keays, R.R., 1990. Sulfide melt-silicate melt distribution coefficients for noble metals and other chalcophile elements as deduced from MORB: Implications for partial melting. Geochim. Cosmochim. Acta 54, 3379–3389.

Piña, R., Gervilla, F., Ortega, L., Lunar, R., 2008. Mineralogy and geochemistry of platinum-group elements in the Aguablanca Ni-Cu deposit (SW Spain). Mineral. Petrol. 92, 259–282.

Polovina, J.S., Hudson, D.M., Jones, R.E., 2004. Petrographic and geochemical characteristics of postmagmatic hydrothermal alteration and mineralization in the J-M Reef, Stillwater Complex, Montana. Can. Mineral. 42, 261–277.

Prichard, H.M., Knight, R.D., Fisher, P.C., McDonald, I., Zhou, M.-F., Wang, C.Y., 2013. Distribution of platinum-group elements in magmatic and altered ores in the Jinchuan intrusion, China: an example of selenium remobilization by postmagmatic fluids. Miner. Deposita 48, 767–786.

Queffurus, M., Barnes, S.-J., 2015. A review of sulfur to selenium ratios in magmatic nickel-copper and platinum-group element deposits. Ore Geol. Rev. 69, 301–324.

Queffurus, M., Barnes, S.-J., 2014. Selenium and sulfur concentrations in country rocks from the Duluth Complex, Minnesota, USA: Implications for formation of the Cu-Ni-PGE sulfides. Econ. Geol. 109, 785–794.

Ripley, E.M., 1990. Se/S ratios of the Virginia Formation and Cu-Ni sulfide mineralization in the Babbitt area, Duluth Complex, Minnesota. Econ. Geol. 85, 1935–1940.

Ripley, E.M., Alawi, J.A., 1986. Sulfide mineralogy and chemical evolution of the Babbitt Cu-Ni deposit, Duluth Complex, Minnesota. Can. Mineral. 24, 347–368.

Ripley, E.M., Li, C., Shin, D., 2002. Paragneiss Assimilation in the Genesis of Magmatic Ni-Cu-Co Sulfide Mineralization at Voisey's Bay, Labrador: δ34S, δ13C, and Se/S Evidence. Econ. Geol. 97, 1307–1318.

Rollinson, H., 1993. Using Geochemical Data: Evaluation, Presentation, Interpretation. Longman.

Ruprecht, P., Wörner, G., 2007. Variable regimes in magma systems documented in plagioclase zoning patterns: El Misti stratovolcano and Andahua monogenetic cones. J. Volcanol. Geotherm. Res. 165, 142–162.

Ruthart, R., 2013. Characterization of High-PGE Low-Sulphur Mineralization at the Marathon PGE-Cu Deposit, Ontario (MSc). University of Waterloo.

Samson, I.M., Fryer, B.J., Gagnon, J.E., 2008. The Marathon Cu-PGE deposit, Ontario: Insights from sulphide chemistry and textures. Presented at the Goldschmidt, p. A820.

Schissel, D., Tsvetkov, A.A., Mitrofanov, F.P., Korchagin, A.U., 2002. Basal platinum-group element mineralization in the Federov Pansky layered mafic intrusion, Kola Peninsula, Russia. Econ. Geol. 97, 1657–1677.

Shahabi Far, M., 2016. The magmatic and volatile evolution of gabbros hosting the Marathon PGE-Cu deposit: evolution of a conduit system (PhD Dissertation). University of Windsor, Windsor.

Shahabi Far, M., Samson, I.M., Gagnon, J.E., Good, D.J., Linnen, R.L., Layne, G.D., Wing, B.A., 2018. Identifying externally derived sulfur in conduit-type Cu–platinum-group element deposits: The importance of multiple sulfur isotope studies. Geology.

Shahabi Far, M., Samson, I.M., Gagnon, J.E., Linnen, R.L., Good, D.J., Ames, D.E., 2015. Textural character and chemistry of plagioclase and apatite in the Marathon Cu-PGE deposit, Ontario: Implications for mineralizing processes, in: Targeted Geoscience

Initiative 4: Canadian Nickel-Copper-Platinum Group Elements-Chromium Ore Systems — Fertility, Pathfinders, New and Revised Models. pp. 235–243.

Smith, J.W., Holwell, D.A., McDonald, I., Boyce, A.J., 2016. The application of S isotopes and S/Se ratios in determining ore-forming processes of magmatic Ni–Cu–PGE sulfide deposits: A cautionary case study from the northern Bushveld Complex. Ore Geol. Rev. 73, 148–174.

Stanton, R.L., 1972. Ore Petrology. McGraw-Hill, New York, N.Y.

Sylvester, P.J., Cabri, L.J., Tubrett, M.N., McMahon, G., Laflamme, J.H.G., Peregoedova, A., 2005. Synthesis and evaluation of a fused pyrrhotite standard reference material for platinum group element and gold analysis by laser ablation-ICPMS, in: 10th International Platinum Symposium: Oulu, Geological Survey of Finland, Extended Abstracts. pp. 16–20.

Theriault, R.D., Barnes, S.-J., 1998. Compositional variations in Cu-Ni-PGE sulfides of the Dunka Road deposit, Duluth Complex, Minnesota: The importance of combined assimilation and magmatic processes. Can. Mineral. 36, 869–886.

Tsujimura, T., Kitakaze, A., 2004. New phase relations in the Cu–Fe–S system at 800°C; constraint of fractional crystallization of a sulfide liquid. Neues Jahrb. Für Mineral. - Monatshefte 2004, 433–444.

Walker, E.C., Sutcliff, R.H., Shaw, C.S.J., Shore, G.T., Penczak, R.S., 1993. Precambrian Geology of the Coldwell Alkalic Complex. Ontario Geological Survey Open File No. 5868.

Watkinson, D.H., 1994. Fluid-rock interaction at contact of Lindsley 4b Ni-Cu-PGE orebody and enclosing granitic rocks, Sudbury, Canada. Trans. Inst. Min. Metall. B121-128.

Watkinson, D.H., Dahl, R., 1988. Platinum-Group Mineral Precipitation from Fluids in Pegmatitic Gabbro: Two Duck Lake Intrusion, Coldwell Complex, Ontario, Canada, in: Geo-Platinum 87. Springer, pp. 237–237.

Watkinson, D.H., Jones, P.C., 1996. Platinum-group minerals in fluid inclusions from the Marathon deposit, Coldwell Complex, Canada. Mineral. Petrol. 57, 91–96.

Watkinson, D.H., Ohnenstetter, D., 1992. Hydrothermal Origin of Platinum-Group Mineralization in the Two Duck Lake Intrusion, Coldwell Complex, Northwestern Ontario. Can. Mineral. 30, 121–136.

Wilson, S.A., Ridley, W.I., Koenig, A.E., 2002. Development of sulfide calibration standards for the laser ablation inductively-coupled plasma mass spectrometry technique. J. Anal. At. Spectrom. 17, 406–409.

Wohlgemuth-Ueberwasser, C.C., Fonseca, R.O.C., Ballhaus, C., Berndt, J., 2013. Sulfide oxidation as a process for the formation of copper-rich magmatic sulfides. Miner. Deposita 48, 115–127.

Wood, S.A., 2002. The aqueous geochemistry of the platinum-group elements with applications to ore deposits, in: Cabri, L.J. (Ed.), The Geology, Geochemistry, Mineralogy and Mineral Beneficiation of Platinum-Group Elements. Canadian Institute of Mining, Metallurgy and Petroleum, pp. 211–249.

Yamamoto, M., 1976. Relationship between Se/S and sulfur isotope ratios of hydrothermal sulfide minerals. Miner. Deposita 11, 197–209.

Yund, R.A., Kullerud, G., 1966. Thermal Stability of Assemblages in the Cu-Fe-S System. J. Petrol. 7, 454–488.

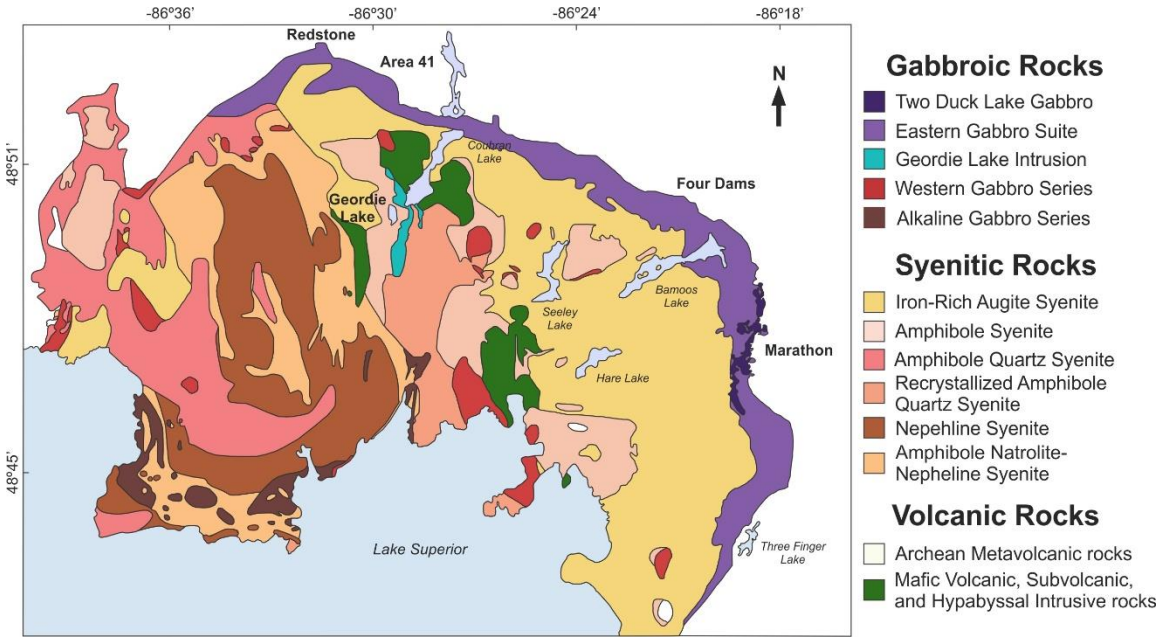

Figure 5.1 Geological map of the Coldwell Complex showing the location of the Marathon Cu-Pd deposit, as well as the mineralized occurrences to the northwest (modified after Good et al., 2015).

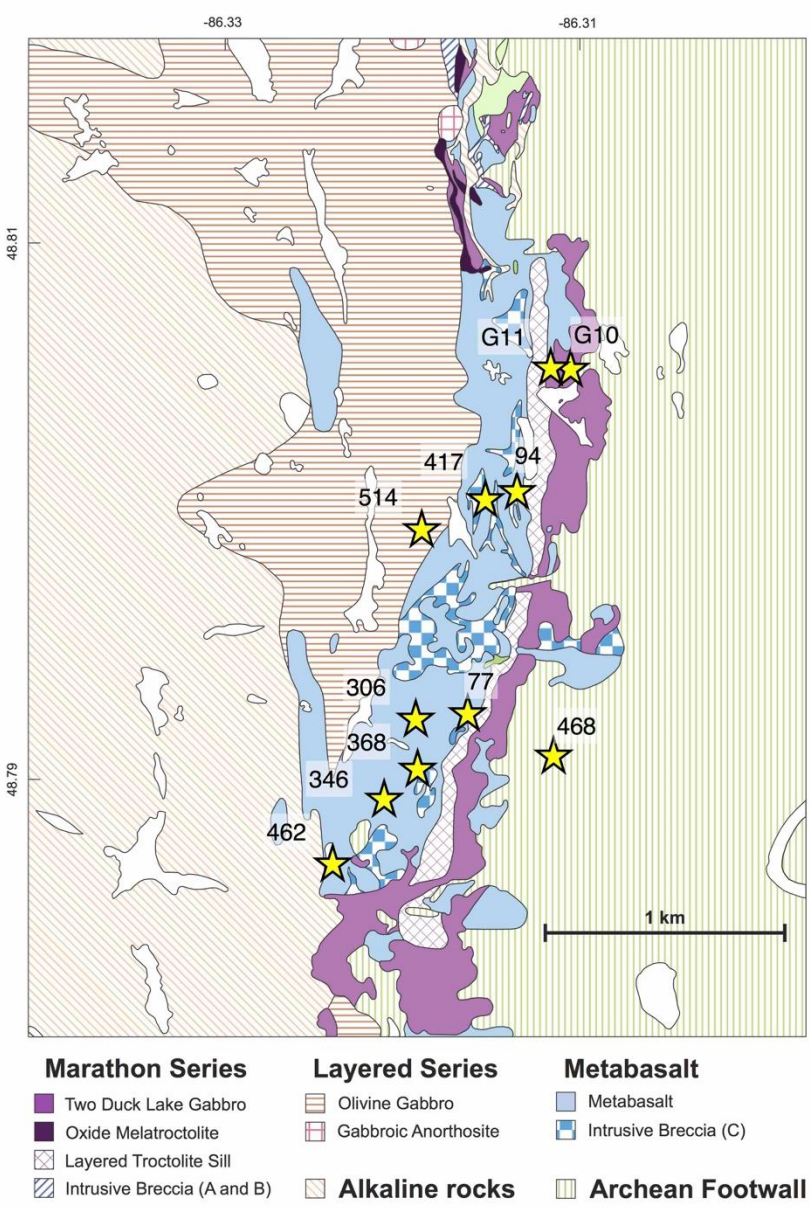

Figure 5.2 Geologic map of the Marathon Cu-Pd deposit showing the spatial relationships of each of the rock series (modified from Good et al., 2015). Drill hole locations for all of the samples used from the Marathon deposit are illustrated.

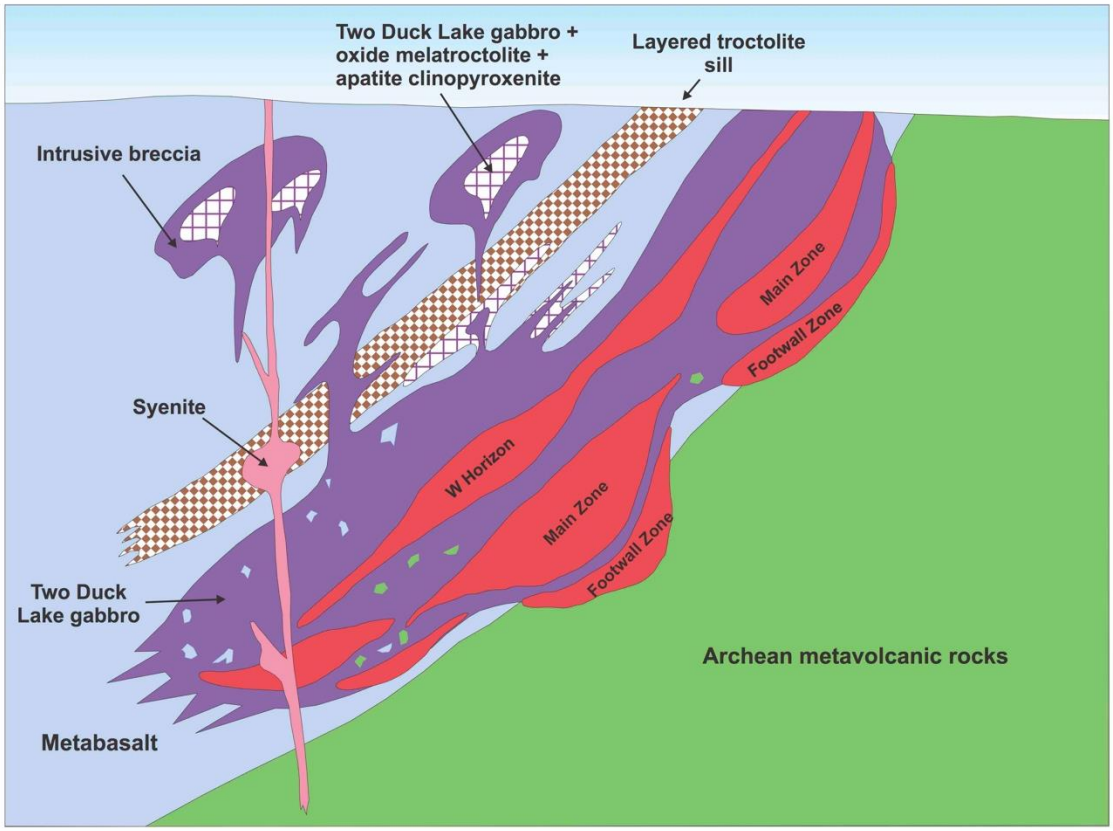

Figure 5.3 Idealized cross-section of the southern portion of the Marathon Cu-Pd deposit showing the locations of the Footwall Zone, Main Zone, and W Horizon (modified after Shahabi Far, 2016). At the north end of the deposit, the Main Zone is continuous and the W Horizon does not occur.

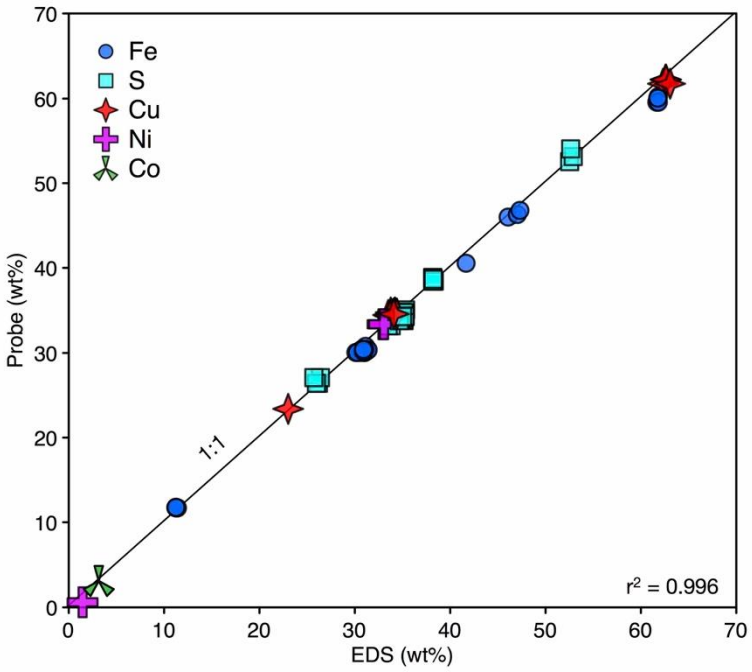

Figure 5.4 Binary diagram illustrating the correlation between the major-element concentrations of sulfides obtained by energy- and wavelength-dispersive spectroscopy. Note the 1:1 relationship between the analytical techniques.

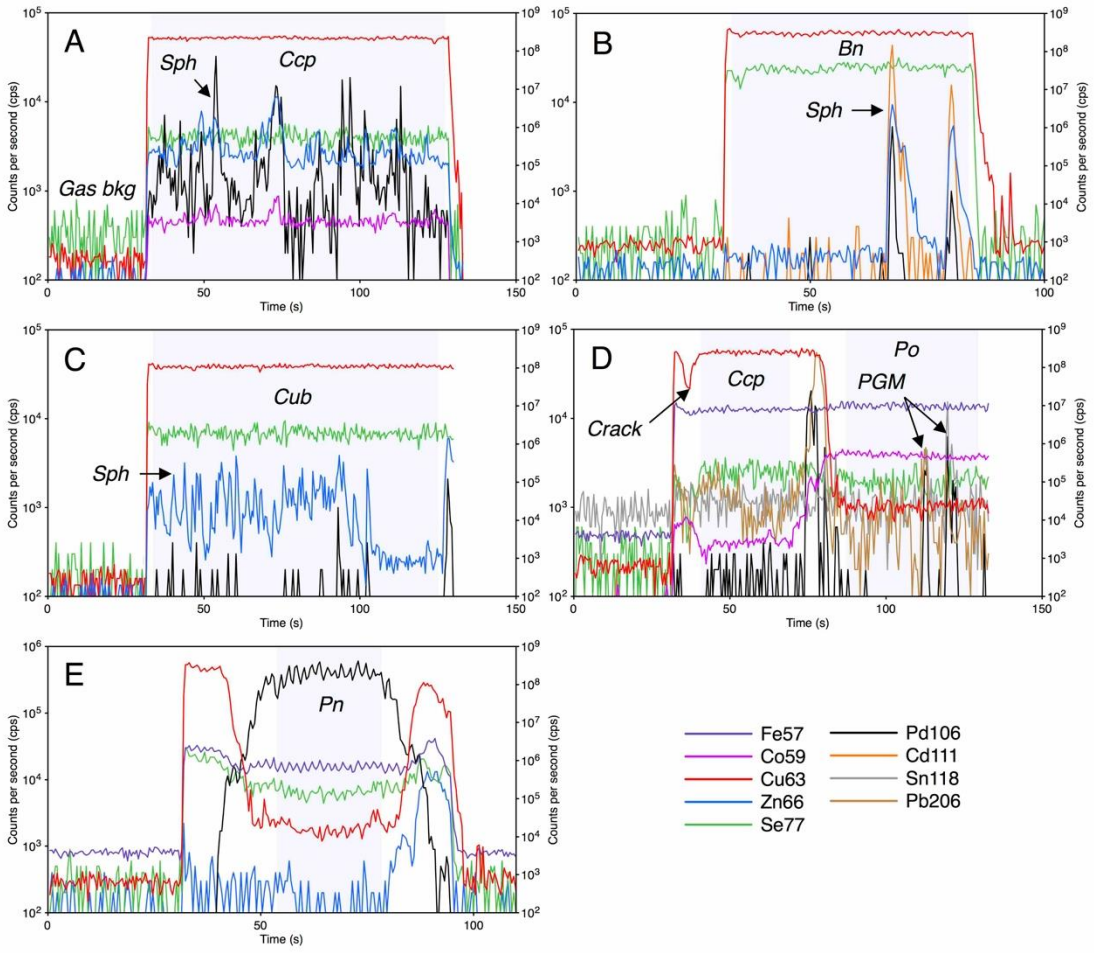

Figure 5.5 Laser ablation spectra of (A) a chalcopyrite grain, (B) a bornite grain, and (C) a cubanite grain, all with micron-sized inclusions of sphalerite, (D) a sulfide aggregate composed of chalcopyrite and pyrrhotite with several Pd-rich platinum-group minerals, and (E) a compositionally-homogenous pentlandite grain. Ccp = chalcopyrite, sph = sphalerite, bn = bornite, cub = cubanite, po = pyrrhotite, PGM = platinum-group mineral, pn = pentlandite.

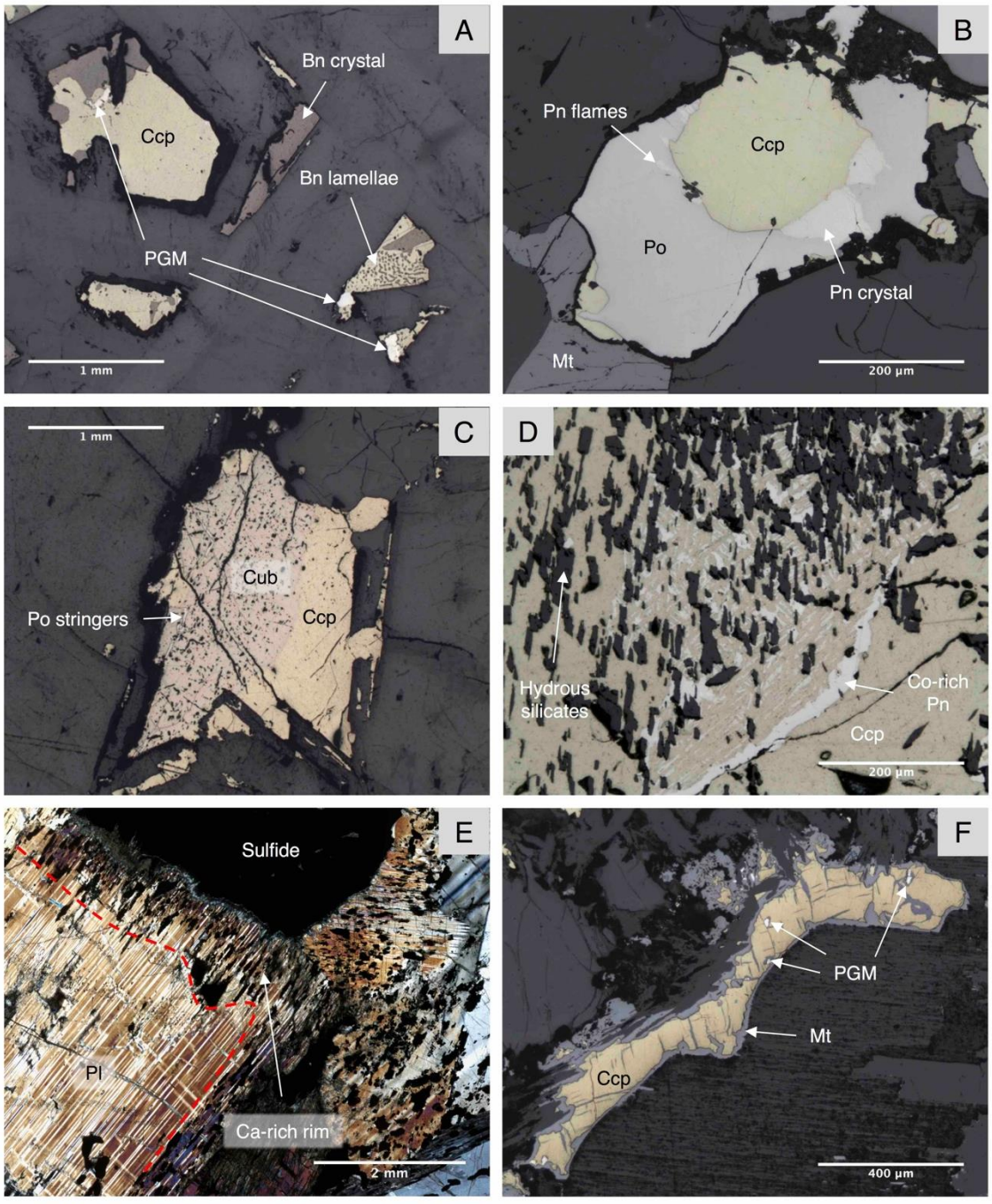
A
Bn crystal
Ccp
Bn lamellae
PGM
1 mm
B
Pn flames
Ccp
Po
Pn crystal
Mt
200 µm
C
1 mm
Cub
Po stringers
Ccp
D
Hydrous silicates
Co-rich Pn
Ccp
200 µm
E
Sulfide
Pl
Ca-rich rim
2 mm
F
PGM
Mt
Ccp
400 µm

Figure 5.6 (A) Reflected-light image of interstitial aggregates of sulfide minerals composed of chalcopyrite and bornite, which exhibit sharp boundaries with each other and the surrounding plagioclase. (B) Reflected-light image of a sulfide aggregate composed of chalcopyrite, pyrrhotite, and pentlandite (as crystals and exsolution flames), which exhibit sharp boundaries with each other and the surrounding silicates and oxides. (C) Reflected-light image of a sulfide aggregate composed of chalcopyrite and cubanite, which exhibit sharp boundaries with each other and the surrounding silicates. (D) Reflected-light image of an intergrowth of chalcopyrite and hydrous silicates with cobaltian pentlandite. The pentlandite shares irregular boundaries with the chalcopyrite. (E) Cross-polarized image illustrating the occurrence of elongate sulfides along a Ca-rich rim on plagioclase (denoted by the red dotted line). (F) Reflected-light image of a crystal of chalcopyrite that contains magnetite as a rim around it and as protrusions throughout it. Ccp = chalcopyrite, cub = cubanite, po = pyrrhotite, pn = pentlandite, PGM = platinum-group mineral, mt = magnetite.

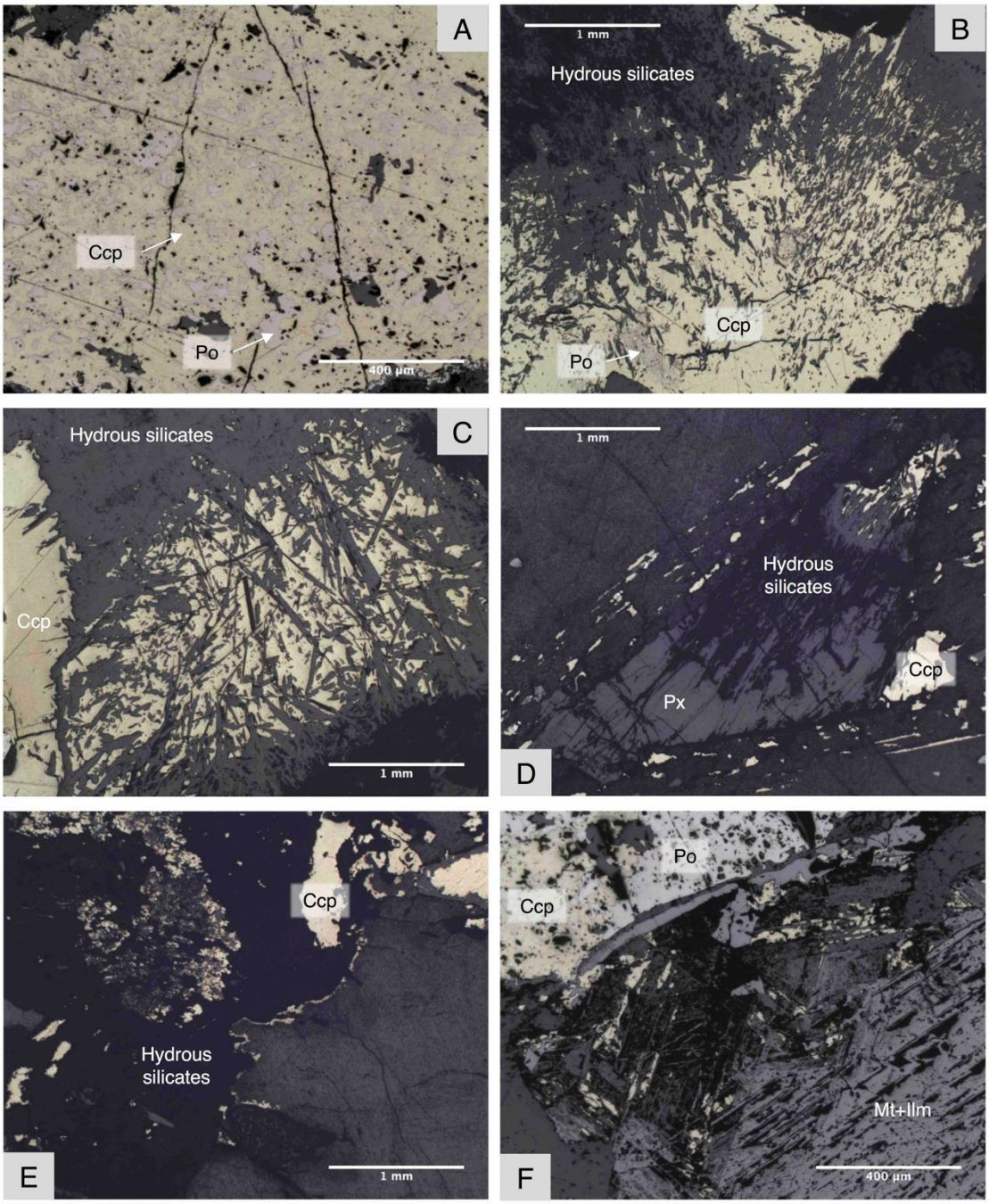
A
Ccp
Po
400 µm
B
1 mm
Hydrous silicates
Ccp
Po
C
Hydrous silicates
Ccp
1 mm
D
1 mm
Hydrous
silicates
Ccp
Px
E
Ccp
Hydrous
silicates
1 mm
F
Po
Ccp
Mt+Ilm
400 µm

Figure 5.7 (A) Reflected-light image of an aggregate of chalcopyrite and pyrrhotite, which share ragged boundaries. Many of the islands of pyrrhotite are in optical continuity. (B) Reflected-light image of aligned, euhedral actinolite blades protruding into sulfides, but not associated with altered pyroxene. (C) Reflected-light image of randomly-oriented, euhedral actinolite blades within sulfides. (D) Reflected-light image of aligned, euhedral actinolite blades protruding from altered pyroxene into sulfides. (E) Reflected-light image of Chalcopyrite within pyroxene that has been partially to completely replaced by hydrous silicates. Note that some chalcopyrite occurs as a rim along the boundary of the alteration patch. (F) Reflected-light image of an intergrowth of chalcopyrite and hydrous silicates in between ilmenite lamellae that remain after magnetite had been replaced. Ccp = chalcopyrite, po = pyrrhotite, mt = magnetite, ilm = ilmenite.

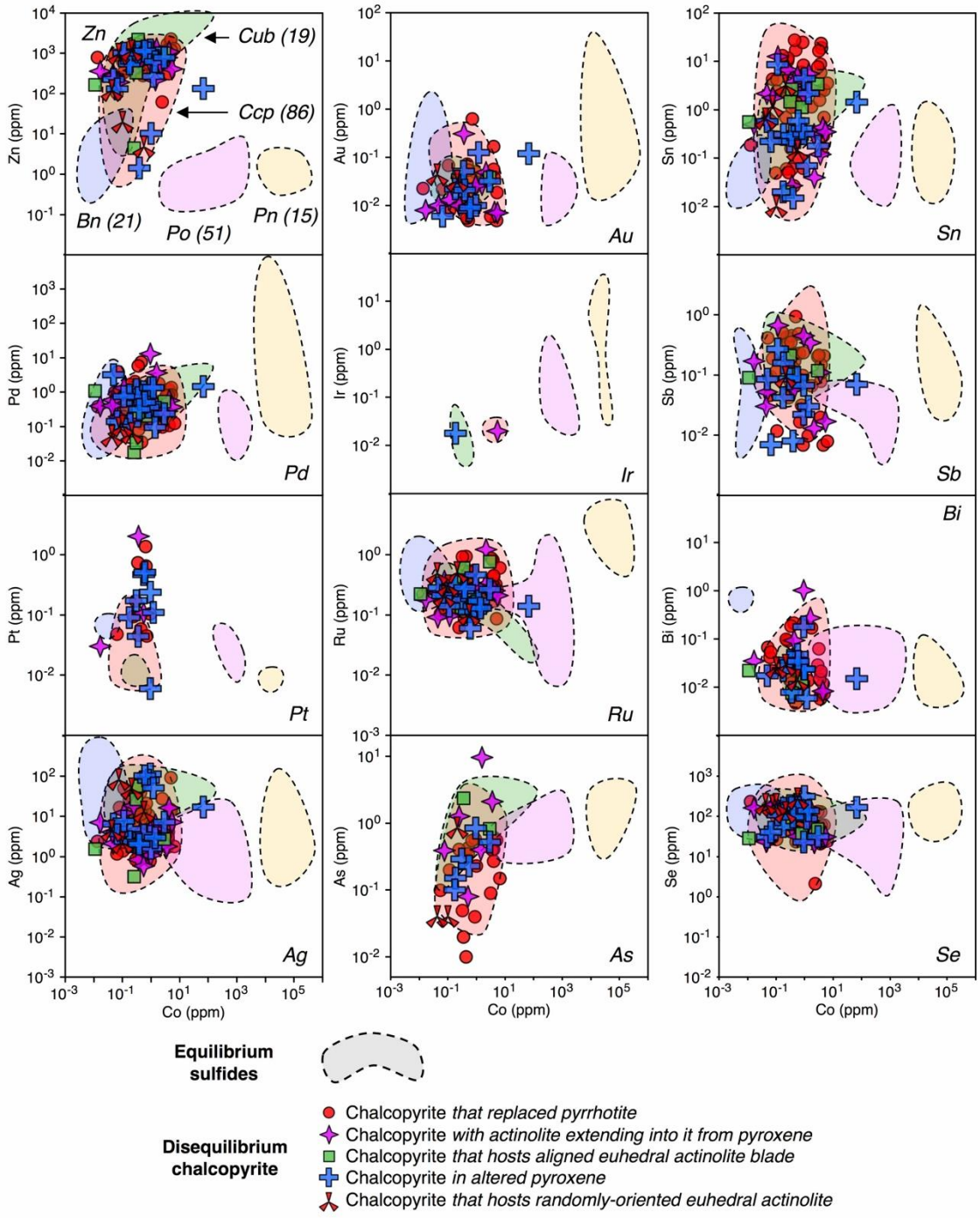
Zn
Cub (19)
Ccp (86)
Bn (21)
Po (51)
Pn (15)
Zn (ppm)
Au
Au (ppm)
Sn
Sn (ppm)
Pd
Pd (ppm)
Ir
Ir (ppm)
Sb
Sb (ppm)
Pt
Pt (ppm)
Ru
Ru (ppm)
Bi
Bi (ppm)
Ag
Ag (ppm)
As
As (ppm)
Se
Se (ppm)
Co (ppm)
Equilibrium sulfides
Disequilibrium chalcopyrite
Chalcopyrite that replaced pyrrhotite
Chalcopyrite with actinolite extending into it from pyroxene
Chalcopyrite that hosts aligned euhedral actinolite blade
Chalcopyrite in altered pyroxene
Chalcopyrite that hosts randomly-oriented euhedral actinolite

Figure 5.8 Binary diagrams illustrating the trace-element composition of chalcopyrite, bornite, cubanite, pyrrhotite, and pentlandite. The colored fields represent the composition of sulfides that exhibit equilibrium textures. The colored data points represent the composition of chalcopyrite that exhibit various disequilibrium textures. The number in brackets represents the number of analyses of each sulfide mineral in magmatic equilibrium. It should be noted that the composition of chalcopyrite in each of the mineralized zones is comparable, except for the chalcopyrite in the W Horizon, which has Zn concentrations that extend to lower values. Ccp = chalcopyrite, bn = bornite, cub = cubanite, po = pyrrhotite, pn = pentlandite.

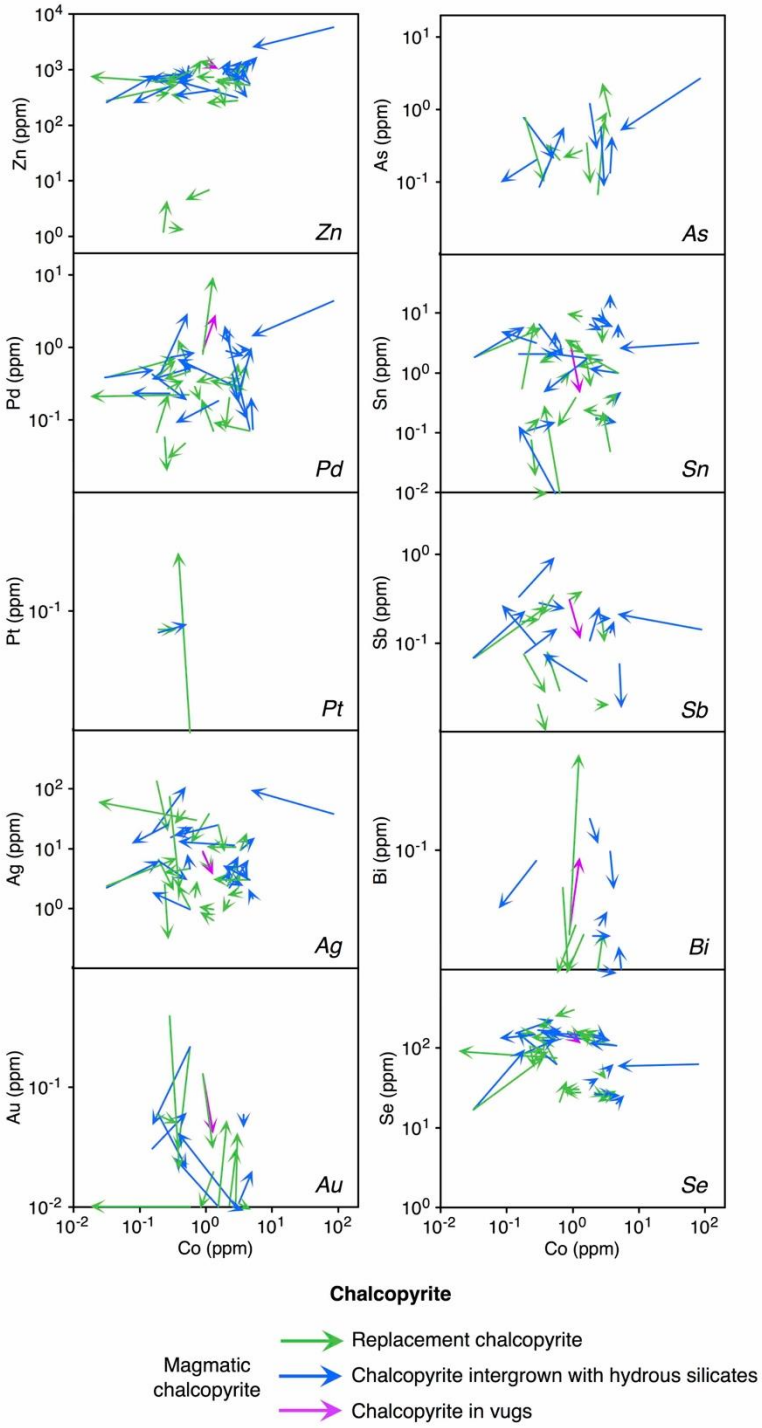

Figure 5.9 Vector diagrams illustrating the difference in trace-element composition of chalcopyrite that exhibit equilibrium textures and chalcopyrite that exhibit various disequilibrium textures. Each of the arrows represent chalcopyrite from a single thin section. The start of the arrow represents the average composition of equilibrium chalcopyrite. The end of the arrow represents the average composition of disequilibrium chalcopyrite.

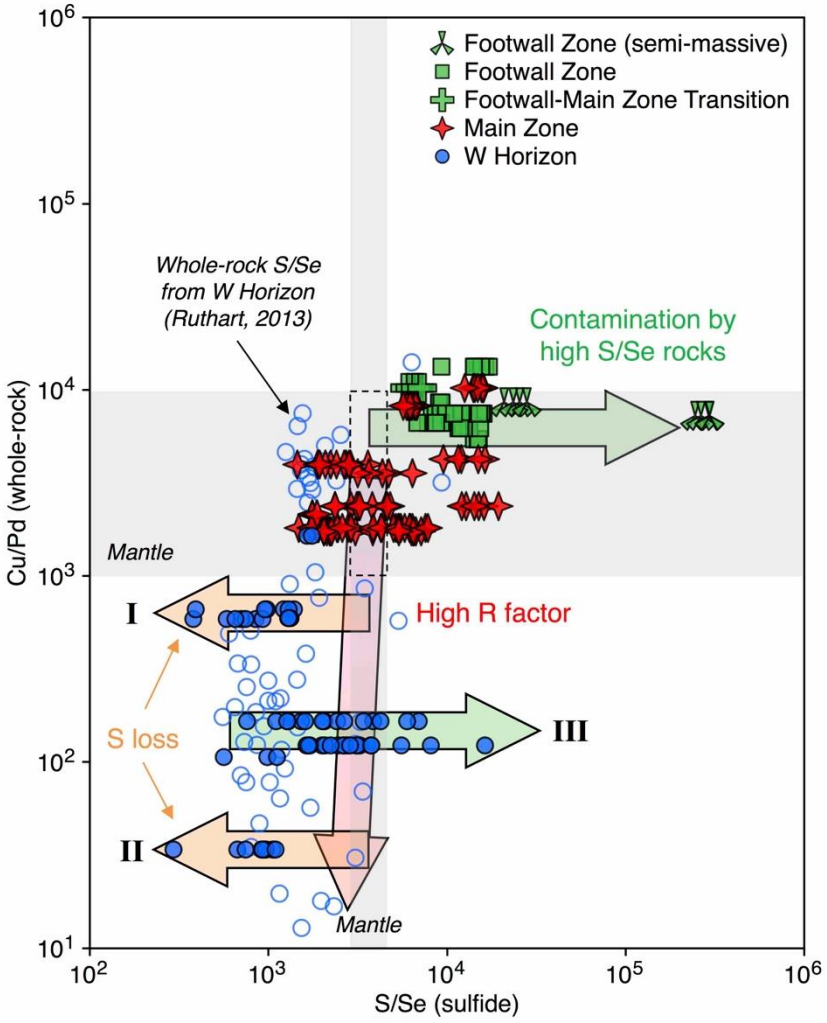

Figure 5.10 A binary diagram illustrating the S/Se ratio of sulfides and whole-rock Cu/Pd ratio of their corresponding host rocks. The closed symbols represent data from the Footwall Zone (green), Main Zone (red), and W Horizon (blue) of the Marathon deposit obtained during this study. The open circles represent whole-rock data obtained from Ruthart (2013). The arrows represent how a given magmatic process will affect the Cu/Pd and S/Se ratio of sulfides. The roman numerals denote the three sulfide populations that are characterized by distinct Cu/Pd and S/Se ratios.

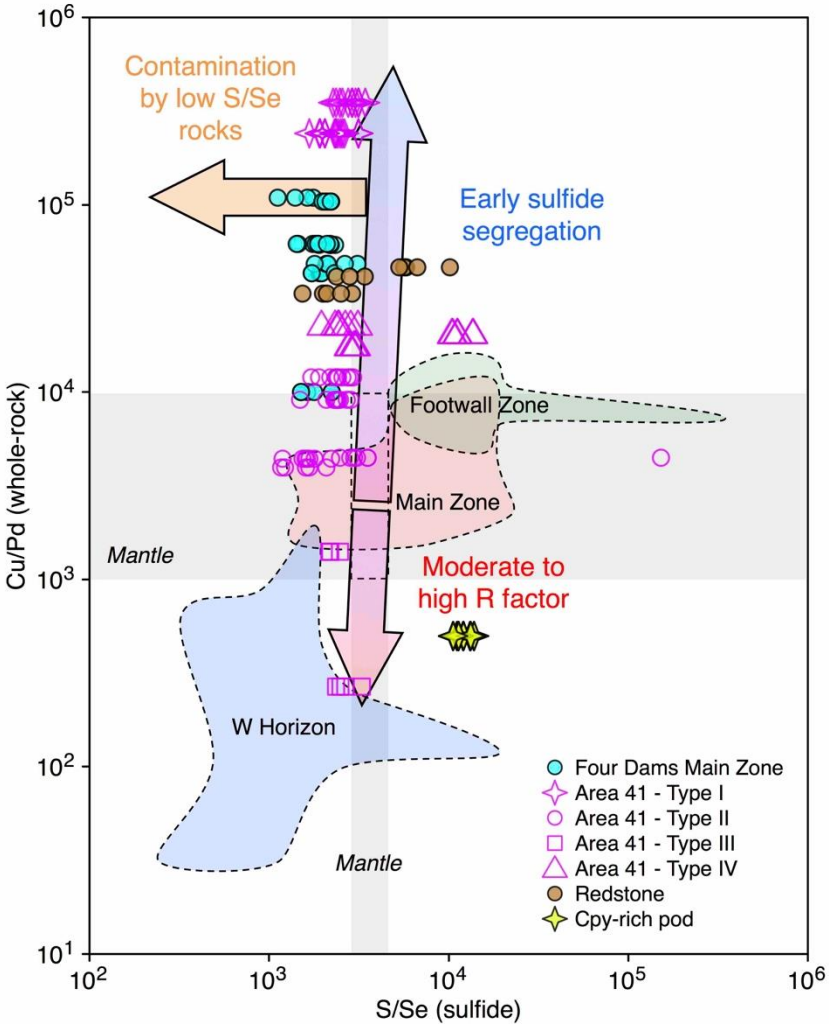

Figure 5.11 A binary diagram illustrating the S/Se ratio of sulfides and whole-rock Cu/Pd ratio of their corresponding host rocks. The symbols represent data from the Four Dams, Area 41, and Redstone mineralized occurrences that occur north of the Marathon deposit, as well as the chalcopyrite-rich pods. The green, red, and blue fields outline the S/Se and Cu/Pd ratios exhibited by the Footwall Zone, Main Zone, and W Horizon, respectively, at the Marathon deposit.

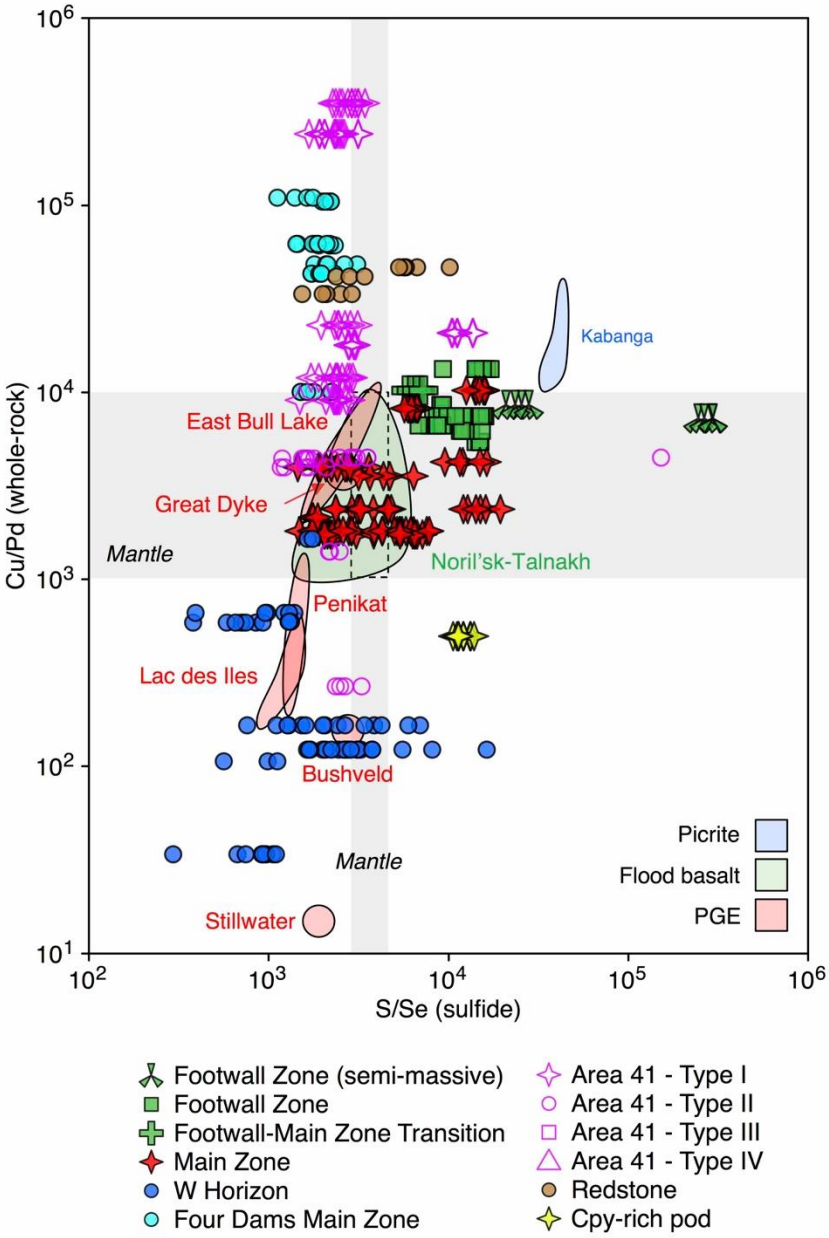

Figure 5.12 A binary diagram comparing the S/Se and Cu/Pd ratio of the various mineralized zones that occur throughout the Eastern Gabbro (symbols) with the ratios exhibited by a variety of Ni-Cu-PGE deposits worldwide (colored fields) (Queffurus and Barnes, 2015).

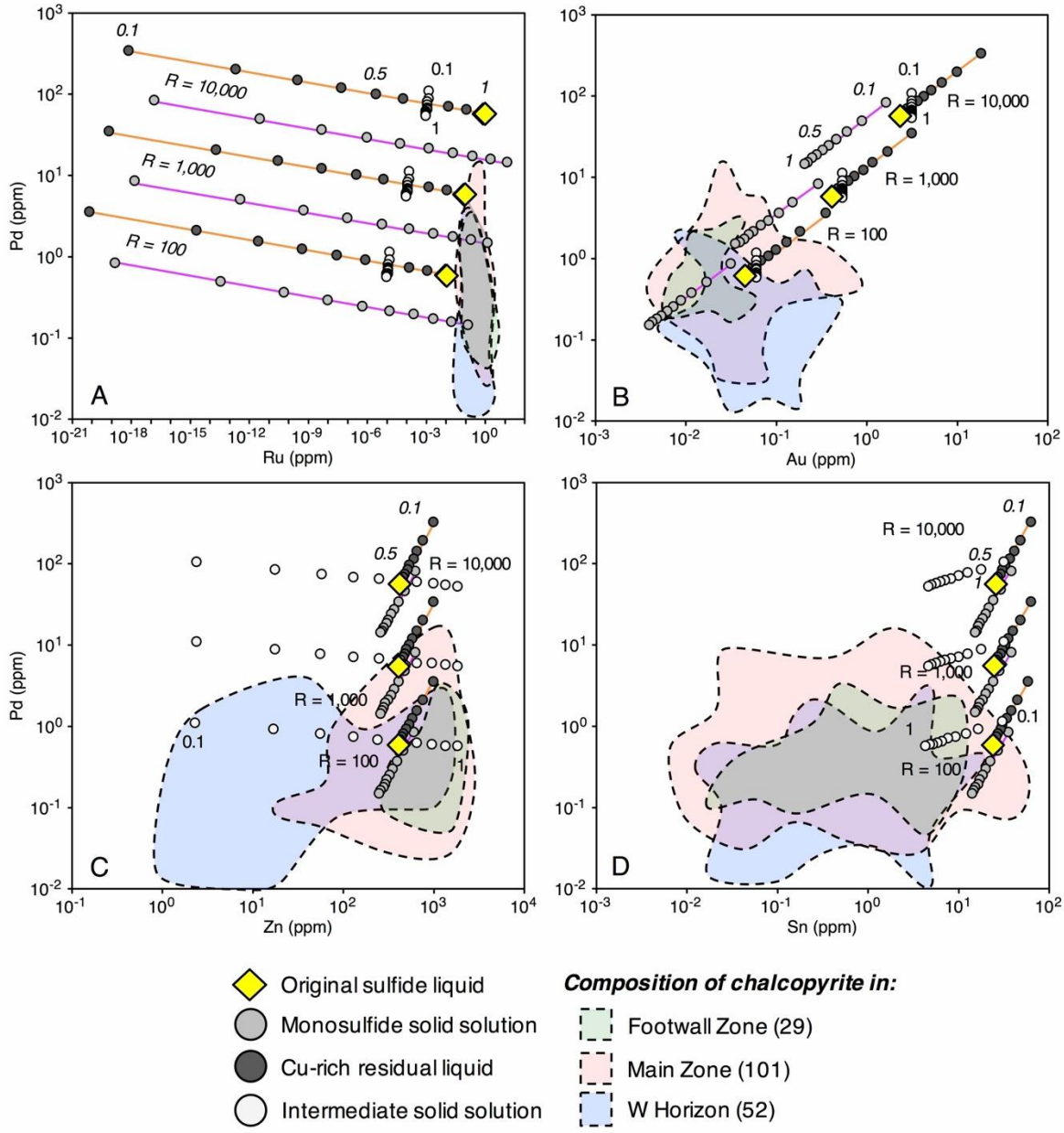

Figure 5.13 Binary diagrams illustrating the modelled compositions of monosulfide solid solution, Cu-rich residual liquid, and intermediate solid solution obtained using the closed-system R factor model of Campbell and Naldrett (1979) and variable R factors. The number above each of the data points represents the degree of fractionation (*F*). The colored fields represent the composition of chalcopyrite from the Footwall Zone, Main Zone, and W Horizon of the Marathon deposit. The numbers in brackets in the legend represent the number of analyses of chalcopyrite from the Footwall Zone, Main Zone, and W Horizon.

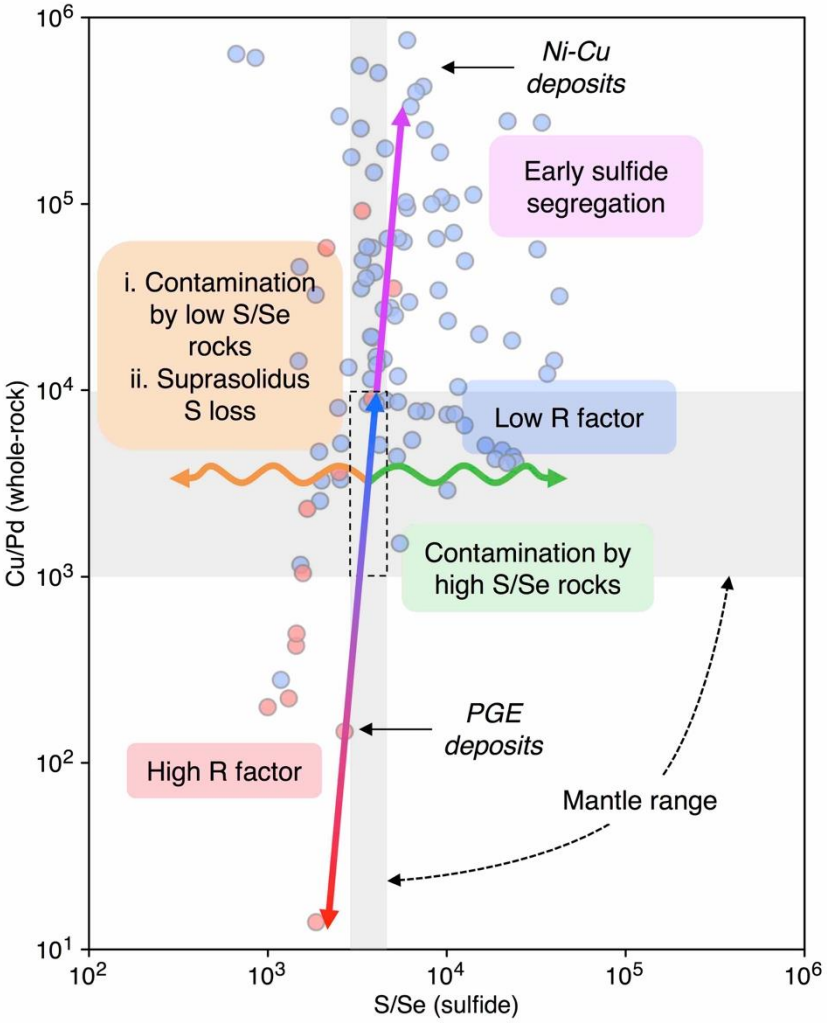

Figure 5.14 A binary diagram illustrating the effects that various magmatic processes have on the S/Se ratios of sulfides and whole-rock Cu/Pd ratios. The grey fields represent the mantle ranges of S/Se (2850 to 4350; Eckstrand and Hulbert, 1987) and Cu/Pd (Barnes et al., 1993). The blue and red data points illustrate the S/Se and Cu/Pd ratios exhibited by a variety of Ni-Cu and PGE deposits, respectively (Queffurus and Barnes, 2015).

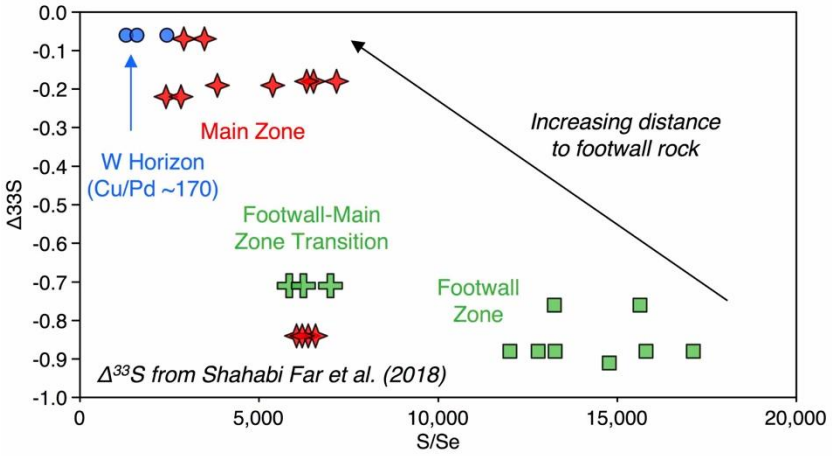

Figure 5.15 A binary diagram comparing the S/Se ratio of sulfides from the Footwall Zone, Main Zone, and W Horizon of the Marathon deposit with their corresponding $\Delta^{33}S$ from Shahabi Far et al. (2018). Note that from right to left in the diagram represents an increase in distance from the footwall contact.

Table 5.1 Argide production on Pd and Rh during laser ablation ICP-MS analyses

Material	Analysis	Zn66	Zn68	Cu63	Cu65	Rh103	Pd105	Pd106	Pd108
Zn metal	*Traverse 1*	8.52E+07	5.95E+07	-	-	-	2.49E+01	2.74E+03	1.86E+03
	Traverse 2	1.13E+08	8.04E+07	-	-	-	1.90E+01	3.71E+03	2.46E+03
	Traverse 3	1.08E+08	7.60E+07	-	-	-	1.18E+01	3.75E+03	2.57E+03
	Traverse 4	1.07E+08	7.45E+07	-	-	-	2.63E+01	3.54E+03	2.42E+03
	Traverse 5	1.21E+08	8.47E+07	-	-	-	1.19E+01	3.90E+03	2.75E+03
Cu metal	*Traverse 1*	-	-	2.32E+07	1.11E+07	2.22E+03	9.36E+02	-	-
	Traverse 2	-	-	1.01E+07	4.84E+06	9.58E+02	3.98E+02	-	-
	Traverse 3	-	-	1.01E+07	4.87E+06	9.53E+02	4.46E+02	-	-
Sphalerite	*Traverse 1*	4.46E+08	2.95E+08	1.26E+06	6.14E+05	1.01E+02	4.49E+01	2.42E+05	1.85E+05
	Traverse 2	4.75E+08	3.46E+08	1.26E+06	6.01E+05	9.40E+01	4.10E+01	2.98E+05	1.99E+05

Table 5.1 Continue

Material	Analysis	Rh103/Cu63	Pd105/Cu65	Pd106/Zn66	Pd108/Zn68
Zn metal	*Traverse 1*	-	-	3.22E-05	3.12E-05
	Traverse 2	-	-	3.29E-05	3.06E-05
	Traverse 3	-	-	3.46E-05	3.38E-05
	Traverse 4	-	-	3.32E-05	3.25E-05
	Traverse 5	-	-	3.24E-05	3.25E-05
Cu metal	*Traverse 1*	9.57E-05	8.47E-05	-	-
	Traverse 2	9.53E-05	8.22E-05	-	-
	Traverse 3	9.44E-05	9.16E-05	-	-
Sphalerite	*Traverse 1*	8.05E-05	7.31E-05	5.42E-04	6.26E-04
	Traverse 2	7.46E-05	6.82E-05	6.27E-04	5.74E-04

Table 5.2 Trace-element content of sulfides in different mineralized zones in the Eastern Gabbro

			Isotope	59Co	66Zn	75As	77Se	101Ru	106 Pd	107Ag	111Cd	118Sn	123Sb	194Pt	197Au	209Bi
				ppm	ppm	ppm	ppm	ppm	ppm	ppm	ppm	ppm	ppm	ppm	ppm	ppm
Mineralized Zone	**Sulfide**		**Ref. Mat.**	MASS-1	MASS-1	MASS-1	MASS-1	Po725	Po725	MASS-1	MASS-1	MASS-1	MASS-1	Po725	Po725	MASS-1
Footwall Zone (N = 7)	Ccp	n = 29	*med.*	3.4	970	0.6	30	0.3	0.3	3	10	0.5	0.02	0.01	< 0.02	0.01
			min.	0.8	320	< 0.1	20	0.09	0.06	1	3	< 0.07	< 0.02	0.01	< 0.02	0.006
			max.	6.3	1900	2	40	1	3	50	30	9	0.2	0.01	0.05	0.5
	Po	n = 24	*med.*	970	2	0.8	30	0.1	0.05	0.5	0.1	0.2	0.03	< 0.002	0.02	0.02
			min.	180	0.7	0.2	30	< 0.05	0.02	0.1	< 0.04	0.01	0.01	< 0.002	0.008	0.005
			max.	1900	6	2	60	0.2	0.6	2	0.4	1	0.08	< 0.002	0.03	0.1
Main Zone (N = 15)	Ccp	n = 97	*med.*	0.3	840	0.3	120	0.3	0.5	3	10	1	0.09	0.09	0.03	0.03
			min.	< 0.02	20	< 0.1	20	0.06	0.04	0.7	0.6	< 0.07	< 0.02	< 0.01	< 0.02	0.006
			max.	70	2200	10	240	1	10	90	50	50	0.7	2	0.6	1
	Po	n = 32	*med.*	210	0.7	0.6	70	0.05	0.04	0.9	0.05	0.1	0.05	< 0.002	0.03	0.02
			min.	3	0.1	0.05	20	< 0.05	0.02	0.2	< 0.04	0.03	0.02	< 0.002	0.006	0.006
			max.	1600	210	2	230	0.3	8	20	2	0.5	0.6	< 0.002	0.3	1
	Pn	n = 6	*med.*	28000	2	0.9	110	2	140	3	0.2	0.4	0.1	< 0.02	10	0.01
			min.	13000	0.7	< 0.7	40	1	0.4	0.3	0.1	0.3	< 0.1	< 0.02	< 0.04	0.005
			max.	51000	3	2	160	5	920	90	0.2	0.9	0.6	< 0.02	20	0.03
W Horizon (N = 17)	Ccp	n = 52	*med.*	0.3	8	< 0.1	160	0.2	0.1	3	0.2	0.2	0.1	0.02	0.07	0.02
			min.	0.04	0.9	< 0.1	2	0.05	0.01	0.1	< 0.02	< 0.07	< 0.02	0.01	< 0.02	0.006
			max.	2	1200	0.5	1200	1	3	230	30	20	2	0.1	2	1
	Bn	n = 25	*med.*	0.02	0.8	0.1	130	0.4	0.05	10	0.3	< 0.06	0.1	0.06	0.05	1
			min.	< 0.01	0.3	< 0.1	20	0.1	0.01	0.4	0.06	< 0.06	< 0.02	0.06	< 0.01	0.01
			max.	0.09	30	0.4	670	2	4	700	130	0.3	4	0.06	2	60
	Po	n = 2	*med.*	120	0.5	< 0.02	10	< 0.05	< 0.02	0.9	< 0.04	0.04	< 0.003	< 0.002	< 0.001	< 0.00004
			min.	30	0.3	< 0.02	3	< 0.05	< 0.02	0.4	< 0.04	0.04	< 0.003	< 0.002	< 0.001	< 0.00004
			max.	200	0.6	< 0.02	30	< 0.05	< 0.02	1	< 0.04	0.04	< 0.003	< 0.002	< 0.001	< 0.00004
	Pn	n = 6	*med.*	36000	2	0.8	240	3	220	0.8	2	< 0.3	< 0.1	< 0.02	0.8	< 0.002
			min.	13000	0.6	< 0.7	140	0.5	90	0.3	1	< 0.3	< 0.1	< 0.02	0.1	< 0.002
			max.	81000	3	1	450	7	5000	70	10	0.4	< 0.1	< 0.02	2	< 0.002

Table 5.2 Continue

Mineralized Zone	Sulfide		Isotope	59Co	66Zn	75As	77Se	101Ru	106 Pd	107Ag	111Cd	118Sn	123Sb	194Pt	197Au	209Bi
				ppm	ppm	ppm	ppm	ppm	ppm	ppm	ppm	ppm	ppm	ppm	ppm	ppm
			Ref. Mat.	MASS-1	MASS-1	MASS-1	MASS-1	Po725	Po725	MASS-1	MASS-1	MASS-1	MASS-1	Po725	Po725	MASS-1
Four Dams Main Zone (N = 7)	Ccp	n = 23	*med.*	0.4	460	0.6	180	0.3	0.2	20	5	2	0.3	0.1	0.02	0.007
			min.	0.07	270	< 0.1	150	0.1	0.03	7	1	0.07	< 0.02	0.1	< 0.02	0.005
			max.	1	1300	1	260	0.8	1	140	40	10	1	0.1	0.06	0.02
	Cub	n = 10	*med.*	0.2	150	< 0.9	190	0.3	0.2	60	3	2	0.3	< 0.04	0.03	0.009
			min.	0.03	6	< 0.9	160	0.2	0.04	40	0.5	0.5	0.09	< 0.04	< 0.02	0.006
			max.	0.6	5400	1	310	0.5	1	110	40	5	0.8	< 0.04	0.07	0.01
	Po	n = 5	*med.*	430	0.9	0.9	180	0.2	0.05	0.9	< 0.04	0.3	0.3	< 0.002	0.04	0.02
			min.	150	0.6	0.4	120	0.2	0.05	0.5	< 0.04	0.2	0.3	< 0.002	0.03	0.006
			max.	560	2	1	220	0.3	0.05	80	< 0.04	0.3	0.3	< 0.002	0.05	0.02
Area 41 - Type I (N = 2)	Ccp	n = 13	*med.*	0.6	570	0.2	150	0.2	0.4	10	20	2	0.03	< 0.01	0.02	0.02
			min.	0.08	260	0.1	110	0.05	0.2	2	9	0.8	0.02	< 0.01	< 0.02	0.006
			max.	3	1000	0.2	180	0.5	0.8	50	30	9	0.05	< 0.01	0.04	0.1
	Cub	n = 2	*med.*	1	490	< 0.9	150	0.2	0.8	60	30	3	< 0.09	< 0.04	0.03	0.01
			min.	1	280	< 0.9	120	0.1	0.5	30	20	2	< 0.09	< 0.04	0.03	0.01
			max.	2	710	< 0.9	170	0.2	1	100	30	5	< 0.09	< 0.04	0.03	0.01
	Po	n = 10	*med.*	300	1	< 0.02	140	< 0.05	< 0.02	1	0.09	0.08	0.02	< 0.002	0.03	0.03
			min.	140	0.4	< 0.02	110	< 0.05	< 0.02	0.6	< 0.04	0.02	0.02	< 0.002	0.02	0.005
			max.	620	1	< 0.02	230	< 0.05	< 0.02	2	0.2	0.1	0.02	< 0.002	0.05	0.05
Area 41 - Type II (N = 5)	Ccp	n = 23	*med.*	0.5	370	0.2	160	0.2	0.2	9	4	0.7	0.09	0.7	0.02	0.04
			min.	0.06	5	0.1	110	0.07	0.01	2	0.1	< 0.07	< 0.02	0.05	< 0.02	0.007
			max.	8	1100	0.8	300	0.4	2	110	20	5	2	1	0.05	0.2
	Cub	n = 3	*med.*	0.2	1300	< 0.9	150	0.2	0.08	20	7	3	0.3	< 0.04	< 0.02	0.04
			min.	0.2	8	< 0.9	150	0.2	0.04	10	1	< 0.4	0.3	< 0.04	< 0.02	0.04
			max.	0.3	1900	< 0.9	220	0.2	0.7	30	30	5	0.4	< 0.04	< 0.02	0.04
	Po	n = 11	*med.*	90	1	0.8	130	0.2	2	2	0.5	0.2	0.09	0.1	0.05	0.09
			min.	4	0.02	0.3	3	0.1	0.1	0.008	0.2	0.05	0.01	0.1	0.01	0.009
			max.	1600	2	1	330	0.4	3	30	0.8	1	0.2	0.2	0.1	0.3

Table 5.2 Continue

Mineralized Zone	Sulfide		Isotope	59Co	66Zn	75As	77Se	101Ru	106 Pd	107Ag	111Cd	118Sn	123Sb	194Pt	197Au	209Bi
				ppm	ppm	ppm	ppm	ppm	ppm	ppm	ppm	ppm	ppm	ppm	ppm	ppm
			Ref. Mat.	MASS-1	MASS-1	MASS-1	MASS-1	Po725	Po725	MASS-1	MASS-1	MASS-1	MASS-1	Po725	Po725	MASS-1
Area 41 - Type III (N = 2)	Ccp	n = 4	*med.*	2	740	< 0.1	150	0.3	0.5	2	20	3	< 0.02	< 0.01	0.02	0.02
			min.	2	570	< 0.1	130	0.1	0.07	1	4	0.3	< 0.02	< 0.01	0.02	0.02
			max.	4	880	< 0.1	160	0.3	0.9	3	40	9	< 0.02	< 0.01	0.02	0.02
	Po	n = 3	*med.*	940	1	< 0.02	150	0.2	< 0.02	0.3	< 0.04	0.08	< 0.003	0.01	< 0.001	< 0.00004
			min.	400	1	< 0.02	120	0.06	< 0.02	0.1	< 0.04	0.05	< 0.003	0.01	< 0.001	< 0.00004
			max.	1500	1	< 0.02	150	2	< 0.02	0.3	< 0.04	0.1	< 0.003	0.01	< 0.001	< 0.00004
Area 41 - Type IV (N = 3)	Ccp	n = 11	*med.*	2	1100	0.6	120	0.1	0.3	3	10	7	0.2	0.1	0.008	0.03
			min.	0.6	700	0.09	30	0.08	0.08	0.6	4	2	0.07	0.1	0.005	0.01
			max.	4	1500	1	180	0.2	1	20	40	10	0.3	0.1	0.04	0.2
	Po	n = 7	*med.*	770	0.9	1	130	0.1	< 0.02	0.6	< 0.04	0.1	0.005	0.05	0.008	0.01
			min.	310	0.6	0.5	40	< 0.05	< 0.02	0.2	< 0.04	0.03	0.005	0.05	0.006	0.006
			max.	1600	1	2	160	0.2	< 0.02	2	< 0.04	0.4	0.005	0.05	0.03	0.07
Redstone (N = 3)	Ccp	n = 5	*med.*	0.5	290	2	150	0.2	0.2	10	6	1	0.2	< 0.01	0.007	< 0.0003
			min.	0.3	260	0.6	60	0.06	0.1	10	5	0.7	0.1	< 0.01	0.005	< 0.0003
			max.	5	2300	2	230	0.2	1	90	60	3	0.4	< 0.01	0.008	< 0.0003
	Cub	n = 5	*med.*	0.2	410	2	120	0.1	0.7	20	20	0.6	0.2	< 0.04	0.02	< 0.001
			min.	0.05	7	1	50	< 0.08	0.03	6	0.7	< 0.4	< 0.09	< 0.04	0.02	< 0.001
			max.	80	6000	3	170	0.3	4	40	190	3	0.4	< 0.04	0.02	< 0.001
	Po	n = 3	*med.*	330	0.7	1	70	0.5	< 0.02	1	< 0.04	0.2	0.04	< 0.002	< 0.001	< 0.00004
			min.	320	0.6	0.7	40	0.5	< 0.02	0.9	< 0.04	0.2	0.04	< 0.002	< 0.001	< 0.00004
			max.	400	2	2	110	0.5	< 0.02	1	< 0.04	0.4	0.04	< 0.002	< 0.001	< 0.00004

**N = number of thin sections n = number of analyses Ccp = chalcopyrite Cub = cubanite Bn = bornite Po = pyrrhotite Pn = pentlandite*

Less than values represent minimum detection limits

Table 5.3 Range of Cu/Pd and S/Se in the various mineralized zones in the Eastern Gabbro

Location of Mineralized Zone	Mineralized Zone	Sulfide Texture	Low Cu/Pd	High Cu/Pd	Low S/Se	High S/Se
Marathon deposit	Footwall Zone	Disseminated	5,427	13,352	6,817	17,117
		Semi-massive	7,250	8,555	21,000	296,328
	Main Zone	Disseminated	1,740	10,207	1,448	19,444
	W Horizon	Disseminated	34	1,650	293	16,344
Northwest of the Marathon deposit	Four Dams	Disseminated	10,036	109,500	1,115	3,103
	Area 41 - Type I	Disseminated	241,000	351,000	1,672	3,427
	Area 41 - Type II	Disseminated	3,961	11,969	1,167	152,520
	Area 41 - Type III	Disseminated	267	1,405	2,167	3,274
	Area 41 - Type IV	Disseminated	17,850	22,857	1,961	13,726
	Redstone	Disseminated	33,500	46,500	1,532	10,167
Other	Chalcopyrite-rich pod	Semi-massive	498		10,582	13,863

Table 5.4 Distribution coefficients between sulfide liquid, MSS, ISS, and silicate melt

Element	$D_x^{SL/SM}$	$D_x^{MSS/SM}$	$D_x^{ISS/SM}$
Zn	3.5	0.62	3.9
Pd	536,000	0.24	0.7
Ru	485,000	19	0.84
Au	11,200	0.09	1
Sn	8.6	0.6	0.16

**Data from Barnes and Ripley (2016) and references therein*

Chapter 6

Conclusion

This study integrates detailed mineralogy and textural characterization with high-resolution in situ chemical analyses to i) test whether mineral chemistry (Fe-Ti oxides and vein-hosted silicates) can be used as an exploration tool to identify fertile rock and ii) develop a genetic model for the formation of the Eastern Gabbro of the Coldwell Complex and the mineralization that it contains. The *exploration* aspect characterizes the chemistry of post-mineralization veins and how they vary with proximity to mineralization, characterizes the geochemical signatures of mineralized and unmineralized gabbros, and evaluates the applicability of current exploration tools to Ni-depleted, Cu-PGE systems. The *genetic* aspect characterizes the magmatic and post-magmatic histories of the various rock series in the Eastern Gabbro with emphasis on defining their petrogenetic relationship, and characterizes the magmatic and hydrothermal processes that formed the variable base metal and PGE enrichment.

6.1 Applicability of mineral chemistry to exploration for low-Ni, Cu-PGE systems

6.1.1 Vein-hosted mineral chemistry

Few studies have characterized the composition of vein-hosted minerals with proximity to mineralization in magmatic Ni-Cu-PGE sulfide deposits, and none have characterized how the chemistry of vein minerals varies in response to their local environment (e.g., host rock and mineral chemistry). To be a useful as an exploration tool, however, the chemistry of vein minerals must be independent of local effects and be primarily controlled by the composition of the fluids from which they precipitated.

At Marathon, vein-hosted minerals comprise a complex mixture of Fe-Mg chlorite, serpentine, saponite, and Ca-bearing amphibole, whereas the mineralogy of patchy alteration is simpler and consists predominantly of Ca-rich amphibole with lesser Fe-Mg chlorite. Vein-hosted minerals and minerals in patchy alteration crystallized from different

fluids during temporally-different events, with the vein minerals having formed later and from lower-temperature fluids. This is supported by the distinct mineralogy of veins and patchy alteration, the occurrence of veins that crosscut patchy alteration, and the distinct trace-element chemistry of vein-hosted and patchy alteration minerals, which was not influenced by local reaction with the host rocks and minerals.

Although the Co, Ni, and Zn content of vein-hosted minerals systematically decreases with proximity to mineralization, this apparent relationship is unrelated to mineralization. The host rock cannot be the source of these metals because vein-mineral chemistry does not correlate with the chemistry of the host rock. Pyroxene and Fe-Ti oxides likewise could not have been the source of these metals because veins hosted by these minerals are enriched in Ti, V, and Cr, whereas the Co, Ni, and Zn content are unaffected. Whereas sulfides are significant hosts of Co, Ni, and Zn, they also cannot be the source of these metals for the fluids because the metal content of vein minerals exhibit a negative, rather than positive, correlation with whole-rock Cu. Rather, the fluids derived Co, Ni, and Zn by progressive interaction with olivine, pyroxene, and Fe-Ti oxides as they migrated upwards through the pluton (i.e., increasing cumulative fluid-rock interaction with increasing height in the pluton). This is demonstrated by the systematic increase in Co, Ni, and Zn concentration with height in the pluton, which mimics the relationship with distance to mineralization. Consequently, because the Co, Ni, and Zn content of vein-hosted minerals increases systematically with height in the pluton, and the mineralized zones (Footwall Zone, Main Zone, W Horizon) occur at different heights in the pluton, the correlation between vein-hosted mineral chemistry and mineralization is a coincidence and does not relate to the Co, Ni, and Zn content of mineralization. These results act as an example of how mis-characterization of the small- and large-scale controls on mineral chemistry can lead to erroneous interpretations and should be viewed as a cautionary example for the application of the chemistry of such minerals as exploration tools in other systems.

Although the chemistry of vein minerals is not indicative of buried mineralization, variations in vein density may provide a valuable tool for locating zones of low-sulfide mineralization because vein density is lower in areas where mineralization is present. The

presence of sulfides is an obvious indication of mineralization, however, in mineralized zones characterized by high PGE grades, but low sulfide content, mineralization can only be identified from whole-rock assays, which are not available during core logging. Because vein-density is routinely measured during core logging, it can be used as a preliminary indication of mineralization, providing a basis for targeted assaying.

6.1.2 Fe-Ti oxide chemistry

Dare et al. (2014a) and Ward et al. (2018) both suggested that the Ni content of magnetite can be used as an indicator of mineralization, with the former suggesting that magnetite from mineralized plutons are depleted in Ni and the latter suggesting that they are enriched. Neither of these relationships applies to the Ni-depleted Eastern Gabbro. In the Eastern Gabbro, the Ni concentration of Fe-Ti oxide intergrowths hosted by mineralized Marathon Series is indistinguishable from those hosted by barren Marathon Series, whereas intergrowths from unmineralized metabasalt and Layered Series have higher and lower concentrations, respectively, compared to mineralized Marathon Series. The other chalcophile elements likewise show no distinct difference between mineralized and barren rock. This suggests that the chalcophile element content of oxides is not a robust indicator of mineralization, and that other factors need to be considered, such as the timing of sulfide liquation relative to oxide crystallization. The lack of chalcophile element variation between Fe-Ti oxides in mineralized and barren rock is likely due to the fact that sulfide liquated in all of the batches of magma from which the Marathon Series crystallized. Consequently, regardless of the timing of Fe-Ti oxide crystallization relative to sulfide liquation, their concentration of chalcophile elements would be similar. This is consistent with the interpretations of Shahabi Far et al. (2018), based on multiple S isotopes ($\Delta^{33}S$, $\Delta^{36}S$), that sulfide liquated at depth prior to significant crystallization of the magma.

It is well-established that the mineralization at Marathon, and the other occurrences north of Marathon, principally represent the concentration of metals by an immiscible sulfide liquid (Good et al., 2015; Ruthart, 2013; Shahabi Far et al., 2018). Yet, with respect to the discrimination diagrams of Dupuis and Beaudoin (2011), the composition of Fe-Ti oxide

intergrowths from mineralized areas of the Eastern Gabbro plot outside of the compositional field for Ni-Cu-PGE deposits, but plot within the compositional field for Fe-Ti, V deposits. Similar to Dupuis and Beaudoin (2011), the discrimination diagrams of Ward et al. (2018) do not accurately distinguish oxides from barren and mineralized rock in Ni-depleted systems given the large overlap in Ni contents of Fe-Ti oxide intergrowths from mineralized and barren rock in the Ni-depleted Eastern Gabbro. Nor does it accurately distinguish intergrowths from mafic and ultramafic rocks in these systems given that intergrowths from mafic and ultramafic rocks in the Eastern Gabbro have indistinguishable Cr/V.

Because these fertility indicators and discrimination diagrams are designed to be used for mineral exploration, it is often not known what mineral deposit type might be found in a given environment. Since these discrimination diagrams are not reliable in discerning magnetite from barren and mineralized rock hosted in different types of sulfide deposits, their application could lead to erroneous interpretations. Consequently, their application should be used with caution.

6.2 Application of mineralogy and mineral chemistry to petrogenesis

6.2.1 Magmatic history of the Eastern Gabbro

Whole-rock chemistry is often used to make inferences regarding the genesis of a suite of rocks. If those rocks represent cumulates, however, than the use of whole-rock chemistry is problematic because it does not represent bulk magma composition. This is, in fact, the case in the Eastern Gabbro. In situations such as these, the trace-element chemistry of minerals is a better proxy as it reflects magma composition at the time the mineral crystallized. Accordingly, the composition of Fe-Ti oxides is used to deduce the petrogenesis of the Eastern Gabbro, and build upon the interpretations made by Good et al. (2015).

The metabasalt, Layered Series, and Marathon Series all crystallized from magmas that originated from compositionally distinct magmas and that experienced different magmatic histories prior to intrusion. According to the Rayleigh fractional crystallization model, the metabasalt and Layered Series magmas experienced little to no magma mixing, with the Layered Series having crystallized from a more evolved magma than the metabasalt. The Marathon Series and the various rock types that it includes, however, crystallized from a mixture of several physically-distinct magma batches, some of which were more evolved than others. The degree of this mixing was controlled by the location and timing of emplacement of the magmas, in which the Two Duck Lake gabbro and apatitic clinopyroxenite experienced the greatest degree of mixing with primitive melt. The oxide melatroctolite exhibits the least amount of mixing, likely because it occurs as pod-like bodies that are isolated from the main Marathon Series intrusion. The Footwall Zone, Main Zone, and W Horizon of the Marathon deposit likewise could not have all crystallized from a single batch of magma that underwent fractional crystallization. This is because the distribution of compatible and incompatible elements in Fe-Ti oxides amongst these zones cannot be explained by the Rayleigh fractional crystallization model. Rather, these variations are likely due to variations in the composition of the melts from which each of the mineralized zones crystallized.

These interpretations are in agreement with previous work by Good et al. (2015) who concluded that the rocks of the Eastern Gabbro are genetically distinct from one another, and with the work of Shahabi Far (2016) that the Marathon Series experienced a late input of primitive melt. They are also in agreement with the recent classification of the Marathon deposit as a conduit-type Cu-PGE system. These results support the foundational work of previous studies (e.g., Dare et al., 2014b) that the chemistry of Fe-Ti oxides can be a valuable tool in characterizing the petrogenesis of complex igneous suites.

6.2.2 Post-magmatic history of the Eastern Gabbro

Two mineralogically- and texturally-distinct end-member varieties of Fe-Ti oxides occur throughout the Eastern Gabbro: i) cloth-textured magnetite-ulvöspinel intergrowths and ii)

trellis-textured magnetite-ilmenite intergrowths. A continuous series of textures also occur that are mineralogically and texturally intermediate to the cloth and trellis varieties. Several lines of mineralogical, textural, and compositional evidence indicate that these intergrowths formed via subsolidus, fluid-induced oxidation, or oxy-exsolution, of ulvöspinel (Buddington and Lindsley, 1964; Verhoogen, 1962). Although some of the textural evidence described in the dissertation has been noted in previous studies (e.g., Duchesne, 1970; Speczik et al., 1988; von Gruenewaldt et al., 1985), few studies have characterized, in situ, the mineralogy of the cloth lamellae, and there are no published data from any setting on the trace-element chemistry of the various textural types of Fe-Ti oxide intergrowths.

Using Raman spectroscopy, the mineralogy of the cloth lamellae was characterized, in situ, as ulvöspinel. The bulk major-element composition of the different intergrowth varieties are indistinguishable, precluding the possibility that they formed from compositionally distinct magnetite-ulvöspinel solid solutions. In addition, cloth-textured Fe-Ti oxide intergrowths consistently have lower Fe^{3+} : Fe^{2+} than the trellis varieties, indicating that the latter had to have formed via oxidation of the former. With regards to their trace-element chemistry, trellis-textured intergrowths are consistently enriched in the multivalent elements Ge, Mo, W, Sn, and Cu compared to cloth-textured intergrowths, indicating that the fluid carried these metals. Additionally, because these metals are only compatible in Fe-Ti oxides in their oxidized state, the fluid must also have been oxidizing. The concentration of the multivalent element V, however, exhibits no systematic variation among the various textural types of Fe-Ti oxide intergrowths. Because all of the terrestrially-relevant oxidation states of V are compatible in Fe-Ti oxides, this suggests that it was not present in the oxidized fluid. Similarly, the elements of interest with single oxidation states at terrestrially-relevant conditions (Zn, Ni, Co, Sc, Cr, HFSE) exhibit no systematic variation among the intergrowths. Because these elements behave compatibly in magnetite, ulvöspinel, and/or ilmenite, this suggests that they were either not present in significant concentrations in the oxidized fluid and/or that their concentrations were unaffected by the change in Fe^{2+}, Fe^{3+}, and Ti^{4+} sites during oxidation.

Given the occurrence of CO_2 and CH_4 in apatite- and pyroxene-hosted fluid inclusions in the Eastern Gabbro, it is proposed that CO_2 rather than O_2 was the main oxidizing agent in such systems, where the C in CO_2 was reduced to form CH_4:

$$9Fe_2^{2+}TiO_4 + 0.75CO_2 + 1.5H_2O \leftrightharpoons 9Fe^{2+}TiO_3 + 3Fe_2^{3+}Fe^{2+}O_4 + 0.75CH_4 \quad \text{eq. 6.1}$$

This model has two important implications. First, previous models invoked O_2 in water as the oxidizing agent, but crustal fluids have very low pO_2. This model, however, invokes C in CO_2 as the oxidizing agent, which is a common component in fluids in Ni-Cu-PGE deposits. Second, this oxidation model can generate magnetite-ilmenite intergrowths and CH_4 without generating hydrous alteration, features that are characteristic of many mafic rocks, including those that host Ni-Cu-PGE mineralization.

Variable distribution of the different textural varieties of Fe-Ti oxides throughout the Eastern Gabbro suggests that different rock types and mineralized occurrences experienced different degrees of fluid-induced oxidation. Of the rock series, the Marathon Series must have experienced a much greater degree of postcumulus, fluid-induced oxidation compared to the metabasalt and Layered Series as trellis-textured Fe-Ti oxide intergrowths are more common in the former. In fact, trellis-textured Fe-Ti oxide intergrowths are absent altogether in the Layered Series, suggesting these rocks experienced the least amount of oxidation. With regards to the mineralized occurrences in the Eastern Gabbro, from lowest to highest degree of fluid-induced oxidation, they are i) Redstone and Four Dams, ii) magnetite-apatite-clinopyroxene cumulate, iii) W Horizon and Area 41, and iv) Main Zone and Footwall Zone. The relatively high degree of oxidation that is observed in the W Horizon is consistent with the recent work of Ames et al. (2017), who interpreted the association of PGM with millerite and secondary magnetite in the W Horizon as the result of oxidation of Fe^{2+} to Fe^{3+}. Secondary mineralization in the Layered Series only hosts cloth-textured Fe-Ti oxide intergrowths, suggesting that it experienced the lowest degree of fluid-induced oxidation compared to the other mineralized zones.

6.2.3 Magmatic versus hydrothermal mineralizing processes

Although several studies have suggested that metals were remobilized at the Marathon deposit (e.g., Samson et al., 2008) and in other magmatic Ni-Cu-PGE deposits (e.g., Li et al., 2007, 2004) based on the recognition of equilibrium and disequilibrium sulfide textures, few have characterized the composition of the texturally diverse sulfides. Integration of texture and chemistry, however, is critical to understanding the origin of sulfides and, consequently, understanding the magmatic and postmagmatic processes that generated and modified mineralization.

Sulfides in the mineralization at the Marathon Cu-Pd deposit and those northwest of Marathon are mineralogically, texturally, and chemically distinct, suggesting that the processes that generated each of the mineralized zones were different. In all of the mineralized zones, sulfides exhibit both equilibrium and disequilibrium textures. The equilibrium sulfides, which exhibit planar or curved boundaries with each other, as well as with silicates and other minerals, crystallized from a sulfide liquid as the distribution of IPGE and base metals among them is consistent with partitioning between monosulfide solid solution (MSS) and intermediate solid solution (ISS). However, Pt, Pd, Au, Ag, and main-group element concentrations are similar among all of the sulfides, contrary to their partitioning behavior between MSS and ISS. This is the result of exsolution of Pt- and Pd-rich platinum-group minerals (PGM) and Au-Ag alloys, which would have decreased the concentration of these elements in the sulfide, but would not have affected the concentration of base metals.

The disequilibrium sulfides comprise the replacement of pyrrhotite or pyrite by chalcopyrite and the vari-textured intergrowths of predominantly chalcopyrite with secondary hydrous minerals. The former, which, to the authors knowledge, has not been documented in other mineral deposits, could only have been generated by interaction of pyrrhotite with a Cu-rich hydrothermal fluid because the textures are dissimilar to classic resorption textures. Likewise, most of the sulfide-hydrous silicate intergrowths also must have been precipitated from a hydrothermal fluid based on the textural relationships

between sulfides and the hydrous silicates (e.g., the preferential orientation of actinolite blades in chalcopyrite).

Hydrothermal chalcopyrite is compositionally similar to magmatic chalcopyrite. This similarity can be explained through dissolution of magmatic chalcopyrite in one location followed by the transport and precipitation of the metals as secondary chalcopyrite in another location. This suggests that the fluid from which secondary chalcopyrite precipitated carried similar metals as those hosted in magmatic chalcopyrite and in similar concentrations. This redistribution of metals only occurred locally within a given mineralized zone because the Cu/Pd values of both the Footwall Zone and Main Zone are similar, and both lie within the range of mantle values, indicating that metals were not added or removed on a large scale.

Few studies have made a direct comparison between the composition of magmatic and hydrothermal sulfides (e.g., Keays et al., 1982; Lesher and Keays, 2002), none of which were made between sulfides hosted in the same deposit or even the same type of deposit. This has made it difficult to compare how metals behave during magmatic and hydrothermal mineralizing processes. The integration of sulfide textures and chemistry described above is, therefore, unique in that it is one of few studies that directly compared the composition of sulfides that crystallized from a fractionating sulfide liquid to those that precipitated from high-temperature hydrothermal fluids.

6.2.4 Mineralizing processes in the various mineralized zones

Although the PGE content of sulfides is often modified by the exsolution of PGM, as is the case for sulfides in the Eastern Gabbro, they are still commonly used to make inferences about the magmatic processes that generated mineralization. This, however, can lead to erroneous interpretations. Rather, a proxy for the PGE should be used that was not modified by subsolidus processes, such as S/Se ratios.

Sulfides in the W Horizon of the Marathon deposit experienced the highest R factors, followed by the Main Zone and the Footwall Zone. This is supported by the variation in Cu/Pd among each of the zones. Sulfides in the mineralized occurrences northwest of Marathon experienced lower R factors than all of the zones in the Marathon deposit. This is supported by the higher cubanite to chalcopyrite ratio in the northern occurrences compared to Marathon. These variations in R factor, however, are not reflected in the S/Se of the mineralized zones or the Cu/Pd of the northern occurrences.

The greater-than-mantle S/Se in all of the Footwall Zone sulfides and a subset of the Main Zone sulfides, which have correspondingly low $\Delta^{33}S$ (Shahabi Far et al., 2018), are indicative of contamination by high S/Se sedimentary rocks. This is consistent with the interpretations made by Shahabi Far et al. (2018), based on multiple S isotopes, that the Footwall Zone experienced the highest degree of contamination out of all of the mineralized zones at Marathon, followed by the Main Zone. The general positive correlation between Cu/Pd and S/Se for most of the W Horizon sulfides suggests that the S/Se values are, at least to some degree, controlled by variability in R factor. Few sulfides, however, have values greater than the mantle range and are indicative of contamination by high S/Se rocks, whereas many sulfides have values much lower than the mantle range and are indicative of S loss. Sulfur loss has been previously proposed by Good (2010) and Ruthart (2013) in the form of multistage dissolution upgrading (Kerr and Leitch, 2005) to account for the high PGE, low sulfide content of the W Horizon. The presence of significant amounts of bornite in the W Horizon further supports the occurrence of S loss. The greater-than-mantle Cu/Pd in the northwestern occurrences were generated by removal of Pd through the segregation of sulfides at depth because low R factors cannot generate Cu/Pd values greater than mantle values (Barnes et al., 1993). This process, however, is not reflected in the S/Se, which are consistently lower than the mantle range. Therefore, in addition to sulfide removal, the northwestern occurrences must also have experienced contamination by low S/Se rocks, potentially the metavolcanic and granitoid country rocks to the Eastern Gabbro (Walker et al., 1993). The semi-massive chalcopyrite-rich pod represents a unique style of mineralization in the vicinity of the Coldwell Complex, with Pd grades of up to 100 ppm. To generate its unique lower-than-mantle Cu/Pd and higher-

than-mantle S/Se, the sulfides that it hosts must have experienced both high R factors similar to the W Horizon, as well as contamination by high S/Se rocks, similar to the Footwall Zone.

These results support the recent interpretation that the Marathon deposit experienced variable degrees of S contamination, including the PGE-rich W Horizon (Shahabi Far et al., 2018). They also support the multistage dissolution upgrading model as a mechanism that played a role in generating the high PGE abundances in the W Horizon. Significantly, these results provide a first look into the processes that generated mineralization in the occurrences northwest of Marathon, which, until now, were unknown. The diversity of magmatic processes that were characterized for the various mineralized zones that occur throughout the Eastern Gabbro illustrate the complexity of this system and highlight the importance of integrating detailed mineralogy and textural characterization with mineral chemistry.

6.3 References

Ames, D.E., Kjarsgaard, I.M., McDonald, A.M., Good, D.J., 2017. Insights into the extreme PGE enrichment of the W Horizon, Marathon Cu-Pd deposit, Coldwell Alkaline Complex, Canada: Platinum-group mineralogy, compositions and genetic implications. Ore Geol. Rev. 90, 723–747.

Barnes, S.-J., Couture, J.-F., Sawyer, E.W., Bouchaib, C., 1993. Nickel-Copper Occurrences in the Belleterre-Angliers Belt of the Pontiac Subprovince and the Use of Cu-Pd Ratios in Interpreting Platinum-Group Element Distributions. Econ. Geol. 88, 1402–1418.

Buddington, A.F., Lindsley, D.H., 1964. Iron-titanium oxide minerals and synthetic equivalents. J. Petrol. 5, 310–357.

Dare, S.A.S., Ames, D.E., Lightfoot, P.C., Barnes, S.-J., Beaudoin, G., 2014a. Mineral chemistry and supporting databases for TGI4 project on “Trace elements in Fe-oxides from fertile and barren igneous complexes: Investigating their use as a

vectoring tool in the intrusions that host Ni-Cu-PGE deposits". Geological Survey of Canada Open File No. 7538.

Dare, S.A.S., Barnes, S.-J., Beaudoin, G., Méric, J., Boutroy, E., Potvin-Doucet, C., 2014b. Trace elements in magnetite as petrogenetic indicators. Miner. Deposita 49, 785–796.

Duchesne, J.-C., 1970. Microtextures of Fe-Ti oxide minerals in the South-Rogaland anorthositic complex (Norway). Ann. Société Géologique Belg. 935, 527–544.

Dupuis, C., Beaudoin, G., 2011. Discriminant diagrams for iron oxide trace element fingerprinting of mineral deposit types. Miner. Deposita 46, 319–335.

Good, D.J., 2010. Applying multistage dissolution upgrading and 3D-GIS to exploration at the Marathon Cu-PGE deposit, Canada, in: 11th International Platinum Symposium, Sudbury, Ontario, Canada.

Good, D.J., Epstein, R., McLean, K., Linnen, R., Samson, I., 2015. Evolution of the Main Zone at the Marathon Cu-PGE Sulfide Deposit, Midcontinent Rift, Canada: Spatial Relationships in a Magma Conduit Setting. Econ. Geol. 110, 983–1008.

Keays, R.R., Nickel, E.H., Groves, D.I., McGoldrick, P.J., 1982. Iridium and palladium as discriminants of volcanic-exhalative, hydrothermal, and magmatic nickel sulfide mineralization. Econ. Geol. 77, 1535–1547.

Kerr, A., Leitch, A.M., 2005. Self-Destructive Sulfide Segregation Systems and the Formation of High-Grade Magmatic Ore Deposits. Econ. Geol. 100, 311–332.

Lesher, C.M., Keays, R.R., 2002. Discrimination between Magmatic and Hydrothermal Ni-Cu-PGE and PGE Mineralization, in: 9th International Platinum Symposium. Stillwater, USA.

Li, C., Ripley, E.M., Merino, E., Maier, W.D., 2004. Replacement of base metal sulfides by actinolite, epidote, calcite, and magnetite in the UG2 and Merensky Reef of the Bushveld Complex, South Africa. Econ. Geol. 99, 0173–0184.

Li, C., Ripley, E.M., Oberthür, T., Miller, J.D., Joslin, G.D., 2007. Textural, mineralogical and stable isotope studies of hydrothermal alteration in the main sulfide zone of the

Great Dyke, Zimbabwe and the precious metals zone of the Sonju Lake Intrusion, Minnesota, USA. Miner. Deposita 43, 97.

Ruthart, R., 2013. Characterization of High-PGE Low-Sulphur Mineralization at the Marathon PGE-Cu Deposit, Ontario (MSc). University of Waterloo.

Samson, I.M., Fryer, B.J., Gagnon, J.E., 2008. The Marathon Cu-PGE deposit, Ontario: Insights from sulphide chemistry and textures. Presented at the Goldschmidt, p. A820.

Shahabi Far, M., 2016. The magmatic and volatile evolution of gabbros hosting the Marathon PGE-Cu deposit: evolution of a conduit system (PhD Dissertation). University of Windsor, Windsor.

Shahabi Far, M., Samson, I.M., Gagnon, J.E., Good, D.J., Linnen, R.L., Layne, G.D., Wing, B.A., 2018. Identifying externally derived sulfur in conduit-type Cu–platinum-group element deposits: The importance of multiple sulfur isotope studies. Geology 46, 235–238.

Speczik, S., Wiszniewska, J., Diedel, R., 1988. Minerals, exsolution features and geochemistry of Fe-Ti ores of the Suwalki District (North-East Poland). Miner. Deposita 23, 200–210.

Verhoogen, J., 1962. Oxidation of iron-titanium oxides in igneous rocks. J. Geol. 70, 168–181.

von Gruenewaldt, G., Klemm, D.D., Henckel, J., Dehm, R.M., 1985. Exsolution Features in Titanomagnetites from Massive Magnetite Layers and Their Host Rocks of the Upper Zone, Eastern Bushveld Complex. Econ. Geol. 80, 1049–1061.

Walker, E.C., Sutcliff, R.H., Shaw, C.S.J., Shore, G.T., Penczak, R.S., 1993. Precambrian Geology of the Coldwell Alkalic Complex. Ontario Geological Survey Open File No. 5868.

Ward, L.A., Holwell, D.A., Barry, T.L., Blanks, D.E., Graham, S.D., 2018. The use of magnetite as a geochemical indicator in the exploration for magmatic Ni-Cu-PGE sulfide deposits: A case study from Munali, Zambia. J. Geochem. Explor. 188, 172–184.

VITA AUCTORIS

Matthew Brzozowski was born in 1990 in Windsor, Ontario, Canada. He studied Geological Sciences at the University of Windsor, where he obtained his B.Sc. degree in 2012. He began his M.Sc. at the University of Windsor in 2012 and transferred to his Ph.D. in 2014.